# Cosmological Applications of Weak Gravitational Flexion

BARNABY THOMAS PETER ROWE

Institute for Astronomy

School of Physics


A thesis submitted to the University of Edinburgh

for the degree of Doctor of Philosophy

May 2008

# Abstract

Modern cosmology has reached an important juncture, at which the ability to make measurements of unprecedented accuracy has led to conclusions that are a fundamental challenge to natural science. The discovery that, in our current best model, the dynamics of the Universe are completely dominated by unseen dark matter and dark energy can do little but completely alter the shape of physics research in the 21st Century. Unfortunately, much of our insight into these phenomena must come from observations of visible matter alone; this raises serious problems, as the tracing of dark matter by visible matter is as yet poorly understood.

Gravitational lensing offers strong prospects for probing the interwoven history of dark and visible matter, as mass in any form may be detected where it exists untraced by baryons. In this Thesis I describe advances made in the field of weak gravitational lensing, which constrains the properties of the matter distribution on cosmological scales using a statistical analysis of the coherent gravitational distortions of distant galaxy images. I summarize the development of gravitational flexion, a higher order extension to traditional weak lensing, and describe my work done to bring the study of flexion to a stage where it may be employed to make accurate cosmological measurements. I show how flexion is sensitive to matter structure on smaller physical scales than existing lensing techniques and, therefore, promises to shed new light upon key untested predictions of cosmological models if it can be measured to sufficient accuracy. I discuss the success of my efforts in this direction, and describe the issues to be encountered in the careful analysis of this subtle gravitational signal.

This research has involved advances in many areas: the calculation of theoretical flexion predictions, the refinement of image analysis methods for accurate galaxy shape estimation, and the practical application of these new flexion techniques to extragalactic imaging data. The culmination of these efforts is a new maximum likelihood analysis of the galaxy-galaxy lensing signal in the *Hubble Space Telescope* Galaxy Evolution from Morphology and SEDs (GEMS) Survey, incorporating improvements and modifications necessary for the combination of flexion with traditional weak lensing measurements. The results of this work, and particularly the extent to which measurements of flexion provide extra cosmological insight, are discussed in detail.

The conclusion is a summary of all that has been learned about the use of flexion as an accurate probe of cosmology, and a discussion of its prospects for answering some of the many questions that remain about dark matter. Within the next few year wide-area survey telescopes will begin imaging huge volumes of deep space, with the measurement of the gravitational lensing signal being given high priority in the analysis of these data. Within this context, the primary inquiry of this Thesis is the extent to which the application of flexion measurement techniques will help shed new light upon the unseen, and currently poorly understood, components of the Universe.

# Declaration

I hereby declare that this thesis entitled *Cosmological Applications of Weak Gravitational Flexion* is not substantially the same as any that I have submitted for a degree or diploma or other qualification at any other University. I further state that no part of my thesis has already been or is being concurrently submitted for any such degree, diploma or other qualification.

Parts of the work contained in this thesis have been published, or are due to be published, in refereed scientific journals.

Flexion theory and predictions – *'Weak gravitational flexion'*, Bacon, D. J., Goldberg, D. F., Rowe, B. T. P., Taylor, A. N. 2006, Monthly Notices of the Royal Astronomical Society, Volume 365, Issue 2, pp. 414-428.

Shear and flexion estimation – *'Weak gravitational shear and flexion with polar shapelets'*, Massey, R., Rowe, B., Refregier, A., Bacon, D. J., Bergé, J. 2007, Monthly Notices of the Royal Astronomical Society, Volume 380, Issue 1, pp. 229-245.

Shapelet pipeline and results including calibration with simulations – *'Shapelet measurements of shear and flexion in the* HST *STAGES and GEMS surveys'*, Rowe, B., Bacon, D. J., Heymans, C., Taylor, A., Goldberg, D. M., Massey, R., Barden, M., Caldwell, J. A. R., Monthly Notices of the Royal Astronomical Society, in preparation.

Galaxy-galaxy lensing results – *'Halo properties from combined galaxy-galaxy flexion and shear in the* HST *GEMS survey'*, Rowe, B., Bacon, D. J., Heymans, C., Taylor, A., Goldberg, D. M., Massey, R., Barden, M., Bell, E. F., Caldwell, J. A. R., Monthly Notices of the Royal Astronomical Society, in preparation.

This thesis is the outcome of my own work except where specifically indicated in the text.

Barnaby Rowe
Edinburgh,
May 2008.

# Acknowledgements

My most sincere thanks must firstly go to my Primary Supervisor David Bacon, for his tireless enthusiasm, warm encouragement and dedication to my studies. His willingness to give up his time to forward this work was remarkable, and is recognised with real gratitude. I would also like to thank my Secondary Supervisor Andy Taylor, for his encouragement and similar willingness to enter into many fruitful and instructive discussions with me.

Catherine Heymans must also be thanked for her kind help, the benefits of her experience with the GEMS data and for giving access to a variety of extremely useful GEMS object catalogues. I would also like to thank Richard Massey; His knowledge and experience of shapelet theory and practice was invaluable in this Thesis. I enjoyed working with Catherine and Richard very much and hope that I will get further chances in the future. For a variety of useful discussions, encouragement, practical suggestions and provision of data I would also like to thank: Alan Heavens, Bob Mann, Avery Meiksin, John Peacock, Peder Norberg, Dave Goldberg, Stella Seitz, Xinzhong Er, Eric Bell and Marco Barden.

On a more personal note, I want to thank all of my friends in Edinburgh and elsewhere for their love and support (some of whom even love and support me still), with fondest thanks in particular going to Annie, Dan, Mairi, Sophie and Will. Equal thanks should go to the blokes in the band, Andy, Ben and Henrik, for being such close friends and for making my time in the city so happy and memorable. Finally, I wish to thank those closest in my family: my parents Peter and Elizabeth, and my siblings Sophie and Gregory. You have all shown me a wonderful amount of love, kindness and encouragement. Sometimes it was needed; it has been very gratefully received.

# Contents

# List of Figures

# CHAPTER 1

# INTRODUCTION

The last ten years have seen dramatic developments in our understanding of the Universe, leaving a picture that few would have predicted within even the recent past. Unseen dark energy and dark matter, which are necessary in order to match observations of both the afterglow of early expansion and latter-day structure in the Universe, present all of physics with an unforeseen challenge. Are we really seeing the effects of exotic new forms of matter and energy? If so, what impact will this have on our understanding of physics?

In this Chapter, I make a brief summary of the cosmological model that describes the expansion of the Universe from the first moments after the Big Bang to the present day, a model in which dark matter and dark energy play key roles. The formation of large scale structure through gravitational collapse is also discussed, before an introduction to *gravitational lensing*, an important technique for observing dark matter and inferring the properties of dark energy. Finally, I review the theory behind *weak gravitational flexion*, a recent extension to the formalism of weak lensing. In this way I introduce the background necessary for the central topics of this Thesis: the application of flexion to accurate cosmological measurements and the promise such measurements show for illuminating dark matter structure and thereby the dynamics of the Universe as a whole.

## 1.1 Background cosmology

The concordance cosmological model describes a Universe that is spatially flat, undergoing accelerating expansion due to the presence of dark energy (DE or $\Lambda$), and which forms large scale matter structure through the collapse of invisible cold dark matter (CDM). Due to the lack of an equallly successful alternative theory, this model has come to a somewhat lonely prominence, despite its reliance on dark components that remain to be directly observed. Although we remain without an understanding of these unseen phenomena on a particle level, the $\Lambda$CDM model has been extremely successful in reproducing many of the features of the cosmic microwave background (CMB) as revealed by the Wilkinson Microwave Anisotropy Probe (WMAP, see Figure 1.1; Spergel et al. 2007; Bennett et al. 2003; Spergel et al. 2003). It is also the strongest explanation for a large number of other astronomical observations, including distance measurements made using Type Ia supernovae (see, e.g., Riess et al. 2007; Astier et al. 2006; Conley et al. 2006; Riess et al. 2004), the shape and amplitude of the large-scale structure seen in the distribution of galaxies (Sánchez et al. 2006; Tegmark et al. 2006; Percival et al. 2007b) and more recently the imprint of baryon acoustic oscillations in the early Universe (e.g. Percival et al. 2007a). These and other measurements support the picture of a flat Universe dominated by vacuum energy (or a cosmological constant) at a proportion of around 75 per cent, with CDM making up the majority of the remaining $\simeq 25$ per cent of the energy density; baryonic matter is thought to make up only 4-5 per cent of the Universe at most. A short summary of current best constraints on this cosmological model will be given in Section 1.1.8.

This broad picture of the matter and energy budget, in combination with two powerful simplifying assumptions about inherent symmetries in cosmic dynamics, allows us to construct a simple but successful model of cosmological expansion. In Sections 1.1.1 and 1.1.2 a brief outline of this basic Big Bang cosmology is presented, described as an expanding solution to the field equations of Einstein's General Relativity. Building on these topics, Sections 1.1.3 and 1.1.4 explain the notion of redshift and the definition of distances within curved, expanding spacetimes, fundamental concepts in the concordance cosmological picture.

Observed structure, such as stars, galaxies and galaxy clusters, is believed to form within this model via gravitational instability and collapse. The seeds of this instability are tiny density perturbations, thought to exist due to quantum fluctuations during the initial expansion of an early Universe that is otherwise homogeneous. These perturbations then become amplified by the action of gravitational attraction, eventually reaching the beautiful complexity and diversity of structure we observe today. Wherever the local self-gravitation of matter is negligible, the dynamics of these fluctuations may be described using linear perturbation theory, as described in depth by Peacock (1999) and briefly in Section 1.1.5. However, this condition is clearly not met in the regions of the local Universe where we observe gravitationally collapsed structures such as stars and galaxies.

Perhaps the critical test of the $\Lambda$CDM model will be its ability to accurately predict the distribution of this observable matter, and its evolution. Some simple results describing self-gravitational collapse in this non-linear regime can be solved analytically, as described in Section 1.1.5. In Section 1.1.6 the spherical or 'top hat' collapse model is outlined, from which the cosmological definition of the bound, collapsed objects known as haloes is generally drawn. These dark matter objects are thought to surround galaxies and galaxy clusters, thus providing one explanation both for the discrepancies between galaxy rotation curves and luminous matter distributions (see, e.g., Noordermeer et al. 2007), and for the high galaxy velocity dispersions within galaxy clusters (Zwicky 1933, 1937).

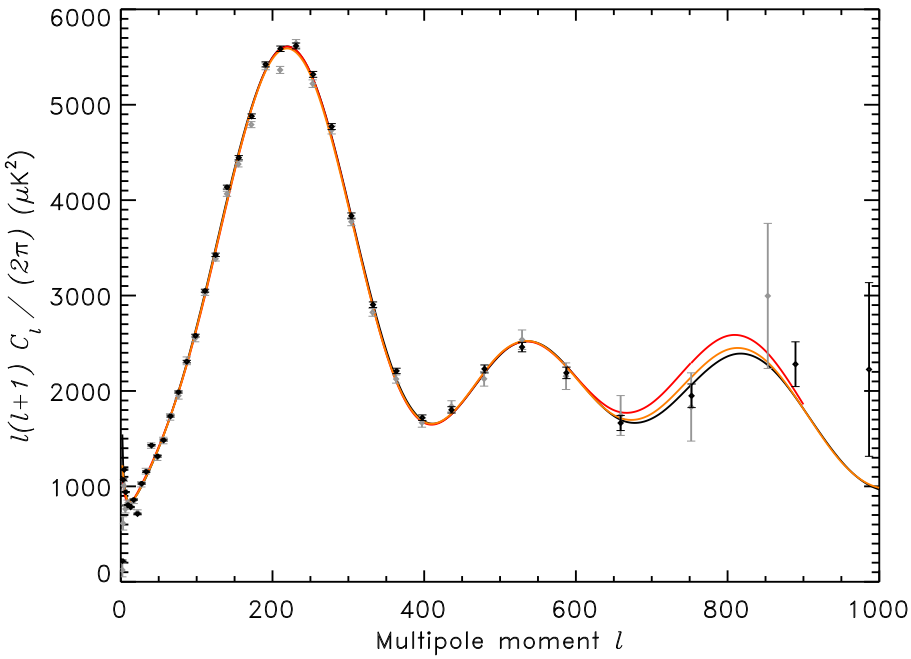


Figure 1.1: Comparison of the best-fit ΛCDM models to the WMAP 1- and 3-year TT (temperature-temperature) angular power spectrum data. The solid data points are for the 3-year data and the grey points the 1-year data. Figure taken from Spergel et al. (2007).

However, more realistic modelling of dark matter structure is impossible without employing numerical calculations, and to this end a vast amount of work has taken place in the field of cosmological N-body simulation, described briefly in Section 1.1.7. These simulate the evolution of fluid, pressureless CDM over cosmological timescales, with the largest and most recent example being the Millennium Simulation carried out by the Virgo Consortium (see Springel et al. 2005). At recent epochs these simulations predict a filamentary dark matter distribution, populated by many dark matter haloes on a wide variety of mass scales. Importantly, theoretical results for the profiles of dark matter haloes, summarized in greater detail in Section 1.1.9, are yet to be well constrained by actual observations of the physical Universe.

Finally, the concordance model not only makes detailed predictions for the size, shape and distribution of dark matter haloes, but also for the abundance and spatial distribution of subhaloes within haloes, or halo substructure. Simulation work supports the picture of hierarchical formation of CDM haloes by multiple mergers and accretion (see White & Rees 1978), and this leaves large amounts of this remnant substructure. In Section 1.1.10 these predictions are described and summarized, and compared against the current constraints available from observational data. To begin with, however, we review the founding concepts of modern cosmology, a Universe governed on the largest scales by the dynamics of an expanding spacetime.

### 1.1.1 Friedmann-Lemaître cosmological models

The standard model of our Universe is a solution of Einstein's field equations within the framework of General Relativity, underpinned by the following two postulates (see, e.g., Peacock 1999; Rindler 2001):

1. When averaged over sufficiently large scales, there exists a mean motion of radiation and matter in the Universe with respect to which all averaged observable properties are *isotropic* – they look the same in any direction.

2. All 'fundamental observers', imagined observers that follow this mean motion, experience the same history of the Universe, i.e. the same averaged observable properties, provided they set their clocks suitably. Such a Universe is called observer-*homogeneous* – it looks the same from any position.

The second postulate follows on from the first if we invoke what is known as the Copernican principle, that we occupy no special position in the Universe. The assumption that on average the Universe is both isotropic and homogeneous is known as the cosmological principle, and allows us to define a universal time coordinate which we call the cosmological time $t$. This is the time as measured by fundamental observers and is synchronised by these observers setting their clocks to a standard time when the universal uniform density reaches a given value.

These two postulates also significantly constrain the metric tensor $g_{\mu\nu}$, used in writing the general line element in relativistic spacetime:

$$\mathrm{d}s^2 = c^2\mathrm{d}\tau^2 = g_{\mu\nu}\mathrm{d}x^\mu\mathrm{d}x^\nu. \tag{1.1}$$

This is an infinitesimal statement of Pythagoras' Theorem and is used to describe the geometry of spacetime. We then have the freedom to write the metric in the following form, with a part corresponding to cosmic time, and a spatial part:

$$c^2\mathrm{d}\tau^2 = c^2\mathrm{d}t^2 - g_{ij}\mathrm{d}x^i\mathrm{d}x^j. \tag{1.2}$$

A metric tensor of this form, in which the off-diagonal components $g_{0i}$ vanish, is a choice that is admitted within an isotropic Universe. Here then $g_{ij}$ is the metric tensor of 3-space, a hypersurface within four-dimensional spacetime.

Isotropy and homogeneity then force conditions upon the spatial part of the metric we have written in Equation (1.2). It must only be able to expand or contract isotropically by a scaling factor we call $a$, which must be a function of time $a(t)$ only, otherwise the expansion would be different at different places in the Universe, violating homogeneity. Hence the metric further simplifies to

$$c^2\mathrm{d}\tau^2 = c^2\mathrm{d}t^2 - [a(t)]^2\mathrm{d}\ell^2 \tag{1.3}$$

where $\mathrm{d}\ell$ is the line element of the isotropic, homogeneous 3-space.

Due to homogeneity, we expect that the degree of spatial curvature must be the same at all places and this is enough to determine the form of the metric. Isotropy requires spherical symmetry: spatial surfaces (not the three-dimensional spatial hypersurface), if a constant distance from an arbitrary point, need to be two-spheres, i.e., normal spheres. Homogeneity allows an arbitrary point to be chosen as the origin for our set of coordinates, and the spherical symmetry allows the spatial part of the metric to be decomposed into a radial and a transverse part, written in its most generally admissible form as

$$\mathrm{d}\ell^2 = \mathrm{d}r^2 + S_k^2(r)\mathrm{d}\psi^2 = \mathrm{d}r^2 + S_k^2(r)\{\mathrm{d}\theta^2 + \sin^2\theta\,\mathrm{d}\phi^2\} \tag{1.4}$$

where the two angles $\theta$ and $\phi$ are those of spherical polar coordinates, which uniquely identify positions on the unit sphere around the origin.

It is the postulate of homogeneity which determines the form of the radial function $S_k^2(r)$, as it demands that spatial curvature is uniform across the Universe. This curvature, labelled $k$, must therefore be either constant negative, constant positive or zero (flat), and this allows us to set

$$S_k(r) = \begin{cases} \frac{1}{\sqrt{-k}} \sinh(r\sqrt{-k}) & k < 0 \\ r & k = 0 \\ \frac{1}{\sqrt{k}} \sin(r\sqrt{k}) & k > 0 \end{cases} . \tag{1.5}$$

The overall metric for an isotropic, homogeneous Universe may then be written as

$$c^2 \mathrm{d}\tau^2 = c^2 \mathrm{d}t^2 - [a(t)]^2 \{\mathrm{d}r^2 + S_k^2(r)(\mathrm{d}\theta^2 + \sin^2\theta \, \mathrm{d}\phi^2)\}, \tag{1.6}$$

which is known as the Robertson-Walker metric. We note that conventionally, at the present epoch $t = t_0$, we set the scale factor of the Universe to be $a_0 = a(t = t_0) = 1$.

### 1.1.2 Expansion and the Friedmann equation

In order to the derive the equations which describe the expansion and possible contraction of the Universe, and which relate this action to the matter-energy content of the Universe, we need to resort to further aspects of General Relativity; for good introductions to this subject in the cosmological context see either Peacock (1999) or Rindler (2001). The Einstein Tensor is defined as

$$G^{\mu\nu} = R^{\mu\nu} - \frac{1}{2} g^{\mu\nu} R, \tag{1.7}$$

where $R^{\mu\nu}$ is the Ricci Tensor and $R$ is the related curvature scalar, $R = g_{\mu\nu} R^{\mu\nu}$. Again the reader is referred to Rindler (2001) for the precise details of these objects. Einstein's field equations, relating the Einstein-Tensor to the energy-momentum tensor $T^{\mu\nu}$ of the matter in the Universe, are written as:

$$G^{\mu\nu} + g^{\mu\nu}\Lambda = -\frac{8\pi G}{c^4} T^{\mu\nu}. \tag{1.8}$$

The second term of Equation (1.8), proportional to the metric tensor $g^{\mu\nu}$, is a generalization which Einstein originally introduced to allow static cosmological solutions of the field equations, $\Lambda$ being hence known as the cosmological constant.

The highly symmetric form of the Robertson-Walker metric seen in Equation (1.6), together with the requirement that the Universe be both homogeneous and isotropic, constrains the form of the energy-momentum tensor to being that of the perfect fluid. In the rest frame then

$$T^{\mu\nu} = diag(\, \rho(t)c^2, P(t), P(t), P(t)\,), \tag{1.9}$$

where $\rho(t)$ denotes the energy density of the Universe and $P(t)$ the pressure (flux density of x-momentum in the x-direction, etc.). We note that both these quantities are time varying only, again due to the requirement of homogeneity.

Using this energy-momentum tensor for the Universe, the field equations then simplify to the two indepen-

dent equations:

$$\left(\frac{\dot{a}}{a}\right)^2 = \frac{8\pi G}{3}\rho - \frac{kc^2}{a^2} + \frac{\Lambda}{3} \tag{1.10}$$

and

$$\frac{\ddot{a}}{a} = -\frac{4}{3}\pi G\left(\rho + \frac{3P}{c^2}\right) + \frac{\Lambda}{3}. \tag{1.11}$$

Equation (1.10) is known in particular as Friedmann's Equation. We noted above that the metric of the form given by Equation (1.6) was known as the Robertson-Walker metric; if its scale factor $a(t)$ obeys equations (1.10) and (1.11), it is called the Friedmann-Lemaître-Robertson-Walker (FLRW) metric.

We will now define some of the parameters prevalent in the literature, and used in this Thesis, to describe cosmologies which are solutions to equations (1.10) and (1.11). The relative expansion rate $(\dot{a}/a)$ of the Universe is called the *Hubble parameter*:

$$H(t) \equiv \frac{\dot{a}}{a}. \tag{1.12}$$

Its value at the present epoch $t = t_0$ is the *Hubble constant*, $H(t_0) = H_0$. Although now a somewhat dated convention, given the accuracy of modern measurements, observational uncertainty in the value of the Hubble constant is commonly expressed in terms of the *dimensionless Hubble parameter*, $h$, as follows:

$$H_0 \equiv 100\,h\,\mathrm{kms}^{-1}\mathrm{Mpc}^{-1}. \tag{1.13}$$

The most recent measurements put $h \approx 0.72$ (see, e.g., Spergel et al. 2007).

The *critical density* of the Universe, that required for $k = 0$ and hence a flat overall geometry, is given at time $t$ by

$$\rho_{\mathrm{crit}}(t) = \frac{3H^2(t)}{8\pi G}. \tag{1.14}$$

This therefore leads us to define a *density parameter* as the ratio of density (whether it be dark matter, baryonic-matter, radiation density etc.) to the critical density:

$$\Omega_x \equiv \frac{\rho_x}{\rho_{\mathrm{crit}}} = \frac{8\pi G\rho_x}{3H^2}. \tag{1.15}$$

Since $\rho$ and $H$ change with time, this defines an epoch-dependent density parameter.

A powerful approximate model for the energy content of the Universe is to divide it into pressureless matter and radiation, for which $\rho_m \propto a^{-3}$ and $\rho_r \propto a^{-4}$. These two relations describe the varying energy density of particles as they become diluted by the expansion; photons suffer an extra power of $a^{-1}$ as their energy is reduced by redshifting (see Section 1.1.3 below). This allows the density to be written as

$$\frac{8\pi G\rho}{3} = H_0^2(\Omega_{m,0}a^{-3} + \Omega_{r,0}a^{-4}) \tag{1.16}$$

where the subscript 0s denote the density parameter value at the present time. By examining the Friedmann equation we see that it is possible for us to consider the term $\Lambda/3$ as an additional contribution to the density of the Universe, a 'vacuum energy' so to speak. If we choose to combine these two terms under the overall umbrella of density, then by defining

$$\Omega_\Lambda \equiv \frac{\Lambda}{3H^2} \tag{1.17}$$

we may then re-write equation (1.16) as

$$\frac{8\pi G\rho}{3} = H_0^2(\Omega_{m,0}a^{-3} + \Omega_{r,0}a^{-4} + \Omega_{\Lambda,0}). \tag{1.18}$$

This allows us to write the first of the Friedmann equations in the following highly useful form:

$$H^2(a) = H_0^2\left\{\Omega_{\Lambda,0} + \Omega_{m,0}a^{-3} + \Omega_{r,0}a^{-4} - (\Omega_{\mathrm{tot},0} - 1)a^{-2}\right\} \tag{1.19}$$

where $\Omega_{\mathrm{tot},0}$ is the sum of all the other density parameters combined. A spatially flat Universe has $\Omega_{\mathrm{tot},0} = 1$ exactly.

### 1.1.3 Redshift

Due to the expansion of space, photons are redshifted while they propagate from the source to the observer. Following Peacock (1999) and Bartelmann & Schneider (2001), we consider a light source *comoving* with the expansion of the Universe; this means that relative to the source all other points move away isotropically at the cosmological expansion rate. This light source emits a signal at time $t_\mathrm{e}$, which reaches a similarly comoving observer at the coordinate origin $r = 0$, at time $t_\mathrm{o}$.

Light travels along null geodesics in spacetime, thus we know that $\mathrm{d}\tau = 0$ along the path of this light signal, and that from the FLRW metric we have

$$c^2\mathrm{d}\tau^2 = [a(t)]^2\mathrm{d}r^2. \tag{1.20}$$

The radial coordinate distance between emitter and observer (labelled $r_\mathrm{oe}$) remains constant, since both are comoving with the expansion of the Universe and this expansion is parametrised solely by the scale factor $a(t)$: it is thus common to refer to the spatial coordinates of Equation (1.6) as comoving coordinates. We can write this as

$$r_\mathrm{eo} = \int_\mathrm{o}^\mathrm{e}\mathrm{d}r = \int_{t_\mathrm{e}}^{t_\mathrm{o}}\frac{c\mathrm{d}t}{a(t)} = constant, \tag{1.21}$$

which requires the following condition to hold:

$$\frac{\mathrm{d}t_\mathrm{e}}{\mathrm{d}t_\mathrm{o}} = \frac{a(t_\mathrm{e})}{a(t_\mathrm{o})}. \tag{1.22}$$

The implication of this is that events on distant galaxies appear to suffer time-dilation, depending on how much the Universe has expanded since the photons we now see were emitted.

The frequency of light at emission and observation can be immediately identified with the inverse time intervals $1/\mathrm{d}t_\mathrm{e}$ and $1/\mathrm{d}t_\mathrm{o}$, so we can write

$$\frac{\nu_\mathrm{o}}{\nu_\mathrm{e}} = \frac{\mathrm{d}t_\mathrm{e}}{\mathrm{d}t_\mathrm{o}} = \frac{\lambda_\mathrm{e}}{\lambda_\mathrm{o}}, \tag{1.23}$$

where $\nu$ is the light frequency and $\lambda$ the light wavelength. Since the redshift $z$ of light is defined as

$$z = \frac{\lambda_\mathrm{o} - \lambda_\mathrm{e}}{\lambda_\mathrm{e}} \tag{1.24}$$

we thus have

$$1 + z = \frac{a(t_{\rm o})}{a(t_{\rm e})}. \tag{1.25}$$

Since we who are observing distant objects do so at the current epoch $a = 1$, this relation is usually just written as:

$$1 + z = \frac{1}{a(t_{\rm e})}. \tag{1.26}$$

Hence, the amount by which any known lab-frame spectral feature, in the light from distant galaxies, is redshifted tells us exactly how much the Universe has expanded in the time between emission and observation.

### 1.1.4 Cosmological distance measures

As described both in Bartelmann & Schneider (2001) and Peacock (1999), the meaning of the term 'distance' is no longer unique in a curved spacetime: different definitions of the measurement prescriptions for distances between points lead to different values, in contrast to Euclidean space. Cosmological distance measures are therefore defined in analogy to relations between measurable quantities in Euclidean space. Typically the following four distances are used:

1. The proper distance.
2. The comoving distance.
3. The angular-diameter distance.
4. The luminosity distance.

To define these distances we employ the FLRW metric seen in Equation (1.6). Cosmological distance measures relate an emission event and an observation event on two separate geodesic lines which fall on a common light cone. They are parametrised by the redshifts of the emitter and observer, $z_{\rm e}$ and $z_{\rm o}$, and we assume that the observer is taken to be at the origin of the coordinate system.

The *proper distance* $D_{\rm prop}$ is defined by the travel time of a photon between $z_{\rm e}$ and $z_{\rm o}$. Because cosmic time $t$ increases as the photon approaches the observer, and distances increase away from the observer, this gives us

$$\mathrm{d}D_{\rm prop} = -c\mathrm{d}t = -c\frac{\mathrm{d}a}{\dot{a}} = -c\frac{\mathrm{d}a}{aH(a)}. \tag{1.27}$$

In the local Universe it is true that $\Omega_{r,0} \ll \Omega_{m,0}$, and so assuming the radiation contribution is negligible we can integrate the above equation to give

$$D_{\rm prop} = \int_{z_{\rm o}}^{z_{\rm e}} \frac{c\mathrm{d}z}{H_0} \left\{(1 - \Omega_{\rm tot,0}) + \Omega_{\Lambda,0}(1+z)^{-2} + \Omega_{m,0}(1+z)\right\}^{-\frac{1}{2}}. \tag{1.28}$$

The *comoving distance* $D_{\rm com}$ is simply the distance $r$ in our choice of comoving coordinates between the worldlines of an emitter and an observer both comoving with the cosmic flow. Thus

$$\mathrm{d}D_{\rm com} = \mathrm{d}r. \tag{1.29}$$

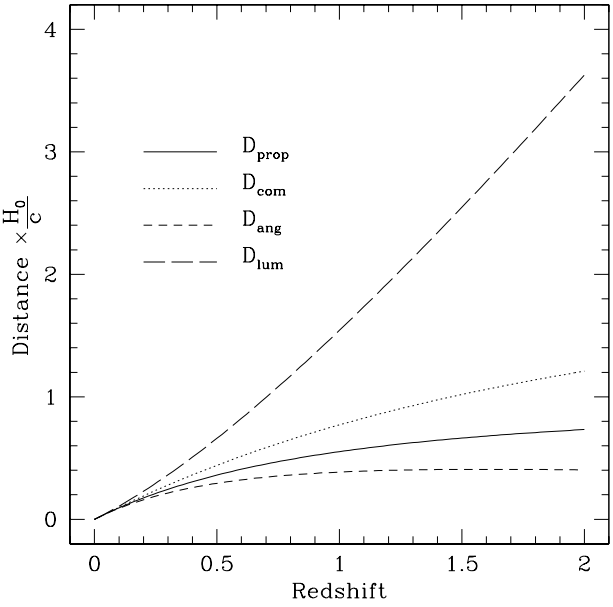


Figure 1.2: Plot of distance (from local space) versus redshift for the four standard distance measures in a ΛCDM Universe with $\Omega_m = 0.3$ and $\Omega_\Lambda = 0.7$

Since light rays propagate along null geodesics, the metric (1.6) gives us $c\mathrm{d}t = -a\mathrm{d}r$ for a photon travelling radially towards the origin (observer). Therefore

$$\mathrm{d}D_{\rm com} = -\frac{c\mathrm{d}t}{a} = -\frac{c\mathrm{d}a}{\dot{a}a} = -\frac{c\mathrm{d}a}{a^2 H(a)}. \tag{1.30}$$

Hence, using Equations (1.26) and (1.19), and again assuming $\Omega_{r,0} \ll \Omega_{m,0}$, we have

$$\begin{aligned} D_{\rm com} &= \int_{z_{\rm o}}^{z_{\rm e}} \frac{c\mathrm{d}z}{H_0} \left\{(1-\Omega_{\rm tot,0})(1+z)^2 + \Omega_{\Lambda,0} + \Omega_{m,0}(1+z)^3\right\}^{-\frac{1}{2}} \\ &= r(z_{\rm e}, z_{\rm o}). \end{aligned} \tag{1.31}$$

For cosmological observations made at the present epoch we may take $z_{\rm o}$ as zero.

The *angular-diameter distance* is defined in analogy to the relation in Euclidean space between the transverse size of an object and the angle it subtends at the observer. At cosmological distances the *proper* transverse size of an object $\mathrm{d}\ell_{\rm trans}$ seen by us is its comoving size $S_k(r)\mathrm{d}\psi$ ($\mathrm{d}\psi$ being the angular separation between two points on the sky) multiplied by the scale factor $a(t_{\rm e})$ at the time of emission:

$$\mathrm{d}\ell_{\rm trans} = \frac{1}{1+z_{\rm e}} S_k(r(z_{\rm e},0))\mathrm{d}\psi \tag{1.32}$$

Thus the angular-diameter distance can be written in terms of Equation (1.31) as:

$$D_{\rm ang} = \frac{1}{1+z_{\rm e}} S_k(D_{\rm com}(z_{\rm e},0). \tag{1.33}$$

The last of the commonly-used distance measures, the *luminosity distance*, is defined to ensure that the flux $S_{\rm tot}$ received by an observer at $z_{\rm o}$ and the luminosity $L_{\rm tot}$ of a source at $z_{\rm e}$ are related by

$$S_{\rm tot} = \frac{L_{\rm tot}}{4\pi D_{\rm lum}^2}. \tag{1.34}$$

However, in order to relate $S_{\rm tot}$ to $L_{\rm tot}$ we need to consider the relationship between the monochromatic flux and luminosity densities, $S_\nu(\nu)$ and $L_\nu(\nu)$ respectively. If the emission from the source can be assumed to be isotropic, then the emitted photons pass uniformly through a sphere of surface area $4\pi S_k^2(D_{\rm com}(z_{\rm e},0))$, upon which we, as observers, sit. However, redshift also affects the observed flux density in further ways. Photon energies are redshifted, reducing the monochromatic flux density by $1/(1+z_{\rm e})$; the reduction in photon arrival rates causes a reduction by the same factor. Conversely, the bandwidth $\mathrm{d}\nu$ at the observer is reduced again by the same factor in comparison to the bandwidth at the source; this therefore counteracts one of the two preceding reductions in the flux density per unit bandwidth. Finally, photons observed at a frequency $\nu$ were, of course, actually emitted at a frequency $\nu(1+z_{\rm e})$. The relationship between monochromatic flux and luminosity densities, for observer and source respectively, is therefore:

$$S_\nu(\nu) = \frac{1}{1+z_{\rm e}} \times \frac{L_\nu(\nu(1+z_{\rm e}))}{4\pi S_k^2(D_{\rm com}(z_{\rm e},0))}. \tag{1.35}$$

Integrating over all frequencies $\nu$, we obtain

$$S_{\rm tot} = \frac{1}{(1+z_{\rm e})^2} \times \frac{L_{\rm tot}}{4\pi S_k^2(D_{\rm com}(z_{\rm e},0))}, \tag{1.36}$$

which when compared to Equation (1.34) gives

$$D_{\rm lum} = (1+z_{\rm e}) S_k(D_{\rm com}(z_{\rm e},0)). \tag{1.37}$$

The four distance measures are plotted as a function of light-source redshift (assuming the observer exists at the current epoch) in Figure 1.2, for an $\Omega_{\rm tot} = 1$ (flat) Universe with $\Omega_\Lambda = 0.7$ and $\Omega_m = 0.3$; $D_{\rm prop}$ is the solid line, $D_{\rm com}$ the dotted line, $D_{\rm ang}$ the short-dashed line and $D_{\rm lum}$ the long-dashed line. These results conclude our description of an isotropic and homogeneous Universe.

However, it is clear that this description is anything but adequate to describe astrophysical observations on any but the largest scales. On the scales of planets, stars, galaxies and clusters of galaxies, the distribution of matter is anything *but* isotropic and homogeneous: the results of Friedmann-Lemaître cosmology merely provide an expanding large scale background upon which the effects of structure formation may then be described. This description is a vital next stage in the modelling of the Universe, and is the topic which I now outline (in some necessary brevity).

### 1.1.5 The growth of matter structure

The reasons for a departure from homogeneity in the early Universe, leading to an unstable collapse to the structure we now observe, are still not clear. Peacock (1999) describes some of the more promising ideas, with the most favoured being the amplification of quantum fluctuations during an initial period of rapid inflation due to an unknown field of vast energy. The most recent results from the WMAP CMB

experiment (Spergel et al. 2007) have begun, remarkably, to be able to rule out some of the proposed scalar field models for this inflationary potential. The results from the *Planck* CMB polarization experiment (The Planck Collaboration 2006), and from other such experiments probing smaller scale fluctuations (such as: QUaD, QUaD Collaboration: P. Ade et al. 2007; BICEP, Yoon et al. 2006; SPUD, Kovac & BICEP/SPUD Collaboration 2006; see also Kovac & Barkats 2007) are eagerly awaited in relation to this question.

Although the mechanism by which the seeds of cosmic structure were put in place is not known, we may assume a certain power spectrum (see Peacock 1999 for a description of this term) for the density perturbations and propagate these perturbations using known physical laws. Such modelling has shown some striking successes, not least the quality of fitting to the results of the WMAP experiment, as described in the references given in the preamble to Section 1.1 (and in more detail in Section 1.1.8 below).

At early times, and even today on the largest scales, the initial conditions of the density field still dominate the dynamics of structure growth. Overall overdensities and underdensities remain small, and the regime can be described perturbatively using what is known as *linear perturbation theory*. It is common to describe the patterns seen in the matter distribution in terms of a dimensionless density perturbation:

$$1 + \delta(\boldsymbol{x}) \equiv \frac{\rho(\boldsymbol{x})}{\langle\rho\rangle}. \tag{1.38}$$

A full discussion of the dynamics of linear perturbation growth lies outside the remit of this introductory Chapter, and the interested reader is referred again to Peacock (1999) for a detailed description of the topic. Instead, I merely quote illustrative results that will inform subsequent discussion in this Chapter. The early growth of *adiabatic* density perturbations (made by the adiabatic and hence isentropic compression or expansion of some volume) in a flat Universe is related to cosmological scale factor as follows:

$$\delta \propto \begin{cases} a^2(t) & (\text{radiation domination}) \\ a(t) & (\text{matter domination; } \Omega_m \simeq \Omega_{\rm tot} \simeq 1). \end{cases} \tag{1.39}$$

The terms radiation and matter domination refer to specific epochs in the early expansion of the Universe. Looking at Equation (1.19) it can be seen that, for very early times ($a(t) \ll 1$), the $\Omega_{r,0}a^{-4}$ term in the Friedmann will dominate; hence, the expansion is radiation dominated. At somewhat later times, where $a^{-4}\Omega_{r,0} \ll a^{-3}\Omega_{m,0}$ and $\Omega_{\Lambda,0} \ll a^{-3}\Omega_{m,0}$, the dynamics of the expansion are matter dominated. It is one of the more interesting facts of cosmology that the present epoch should lie exactly on the cusp between this period of matter dominated expansion and one of vacuum energy domination, with $\Omega_{m,0} \lesssim \Omega_{\Lambda,0}$.

Another, orthogonal mode of density perturbation is possible, and is known as the *isocurvature* mode. These, conversely, perturb the entropy density without perturbing the energy density, and can be shown to be constant at first and then die away rather than grow with time (Peacock 1999):

$$\delta \propto \begin{cases} constant & (\text{radiation domination}) \\ a^{-1}(t) & (\text{matter domination; } \Omega_m \simeq \Omega_{\rm tot} \simeq 1). \end{cases} \tag{1.40}$$

However, for open models and flat models with $\Omega_m + \Omega_\Lambda = 1$ the relationships given in (1.39) and (1.40) cease to accurately describe linear perturbation growth at late times. For these models adiabatic collapse is suppressed by the more rapid expansion of the cosmological background. Carroll et al. (1992) give accurate fitting formula for approximating this growth suppression, relative to the simpler model with $\Omega_m = \Omega_{\rm tot} = 1$.

The picture presented above is merely a brief outline, and overlooks many important details in the growth of linear structure. Smaller scale linear perturbations are modified by the effects of pressure, are damped due to particle free streaming and may eventually become self-gravitating and enter the non-linear regime. In practice, the combined effects of the first two of these considerations may be calculated numerically and then represented using a *transfer* function, $T_k$. These functions describe the ratio between the power in perturbations at a scale $k$ at late times, and the primordial power spectrum at some early epoch of redshift $z$:

$$T_k \equiv \frac{\delta_k(z=0)}{D(z)\delta_k(z)}, \tag{1.41}$$

where $D(z)$ is the linear growth factor between $z$ and the present. The calculation of these functions is a complex numerical exercise: modern examples of fitting functions for model cosmologies an be found in Bardeen et al. (1986) and Eisenstein & Hu (1998). These transfer functions are able to accurately predict many aspects of the linear power spectrum, including so-called 'wiggles' due to baryon-acoustic oscillations (see Percival et al. 2007a for a recent example of the measurement of this signal using galaxy survey data).

In order to describe non-linear collapse fully and accurately it is necessary to resort to large numerical simulations, as described in Section 1.1.7. These simulate a Universe composed of a single, collisionless dark matter component in an expanding background. In Section 1.1.7 I also discuss in brief some of the reasons why it is thought that the mass of the Universe is likely to be dominated by such a non-baryonic matter component.

Before turning to simulation results, however, there is some insight into non-linear structure to be gained from simple analytic calculations. In the following Section, 1.1.6, the collapse of a single, spherically symmetric overdensity is described. This work results in a useful practical definition of the collapsed objects referred to as haloes, and allows for reasonable estimates of the timescales involved in their collapse. Of particular interest to my work is the structural form that these haloes take once collapsed, described by their density profile. The only rigorous and exact analytic solution to this problem is that of a single, scale-free spherical density perturbation in a Friedmann Universe, the so-called secondary infall model (Gunn & Gott 1972; Gunn 1977; Fillmore & Goldreich 1984; Bertschinger 1985). However, this question is best addressed numerically, and so simulation results regarding the density profiles of collapsed objects are discussed in Section 1.1.9. The unsolved question of halo substructure, which can only be addressed using simulation predictions, is discussed in Section 1.1.10.

### 1.1.6 The spherical collapse model of halo formation

A first step in modelling the large scale evolution of matter into non-linear structure is a description of the 'microscopic' case: the collapse of a single overdense region of the Universe into a self-gravitating halo, via a model known as spherical 'top hat' collapse. This model assumes spherical symmetry for the overdensity, but is able to fully describe the early, intermediate and late stages of its evolution and collapse. In the discussion that follows, I make the considerable simplification of only considering results for a flat, matter dominated Universe with density parameter

$$\Omega_m = \Omega_{\rm tot} = 1, \tag{1.42}$$

referred to as the Einstein-de Sitter model. Although this does not accurately represent the vacuum energy dominated Universe we believe to exist around us, most of the basic results for such a cosmology can be obtained without numerical integration. The simpler case of equation (1.42) is thus chosen as an attempt to utilise the extra insight available from analytically derived results.

It is a highly useful result within General Relativity that Friedmann's Equation, written in its dimensional form as

$$\dot{R}^2 = \frac{8\pi G}{3}\rho R^2 - kc^2, \tag{1.43}$$

applies equally to a spherical overdensity (see Peacock 1999). The radius $R$ of an overdense sphere behaves in the same way as the expansion factor for a closed sub-universe, and we are therefore able to model the general growth of a spherically symmetric density perturbation using the same equations as classical cosmology.

Equation (1.43) can be most easily solved with a re-parameterization in terms of the *conformal time* $\eta$, defined so that $\mathrm{d}\eta = c\mathrm{d}t/R(t)$. Assuming that $\rho(t)$ can be written as $\rho(t) = \rho_0 R_0^3/R^3$, we then have

$$\left(\frac{\mathrm{d}R}{\mathrm{d}\eta}\right)^2 = \frac{8\pi G\rho_0 R_0^3}{3c^2}R - kR^2. \tag{1.44}$$

Defining the useful scaling constant

$$R_* = \frac{4\pi G\rho_0 R_0^3}{3c^2} = \frac{GM}{c^2}, \tag{1.45}$$

where M is the mass initially (and subsequently) enclosed in our overdense sphere, we can rewrite Equation (1.44) in the following simple form:

$$\left[\frac{\mathrm{d}}{\mathrm{d}\eta}\left(\frac{R}{R_*}\right)\right]^2 = 2\left(\frac{R}{R_*}\right) - k\left(\frac{R}{R_*}\right)^2. \tag{1.46}$$

For an overdense region $k = +1$, and this equation has the solution

$$\frac{R(\eta)}{R_*} = 1 - \cos\eta. \tag{1.47}$$

The cosmic time can be found by recalling our definition of $\eta$, from which

$$t(\eta) = \int_0^\eta \mathrm{d}\eta' \frac{R(\eta')}{c}. \tag{1.48}$$

The two equations which completely describe the evolution of our spherically symmetric overdensity are thus

$$R(\eta) = R_*(1 - \cos\eta) \tag{1.49}$$

$$t(\eta) = \frac{R_*}{c}(\eta - \sin\eta), \tag{1.50}$$

where $R_*$ is given by Equation (1.45). This solution forms the basis of an approximate theory of non-linear collapse, but to understand its consequences we need to examine its behaviour at some important epochs

in the history of the overdensity.

### Evolution for $\eta \ll 1$

In order to describe the early expansion of the sphere as a function of $t$, we must expand the solutions given in (1.49) and (1.50) as power series in $\eta$. Doing so around $\eta = 0$, and ignoring terms of order greater than $\eta^5$, we find

$$R(t) \simeq \frac{R_*}{2}\left(\frac{6ct}{R_*}\right)^{2/3}\left[1 - \frac{1}{20}\left(\frac{6ct}{R_*}\right)^{2/3}\right]. \tag{1.51}$$

Here are recovered, as should be rightly hoped, two important results from both the underlying cosmological expansion and linear theory. The leading-order term

$$R(t \to 0) = \frac{R_*}{2}\left(\frac{6ct}{R_*}\right)^{2/3} = \left(\frac{9GMt^2}{2}\right)^{1/3} \tag{1.52}$$

can be rearranged to give the early-epoch density dependence,

$$\rho(t \to 0) = \frac{3M}{4\pi R^3(t \to 0)} = \frac{1}{6\pi G t^2} = \rho_0(t), \tag{1.53}$$

recovering the standard result for the evolution of the cosmological (critical) density of an Einstein-de Sitter Universe (see, e.g., Coles & Lucchin 1995).

The next order term in the expansion can also be examined. Since the density of the sphere is given by $\rho \propto 1/R^3$, the fractional overdensity is thus

$$\frac{\delta\rho}{\rho} = -3\frac{\delta R}{R} = \frac{3}{20}\left(\frac{6ct}{R_*}\right)^{2/3}, \tag{1.54}$$

to first order. Remembering that for an Einstein-de Sitter Universe $a(t) \propto t^{2/3}$, we are clearly recovering a correctly-scaled version of the linear theory result of the expression seen in Equation (1.39).

### Turnaround

At later times, the evolution of the sphere will differ significantly from that of the cosmological background. Examination of Equation (1.49) shows immediately that a maximum radius $R_{\max} = 2R_*$ is reached when $\eta = \pi$, occurring at a time $t_{\max} = \pi R_*/c$. Using our result from equations (1.52) and (1.53), we calculate the density enhancement of our evolving sphere relative to the cosmological background as

$$1 + \delta_{\max} = \frac{\rho_{\max}}{\rho_0(t_{\max})} = \frac{(R_*/2)^3(6ct_{\max}/R_*)^2}{R_{\max}^3} = \frac{9\pi^2}{16} \simeq 5.55. \tag{1.55}$$

Using Equation (1.54) we can also calculate what linear theory would have predicted for the perturbation at this time:

$$\delta_{\rm lin} = \frac{3}{20}(6\pi)^{2/3} \simeq 1.08. \tag{1.56}$$

It can be seen that the top hat model, used in this way, allows basic results in non-linear theory to be compared to those of linear theory in a very simple manner.

## Collapse and virialization

The collapse of the perturbation into a bound self-gravitating object, commonly known as a 'halo', is the final stage of its non-linear evolution as described by the top hat model. If only gravity operates on a perfectly spherically symmetric perturbation the region will collapse to a black hole when $\eta = 2\pi$, at a time we label $t_{\rm coll} = 2\pi R_*/c$. When this occurs the corresponding linear prediction for the density perturbation in this region is $\delta_{\rm lin} = (3/20)(12\pi)^{2/3} \simeq 1.69$.

However, total collapse will never occur in practice; slight departures from pure spherical symmetry will cause the kinetic energy of collapse to be converted into random motions. The perturbation will thus eventually reach some form of thermalized, bound, equilibrium state. If we invoke the virial theorem in this cosmological context (see Coles & Lucchin 1995), the perturbation will have total kinetic energy $K$ related to potential energy $V$ by

$$V = -2K. \tag{1.57}$$

Assuming energy conservation during the transition to this equilibrium state, Equation (1.57) can be shown to imply that the radius $R_{\rm vir}$ of such a virialized perturbation, *which we define as being a halo*, is given by

$$R_{\rm vir} = \frac{1}{2} R_{\rm max} = R_*. \tag{1.58}$$

In our simple top hat model this will occur at $\eta = 3\pi/2$, and the epoch this defines is often chosen to roughly estimate the density contrast we should expect for collapsed, relaxed objects.

It should be expected, however, that this process of virialization take longer than predicted by this simple symmetric model, and it is common for authors to assume that this $R_{\rm vir}$ is in fact only reached after $t_{\rm coll}$. The full non-linear density contrast at virialization is then

$$\Delta_{\rm vir} \equiv 1 + \delta_{\rm vir} = \frac{(R_*/2)^3 (6ct_{\rm coll}/R_*)^2}{R_{\rm vir}^3} = \frac{(6\pi)^2}{2} \simeq 178. \tag{1.59}$$

As before, linear theory predicts a perturbation of $\delta_{\rm lin} \simeq 1.69$ at $t_{\rm coll}$ for the region corresponding to this collapsed halo.

As stated at the beginning of this Section, this treatment is only approximately accurate for Universes in which $\Omega_m \neq 1$. For a flat Universe with $\Omega_\Lambda + \Omega_m = 1$, Eke et al. (1996) found that the density contrast for spherical collapse and virialization is given by

$$\Delta_{\rm vir} = 178 \left[\Omega_m(z)\right]^{0.45}; \tag{1.60}$$

see also Heymans et al. (2006a), and Mainini et al. (2003) who give more detailed fitting formulae for different dark energy models. Note that this contrast relates the matter density in the overdensity to the critical density for closure, which now includes non-matter contributions. This has caused some authors to instead define the contrast relative to the mean matter density, putting $\Delta_{\rm vir} = \rho_{\rm vir}/\bar{\rho}_m$ (see, e.g., Bacon et al. 2006: Appendix A). In this Thesis, I define $\Delta_{\rm vir} = \rho_{\rm vir}/\rho_{\rm crit}$.

There is a further, more important limitation to this treatment: the assumption of spherical symmetry. There is to good reason to expect that overdense (or underdense) regions in our Universe will display a significant degree of asphericity. For this reason we must turn to the results of numerical simulations, outlined in the following Section. Due to the simplifications that go into the spherical collapse model, many authors simply ignore the weak $\Omega_m$ dependence of the density contrast and define simulation haloes as regions with $\Delta_{\rm vir} = 200$. The mass of a halo is then $M_{200}$, defined as the mass encompassed by a sphere centred on this halo within which $\Delta_{\rm vir} = 200$. This is the definition used by Navarro et al. (1997) to define their universal halo profile (see Section 1.1.9) and, as such, is now the most commonly-used description of collapsed haloes and the definition used in this Thesis.

### 1.1.7 Numerical simulations of dark matter

The limited number of analytic results for realistic non-linear structure formation has led to it being instead explored by means of numerical studies known as cosmological N-body simulations: see White (1976) for an early example and Springel et al. (2005) for details of the largest simulation to date (depicted in Figure 1.3). These describe the Universe as a fluid of collisionless dark matter particles; therefore, before beginning a discussion of the simulations themselves, it will be useful to summarize (in brief) the evidence that matter of this sort dominates the mass budget of the Universe (see Peacock 1999 for a more detailed summary). I will also make brief mention of competing, non-dark matter theories, before going on to describe modern N-body simulations.

The first evidence for unseen dark mass in the largest structures in the Universe was found by Zwicky (1933, 1937); observations of the Coma cluster showed that the velocity dispersion of the individual member galaxies was too high for the cluster to remain bound without some additional source of gravitational attraction. Important evidence also came from measurements of rotation curves of external disc galaxies (e.g., van Albada et al. 1985; van Albada & Sancisi 1986, see also Noordermeer et al. 2007; Salucci 2007 for recent examples of these measurements). These showed a highly significant flattening of the rotation curve at large distances from the galaxy centre, something very difficult to explain from the distribution of baryonic mass.

However, galaxy rotation curves pose some problems for ΛCDM; it was such measurements that prompted Milgrom (1983) to suggest modified Newtonian dynamics (MOND) as an alternative solution to the flatness of rotation curves. This theory, made fully relativistic by the Tensor-Vector-Scalar field theory (TeVeS) of Bekenstein (2004), has gone on to show remarkable success in the description of galaxy rotation curves (see, e.g., McGaugh & de Blok 1998; Sanders & Verheijen 1998; Milgrom & Sanders 2007; Sanders & Noordermeer 2007), without requiring a non-baryonic dark matter component.

Recently, Clowe et al. (2006) and Bradač et al. (2006) presented an analysis of the 'Bullet cluster' (1E 0657-558) which it was claimed provided a 'direct empirical proof of the existence of dark matter'. This cluster appears to be in the midst of a collision, causing the bulk of the mass (as detected by a lensing analysis, see Section 1.2) to be in a spatially distinct location to the most significant contributor to the baryonic mass, the hot X-ray emitting gas. However, the extent to which this system can still be explained by modified gravity theories remains a topic of some controversy (see, e.g., Brownstein & Moffat 2007; Angus et al. 2007).

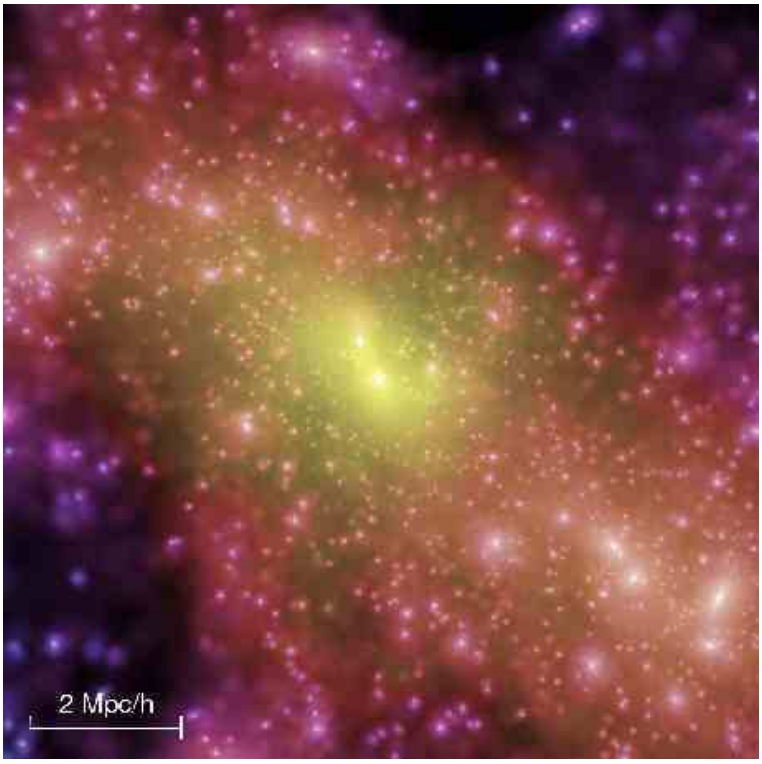


Figure 1.3: Image of the dark matter distribution within a cluster from the Millennium Simulation: note the vast abundance of subhaloes throughout the structure. Figure taken from Springel et al. (2005).

It is also unclear as to whether other cosmological observations can be matched by MOND/TeVeS theories with as much success as more established ΛCDM models. One important example is in the modelling of large scale structure, for which TeVeS predictions remain relatively underdeveloped. ΛCDM presents a detailed and largely consistent description of the growth of non-linear structure in the Universe by the hierarchical merging of dark matter haloes, as realised in large N-body simulations. Predictions for large scale structure made using these models prove to be a good match to the distribution of galaxies, once galaxy biasing is taken into account (see, e.g., Springel et al. 2006; Sánchez et al. 2006; Percival et al. 2007b).

In an N-body simulation the density-velocity field of collisionless dark matter is represented by a set of particles. The essential strategy is to solve the Newtonian equation of motion for each particle, based on the gravity of all the other particles, calculating its acceleration and then evolving its position and velocity over some small time step. The process can then begin again, and thus the evolution of the density field is simulated iteratively. Summing over all the contributions to the gravity field in real space becomes extremely slow for large numbers of particles (order $N^2$ calculations), and so it is instead useful to solve Poisson's equation in Fourier space. This allows the use of the powerful fast Fourier transform algorithm (e.g. Press et al. 1992), reducing the number of calculations to order $N \log N$.

Advances in the techniques used to calculate the evolution of dark matter in N-body simulations have culminated in the 'TreePM' method used in the Millennium Simulation, the largest and most advanced N-body simulation at the current time (Springel et al. 2005; Figure 1.3). This method combines a hierarchical mul-

tipole expansion algorithm (also known as a tree algorithm: see, e.g., Barnes & Hut 1986; Hernquist et al. 1991) with particle-mesh (PM) and particle-particle-particle-mesh ($P^3M$) methods (see Efstathiou et al. 1985; Hockney & Eastwood 1988). Starting with a homogeneous particle distribution given a realization of a Gaussian random field, with a ΛCDM linear power spectrum at redshift $z = 127$, the simulation was then advanced to the present epoch using up to 11 000 adaptive timesteps, as described in Springel et al. (2005).

Springel et al. (2006) describe the successes of the Millennium Simulation in capturing many aspects of observed large scale structure. Fundamentally, the hierarchical structure formation model of White & Rees (1978), within which larger haloes form from competitive merger and accretion of smaller haloes, is well supported by this and previous simulation results (see, e.g., Davis et al. 1985; Ghigna et al. 1998; Reed et al. 2005; Springel et al. 2006). Simulation work has also established that of the possibilities for the fluid properties of dark matter, it is *cold* dark matter (CDM, rather than hot dark matter, HDM) that is able to collapse quickly enough to form a sufficient amount of structure within the age of the Universe. The collapsed overdense regions necessary to form the structure observed in the form of galaxies, clusters and super-clusters are much more difficult to form in an HDM Universe (see, e.g., Davis et al. 1985).

### 1.1.8 Measured constraints on the concordance cosmological model

Having thus far given a brief outline of the ΛCDM model, we have sufficient background information to consider a short summary of the current best observational evidence for the concordance cosmological picture. I will attempt to discuss constraints both upon the cosmological parameters discussed in Sections 1.1.1-1.1.2, and upon the power spectrum of primordial fluctuations very briefly discussed in Section 1.1.5 (see also Peacock 1999). At the time of writing this Thesis, these constraints come from a combination of measurements that can be broadly categorized into three groups: statistics describing temperature and polarization anisotropies in the CMB, the measurement of luminosity distances for large samples of Type Ia Supernovae (SNIa), and statistics describing the large scale structure (LSS) of collapsed matter objects in the Universe. These will be tackled in turn.

#### Anisotropies in the cosmic microwave background

As discussed in the early preamble to this Section, and in Section 1.1.5, the most powerful constraints upon the concordance cosmological picture come from the striking fit to the angular power spectrum of TT (temperature-temperature) anisotropies in the CMB shown in Figure 1.1. The measurements of the CMB TT, temparature-polarization and polarization-polarization power spectra provided by the WMAP 3-year data (see Spergel et al. 2007 and references therein) have allowed a simple, flat, six parameter ΛCDM model to be fit with unprecedented precision, although the correct interpretation of these results in well-understood physical terms is still largely unclear.

The six directly-fitted parameters of the flat ΛCDM model shown by (Spergel et al. 2007) to provide an excellent agreement with the CMB power spectra are as follows: $\Omega_{m,0}h^2$, $\Omega_{b,0}h^2$, $\mathrm{e}^{-2\tau}$, $\Theta_\mathrm{s}$, $n_\mathrm{s}$ and $C_{l=220}^{TT}$. I will now briefly describe these parameters, but at all times refer the reader to Spergel et al. (2007), Spergel et al. (2003) and Kosowsky et al. (2002) for a far more detailed discussion than is merited in this introductory Chapter. The first two $\Omega_{m,0}h^2$ and $\Omega_{b,0}h^2$ parameters describe the density of overall matter

(cold and baryonic) and baryonic matter respectively, where $\Omega_{m,0}$ and $\Omega_{b,0}$ are defined as in Equation (1.15), and the dimensionless Hubble parameter is defined as in Equation (1.13). The parameter $\mathrm{e}^{-2\tau}$ is the factor by which CMB anisotropies on small scales are damped due to scattering by free electrons after the Universe is reionized by the formation of stars and galaxies, defining the optical depth to reionization $\tau$. This reionization scattering has differing effects upon the TT and temperature-polarization power spectra at different scales (see, e.g., Kogut et al. 2003).

The quantity $\Theta_{\mathrm{s}}$ is the angular scale of corresponding to the first and largest acoustic peak in the TT power spectrum. This can be written as

$$\Theta_{\mathrm{s}} = \frac{r_{\mathrm{s}}(z_{\mathrm{dec}})}{D_{\mathrm{ang}}(z_{\mathrm{dec}})}. \tag{1.61}$$

Here $D_{\mathrm{ang}}(z_{\mathrm{dec}})$ is the angular diameter distance (see Equation 1.33) to the surface of last photon scattering at the redshift $z_{\mathrm{dec}} \simeq 1100$ of the decoupling of the photon-baryon plasma, and $r_{\mathrm{s}}$ is the comoving acoustic horizon size of this plasma, which may be simply calculated using the result of Hu & Sugiyama (1995). The parameter $n_{\mathrm{s}}$ gives the power law scaling of the power spectrum of primordial matter fluctuations $P(k) \propto k^{n_{\mathrm{s}}}$, left as an imprint of a hypothesized inflationary period in the early Universe (see, e.g., Peacock 1999). Finally, the $C_{l=220}^{TT}$ parameter simply describes the amplitude of the TT power spectrum at the multipole scale $l = 220$ which approximately corresponds to the angular scale $\Theta_{\mathrm{s}}$ of the acoustic peak.

In the analysis performed by Spergel et al. (2007), the CMB anisotropy code CAMB of Lewis et al. (2000) was used to perform a maximum likelihood fit to the six parameter model described above. From these best fits constraints were derived upon cosmological parameters of direct interest, such as $\Omega_{m,0}$, $h$, and $\sigma_8$, which provides a normalization of the linear matter power spectrum as the variance of matter fluctuations on scales of $8h^{-1}\mathrm{Mpc}$ (Peacock 1999). These derived constraints are shown in Table 1.1. However, as described by Kosowsky et al. (2002) and Page et al. (2003), it is possible to get somewhat more direct insight into the placing of cosmological constraints by considering the positions, amplitudes and ratios of acoustic peaks and troughs in the CMB power spectra. For example, the amplitude of the first peak and the ratio of this amplitude to that of the second peak allows $\Omega_{m,0}h^2$ and $\Omega_{b,0}h^2$ to be determined, while considering the amplitude of the third peak in addition allows constraints upon $n_{\mathrm{s}}$ (Page et al. 2003).

Whilst not wishing to enter into a detailed discussion of these aspects of the CMB power spectra, it is worth briefly mentioning the information that the position of the first peak (given by $\Theta_{\mathrm{s}}$ in Equation 1.61) gives regarding the geometry of the Universe. As discussed by Page et al. (2003) and Spergel et al. (2007), this peak position tells us that the Universe is spatially flat when it is combined with almost any other cosmological measurement of $\Omega_{m,0}$ or $h$. The primary WMAP constraints upon $\Lambda$CDM presented in Table (1.1) are made assuming flatness; however, allowing the curvature $k$ to vary and combining the CMB measurements with other cosmological data shows that the Universe is indeed extremely flat and appears to have been throughout its past (Spergel et al. 2007). I will now discuss some of these other measurements of cosmological geometry and matter density, and describe the constraints they place upon the $\Lambda$CDM model and when combined with the WMAP results.

### Luminosity distances to Type Ia supernovae

Early observations of the luminosities and surprising homogeneity of Type Ia supernovae (SNIa: see Filippenko 1997 for a review of supernova class definitions) in the local Universe led to these objects being

Table 1.1: Derived, 1-$\sigma$ constraints upon the flat ($\Omega_\Lambda = 1 - \Omega_m$), power-law, $\Lambda$CDM cosmological model

| Parameter | WMAP 3-year | SNIa[1] | 2dFGRS[2] | SDSS[2] | BAO[2] |
|---|---|---|---|---|---|
| $\Omega_{m0}$ | $0.239^{+0.037}_{-0.032}$ | $0.267^{+0.028}_{-0.018}$ | $0.237 \pm 0.020$ | $0.239^{+0.018}_{-0.017}$ | $0.252 \pm 0.027$ |
| $\Omega_{b0}$ | $0.0416^{+0.0054}_{-0.0046}$ | — | $0.041 \pm 0.002$ | $0.0416^{+0.0054}_{-0.0046}$ | — |
| $h$ | $0.730^{+0.033}_{-0.031}$ | — | $0.74 \pm 0.02$ | $0.0730 \pm 0.019$ | — |
| $\sigma_8$ | $0.758^{+0.050}_{-0.051}$ | — | $0.77 \pm 0.05$ | $0.756 \pm 0.035$ | — |
| $n_s$ | $0.954^{+0.017}_{-0.016}$ | — | $0.954 \pm 0.023$ | $0.953 \pm 0.016$ | — |
| $\tau$ | $0.089 \pm 0.030$ | — | — | — | — |

[1]From combined measurements of the ESSENCE and SLS supernova surveys, but including marginalization over a dark energy equation of state parameter $w$ that is allowed to vary from $w = -1$ (Wood-Vasey et al. 2007).
[2]From large scale structure measurements after combining with WMAP 3-year data (see Sánchez et al. 2006; Tegmark et al. 2006, Table III; Percival et al. 2007a)

suggested as a standard distance measure at the very beginning of observational cosmology (e.g., Wilson 1939). Improvements in technology such as stable photometry from charge-coupled detectors (CDDs), and increased supernova sample sizes, led Phillips (1993) to propose an empirical relationship between the intrinsic brightness of each SNIa and the shape of the light curve as it decays from maximum brightness. Subsequently, many variations and refinements upon the modelling of this initial work, including improvements to extinction corrections, have now led to the achievement of approximately $\sim 10\%$ precision on a given SNIa distance estimate (e.g. Phillips et al. 1999; Wang et al. 2003; Guy et al. 2007; Jha et al. 2007). These advances, in combination with ever improving sample sizes, propelled SNIa distances measurements to the forefront of modern cosmology with the discovery of a Universe undergoing accelerating expansion at late times (Riess et al. 1998; Perlmutter et al. 1999).

The technique for using SNIa distances to constrain cosmological parameters is conceptually very simple: once a SNIa is detected observations of the host galaxy spectra are made, along with follow-up photometry so as to capture the decaying light curve. The observed brightness of the SNIa can then be compared with the intrinsic brightness inferred from the observations of the light curve, giving an estimate of the luminosity distance $D_{\rm lum}(z)$ as defined in Equation (1.37). The redshift $z$ of the SNIa host galaxy, determined from observations of emission lines in its spectrum, can then be used to place the supernova measurement upon a luminosity distance-redshift curve as shown in Figure 1.2. Given a sufficient sample of SNIa measurements, the luminosity distance-redshift relationship can be fit to give constraints upon the cosmological parameters $\Omega_{m,0}$, $\Omega_{\Lambda,0}$ and, more recently, upon the parameter $w$ which describes the equation of state for the pressure of a hypothesized dark energy as $P = w\rho c^2$ (see, e.g., Riess et al. 2007; Astier et al. 2006).

In the flat, $\Lambda$CDM model the dark energy is a pure cosmological constant which requires $w = -1$ , and current constraints from supernova measurements (Riess et al. 2004; Astier et al. 2006; Riess et al. 2007; Wood-Vasey et al. 2007) show no significant evidence for $w \neq -1$. The most recent constraints, coming from the combination of measurements from the ESSENCE supernova survey (Wood-Vasey et al. 2007) and The Supernova Legacy Survey (SLS: Astier et al. 2006), find $w = -1.07 \pm 0.09 \pm 0.13$ (where the second uncertainty comes from estimates of systematic errors) and $\Omega_{m,0} = 0.267^{+0.028}_{-0.018}$ for a spatially flat ($\Omega_\Lambda = 1 - \Omega_m$) cosmology. This is the result I quote in Table 1.1, although it should be stressed that this value and uncertainties for $\Omega_{m,0}$ includes the margninalization over $w$ implicit in the placing of these joint constraints.

### Large-scale structure (LSS)

The recent measurements of the power spectrum of galaxy clustering on large scales, from the spectroscopic 2 degree Field Galaxy Redshift Survey (2dFGRS: see, e.g., Cole et al. 2005; Sánchez et al. 2006) and Sloan Digital Sky Survey (SDSS: see, e.g., Tegmark et al. 2004, 2006; Percival et al. 2007b), have placed important further constraints upon the $\Lambda$CDM model. These measurements complement those from the CMB as they help to break certain inherent degeneracies between parameters in the WMAP measurements. As an example, measurements of the statistics of LSS such as those from SDSS and 2dFGRS are directly sensitive to $h\Omega_{m,0}$ rather than $\Omega_{m,0}h^2$ as was the case for WMAP. The degeneracy between $h$ and $\Omega_{m,0}$ is one of the largest in the WMAP results (Page et al. 2003), and so the extra constraints provided by LSS allow tighter constraints on both $\Omega_{m,0}$ and $h$. These constraints then help break other degeneracies, such as that between $\sigma_8$ and $\Omega_{m,0}$. In Table 1.1 we show the results of Sánchez et al. (2006), who combined cosmological constraints from the full sample of 2dFGRS galaxies with the WMAP 3-year data, and Tegmark et al. (2006) who did a similar combination of the WMAP data with a measurement of the power spectrum of luminous red galaxies (LRGs) in the SDSS. These more recent LRG measurements provide sharper constraints than those of the larger, but generally fainter sample presented by Tegmark et al. (2004).

However, in the most recent analysis of the SDSS Data Release 5 galaxy sample, Percival et al. (2007b) found that there was significant evidence for tension between the SDSS and 2dFGRS results, SDSS favouring Universes with a larger matter density. Both 2dFGRS and SDSS analyses use a relatively simple model of the galaxy bias $b$, defined by $\delta_{\rm gals} = b\delta$, where $\delta$ is defined as in Equation (1.38) and $\delta_{\rm gals}$ is its equivalent for the number density of galaxies (see Peacock 1999 for a far more detailed discussion of bias). Given that the 2dFGRS galaxies are predominantly blue through selection, and the SDSS galaxies red selected, it may be necessary to have a far better understanding of differences in the clustering properties of these two different galaxy types, and therefore $b$, before a correct interpretation of LSS results can be made. In addition Percival et al. (2007b) found that there was internal discrepancy within the SDSS results: the power spectrum on large scales favoured a low matter density Universe with $\Omega_{m,0} = 0.22 \pm 0.04$ but supported a far higher $\Omega_{m,0} = 0.32 \pm 0.01$ when the fit to the power spectrum wass extended to smaller scales. These authors suggested that this could be explained by a galaxy bias $b$ for the SDSS sample that varies significantly with scale and $r$-band luminosity. Clearly the question of galaxy bias $b$ will be important as LSS data sample sizes increase with the planned surveys of the future.

A recent, extremely promising development in the study of large scale structure has come via measurements of the signature of Baryon Acoustic Oscillations (BAO), firstly in the SDSS galaxy power spectrum (Eisenstein et al. 2005) and now the combined power spectra of the SDSS and 2dFGRS galaxies (Percival et al. 2007a). Although a description of these phenomena must be necessarily brief in a Thesis such as this, the physics describing the production of a standing wave oscillatory signature in the matter power spectrum has been known for some time (see, e.g., Silk 1968; Peebles & Yu 1970; Sunyaev & Zeldovich 1970; Bond & Efstathiou 1984; Hu & Sugiyama 1996). That these signatures should also be visible in the galaxy distribution is a consequence of their occurence on relatively large, approximately non-linear scales (see, e.g., Meiksin et al. 1999; Eisenstein et al. 2007).

The acoustic peaks occur originate from the excitation, by cosmological matter perturbations, of sound waves in the relativistic plasma of the early Universe. The small but significant fraction of baryons in the Universe ensures that these peaks persist, having been frozen by decoupling at $z_{\rm dec} \simeq 1100$, and cosmological theory predicts that the acoustic oscillations in the plasma will also be imprinted onto the

late-time power spectrum of the nonrelativistic matter (Bond & Efstathiou 1984; Hu & Sugiyama 1996; Eisenstein & Hu 1998). The primary imprint is a first peak resonance at a comoving length scale of $\sim 100h^{-1}\mathrm{Mpc}$. This then gives a characteristic length scale which can be measured from the structure in the Universe, and which can used to probe the distance-redshift relationship (see, e.g., Eisenstein et al. 2005).

The most recent BAO results presented by Percival et al. (2007a) use a joint SDSS-2DFGRS galaxy sample to constrain the distance-redshift at $z = 0.2$, and the SDSS LRG sample to give another constraint at $z = 0.35$. Combining these measurements with WMAP 3-year data, and assuming a flat, $\Lambda$CDM cosmology they find the value for $\Omega_{m,0}$ presented in Table 1.1. Forcing the cosmological model to be flat but allowing $w$ to vary these authors find $\Omega_{m,0} = 0.249 \pm 0.018$ and $w = -1.004 \pm 0.089$.

However, many aspects of the $\Lambda$CDM model, particularly the more detailed results of N-body simulations, have proved more difficult to test by observation. In the following Sections I now describe two unresolved issues of structure formation: the questions of halo density profiles and halo substructure.

### 1.1.9 Dark matter halo profiles

An especially interesting result of simulation work is the seeming 'universality' of the shape of dark matter haloes: over three to four decades in mass, halo densities appear to be able to be well described by one appropriately scaled profile. This was famously noted by Navarro et al. (1997), whose suggested universal halo density distribution became known as the NFW profile. The exact form of this density profile can be described by two parameters: the virial mass of the collapsed halo and a parameter known as the concentration, which sets the scale for the transition between the $\rho \propto r^{-1}$ behaviour of the halo interior and the $\rho \propto r^{-3}$ density drop-off in the outer regions. Constraining the relationship between these parameters observationally will be an important test of high-resolution $\Lambda$CDM simulations, as reasonably robust agreement exists between theoretical predictions (see, e.g., Macciò et al. 2007; Neto et al. 2007).

Aiming to improve upon NFW, there has been less agreement regarding the exact form of the 'best' universal profile, i.e., the one which best fits simulation data. Predictions differ particularly in the halo interior where resolution becomes an issue (Moore et al. 1999b; Navarro et al. 2004), but in these regions baryonic effects are likely to become important in a way that N-body simulations are yet unable to accurately predict. All of these issues will now be discussed, but we begin with a description of the simplest realistic density profile.

#### The singular isothermal sphere (SIS)

The approximately flat rotation curves observed in galaxies can be most simply reproduced by a model density profile which scales as $\rho \propto r^{-2}$. Such a profile can be obtained by assuming a constant velocity dispersion for the dark matter throughout the halo, and so is known as the *singular isothermal sphere* (SIS) (see, e.g., Binney & Tremaine 1987; Narayan & Bartelmann 1999):

$$\rho(r) = \frac{\sigma_v^2}{2\pi G r^2} \tag{1.62}$$

where $\sigma_v$ is the line-of-sight velocity dispersion of the test particles (i.e. stars) in the gravitational potential of the mass distribution. The mass $M(r)$ interior to $r$ thus increases $\propto r$, and the rotational velocity of test particles in circular orbits within the potential is given by

$$v_{\rm rot}^2 = \frac{GM(r)}{r} = 2\sigma_v^2 = constant, \tag{1.63}$$

demonstrating the flat rotation curve desired for the description of galaxies. One significant shortfall of this model is the divergent total mass, which led Brainerd et al. (1996) to model galaxy haloes using a *truncated* singular isothermal sphere (TSIS):

$$\rho(r) = \frac{\sigma_v^2 s^2}{2\pi G r^2 (r^2 + s^2)}, \tag{1.64}$$

where $s$ defines the truncation scale, i.e. the radius beyond which the profile steepens to $\rho \propto r^{-4}$. Other modifications of the SIS in an attempt to better fit the observed Universe include the *softened* singular isothermal sphere (SSIS), which seeks to reproduce the central density core often posited to better fit the observed rotation curves of disc galaxies (see, e.g., Salucci 2007). This profile has the following form:

$$\rho(r) = \frac{\sigma_v^2}{2\pi G (r^2 + r_{\rm c}^2)}, \tag{1.65}$$

where here $r_{\rm c}$ defines the scale radius of the central core. The issue of whether galaxy haloes exhibit such a core is perhaps one of the great unsolved problems for the ΛCDM paradigm (again see Salucci 2007, and references therein). Collisionless simulations (Navarro et al. 1997; Moore et al. 1999b; Navarro et al. 2004) suggest that the halo interior instead displays a density cusp, and the effects of adiabatic baryonic contraction are predicted to steepen the cusp rather than smooth it to a constant core (see, e.g., Blumenthal et al. 1986; Sellwood & McGaugh 2005; Gustafsson et al. 2006, but also Tonini et al. 2006 who propose a possible mechanism for erasing the cusp).

As the problem manifests itself most strongly in the extreme interiors of galaxies, weak gravitational lensing and even flexion is unlikely to constrain the core regions of smaller CDM haloes. In order to solve this question, a better understanding will be necessary of the many possible issues affecting the fair comparison galaxy rotation curves and velocity dispersions, in projection, with ΛCDM predictions. These might include observational biases such as beam smearing, inclination effects or slit offsets, which may all cause an underestimation of the rotation velocity in central galaxy regions. In addition, it will be necessary to wait for more detailed theoretical understanding of galaxy formation and dynamics. This requires accurate, high resolution hydrodynamical simulations of joint dark matter-baryon collapse and star formation (see, e.g., Sales et al. 2007); such simulations will not be available for some time.

However, it is likely that ΛCDM results will be more accurate in the outer regions of galaxies, where baryons no longer dominate. It is exactly these regions which can be usefully probed using weak lensing, and so I now describe some of the more important halo profile predictions from collisionless simulations.

### The NFW halo profile

Using N-body simulations, Navarro et al. (1995, 1996, 1997) have shown that the equilibrium density profiles of cold dark matter (CDM) haloes can be very well fitted over two orders of magnitude in radius

by the formula

$$\frac{\rho(x)}{\rho_{\rm crit}(z)} = \frac{\Delta_{\rm c}}{x(1+x)^2}, \tag{1.66}$$

known as the *NFW profile*, where the radial coordinate $x$ is the radius in units of a scaling radius $r_{\rm s}$ such that $x \equiv r/r_{\rm s}$, $\rho_{\rm crit}(z)$ is the critical density for closure at the epoch of the halo, and $\Delta_{\rm c}$ is a dimensionless scaling density. The radius of the sphere within which the total mass is $M_{200}$, designated by the virial radius $r_{200}$, is used to define a second dimensionless scaling parameter for the NFW profile, namely the concentration $c = r_{200}/r_{\rm s}$. This profile describes simulation haloes accurately over a broad mass range.

A procedure for finding values of $\Delta_{\rm c}$ and $c$ which agree with the numerical simulations is detailed by Navarro et al. (1997); the parameters are functions of the halo redshift $z$, $M_{200}$ and the background cosmology. A routine (`charden.f`) which carries out these calculations and outputs values for these scaling parameters has been made available by Julio Navarro (see Navarro et al. 1997). Subsequently, a number of authors (Jing 2000; Bullock et al. 2001; Eke et al. 2001; Zhao et al. 2003; Dolag et al. 2004; Kuhlen et al. 2005) presented further analytic models for calculating $c$ as a function of redshift, mass and cosmology, based on larger simulations with higher resolution.

The most recent analyses, using the Millennium Simulation (Neto et al. 2007) and a suite of smaller but higher resolution simulations (Macciò et al. 2007), have arrived at the startling result that a single power law fits the concentration-mass dependence over six decades in mass, from $\sim 10^9 M_\odot$ to $\sim 10^{15} M_\odot$. These authors appear to agree that

$$c \simeq 11.7 (M_{200}/10^{12} h^{-1} M_\odot)^{-0.10}, \tag{1.67}$$

for flat, concordance cosmologies at the present epoch. However, Macciò et al. (2007) use $\Delta_{\rm vir} \simeq 98$ (calculated using the results of Mainini et al. 2003) rather than the $\Delta_{\rm vir} = 200$ of Neto et al. (2007), which is the result quoted above.

This strong theoretical prediction presents an immediate challenge to observational cosmology. While some results are beginning to emerge for large, cluster-sized haloes (Comerford & Natarajan 2007), there are few constraints upon this relationship available for galaxy-sized haloes. Weak lensing, and flexion in particular, may be an extremely important tool for testing these predictions.

## Zhao-Hernquist halo profiles

The NFW profile is one in a family of spherically-symmetric radial profiles first proposed by Hernquist (1990) and explored in far greater detail by Zhao (1996):

$$\rho(r) = \frac{C}{r^\gamma (1 + r^{1/\alpha})^{(\beta-\gamma)\alpha}}, \tag{1.68}$$

where $(\alpha, \beta, \gamma)$ are the three free parameters which describe the changing profile shape and $C$ is a normalization constant. As pointed out by Zhao (1996), Equation (1.68) parameterizes the volume density as a general double power law, with slope $-\gamma$ for $r \ll 1$ and slope $-\beta$ for $r \gg 1$. The third parameter $\alpha$ is a measure of the width of the transition region, this region widening with increasing $\alpha$. Hernquist (1990) originally considered a profile with $(\alpha, \beta, \gamma) = (1, 4, 1)$, and it can be seen that the NFW profile is a (1,3,1) member of the family.

### The M99 halo profile

Because of its success in describing a broad mass range of simulated dark matter haloes the NFW profile was hailed as 'universal', and this universality has become the subject of much further work, both analytic and numeric. However, there is some disagreement as to whether it represents the best possible fit to halo profiles, especially at smallest radial scales (less than 1 per cent of the virial radius). Having resolved simulated haloes to smaller radii than Navarro et al. (1997), Moore et al. (1999b) found evidence for an inner slope (cusp) of -1.5 rather than that of -1 found for the NFW profile. Overall, these authors concluded that their simulation data favoured a Zhao-Hernquist profile of the form (1.5,3,1/1.5), referred to as the M99 profile.

### The N04 halo profile

More recently, Navarro et al. (2004) found that density cusps as steep as -1.5 were inconsistent with their simulation data, and finding no evidence for a well-defined asymptotic value of the inner slope at all, preferred instead a model where the local logarithmic slope of the density profile, here referred to as $\epsilon$, takes the form of a power law with radius:

$$\epsilon = -\frac{\mathrm{d}\ln\rho}{\mathrm{d}\ln r} = 2\left(\frac{r}{r_{-2}}\right). \tag{1.69}$$

Here Navarro et al. (2004) have defined $r_{-2}$ as a characteristic radius at which the slope of the profile is exactly isothermal, i.e. $\epsilon = 2$. This leads to a density profile $\rho_\alpha$, referred to as the N04 profile, given by

$$\ln\left(\frac{\rho_\alpha}{\rho_{-2}}\right) = -\left(\frac{2}{\alpha}\right)\left[\left(\frac{r}{r_{-2}}\right)^\alpha - 1\right], \tag{1.70}$$

where the scaling density $\rho_{-2} = \rho(r_{-2})$ is to be measured from simulation data. This profile has finite total mass due to the exponential cutoff at large radius, and a logarithmic slope that decreases inward more gradually than the NFW or M99 profiles.

### A summary of the current picture

The most recent work by Reed et al. (2005) and Diemand et al. (2005) reverts back to the former conclusion of Navarro et al. (1997) and Moore et al. (1999b) that an asymptotic inner slope *is* reached, finding a figure in the region $\gamma \approx 1.2 - 1.3$, after investigating regions as far into the interior as 0.1 per cent of the virial radius. However, as described above, the precise interior shape of the dark matter distribution is likely to be highly influenced by baryonic physics, especially in haloes which form galaxies. Observations of baryon dynamics in these regions will likely give the best constraints upon the distribution of matter. It is likely that the field is reaching the stage at which simulations of purely collisionless dark matter are no longer sufficiently accurate approximations to the physical Universe to provide observationally testable predictions of the $\Lambda$CDM paradigm.

Accurate predictions based on hydrodynamical simulations (see, e.g., Abadi et al. 2003; O'Shea et al. 2005) will come. Largely untested predictions for the distribution of shape parameters of halo profiles

already exist; these include the theoretical results mentioned for the mass-concentration dependence of NFW haloes and predictions for the of ellipticity, and triaxility, of haloes (see, e.g., Jing & Suto 2002; Kasun & Evrard 2005; Hopkins et al. 2005; Allgood et al. 2006; Macciò et al. 2007). The challenges to the observer attempting to constrain the dark matter distribution around objects such as galaxies and clusters are great, but these challenges can be met using a combination of gravitational lensing and accurate rotation curve data. This will allow not only for simulation models to be tested, but also a better understanding of the mechanisms driving galaxy formation.

### 1.1.10 Dark matter halo substructure

I now go on to describe a second important prediction of the ΛCDM cosmological model. The hierarchical structure formation scenario of White & Rees (1978) should, according to simulation work, leave an abundance of dark matter substructure composed of bound subhaloes within each host halo. This is an inevitable consequence of ongoing halo mergers, combined with a relatively long predicted timescale for the complete tidal disruption of accreted subhaloes.

Early computational work that attempted to model the merging hierarchy ubiquitously failed to find surviving substructure within clusters, producing a final dark matter structure that was very nearly smooth (see, e.g., White 1976; White et al. 1987; Summers et al. 1995). Analytic work suggested that this 'overmerging' problem was a symptom of poor spatial and mass resolution (Moore et al. 1996), and later, higher resolution simulations of clusters confirmed this using resampling methods (Moore et al. 1998; Ghigna et al. 1998; Klypin et al. 1999a). It is now thought that current N-body work is able to simulate remnant CDM substructure to reasonable accuracy, although semi-analytic modelling by Taylor & Babul (2004, 2005a,b) suggests that there may still be a need for greater mass and force resolution before numerical overmerging problems are totally negligible.

Interestingly, the most recent simulation results (Shaw et al. 2007; D'Onghia et al. 2007; Nurmi et al. 2006; Reed et al. 2005; De Lucia et al. 2004; Gao et al. 2004) predict subhalo mass functions that vary only weakly with the mass of the hosting halo. This near self-similarity in substructure was first pointed out qualitatively by Moore et al. (1999a), and is now a strong prediction of structure formation in a collisionless ΛCDM Universe. Observational data is not yet available in sufficient quantity to place meaningful constraints upon the subhalo mass function; however, it is likely that surveys in the near future will be able to measure the subhalo mass *fraction* to increasing accuracy, over a range of host halo masses (see, e.g., Yoo et al. 2006; Koopmans 2005; Metcalf 2005; Bradač et al. 2004; Natarajan & Springel 2004). The mass fraction $f_m$ is defined as the ratio of the mass contained in bound subhaloes to the total mass of the host halo, and is predicted to lie in the range $0.05 \lesssim f_m \lesssim 0.2$ for galaxy and cluster mass haloes. Again, there is weak mass dependence, with some evidence for $f_m$ decreasing with decreasing host halo mass.

Once it became clear that haloes the size of the Milky-Way (MW) should contain an abundance of dark matter substructure, enough to rival that found in clusters, an immediate problem was to reconcile this fact with the paucity of known dwarf spheroidal (dSph) satellite galaxies around our own Galaxy (Moore et al. 1999a; Klypin et al. 1999b). The proposal that this constituted a 'small scale crisis' for ΛCDM was subsequently disputed by Stoehr et al. (2002), who found a good match between the observed kinematics of simulation subhaloes and MW satellite galaxies, although their own conclusions conceded that this only provided an explanation if known dSph satellites could be associated with haloes of far greater mass than

previously assumed. D'Onghia & Lake (2004) then pointed out the apparent persistence of the small scale crisis for objects such as RX J1340.6+4018, a fossil group at $z = 0.171$.

A further issue, the anisotropic spatial distribution of MW satellites in a great circle oriented at close to $90^\circ$ from the Galactic disc, was pointed out by Kroupa et al. (2005) who claimed that this was inconsistent with their being drawn from a $\Lambda$CDM subhalo distribution. However, high resolution simulation work, followed by merger tree construction and semi-analytic galaxy formation modelling (Libeskind et al. 2005), argued that the spatial distribution of star-forming satellites might be necessarily significantly different from that of the most massive subhaloes. It was found that the subhaloes having the most massive progenitors at *early* times shared a similarly anisotropic spatial distribution, explainable by the slow infall of satellites along filaments in the dark matter field. Using a different approach, the maximum likelihood comparison of observed dSph satellite mass functions and those of simulated subhaloes, Strigari et al. (2007) found independent evidence of this association between satellite galaxies and the earliest-forming subhaloes.

Ongoing improvements to observational data for dSphs in the Galactic halo (see, e.g., Gilmore et al. 2007; Walker et al. 2007; Koch et al. 2007; Koposov et al. 2007; Zucker et al. 2006) appear to pose no further significant problems for $\Lambda$CDM substructure predictions, although cusp-core issues remain (see Section 1.1.9). The history of this debate perhaps serves best to illustrate the difficulty of interpreting observations of luminous matter in terms of dark matter simulations, especially given the limited results available from hydrodynamical simulations (see, e.g., Sales et al. 2007) and incomplete models of star formation.

Predictions of simulations at larger mass scales have proved easier to interpret, as strong gravitational lensing provide a unique constraints upon substructure for many clusters and superclusters (see, e.g., Hennawi et al. 2007). The situation is not, however, conclusive: Diemand et al. (2004) found a significant spatial biasing of CDM subhaloes away from cluster centres, which is not observed in galaxy position data from the CNOC cluster survey (Carlberg et al. 1997) or the Coma Cluster (Łokas & Mamon 2003). As in the case of substructure on smaller scales, and as Diemand et al. (2004) conclude, it is likely that observational accuracy has gone beyond the level at which simulations of dark matter *alone* can be usefully interpreted. High resolution hydrodynamical simulations will be needed to study the effect of baryons on the physics of halo merging, and this will require considerable time and resources.

Nonetheless, the existence of dark matter substructure is a robust prediction of $\Lambda$CDM; if this prediction proves to be inaccurate, for any reason, it is vital that we understand why. Observing substructure is, therefore, one of the challenges of the next decade, necessary to test model predictions and to simultaneously drive improvements to the theoretical understanding of the interplay between baryons and dark matter. Gravitational lensing offers an extremely attractive means of placing new constraints upon substructure, being unreliant upon an accurate understanding of galaxy formation and complicated gas dynamics. I now go on to outline basic theoretical concepts used to describe gravitational lensing, with emphasis upon the formalisms of weak lensing and flexion. Weak lensing measurements provide one means by which we may make observations of matter substructure, and flexion in particular may offer some hope on the smallest scales.

## 1.2 Gravitational lensing

One of the most powerful methods for constraining the distribution of matter in the Universe is the study of gravitational lensing. As light propagates through an inhomogeneous gravitational field, photons are deflected from straight paths in three-dimensional space, following null geodesics in four-dimensional spacetime. The analysis of this phenomena has seen many important advances in recent years, with the development of its theoretical description being accompanied by rapid technological improvements to the accuracy and sample size of lensing observations.

Gravitational lensing, in its cosmological applications, can be divided into two broad classes: *strong* lensing (see, e.g., Kochanek 2006), in which background galaxies are multiply imaged by massive foreground lenses, and *weak* lensing, in which coherent image distortions are analysed statistically (see, e.g., Schneider 2006; Bartelmann & Schneider 2001 for detailed reviews). In the remainder of this Chapter, I will outline basic gravitational lens theory, describing how lensing distortions are related to the underlying matter field. From Section 1.2.4 onwards I describe fundamental results for the analysis of weak lensing. Set within the background of traditional weak lensing, this Thesis is an exploration of the possibilities opened up by the study of flexion, a new tool which utilizes the higher order distortions responsible for the arc-ed appearance of weakly lensed galaxies. In Sections 1.2.8 and 1.2.9 I introduce the basic formalism of flexion, which is a natural extension of traditional weak lensing methods.

There are a number of approximations which go into what is known as gravitational lens theory, all of which allow for a simpler description of the phenomenon. Almost any conceivable astrophysical situation in which lensing will occur can be described by the weak field limit of General Relativity, in which Einstein's field equations can be linearised. The gravitational light deflection due to an extended mass distribution can then be expressed as the sum of deflections due to many individual lenses, the simplest of which is of course the point mass.

### 1.2.1 Deflection by a point mass

We consider a light ray passing by a point mass $M$. If the ray passes sufficiently far from the strong spacetime curvature close to the object's event horizon, i.e. $\xi \gg 2GM/c^2$ where $\xi$ is the impact parameter of the motion of the ray around the mass, then General Relativity predicts (see, e.g., Rindler 2001; Bartelmann & Schneider 2001) that the deflection angle $\hat{\boldsymbol{\alpha}}$ has magnitude

$$\hat{\alpha} = \frac{4GM}{c^2\xi}. \tag{1.71}$$

We note that since we have assumed that $\xi$ is much larger than the Schwarzchild radius, which will be true in any situation where lensing may be practically observed, the deflection angle $\alpha$ must be small; the small angle approximation is thus implicit in all that follows. The result of Equation (1.71) is twice the value obtained from a Newtonian treatment and is in fact the last time that General Relativity need be called upon in a description of the vast majority of gravitational lensing phenomena.

### 1.2.2 The lensing equation

A typical lensing scenario is shown in Figure 1.4. The reduced reflection angle $\boldsymbol{\alpha}$ is defined as follows:

$$\boldsymbol{\alpha} = \frac{D_{\rm ls}}{D_{\rm s}}\hat{\boldsymbol{\alpha}} \tag{1.72}$$

Using Figure 1.4 the *lensing equation* can be defined:

$$\boldsymbol{\beta} = \boldsymbol{\theta} - \frac{D_{\rm ls}}{D_{\rm s}}\hat{\boldsymbol{\alpha}}(\boldsymbol{\theta}), \tag{1.73}$$

or

$$\boldsymbol{\beta} = \boldsymbol{\theta} - \boldsymbol{\alpha}(\boldsymbol{\theta}). \tag{1.74}$$

The *thin screen approximation* assumes that all the deflection occurs within a distance $\Delta s \sim \pm\xi$ of the point of closest approach. Using this approximation the lensing mass can be assumed to lie on a 'lens plane' and the mass of the lens can be projected onto the plane to gain a surface mass density $\Sigma(\boldsymbol{\xi})$ (where $\boldsymbol{\xi}$ is a 2D vector in the lens plane). The deflection angle can hence be written as the sum of all the deflections due to each mass element in the lens plane:

$$\hat{\boldsymbol{\alpha}}(\boldsymbol{\xi}) = \frac{4G}{c^2}\int \frac{(\boldsymbol{\xi} - \boldsymbol{\xi}')\Sigma(\boldsymbol{\xi}')}{\mid \boldsymbol{\xi} - \boldsymbol{\xi}' \mid^2}{\rm d}^2\xi' \tag{1.75}$$

A further way to define the deflection angle is to define an effective refractive index for the lens, in analogy with an imperfect optical lens. This index may be defined using the Newtonian gravitational potential of the lens system, $\Phi_{\rm N}$ (which comes into the description via its place in the weak field metric of General Relativity, see, e.g., Rindler 2001) as:

$$n = 1 - \frac{2}{c^2}\Phi_{\rm N}. \tag{1.76}$$

The deflection angle can then be defined by integrating the gradient of $n$ perpendicular to the line of sight:

$$\hat{\boldsymbol{\alpha}} = \frac{2}{c^2}\int \boldsymbol{\nabla}_{\perp}\Phi_{\rm N}{\rm d}\ell. \tag{1.77}$$

### 1.2.3 Lensing potential and convergence

We now define the *lensing potential* $\psi(\boldsymbol{\theta})$, a scaled, projected Newtonian potential $\Phi_{\rm N}$, of the lens:

$$\psi(\boldsymbol{\theta}) = \frac{D_{\rm ls}}{D_{\rm l}D_{\rm s}}\frac{2}{c^2}\int \Phi_{\rm N}(D_{\rm l}\boldsymbol{\theta}, s){\rm d}s \tag{1.78}$$

By taking the gradient of $\psi$ on the sky plane, and comparing with Equation (1.77), the reduced deflection angle can be related to the lensing potential:

$$\boldsymbol{\nabla}_{\theta}\psi = \alpha \tag{1.79}$$

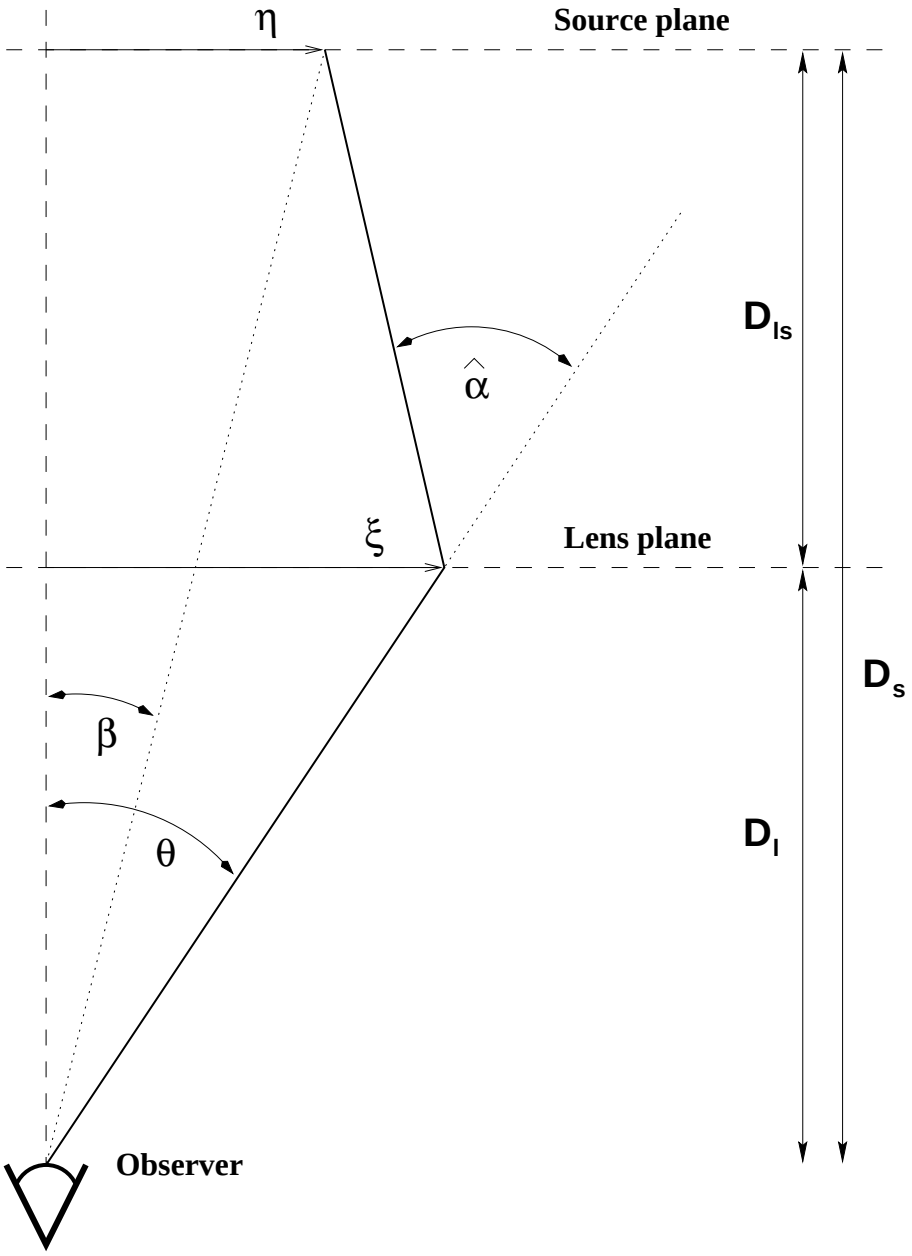


Figure 1.4: Geometry of a gravitational lens system. In the case of the thin lens approximation the deflection through the angle $\hat{\alpha}$ is taken as instantaneous. The angles $\boldsymbol{\theta}$ and $\boldsymbol{\beta}$, which are in general two-dimensional vectors on the sky plane, respectively specify the observed and intrinsic sky positions of the source. $D_{\rm l}$, $D_{\rm s}$ and $D_{\rm ls}$ are angular diameter distances.

Using Poisson's equation in three dimensions, $\nabla_r^2\Phi = 4\pi G\rho(\xi, z)$, we are able to relate the Laplacian of $\psi$ to the projected surface mass density $\Sigma(\boldsymbol{\theta})$:

$$\nabla_\theta^2\psi = 2\frac{\Sigma(\boldsymbol{\theta})}{\Sigma_{\rm crit}} \tag{1.80}$$

where $\Sigma_{\rm crit}$ is a critical surface mass density in the lens plane (for which $\alpha(\boldsymbol{\theta}) = \boldsymbol{\theta}$), taking the value

$$\Sigma_{\rm crit} = \frac{c^2 D_{\rm s}}{4\pi G D_{\rm ls} D_{\rm l}} \tag{1.81}$$

Using this definition we re-express Equation (1.80) in terms of a *dimensionless* surface mass density, known as the *convergence* $\kappa = \Sigma/\Sigma_{\rm crit}$, as follows:

$$\nabla_\theta^2\psi = 2\kappa(\boldsymbol{\theta}). \tag{1.82}$$

The lensing potential can then be related back to the convergence by integration

$$\psi(\boldsymbol{\theta}) = \frac{1}{\pi}\int_{\mathbb{R}^2} {\rm d}^2\theta'\kappa(\boldsymbol{\theta'})\ln(|\boldsymbol{\theta} - \boldsymbol{\theta'}|), \tag{1.83}$$

where here we have used Equations (1.75) and (1.79).

### 1.2.4 Weak gravitational lensing

The solutions $\boldsymbol{\theta}$ of the lensing equation yield the angular positions of the images of a source at $\boldsymbol{\beta}$; note that it is possible to have more than one image of a single source, this situation being known as *strong* lensing (see e.g., Kochanek 2006). Lensing conserves surface brightness, a consequence of Liouville's theorem (see Schneider et al. 1992) and the fact that gravitational light deflection leaves photon numbers unchanged. Hence, if $I^{\rm s}(\boldsymbol{\beta})$ is the surface brightness distribution in the source plane, we know that the observed surface brightness distribution must be

$$I(\boldsymbol{\theta}) = I^{\rm s}(\boldsymbol{\beta}(\boldsymbol{\theta})). \tag{1.84}$$

If a source is much smaller than the angular scale on which the lens properties change, the lens mapping can be locally linearised using the lensing equation and the relationship between $\boldsymbol{\beta}$ coordinates and $\boldsymbol{\theta}$ described by a Jacobian matrix:

$$\begin{aligned} A_{ij}(\boldsymbol{\theta}) &\equiv \frac{\partial\beta_i}{\partial\theta_j} = (\delta_{ij} - \partial_i\partial_j\psi(\theta))\,, \\ \mathsf{A} &= \begin{pmatrix} 1-\kappa-\gamma_1 & -\gamma_2 \\ -\gamma_2 & 1-\kappa+\gamma_1 \end{pmatrix}, \end{aligned} \tag{1.85}$$

where $\partial_i \equiv \partial/\partial\theta_i$, where we have taken the origins of the measured, lensed coordinates and the unlensed source coordinates to be the centres of light for the lensed and unlensed images respectively, and where we have introduced the components of the *shear* $\gamma = \gamma_1 + {\rm i}\gamma_2 = |\gamma|{\rm e}^{2{\rm i}\phi}$. The effect of the shear on an image is to *stretch* it, transforming a circular source into an elliptical image, whereas the effect of the convergence is

to *enlarge*, transforming a source into a larger version of itself whilst conserving surface brightness. From Equation (1.86) we see that the components of shear are related to the lensing potential as follows:

$$\gamma_1 = \frac{1}{2}(\partial_1^2 - \partial_2^2)\psi \tag{1.86}$$

$$\gamma_2 = \partial_1\partial_2\psi. \tag{1.87}$$

If the convergence and shear are effectively constant within a source galaxy image, the galaxy's transformation is simply described as

$$\beta_i \simeq A_{ij}\theta_j. \tag{1.88}$$

The formalism discussed above is as far as traditional weak lensing goes in describing the distortions of images due to gravity, i.e., to first or linear order in the source-image sky coordinate transformation. According to this transformation the images of circular sources are ellipses, the ellipticity of these objects being proportional to the shear for $\kappa \ll 1$. The essence of the study of weak gravitational lensing is then to use the observed ellipticity $\varepsilon$ as a noisy but unbiased estimator of the shear. Although for a single galaxy this will be an extremely poor estimate of $\gamma$, we may assume that unlensed populations of galaxies will have randomly oriented source ellipticities $\varepsilon^{\rm s}$, and therefore that the average ellipticity over an ensemble of lensed galaxies will give an unbiased estimate of the shear as $\langle\varepsilon\rangle \simeq \gamma$. By measuring the ellipticities of many galaxy images we gain a (noisy) estimate of the shear field, and may thus begin to try and determine the surface mass density of lensing systems (see Bartelmann & Schneider 2001 for details).

### 1.2.5 Strong gravitational lensing

The study of strong gravitational lensing applies to lens systems for which the Jacobian of Equation (1.86) vanishes, $\det\mathsf{A}(\boldsymbol{\theta}) = 0$. Such lenses will produce multiple images of background sources, and the positions of such images can place strong constraints upon the mass distribution of the foreground lens. A related, sufficient but not necessary (see Schneider et al. 2006) condition for multiple images is that $\kappa(\boldsymbol{\theta}) > 0$ somewhere upon the image plane. Such lenses are commonly referred to as "strong", and were the first examples of gravitational lensing discovered outside the Milky Way galaxy (the doubly imaged distant quasar QSO 0957+0561, see Walsh et al. 1979).

For a strong lens, the locus in the image plane for which $\det\mathsf{A}(\boldsymbol{\theta}) = 0$ is known as the critical curve. These curves are smooth and closed but their mappings onto the source plane, known as caustics, can and often do show cusps. Along critical curves the ratio of image to sourve flux, referred to as the magnification $\mu = 1/\det\mathsf{A}$, formally diverges. Whilst this is an unphysical picture (source galaxies are of finite extent which keeps their magnification finite) sources near caustics are often nonetheless extremely highly magnified and are observed as large elongated arcs (or sometimes even rings) close to the corresponding critical curve. The number of images of a source in the image plane also depends upon its position relative to the caustic curves (see Schneider et al. 2006) and provide additional constraints upon the geometry of critical curves and caustics.

Many modern uses of strong lensing involve the modelling of foreground lenses by fitting critical curves to observed giant arcs and multiple images in strong lensing clusters (such as the famous lensing cluster Abell 2218, e.g. Saraniti et al. 1996; Kneib et al. 1996) and to the arcs and rings around individual galaxies

observed with the *Hubble Space Telescope* (see, e.g., Bolton et al. 2006; Gavazzi et al. 2007). In the following Section, I will briefly describe these and other such applications of strong lensing, and discuss how these complement some of the applications cosmological and astrophysical applications of weak lensing.

### 1.2.6 Applications of strong and weak gravitational lensing

#### Strong lensing

The study of arcs and multiple images in strong lensing clusters, which began with the independent discovery by two groups (Lynds & Petrosian 1986; Soucail et al. 1987; Lynds & Petrosian 1989) of clear, elongated, luminous features around the clusters Abell 370 and Cluster 2242-04. Since that time there have been many examples of the use of these giant luminous arcs, but also smaller arcs (known as arclets, see Schneider et al. 2006) and multiple images, to model the critical curves, caustic curves and hence mass distributions of strong lensing clusters (see, e.g., Kochanski et al. 1996; Tyson et al. 1998; Broadhurst et al. 2005; Limousin et al. 2007). These have provided much insight into the mass distributions of clusters and, more recently, into the mass distributions of galaxies (Lehár et al. 2000, 2002; Rusin et al. 2003; Bolton et al. 2006; Koopmans et al. 2006; Treu et al. 2006; Gavazzi et al. 2007).

Bartelmann et al. (1998) were the first to compare the incidence rate of giant arcs to the expected values from raytracing calculations in N-body simulations, finding evidence for an excess in the observed number of arcs when compared to $\Lambda$CDM predictions. However, arcs are extremely rare events and the result of extremely non-linear gravitational interactions in high density regions. Debate continues regarding the interpretation of observed arc statistics and the means of making accurate theoretical predictions when the effects of CDM substructure, baryons and simulation resolution are likely to have significant implications for the production of giant arcs (see, e.g., Oguri et al. 2003; Dalal et al. 2004; Horesh et al. 2005; Li et al. 2006; Hennawi et al. 2007)

Other applications of strong lensing data include the use of clusters for which the mass distribution is well constrained as "gravitational telescopes", allowing the imaging of extremely distant galaxies at redshifts of $z \simeq 5$-6 and beyond (Ellis et al. 2001; Kneib et al. 2004; Santos et al. 2004; Egami et al. 2005; Smail et al. 2007), including a claimed detection of a $z = 10$ galaxy (Pelló et al. 2004, but see also Weatherley et al. 2004; Bremer et al. 2004). The recent survey of gravitationally lensed Lyman-$\alpha$ emitters made using the Keck telescope (Stark et al. 2007) has yielded six promising candidates lying between redshifts of $z = 8.7$ and $z = 10.2$, all with emission detections at greater than than 5-$\sigma$ significance. This leads to the conclusion, given the volume surveyed, that there must be a significant population of low luminosity, star forming galaxies at these high redshifts (Stark et al. 2007), and that these may contribute a significant fraction of the UV radiation necessary for cosmic reionization (Peacock 1999).

One further, and slightly different, cosmological use of strong lensing systems is the determination of the Hubble parameter $h$, independently of cosmology, via studies of the gravitational time delay between multiple images of a single, time-varying source (see, e.g., Blandford & Narayan 1986; Schneider et al. 2006). Recent studies of the time delay from strongly lensed variable quasars have placed competitive, independent constraints upon the Hubble parameter, finding $h = 0.72^{+0.08}_{-0.11}$ (Saha et al. 2006), and $h = 0.68 \pm 0.06 \pm 0.08$ (Oguri 2007), where the second uncertainty in this last constraint comes from an estimate of systematic errors due to degeneracies in the mass modelling of the foreground strong lens.

Having completed a brief survey of the cosmological applications of strong lensing, I know turn to a brief overview of what may be learnt from the study of weak lensing phenomena and how, on occasion, strong and weak lensing may be combined.

## Weak lensing

The cosmological applications of weak lensing are as broad as those of strong lensing, with occasional overlap. Although the statistical determination of the shear field (see Section 1.2.4, also Bartelmann & Schneider 2001) cannot constrain the mass distributions of individual objects in a way that competes with strong lensing observations, strongly lensed systems are by their very nature rare. Instead, weak lensing measurements may be taken from any resolved images of galaxies at sufficient cosmological depth, and can be used to gain insight into the average, global properties of the distribution of matter in the Universe.

One example of the use of weak lensing measurments in this fashion is the study of galaxy-galaxy lensing, which places constraints upon the distribution of unseen matter around foreground lens galaxies using redshift information and measurements of the weak shear from lensed background galaxies. Such an analysis was first proposed by Tyson et al. (1984), and was first detected by Brainerd et al. (1996). In recent years, galaxy-galaxy lensing analyses have constrained global properties for large samples of galaxies, as the mass-to-light ratio and the power law slop of this ratio with galaxy luminosity (see, e.g., Guzik & Seljak 2002; Sheldon et al. 2004; Hoekstra et al. 2004; Mandelbaum et al. 2005). Recent work (Mandelbaum et al. 2006a; Kleinheinrich et al. 2006) has begun to split lens samples by galaxy morphology and colour, and in this way galaxy-galaxy lensing potentially has the power to explore more complicated models of the galaxy bias $b$ discussed in Section 1.1.8. In Chapter 6 I describe my attempts to perform a galaxy-galaxy lensing analysis of data from the *Hubble Space Telescope* GEMS survey (Rix et al. 2004).

Another application of weak gravitational lensing is the study of the weak lensing signal imprinted upon the angular power spectra of the CMB, a result of many small angular deflections due to the inhomogeneities in the matter distribution between the current epoch and the surface of last scattering at $z_{\rm dec} \simeq 1100$ (see Lewis & Challinor 2006 for a recent review and Das & Bode 2007 for details of an up-to-date, all sky simulation of this effect). The effects of the weak lensing of the CMB is to cause small but potentially detectable broadening of the acoustic peaks in the TT and polarization power spectra. The cross-correlation of this effect with large scale structure measurements from radio sources in the NRAO-VLA Sky Survey (NVSS) 1.4GHz continuum survey (Condon et al. 1998) has recently yielded a 3.4-$\sigma$ detection of the signal (Smith et al. 2007), and as CMB measurements continue to improve with the advent of the Planck satellite (The Planck Collaboration 2006) and the Atacama Cosmology Telescope (Kosowsky 2003) this technique presents a promising new method of constraining the distribution and evolution of large scale structure.

Weak lensing has also been used in the study of galaxy clusters where, as will be described below, it also complements strong lensing mass reconstructions. However, not all clusters are strong lensing systems, and weak lensing has recently proved to be an extremely useful method of calibrating the mass-temperature relationship of clusters selected via X-ray bremsstrahlung emission from the hot ($10^7$-$10^8$K) intracluster gas (see Smith et al. 2005, who also use strong lensing observations, and Pedersen & Dahle 2007). As sample sizes increase, our understanding of the relationship between X-ray temperature and cluster mass, and of the scatter in this relationship due to cluster relaxation and environment, will improve. This in turn wil improve the constraints on large scale structure that may be placed using the temperature statistics

of X-ray selected clusters (e.g., Eke et al. 1998; Henry 2004; Haiman et al. 2005). Using current weak lensing surveys it is now even possible to detect clusters using maps of $\kappa$ derived from survey-wide mass reconstruction (Gavazzi & Soucail 2007); such "mass selected" cluster catalogues will become increasingly competitive with X-ray selected clusters with the advent of the wide area optical imaging surveys in the near future.

Perhaps the most promising, if also technically challenging, application of weak lensing is the measurement of so-called "cosmic shear", the scale-dependent angular correlation of the shear field due to the clustering of the cosmological matter field. I will discuss this technique, in addition to its future prospects and the constraints upon $\sigma_8$ and $\Omega_{m,0}$ it has yielded to date, in Section 1.2.7 below. However, before moving onto this important topic I will describe some of the recent advances in the combination of strong and weak lensing measurements in the mass modelling of lensing clusters.

### Combined strong and weak lensing

The use of combined measurements of weak and strong lensing for cluster mass determinations (see, e.g., Kneib et al. 2003; Bradač et al. 2005a,b), extending the ideas of Bartelmann et al. (1996) and Seitz et al. (1998), has had some striking successes in recent years. Such modelling has led to extremely accurate reconstructions of cluster lenses suitable for use as gravitational telescopes (e.g., Stark et al. 2007; Smail et al. 2007) that can explore extremely high redshift galaxy formation, and combined measurements of weak and strong lensing around strongly lensed early-type galaxies in the SLACS survey has recently been used to place improved constraints upon the dark matter haloes around these galaxies (Gavazzi et al. 2007). As discussed in Section 1.1.7, combined strong and weak lensing data has recently provided strong evidence for a collisionless dark matter component in the merging cluster 1E 0657-558 that appears to be clearly distinct from the intracluster hot gas (see Section 1.1.7; Clowe et al. 2006; Bradač et al. 2006, but also Angus et al. 2007). Combined weak and strong lensing work has therefore contributed significantly to our understanding of the formation of galaxies and given further evidence for the existence of cold dark matter. In the following Section, I will now go on to describe the use of weak lensing in the placing of cosmological parameter constraints, a study which has come to prominence as a primary science goal in the survey design strategies for future optical survey telescopes.

## 1.2.7 Constraints on cosmological parameters from weak lensing

An extremely promising but challenging application of weak gravitational lensing is in the measurement of cosmic shear, which results from the fact that all light propogating through the Universe is deflected by the gravitational field of the inhomogoneous matter distribution. This causes distortions in the images of distant galaxies that are coherent, although extremely weak. Schneider et al. (2006) provide a thorough derivation of how the power spectrum of the convergence $\kappa$ can be related to the three dimensional matter power spectrum $P(k) = \left\langle \delta_k^2 \right\rangle$ (Peacock 1999), and so I will not not reproduce that derivation here. As also described by Schneider et al. (2006), the shear power spectrum can be determined from measurements of the tiny correlations between lensed galaxy images, as a function of angular scale, and may be directly related to the convergence power spectrum to place constraints upon large scale structure.

The value of cosmic shear as a probe of structure is that it makes no assumptions about the relationship between dark matter clustering and the clustering of baryonic galaxies (no poorly understood parameters such as the bias $b$ are necessary, for example), and therefore provides an independent verification of the results described in Section 1.1.8. In addition, cosmic shear measurements place joint constraints upon $\sigma_8$ and $\Omega_{m,0}$ that intersect with those from CMB measurements in a way that significantly reduces degeneracy in these parameters (Schneider et al. 2006).

However, the measurement of cosmic shear is technically difficult. This is not just because the cosmological signal is extremely weak, but is also due to the nature of the systematic distortions caused in galaxy images by imperfect telescope optics; telescope point spread functions (PSFs) induce correlated distortions in galaxy images that are typically an onrder of magnitude larger than the cosmological signal we wish to detect (see, e.g., Kaiser et al. 1995; Kaiser 2000). Despite this, cosmic shear was successfully detected in 2000 by four groups (Bacon et al. 2000; Kaiser et al. 2000; Van Waerbeke et al. 2000; Wittman et al. 2000) using the KSB method of lensing PSF correction (Kaiser et al. 1995; Luppino & Kaiser 1997; Hoekstra et al. 1998).

Subsequent cosmic shear analyses have been used to place competitive constraints upon large scale structure, with the most recent results being those of Benjamin et al. (2007). These authors combined a total of 100 square degrees of ground based survey data, including the Canada-France-Hawaii Telescope Legacy Survey (CFHTLS) Wide (see Hoekstra et al. 2006) together with the Red Cluster Sequence survey (Gladders et al. 2007), VIRMOS-Descart (Van Waerbeke et al. 2000, 2005a) and the Garching-Bonn Deep Survey (GaBoDS: Hetterscheidt et al. 2007) weak lensing surveys. The analysis also used an accurate calibration of the redshift distribution of lensing sources using the photometric redshifts of the joint CFHTLS-VIMOS VLT Deep Survey (VVDS) analysis (Ilbert et al. 2006). The resulting joint constraints upon the large scale structure were $\sigma_8 = (\Omega_{m,0}/0.24)^{0.59} = 0.84 \pm 0.05$ within a flat, concordance cosmology. This weakened what had been an apparent $\simeq$2-$\sigma$ discrepancy between earlier results from the CFHTLS (Hoekstra et al. 2006) and WMAP constraints (see Spergel et al. 2007), the difference being the accurate calibration of the source galaxy number counts as a function of redshift (Benjamin et al. 2007). It is becoming clear that accurate photometric redshift information, as well as ongoing improvements in shape measurement techniques, will be necessary as lensing surveys increase in size and statistical power. Recent observations of cosmic shear from space (Massey et al. 2007c) are in reasonable agreement with the results of (Benjamin et al. 2007), but currently suffer from the relatively small survey areas that can feasibly observed with the *Hubble Space Telescope*, and from the gradual degradation of on board CCDs due to cosmic rays (known as the Charge Transfer Efficiency problem, see Rhodes et al. 2007).

So far in this Chapter, I have described many basic elements of the concordance cosmological model, and the current constraints we have upon the few parameters that describe it. In addition we have seen some discussion of gravitational lensing, and described some of the results and future prospects of this study. In the remainder of this Chapter I will introduce an extension of weak gravitaional lensing known as flexion, the study and attempted measurement of which is the primary topic of this Thesis.

### 1.2.8 Higher order weak gravitational lensing: flexion

The study of weak gravitational flexion, otherwise known as the higher order weak lensing signal, is a recent development in the broader field of weak lensing (see Goldberg & Natarajan 2002; Irwin & Shmakova

2003; Goldberg & Bacon 2005; Irwin & Shmakova 2005; Bacon et al. 2006, BGRT06 hereafter, Massey et al. 2007d; Irwin et al. 2007). Flexion arises from the fact that the shear and convergence are actually not constant within the image, and so we can expand Equation (1.88) to second-order:

$$\beta_i \simeq A_{ij}\theta_j + \frac{1}{2}D_{ijk}\theta_j\theta_k, \tag{1.89}$$

with

$$D_{ijk} = \partial_k A_{ij}. \tag{1.90}$$

Using results from Kaiser (1995), we find that

$$\begin{aligned} D_{ij1} &= \begin{pmatrix} -2\gamma_{1,1} - \gamma_{2,2} & -\gamma_{2,1} \\ -\gamma_{2,1} & -\gamma_{2,2} \end{pmatrix}, \\ D_{ij2} &= \begin{pmatrix} -\gamma_{2,1} & -\gamma_{2,2} \\ -\gamma_{2,2} & 2\gamma_{1,2} - \gamma_{2,1} \end{pmatrix}. \end{aligned} \tag{1.91}$$

By expanding the surface brightness as a Taylor series and using the relations above, we find that we can approximate the lensed surface brightness of a galaxy in the weak lensing regime as

$$I(\boldsymbol{\theta}) \simeq \left\{1 + \left[(A - \mathcal{I})_{ij}\theta_j + \frac{1}{2}D_{ijk}\theta_j\theta_k\right]\partial_i\right\} I^{\rm s}(\boldsymbol{\theta}) \,, \tag{1.92}$$

where here $\mathcal{I}$ denotes the identity matrix. The distortion described by the $D_{ijk}$ tensor in the above equation is that which is responsible for the curved or arc-ed appearance of lensed galaxies, measurable information which has traditionally been ignored in the study of weak lensing phenomena.

### 1.2.9 Complex representation and the first and second flexion

In this Section we outline the compact and straightforward complex formalism of BGRT06 for the description of second-order lensing distortions; the formalism in fact has wider applicability to all weak gravitational lensing.

We define a complex gradient operator:

$$\partial = \partial_1 + {\rm i}\partial_2, \tag{1.93}$$

which we can think of as a derivative with an amplitude and a direction down the slope of a surface at any point. It transforms under rotations as a vector, $\partial' = \partial {\rm e}^{{\rm i}\phi}$, where $\phi$ is the angle of rotation. This operator can be compared with the covariant derivative formalism of Castro et al. (2005) for weak lensing on the curved sky. Applying the operator to the lensing scalar potential, $\psi$, we can generate the spin-1 (i.e. vector) lensing displacement field

$$\alpha = \alpha_1 + {\rm i}\alpha_2 = \partial\psi. \tag{1.94}$$

This correspondence allows us to interpret the complex gradient, $\partial$, as a spin-raising operator, raising the function it acts on by one spin value. Similarly the spin of a quantity can be lowered by applying the complex conjugate gradient, $\partial^*$. Applying one after the other yields the spin-zero two-dimensional

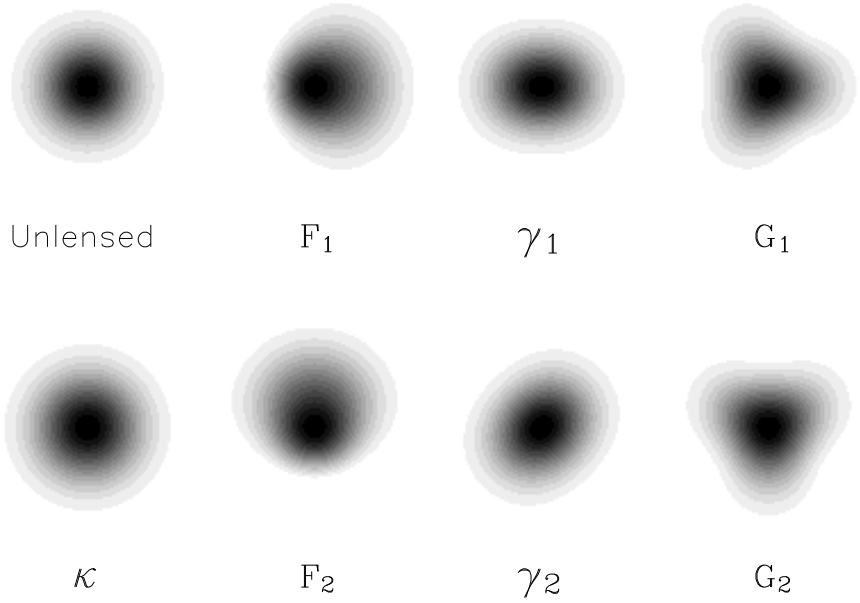


Figure 1.5: Weak lensing distortions with increasing spin values. Here an unlensed Gaussian galaxy with radius 1 arcsec has been distorted with 10 per cent convergence/shear, and 0.28 arcsec$^{-1}$ flexion. Convergence is a spin-0 quantity; first flexion is spin-1; shear is spin-2; and second flexion is spin-3.

Laplacian,

$$\partial\partial^* = \partial^*\partial = \partial_1^2 + \partial_2^2 = \nabla_\theta^2 \tag{1.95}$$

where we have noted that $\partial$ and $\partial^*$ commute. Applying the complex conjugate derivative to the displacement field we find the spin is lowered to the spin-0 convergence field

$$\kappa = \frac{1}{2}(\partial_1^2 + \partial_2^2)\psi = \frac{1}{2}\partial^*\alpha = \frac{1}{2}\partial^*\partial\psi. \tag{1.96}$$

Applying the spin-raising operation to the displacement field raises us to a spin-2 field, the complex shear:

$$\gamma = \frac{1}{2}\partial\partial\psi = \frac{1}{2}(\partial_1^2 - \partial_2^2)\psi + \mathrm{i}\partial_1\partial_2\psi = \gamma_1 + \mathrm{i}\gamma_2, \tag{1.97}$$

just as defined in Equations (1.86) and (1.87). The complex formalism provides a neat way to generalize the analysis of distortions to higher orders. Taking the third derivative of the lensing potential we define the unique combinations

$$\mathcal{F} = |\mathcal{F}|\mathrm{e}^{\mathrm{i}\phi} = \frac{1}{2}\partial\partial^*\partial\psi = \partial\kappa = \partial^*\gamma \tag{1.98}$$

$$\mathcal{G} = |\mathcal{G}|\mathrm{e}^{3\mathrm{i}\phi} = \frac{1}{2}\partial\partial\partial\psi = \partial\gamma, \tag{1.99}$$

where the first flexion, $\mathcal{F}$, is another spin-1 field and the second flexion, $\mathcal{G}$, is seen to be a spin-3 field.

Here $\phi$ represents the position angle determining the direction of the vector or spin-3 component. Using the complex derivative to expand the flexions in terms of the gradients of the shear field we find

$$\mathcal{F} = (\partial_1\gamma_1 + \partial_2\gamma_2) + \mathrm{i}(\partial_1\gamma_2 - \partial_2\gamma_1) \quad (1.100)$$

$$\mathcal{G} = (\partial_1\gamma_1 - \partial_2\gamma_2) + \mathrm{i}(\partial_1\gamma_2 + \partial_2\gamma_1). \quad (1.101)$$

Using these results one then obtains a direct and complete description of the second-order lensing tensor $D_{ijk}$ in terms of the flexion components. Defining $\mathcal{F} = \mathcal{F}_1 + \mathrm{i}\mathcal{F}_2$ and $\mathcal{G} = \mathcal{G}_1 + \mathrm{i}\mathcal{G}_2$ I re-expressed $D_{ijk}$ as the sum of two terms $D_{ijk} = \mathcal{F}_{ijk} + \mathcal{G}_{ijk}$, where the first (spin-1) term is

$$\begin{aligned} \mathcal{F}_{ij1} &= -\frac{1}{2}\begin{pmatrix} 3\mathcal{F}_1 & \mathcal{F}_2 \\ \mathcal{F}_2 & \mathcal{F}_1 \end{pmatrix} \\ \mathcal{F}_{ij2} &= -\frac{1}{2}\begin{pmatrix} \mathcal{F}_2 & \mathcal{F}_1 \\ \mathcal{F}_1 & 3\mathcal{F}_2 \end{pmatrix} \end{aligned} \quad (1.102)$$

and the second (spin-3) term is

$$\begin{aligned} \mathcal{G}_{ij1} &= -\frac{1}{2}\begin{pmatrix} \mathcal{G}_1 & \mathcal{G}_2 \\ \mathcal{G}_2 & -\mathcal{G}_1 \end{pmatrix} \\ \mathcal{G}_{ij2} &= -\frac{1}{2}\begin{pmatrix} \mathcal{G}_2 & -\mathcal{G}_1 \\ -\mathcal{G}_1 & -\mathcal{G}_2 \end{pmatrix}. \end{aligned} \quad (1.103)$$

This thus defines two new lensing measures, $\mathcal{F}$ and $\mathcal{G}$, which afford a complete and compact description of weak lensing distortions to next highest order. The first and second flexion also have simple spin properties, making them a natural description of these distortions when compared to the more complicated rotational behaviour of the derivatives of shear.

In order to obtain a visual understanding of the flexion quantities, the expression of the $D_{ijk}$ matrix in terms of $\mathcal{F}$ and $\mathcal{G}$ is used to calculate how a Gaussian image is transformed by the various operations of weak lensing, according to Equation (1.92). The results are shown in Figure 1.5, which displays the lensing operations in order of their spin properties. The Gaussian galaxy is given a radius (standard deviation) of 1 arcsec; while the convergence and shear imposed on the galaxy are realistic (10 per cent in each case), the flexion is deliberately chosen to be large for visualisation purposes (0.28 arcsec$^{-1}$). We immediately see the shapes induced by flexion: the first flexion leads to a (vectorial, spin-1) skewness, while the second flexion leads to a three-fold (spin-3) shape. For a simple demonstration of how it is both these modes of distortion, added to a shear, which are responsible for lensed arcs, see Figure 1.6, which uses a *combination* of the same, correct transformations upon a Gaussian image as were used to generate Figure 1.5.

Figure 1.6: Illustration of how the combination of shear, first flexion and second flexion is able to describe arc-like distortions in gravitational lensing.

### 1.2.10 Reduced shear and flexion

Before going onto describe theoretical predictions for the shear and flexion based on realistic mass models, I first outline some recent work in flexion theory that has relevance to this Thesis and applications beyond it. It was Schneider & Seitz (1995) who pointed out the weak lensing shear $\gamma$ described above is not strictly observable in practice, but rather the combination

$$g = \frac{\gamma}{1-\kappa}, \tag{1.104}$$

labelled the *reduced* shear. This accounts for the lensing sheet-mass degeneracy (Falco et al. 1985; Gorenstein et al. 1988), under which lensing observables remain unchanged under a change $\kappa \rightarrow \lambda\kappa+(1-\lambda)$. For many cosmological applications, including galaxy-galaxy lensing (Kleinheinrich et al. 2006) and cosmic shear (Hoekstra et al. 2006), the convergence (related to the projected surface mass density, see Chapter 2; also Bartelmann & Schneider 2001) will be small compared to one and so differences between the reduced shear and the shear are typically also small. It is then acceptable to assume $g \simeq \gamma$ on the condition that the bias involved in this approximation is smaller than the overall measurement uncertainty.

This work has very recently been extended to measurements of flexion by Schneider & Er (2007), who similarly find that $\mathcal{F}$ and $\mathcal{G}$ cannot be directly observed. This work finds the corresponding expression for the reduced $\mathcal{F}$ and $\mathcal{G}$ respectively:

$$G_1 = \partial^* g = \frac{\mathcal{F} + g\mathcal{F}^*}{1-\kappa} \qquad G_3 = \partial g = \frac{\mathcal{G} + g\mathcal{F}}{1-\kappa}. \tag{1.105}$$

As can be seen, these observable quantities are now more complex expressions involving the reduced shear and convergence, both of which can bias flexion estimates. Schneider & Er (2007) also point out further difficulties with the flexion measurement, finding that it may be impossible in general to construct an unbiased estimator for either $G_1$ or $G_3$, as was possible for $g$ (Schneider & Seitz 1995).

These considerations are of the greatest importance in the reconstruction of cluster mass distributions using flexion, where it should be expected that significant shears and $\kappa \gtrsim 0.1$ could cause a significant overestimating bias of the shear and flexion (Schneider & Er 2007). However, in the analyses that follow I consider the weak signal around galaxy halo-sized lenses, specifically those in the *HST* GEMS survey (Rix et al. 2004). These regions do not involve extremely large $g$ or $\kappa$ values; therefore, throughout this Thesis I assume the weak limit of $g \approx \gamma$, $G_1 \approx \mathcal{F}$ and $G_3 \approx \mathcal{G}$. I note that this is an approximation, however, but one that causes biasing effects that are well within the sample variance of the GEMS galaxy data. It will be important for future galaxy-galaxy lensing studies of greater sample size to quantify the effect of this bias,

as it will begin to impact upon measurements for the more massive galaxy haloes (see, e.g., Mandelbaum et al. 2005).

# CHAPTER 2

# FLEXION PREDICTIONS

In this Chapter I outline analytic and numerical results and predictions for flexion, many of which I was able to contribute towards Bacon et al. (2006) (BGRT06 hereafter). Here the concern is primarily an understanding of the strength and observability of flexion we might expect for dark matter halos in the physical Universe. I have derived analytic expressions for the flexion due to Singular Isothermal Sphere and NFW halos, and I have discussed the differences between these results. I have added a discussion of flexion for the Truncated Singular Isothermal Sphere, and an explanation the tools which may be used to calculate the flexion signal.

Finally, I present the investigation of simulated galaxy-galaxy lensing data sets using the method I described in BGRT06, but with some update of the discussion in light of subsequent observational findings (see also Chapters 4 and 6). This modelling suggests that flexion has much to offer studies of galaxy-galaxy lensing, but more recent knowledge about the distribution of measured flexion complicates more quantitative interpretation of these results. These issues are discussed, and are ultimately found to provide strong motivation for the analysis of flexion using real data.

## 2.1 Analytic flexion results

In order to describe the flexion signal around common lens models, it is useful to re-express the complex gradient operator (1.93) in polar coordinates upon the sky plane. Labelling as $\theta$ the modulus of the complex sky position vector $\theta_1 + \mathrm{i}\theta_2$, and with $\phi = \arctan(\theta_2/\theta_1)$, the complex gradient may be written as

$$\partial = \mathrm{e}^{\mathrm{i}\phi}\left(\frac{\partial}{\partial\theta} + \frac{\mathrm{i}}{\theta}\frac{\partial}{\partial\phi}\right). \tag{2.1}$$

Using Equations (1.98) and (1.99) it is then very simple to show that

$$\mathcal{F}(\theta,\phi) = \partial\kappa(\theta,\phi) = \left(\frac{\partial\kappa}{\partial\theta} + \frac{\mathrm{i}}{\theta}\frac{\partial\kappa}{\partial\phi}\right)\mathrm{e}^{\mathrm{i}\phi}. \tag{2.2}$$

Writing the complex shear as $\gamma = \tilde{\gamma}(\theta,\phi)\mathrm{e}^{2\mathrm{i}\phi}$, noting that in general $\tilde{\gamma}(\theta,\phi)$ will be complex for non-circularly symmetric lenses, I was also able to calculate the equivalent result for the second flexion:

$$\mathcal{G}(\theta,\phi) = \partial\gamma(\theta,\phi) = \left(\frac{\partial\tilde{\gamma}}{\partial\theta} - \frac{2\tilde{\gamma}}{\theta} + \frac{\mathrm{i}}{\theta}\frac{\partial\tilde{\gamma}}{\partial\phi}\right)\mathrm{e}^{3\mathrm{i}\phi}. \tag{2.3}$$

If the lens model displays circular symmetry this expression may be simplified; for such models $|\gamma(\theta)| = \bar{\kappa}(\theta) - \kappa(\theta)$ (Miralda-Escudé 1991), where $\bar{\kappa}(\theta)$ is the average convergence within $\theta$ from the centre of the lens. For a lens model with shear $\gamma = -|\gamma(\theta)|\mathrm{e}^{2\mathrm{i}\phi}$, the second flexion can then be more simply expressed as

$$\mathcal{G}(\theta,\phi) = \left(\frac{4|\gamma(\theta)|}{\theta} + \frac{\partial\kappa(\theta)}{\partial\theta}\right)\mathrm{e}^{3\mathrm{i}\phi}. \tag{2.4}$$

In the results that follow this expression is used a number of times to quickly calculate predictions for the second flexion.

### 2.1.1 Flexion for the Singular Isothermal Sphere (SIS)

We start by calculating the flexion predictions for the Singular Isothermal Sphere (SIS) lens model, expressed in Equation (1.62). This density profile provides a good first approximation to CDM haloes as it very simply reproduces the flat rotation curves observed in spiral galaxies. Projecting the density onto the two-dimensional lens plane, the surface mass density of the SIS is

$$\Sigma(\xi) = \frac{\sigma_v^2}{2G\xi}, \tag{2.5}$$

where $\xi$ is the distance from the centre of the lens in the projected lens plane and where $\sigma_v$ is the one-dimensional velocity dispersion of 'particles' within the gravitational potential of the mass distribution, such as stars. The dimensionless surface mass density, or convergence, is thus

$$\kappa(\theta) = \frac{\Sigma}{\Sigma_{\mathrm{crit}}} = \frac{\theta_{\mathrm{E}}}{2\theta}, \tag{2.6}$$

where $\theta = \xi/D_{\rm l}$ is the angular distance from lens centre in the sky plane and where $\theta_{\rm E}$ is the Einstein deflection angle, defined as

$$\theta_{\rm E} = 4\pi \left(\frac{\sigma_v}{c}\right)^2 \frac{D_{\rm ls}}{D_{\rm s}}. \tag{2.7}$$

The shear caused by the SIS at an angular separation $\theta$ from the lens centre on the sky plane is

$$\gamma(\theta, \phi) = -\frac{\theta_{\rm E}}{2\theta} {\rm e}^{2{\rm i}\phi} \tag{2.8}$$

(see, e.g., Bartelmann & Schneider 2001). The SIS shear signal falls only weakly with distance from the lens centre, and the ${\rm e}^{2{\rm i}\phi}$ angular dependence reflects the spin-2 rotational symmetry of the shear transformation. Using Equation (2.2), I then found the simple expression for the first flexion to be:

$$\mathcal{F}(\theta, \phi) = -\frac{\theta_{\rm E}}{2\theta^2} {\rm e}^{{\rm i}\phi}. \tag{2.9}$$

As expected, the first flexion for this profile is therefore circularly symmetric, and displays vector-like rotational symmetry with the vector directed radially inwards towards the lens centre. Importantly, the signal strength varies with $\theta^{-2}$ and so the flexion will only be significant for objects close to the line of sight to the SIS lens.

In a similar fashion I calculated the expression for the second flexion using Equation (2.4), finding that

$$\mathcal{G}(\theta, \phi) = \frac{3\theta_{\rm E}}{2\theta^2} {\rm e}^{3{\rm i}\phi} \, . \tag{2.10}$$

The spin-3 rotational symmetries of $\mathcal{G}$ are encapsulated in the ${\rm e}^{3{\rm i}\phi}$ dependence of this expression. The second flexion shares the $\theta^{-2}$ dependence displayed by $\mathcal{F}$ for the SIS, but interestingly has a larger amplitude; as will be seen, this is found to be a common feature of flexion predictions for cosmologically realistic lens models.

### 2.1.2 Flexion for the Softened SIS (SSIS)

The SIS mass distribution can be modified so as to remove one feature which may not be a good physical description of dark matter haloes, the divergence of $\Sigma$ for $\theta \longrightarrow 0$ (see Section 1.1.9 for a discussion of observational evidence for cored dark matter haloes). One simple modification is to cut off the distribution at small distances, defining as in Equation (1.65) the Softened SIS as

$$\rho(r) = \frac{\sigma_v^2}{2\pi G(r^2 + r_{\rm c}^2)}, \tag{2.11}$$

where $r_{\rm c}$ is a core radius within which the density tends to a constant value. Projecting this density onto the lens plane and dividing by the critical density $\Sigma_{\rm crit}$, the convergence is thus found to be

$$\kappa(\theta) = \frac{\theta_{\rm E}}{2\sqrt{\theta^2 + \theta_{\rm c}^2}}, \tag{2.12}$$

where $\theta_{\rm c}$ is defined as $r_{\rm c}/D_{\rm l}$, the angular radius within which the surface mass density flattens off to a value $\kappa_0 = \theta_{\rm E}/2\theta_{\rm c}$ as $\theta \to 0$. For $\theta \gg \theta_{\rm c}$ this mass distribution behaves like the SIS. The shear for the

SSIS lens is then

$$\gamma(\theta,\phi) = \frac{\theta_{\rm E}}{2\sqrt{\theta^2+\theta_c^2}}\left\{1-\frac{2\theta_c}{\theta^2}\left(\sqrt{\theta^2+\theta_c^2}-\theta_c\right)\right\}{\rm e}^{2{\rm i}\phi}, \tag{2.13}$$

which may be calculated using the $|\gamma| = \bar{\kappa} - \kappa$ relationship of Miralda-Escudé (1991). Interestingly this shear signal tends to zero at the origin but behaves like the SIS lens at distance.

Using Equation (2.2), I found the first flexion due to the SSIS lens to be

$$\mathcal{F}(\theta,\phi) = -\frac{\theta_{\rm E}\theta}{2(\theta^2+\theta_{\rm c}^2)^{3/2}}{\rm e}^{{\rm i}\phi}\ . \tag{2.14}$$

Again, for $\theta \gg \theta_{\rm c}$ the flexion is approximately equal to that of the SIS. At small separations the flexion goes to zero, which should be expected as the convergence is tending to a maximum and will thus have zero gradient. From (2.4), the second flexion for the SSIS is then

$$\mathcal{G}(\theta,\phi) = \frac{3\theta_{\rm E}\theta}{2(\theta^2+\theta_c^2)^{3/2}}\left\{1+\frac{4\theta_c^2}{3\theta^2}-\frac{8\theta_c}{3\theta^4}(\theta^2+\theta_c^2)\left(\sqrt{\theta^2+\theta_c^2}-\theta_c\right)\right\}{\rm e}^{3{\rm i}\phi}, \tag{2.15}$$

which can again be seen to reduce to the SIS second flexion when $\theta \gg \theta_{\rm c}$, and tends to zero at the centre of the lens.

### 2.1.3 Flexion for the Truncated SIS (TSIS)

Another issue with the SIS lens model is its divergent total mass, which led authors (see, e.g., Brainerd et al. 1996; Hoekstra et al. 2004) to define a Truncated SIS as follows:

$$\rho(r) = \frac{\sigma_v^2 s^2}{2\pi G r^2(r^2+s^2)}, \tag{2.16}$$

where defines $s$ the truncation radius, beyond which the density falls off as $r^{-4}$. The convergence for this lens model is then

$$\kappa(\theta) = \frac{\theta_{\rm E}}{2\theta}\left\{1-\frac{\theta}{\sqrt{\theta^2+\theta_s^2}}\right\}, \tag{2.17}$$

with $\theta_s = s/D_{\rm l}$, and the shear is given by

$$\gamma(\theta,\phi) = -\frac{\theta_{\rm E}}{2\theta}\left\{1-\frac{\theta}{\sqrt{\theta^2+\theta_2^2}}+\frac{2\theta_s}{\theta}\left(1-\frac{\theta_s}{\sqrt{\theta^2+\theta_s^2}}\right)\right\}{\rm e}^{2{\rm i}\phi}. \tag{2.18}$$

This lens reproduces the shear behaviour of the SIS towards $\theta = 0$, as required, but falls off as $\sim 1/\theta^2$ at large distances. Again, using Equations (2.2) and (2.4) for this circularly symmetric lens, I was able to simply calculate flexion predictions. The first flexion for the TSIS is thus

$$\mathcal{F}(\theta,\phi) = -\frac{\theta_{\rm E}}{2\theta^2}\left\{1-\frac{\theta^3}{(\theta^2+\theta_s^2)^{3/2}}\right\}{\rm e}^{{\rm i}\phi}, \tag{2.19}$$

and the second flexion is given by

$$\mathcal{G}(\theta,\phi) = \frac{3\theta_{\rm E}}{2\theta^2}\left\{1 - \frac{\theta\left(\theta^2+\frac{4}{3}\theta_s^2\right)}{\left(\theta^2+\theta_s^2\right)^{3/2}} + \frac{8\theta_s}{3\theta}\left(1 - \frac{\theta_s}{\sqrt{\theta^2+\theta_s^2}}\right)\right\}\mathrm{e}^{3\mathrm{i}\phi}. \tag{2.20}$$

Both of these flexion results vary like the SIS ($\sim 1/\theta^2$) at small angular radii, but fall off more quickly ($\sim 1/\theta^4$) for $\theta \gg \theta_s$.

### 2.1.4 Flexion for the NFW halo profile

I now turn to the NFW density profile described in Section 1.1.9, which was found by Navarro et al. (1997) to accurately represent simulated CDM haloes and has remained the standard theoretical description of these objects. The NFW profile has the following form for the dimensionless surface mass density (see Bartelmann 1996):

$$\kappa(y) = 2\kappa_{\rm s}\frac{f(y)}{y^2-1}, \tag{2.21}$$

where we define $\kappa_{\rm s} = \rho_{\rm crit}(z)\Delta_{\rm c}r_{\rm s}/\Sigma_{\rm crit}$ and $y \equiv \xi/r_{\rm s}$, with $\xi$ defined as for equation (2.5), and $\Delta_{\rm c}$ and $r_{\rm s}$ defined as described in Section 1.1.9 and Navarro et al. (1997). Bartelmann (1996) give the function $f(y)$ as

$$f(y) = \begin{cases} 1 - \frac{2}{\sqrt{1-y^2}}\mathrm{arctanh}\sqrt{\frac{1-y}{1+y}} & y < 1 \\ 1 - \frac{2}{\sqrt{y^2-1}}\arctan\sqrt{\frac{y-1}{y+1}} & y > 1. \end{cases} \tag{2.22}$$

Taking the gradient of $\kappa$, I found the flexion for the NFW density profile to be given by

$$\mathcal{F} = \partial\kappa = \frac{\partial y}{\partial\theta}\frac{\partial\kappa}{\partial y}. \tag{2.23}$$

Defining $\mathcal{F}_{\rm s} \equiv \kappa_{\rm s}D_{\rm l}/r_{\rm s}$ we then have

$$\mathcal{F} = -2\mathcal{F}_{\rm s}\left[\frac{2yf(y)}{(y^2-1)^2} - \frac{1}{(y^2-1)}\frac{\mathrm{d}f(x)}{\mathrm{d}x}\right]\mathrm{e}^{\mathrm{i}\phi} \tag{2.24}$$

with $y = \theta D_{\rm l}/r_{\rm s} = \theta/\theta_{\rm s}$, and where, from Equation (2.22),

$$\frac{\mathrm{d}f(y)}{\mathrm{d}x} = \begin{cases} \frac{1}{(1-y^2)}\left(\frac{1}{y} - \frac{2y}{\sqrt{1-y^2}}\mathrm{arctanh}\sqrt{\frac{1-y}{1+y}}\right) & y < 1 \\ \frac{1}{(y^2-1)}\left(\frac{2y}{\sqrt{y^2-1}}\arctan\sqrt{\frac{y-1}{y+1}} - \frac{1}{y}\right) & y > 1. \end{cases} \tag{2.25}$$

The analytic form of the second flexion can be found, as for the other circularly symmetric lenses, using Equation (2.4) and the result of Wright & Brainerd (2000) for the magnitude of shear due to an NFW lens. I then found that the second flexion takes the form

$$\mathcal{G} = 2\mathcal{F}_{\rm s}\left[\frac{8}{y^3}\ln\frac{y}{2} + \frac{\left(\frac{3}{y}(1-2y^2)+g(y)\right)}{(y^2-1)^2}\right]\mathrm{e}^{3\mathrm{i}\phi}, \tag{2.26}$$

where

$$g(y) = \begin{cases} \left(\frac{8}{y^3} - \frac{20}{y} + 15y\right) \frac{2}{\sqrt{1-y^2}} \mathrm{arctanh}\sqrt{\frac{1-y}{1+y}} & y < 1 \\ \left(\frac{8}{y^3} - \frac{20}{y} + 15y\right) \frac{2}{\sqrt{y^2-1}} \arctan\sqrt{\frac{y-1}{y+1}} & y > 1. \end{cases} \quad (2.27)$$

This second flexion is larger in amplitude than the first flexion, as was also the case for the SIS results. I now compare in more detail the flexion signals from the NFW and SIS density profile, as confirming the NFW model in the real Universe would be an important success for the ΛCDM model.

### 2.1.5 Comparing NFW and SIS flexion results

To better illustrate these results, I calculated the first and second flexion signals we might expect to measure for a typical galaxy-sized halo with either an SIS or NFW profile. Firstly we consider the calculation of the NFW scaling parameters.

I choose a lens redshift $z_\mathrm{l} = 0.35$ and the halo $M_{200} = 10^{12} h^{-1} M_\odot$, this lens redshift being the median of the lens galaxy sample used by Hoekstra et al. (2004), and the mass having been found to be roughly typical for galaxy halos in weak lensing analyses by Brainerd et al. (1996) and Hoekstra et al. (2004). I also choose $D_\mathrm{ls}/D_\mathrm{s} = 0.5$ (corresponding to a source redshift of $z_\mathrm{s} \approx 0.8$) and model the lensing within a standard, flat ΛCDM cosmology, setting the present-day matter density parameter $\Omega_{m,0} = 0.3$, $\Omega_{\Lambda,0} = 0.7$, the Hubble parameter $h = 0.72$ and $\sigma_8 = 0.8$, based on the 1-year results from the WMAP experiment Spergel et al. (2003).

Julio Navarro has made a publicly available program (`charden.f`[1]) that generates predictions for $c$ and $\Delta_\mathrm{c}$ based on input cosmological parameters and the model outlined in the Appendix of Navarro et al. (1997). This formalism links the characterisic density $\Delta_\mathrm{c}$ of NFW halos to the mean matter density $\Omega_M$ at a collapse redshift $z_\mathrm{coll}(M_{200}, f)$, defined as the redshift at which half the mass of the halo was first contained in progenitors more massive than some fraction $f$ of the final mass $M_{200}$. The simple proportionality relationship $\Delta_\mathrm{c} \sim 10^3 \times \Omega_M(z_\mathrm{coll})/\Omega_M(z_\mathrm{final})$, combined with a value of $f = 0.01$, was found to give good results for all the simulations of Navarro et al. (1997), and the routine `charden.f` implements this calculation for a given input cosmology, halo mass and final halo redshift.

Using `charden.f` I find a concentration of $c = 7.20$ and a corresponding dimensionless characteristic density $\Delta_c = 20267$ for the NFW scaling parameters. These values are again in good agreement with those found by Hoekstra et al. (2004) who measured $\Delta_\mathrm{c} = 2.4^{1.4}_{-0.8} \times 10^4$ as the best fit to their sample of $\sim 10^5$ lenses.

For a flat ΛCDM cosmology, the $\kappa_\mathrm{s}$ scaling parameter of Bartelmann (1996) and Wright & Brainerd (2000) is given by

$$\begin{aligned} \kappa_\mathrm{s}(M_{200}, c, z_\mathrm{l}, z_\mathrm{s}) &= 2.71 \times 10^{-8} \times \frac{\Delta_\mathrm{c}}{c} \left(\frac{D_\mathrm{l}}{h^{-1}\mathrm{Mpc}}\right) \left(\frac{D_\mathrm{ls}}{D_\mathrm{ls}}\right) \\ &\times \left[\Omega_{\Lambda,0} + (1+z_\mathrm{l})^3 \Omega_{m,0}\right]^{2/3} \left(\frac{M_{200}}{10^{12} h^{-1} M_\odot}\right)^{1/3}. \end{aligned} \quad (2.28)$$

[1] available at http://www.astro.uvic.ca/ jfn/mywebpage/home.html

The scaling radius $r_{\rm s}$ is given by

$$\left(\frac{r_{\rm s}}{h^{-1}{\rm Mpc}}\right) = \frac{1}{c}\left(\frac{r_{200}}{h^{-1}{\rm Mpc}}\right) = 0.163 \times \frac{1}{c}\left[\Omega_{\Lambda,0} + (1+z_{\rm l})^3\Omega_{m,0}\right]^{-1/3}\left(\frac{M_{200}}{10^{12}h^{-1}M_{\odot}}\right)^{1/3}, \quad (2.29)$$

and the flexion scaling constant $\mathcal{F}_{\rm s}$ is then given by

$$\begin{aligned}\left(\frac{\mathcal{F}_{\rm s}(c,z_{\rm l},z_{\rm s})}{\rm arcsec^{-1}}\right) &= 8.09\times10^{-13}\times\Delta_{\rm c}\left(\frac{D_{\rm l}}{h^{-1}{\rm Mpc}}\right)^2\left(\frac{D_{\rm ls}}{D_{\rm ls}}\right) \\ &\times \left[\Omega_{\Lambda,0} + (1+z_{\rm l})^3\Omega_{m,0}\right].\end{aligned} \quad (2.30)$$

Interestingly, we note that the flexion scaling parameter is not a function of the virial mass $M_{200}$ of the lensing halo, due to the cancelling of this dependence when taking the ratio of Equations (2.28) and (2.29). The flexion signal at any given function of the scale angle $\theta_{\rm s} = r_{\rm s}/D_{\rm l}$ is therefore independent of halo mass, but it should be noted that (from Equation 2.29) the scaling radius itself varies with mass.

The SIS scaling is straightforward in comparison; the Einstein radius for the SIS lens is given in terms of $M_{200}$ and the halo redshift $z_{\rm l}$ as

$$\theta_{\rm E} = \frac{2\pi G}{c^2}\frac{D_{\rm ls}}{D_{\rm s}}\left(\frac{800\pi\rho_{\rm crit}(z_{\rm l})}{3}\right)^{1/3} M_{200}^{2/3}. \quad (2.31)$$

Using the same values for $M_{200}$, $z_{\rm l}$ and the cosmological parameters as were used for the NFW halo above, this gives an Einstein radius for the SIS halo of $\theta_E = 0.215$ arcsec.

The predicted magnitudes of $\mathcal{F}_{\rm NFW}$, $\mathcal{G}_{\rm NFW}$, $\mathcal{F}_{\rm SIS}$ and $\mathcal{G}_{\rm SIS}$, as a function of angular separation from the lensing halo on the sky, are shown in Figure 2.1. As could be expected the profiles show a good deal of similarity, but it is apparent that both the first and second flexion due to the SIS profile are stronger than those due to the NFW at very small separations. Since one of the important features of the NFW profile is that the density in the extreme interior of the halo varies as $\propto r^{-1}$ compared to the steeper $\propto r^{-2}$ for the SIS, this is not a surprising result.

It can be seen by comparing the lower plot of Figure 2.1, for which the $\theta$ axis is doubled in scale, with the upper plot, that $\mathcal{G}_{\rm NFW}$ is both stronger and longer range than $\mathcal{F}_{\rm NFW}$. Interestingly, we also note that the angular separation at which the SIS halo flexion exceeds that for the NFW halo is larger by about 5 arcsec for second flexion in relation to the first flexion. These two effects are a consequence of the non-locality of $\mathcal{G}$ as a lensing measurement when compared to the directly local $\boldsymbol{\nabla}\kappa$ measurement given by $\mathcal{F}$; for the NFW profile, $\mathcal{G}$ tends to be less steep than $\mathcal{F}$ at small $\theta$ and to die away less rapidly at larger separations.

The middle plot of Figure 2.1 shows another feature of the comparison between the two profiles: an SIS halo of $M_{200} = 1.8\times10^{12}h^{-1}M_{\odot}$ is practically indistinguishable from an NFW halo with $M_{200} = 1\times10^{12}h^{-1}M_{\odot}$ for first flexion measurements over galaxy-galaxy separations greater than about 5 arcsec. This is a very similar property to one found by Wright & Brainerd (2000) in a comparison of the *shear* profiles of SIS and NFW halos. They found that the assumption of an SIS halo profile produced systematic overestimation (by factors of up to 1.5) of the mass of NFW halos. Further work will be required to determine the dependence of this effect upon concentration for flexion measurements as Wright & Brainerd usefully did for the case of shear.

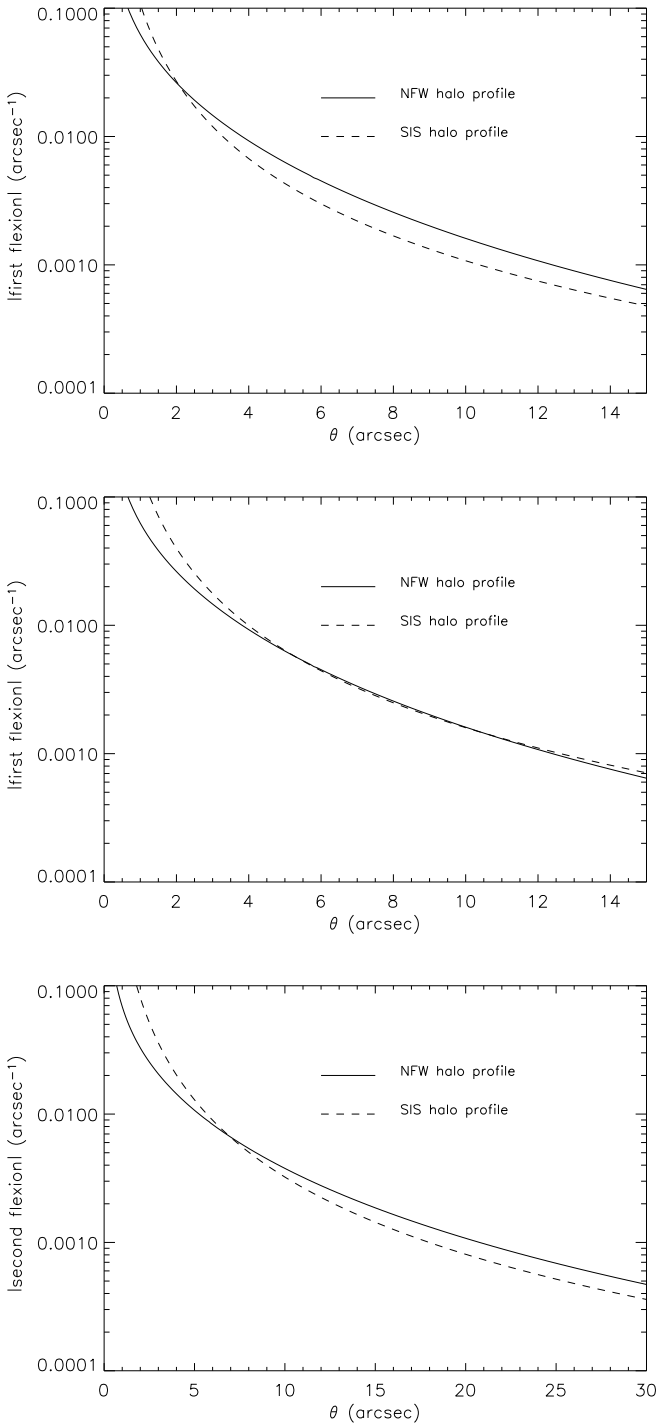


Figure 2.1: Top: Comparison of the magnitude of first flexion due to an NFW and an SIS halo of $M_{200} = 1 \times 10^{12} h^{-1} M_{\odot}$ at redshift $z_{\rm l} = 0.35$. Middle: A similar $\mathcal{F}$ comparison but this time the SIS halo has $M_{200} = 1.8 \times 10^{12} h^{-1} M_{\odot}$. Bottom: The magnitude of $\mathcal{G}$ for an NFW and an SIS halo of $M_{200} = 1 \times 10^{12} h^{-1} M_{\odot}$, where the doubling in scale of the angular separation axis highlights the larger range and amplitude of the second flexion.

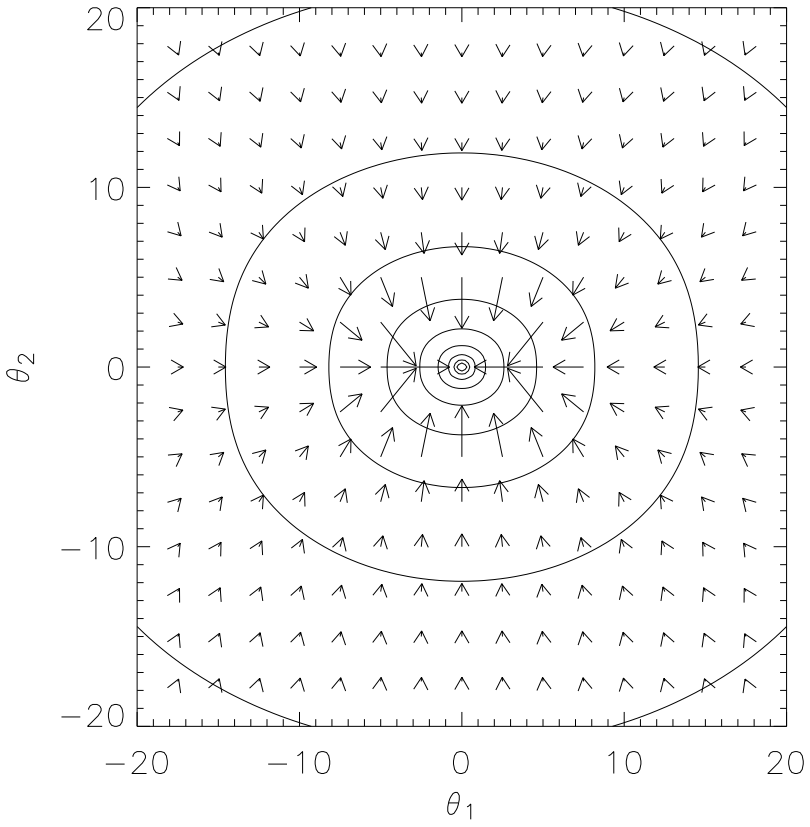


Figure 2.2: Flexion vector field for an elliptical isothermal density distribution with minor-to-major axis ratio of 0.67. Points in the extreme interior of the diagram have been omitted for clarity and the elliptical contours follow the logarithm of $|\mathcal{F}|$.

### 2.1.6 Flexion for elliptical profiles

We now discuss the more general prospect of using flexion to measure the ellipticity of lenses. When describing elliptically flattened halo mass distributions, it is often simplest to work with elliptical lensing potentials. Unfortunately these descriptions have some severe limitations, most notably that they produce dumbbell-shaped isodensity contours for large ellipticities and can even produce negative surface-mass densities (see Kassiola & Kovner 1993). It is thus best to consider models where the isodensity contours of the mass distribution are elliptical, despite the increased complexity of the lens potential. The simplest generalization of the softened isothermal sphere to an elliptical density profile can be written

$$\kappa(\theta_1,\theta_2) = \frac{\theta_{\rm E}}{2\sqrt{\theta_{\rm c}^2 + \dfrac{\theta_1^2}{(1+\epsilon)^2} + \dfrac{\theta_2^2}{(1-\epsilon)^2}}}, \tag{2.32}$$

where the major axis of the elliptical isodensity contours lie along the $\theta_1$ axis in the sky plane, and the ellipticity $\epsilon$ is defined by the ratio of minor-to-major axes ($b$ and $a$ respectively):

$$\frac{b}{a} = \frac{1-\epsilon}{1+\epsilon}. \tag{2.33}$$

The flexion vector at $(\theta_1, \theta_2)$ in the sky plane is then

$$\mathcal{F} = -\frac{\theta_{\rm E}}{2\left(\theta_c^2 + \frac{\theta_1^2}{(1+\epsilon)^2} + \frac{\theta_2^2}{(1-\epsilon)^2}\right)^{3/2}} \left(\frac{\theta_1}{(1+\epsilon)^2} + \frac{{\rm i}\theta_2}{(1-\epsilon)^2}\right). \tag{2.34}$$

We note that interestingly, $\mathcal{F}$ is no longer directed towards the centre of the lens for all $(\theta_1, \theta_2)$; it will in fact be centrally directed only when either $\theta_1$ or $\theta_2$ are equal to zero.

It is simple to show that the first flexion vector at a point $(\theta_1, \theta_2)$ will be directed towards a point on the major axis of the ellipse with coordinates $(a_{\rm int}, 0)$ where

$$a_{\rm int} = \left[1 - \left(\frac{1-\epsilon}{1+\epsilon}\right)^2\right]\theta_1 = \left[1 - \left(\frac{b}{a}\right)^2\right]\theta_1. \tag{2.35}$$

Due to the $(b/a)^2$ term, even relatively modest ellipticities in the density distribution cause $a_{\rm int}$ to represent a significant fraction of $\theta_1$. This tendency for the flexion vector to be aimed at a point significantly off lens-centre can also be seen in Figure 2.2, drawn for an axis ratio of $0.67$ which may be typical of galaxy halos (see e.g. Hoekstra et al. 2004, also Mandelbaum et al. 2005 who find a lower value). This implies that measurements of the direction of flexion in galaxy-galaxy lensing may be able to give good further constraints on the ellipticity of dark matter halos.

This concludes the description of analytical flexion results I contributed towards BGRT06. For completeness, I describe the following extra result taken from this paper, the second flexion for an unsoftened elliptical profile. Setting $\theta_{\rm c} = 0$, the elliptical isothermal profile can be conveniently rewritten, beginning by defining the following radial term:

$$\rho \equiv \sqrt{\theta_1^2 + f^2\theta_2^2}, \tag{2.36}$$

where $f^2 = (a/b)^2$, $a$ being the semi-major axis and $b$ the semi-minor axis as before. The density profile can then be simply written as $\kappa = A/\rho$, where $A = a\theta_{\rm E}/(a+b)$. For this distribution, the shear can be shown to be given by

$$\gamma_1 = -A\frac{\cos(2\phi)}{\rho} = -A\frac{\theta_1^2 - \theta_2^2}{\rho\theta^2}, \qquad \gamma_2 = -A\frac{\sin(2\phi)}{\rho} = -A\frac{2\theta_1\theta_2}{\rho\theta^2}. \tag{2.37}$$

The derivatives of these terms may be calculated to find the corresponding complex first and second flexion:

$$\mathcal{F} = \left(-\frac{A\theta_1}{\rho^3}\right) + {\rm i}\left(-\frac{Af^2\theta_2}{\rho^3}\right) \tag{2.38}$$

and

$$\mathcal{G} = A\left(\frac{3\theta_1^5 - \theta_1\theta_2^4 - 6\theta_1^3\theta_2^2 - 8f^2\theta_1\theta_2^4}{\rho^3\theta^4}\right) + {\rm i}A\left(\frac{8\theta_1^4\theta_2 + 6\theta_1^2f^2\theta_2^3 + f^2\theta_1^4 t - 3f^2\theta_2^5}{\rho^3\theta^4}\right). \tag{2.39}$$

These results conclude the discussion of analytical results for flexion from physically-motivated CDM halo models. We now turn to an simulated investigation into what extra information into dark matter halo structure might be gained from the measurement of flexion, compared to measurements of shear alone.

## 2.2 Predicting halo constraints

Previous studies of galaxy-galaxy lensing which have aimed to constrain values of halo parameters such as $M_{200}$ or $c$ for the NFW profile have used measurements of shear exclusively (see, e.g., Brainerd et al. 1996; Hoekstra et al. 2004, hereafter HYG04 in this Section; Kleinheinrich et al. 2006; see also Schneider & Rix 1997). It is therefore worthwhile considering whether combining measurements of shear and flexion might improve constraints for the halo parameters such as $c$ or $M_{200}$ when compared to those derived from measurements of shear alone.

### 2.2.1 A simple model of galaxy-galaxy lensing data

In order to do this I constructed a simplified but illustrative model of data we might expect from both shear *and* flexion measurements. We can generate mock galaxy-mass correlation function data for a sample of lens and source galaxies such as might be available using current or forthcoming galaxy imaging surveys. I model lens haloes as NFW profiles, and then make the important first simplification that every lens galaxy in our sample is of B-band luminosity $L_B^*$, with a single associated fiducial mass $M_{200}$ and concentration $c$. Such fiducial values are assigned in HYG04 to galaxies with a wide range of luminosities, using an observationally motivated power law scaling relation such as proposed by Guzik & Seljak (2002). Rather than modelling a range of galaxy luminosities as will be seen in real survey data, we simply model each galaxy as being of "typical" luminosity $L_B^*$ and make no attempt to include variation in galaxy mass, concentration, mass-to-light ratio or concentration-to-light ratio.

This single-luminosity approximation will limit the overall accuracy of the model, as it does not take detailed account of the balance struck between the contributions from large and small galaxies: in galaxy-galaxy lensing the majority of the signal is due to galaxies larger than $L_B^*$, whilst those smaller than $L_B^*$ in fact make up the majority of the population. However, the purpose of this investigation is the comparison of shear versus flexion measurements and so it is the *relative* signal-to-noise properties that are of interest. We assume that, as a first approximation, this simplification to the mass model will not significantly prejudice results towards either shear or flexion. As a final check, we can estimate the overall accuracy of the model by comparing modelled constraints on shear alone to those published in the literature. This is the most severe test of the viability of the single-luminosity approximation; if passed it provides further evidence that this model will allow a fair comparison of shear and flexion signals.

### 2.2.2 Noise on individual shear and flexion measurements

In order to estimate the confidence limits we expect from weak lensing measurements we must estimate the noise upon the measured signal. We assume this noise will be dominated by the scatter in measured

ellipticities and flexion that is present even in the absence of gravitational lensing; this we refer to as the intrinsic scatter. In this simple model I approximate this scatter as being normally distributed around zero, with a standard deviation that can be found from the root mean square (rms) measured shear or flexion from survey data. In this work I use values of $\gamma_{\rm int} = 0.3$, $\mathcal{F}_{\rm int} = 0.1$ arcsec$^{-1}$ and $\mathcal{G} = 0.3$ arcsec$^{-1}$ for the rms intrinsic shear and flexion. These flexion values, based on early measurements from my work which ignored the effects of an anisotropic PSF, are significantly larger than the $\mathcal{F}_{\rm int} = 0.04$ found by Goldberg & Bacon (2005).

However, the modelling of flexion measurement errors as normally distributed represents a considerable oversimplification; measurements of $\mathcal{F}$ and $\mathcal{G}$ are found to be distributed in a non-Gaussian manner, with broad wings containing significant numbers of outliers. Strategies for accurately dealing with this property of flexion are discussed in later Chapters, but we retain the assumption of Gaussian errors in this modelling. This simplifies both the error model and the interpretation of parameter likelihood contours, but may have consequences for the interpretation of our modelling results. As a first investigation we make this simplification but proceed with caution.

### 2.2.3 Noise due to redshift measurements

Possible errors in the redshift determinations must also be considered; I assume for this simple simulation that we have access to photometric redshifts for each galaxy, with an uncertainty of $\Delta z$ on each individual redshift measurement. Values for $\Delta z$ are assigned below as appropriate for broad-band and medium-band photometric redshift surveys. We note (see Wright & Brainerd 2000) that the strength of the shear signal due to an NFW halo depends on the lens geometry via a factor $\gamma_{\rm NFW} \propto D_{\rm l} D_{\rm ls}/D_{\rm s}$, whereas I found in Section 2.1.4 that the strength of the flexion varies as $\mathcal{F}_{\rm NFW} \propto D_{\rm l}^2 D_{\rm ls}/D_{\rm s}$. I thus model the error on measurements of the shear and flexion due to redshift uncertainties by calculating fractional uncertainties on on values of $D_{\rm l} D_{\rm ls}/D_{\rm s}$ and $D_{\rm l}^2 D_{\rm ls}/D_{\rm s}$. This can be done by considering the four following integral terms:

$$\left\langle \frac{D_{\rm l} D_{\rm ls}}{D_{\rm s}} \right\rangle = \int_0^\infty {\rm d}z'_{\rm s} P(z'_{\rm s}|z_{\rm s}) \int_0^\infty {\rm d}z'_{\rm l} P(z'_{\rm l}|z_{\rm l}) \frac{D_{\rm l'} D_{\rm l's'}}{D_{\rm s'}} \tag{2.40}$$

$$\left\langle \left( \frac{D_{\rm l} D_{\rm ls}}{D_{\rm s}} \right)^2 \right\rangle = \int_0^\infty {\rm d}z'_{\rm s} P(z'_{\rm s}|z_{\rm s}) \int_0^\infty {\rm d}z'_{\rm l} P(z'_{\rm l}|z_{\rm l}) \frac{D_{\rm l'}^2 D_{\rm l's'}^2}{D_{\rm s'}^2} \tag{2.41}$$

$$\left\langle \frac{D_{\rm l}^2 D_{\rm ls}}{D_{\rm s}} \right\rangle = \int_0^\infty {\rm d}z'_{\rm s} P(z'_{\rm s}|z_{\rm s}) \int_0^\infty {\rm d}z'_{\rm l} P(z'_{\rm l}|z_{\rm l}) \frac{D_{\rm l'}^2 D_{\rm l's'}}{D_{\rm s'}} \tag{2.42}$$

$$\left\langle \left( \frac{D_{\rm l}^2 D_{\rm ls}}{D_{\rm s}} \right)^2 \right\rangle = \int_0^\infty {\rm d}z'_{\rm s} P(z'_{\rm s}|z_{\rm s}) \int_0^\infty {\rm d}z'_{\rm l} P(z'_{\rm l}|z_{\rm l}) \frac{D_{\rm l'}^4 D_{\rm l's'}^2}{D_{\rm s'}^2}, \tag{2.43}$$

where $P(z'_{\rm l}|z_{\rm l})$ and $P(z'_{\rm s}|z_{\rm s})$ are the probability of measuring a redshift $z'_{\rm l}$ or $z'_{\rm s}$ for a lens or source galaxy respectively, given that its true redshift is $z_{\rm l}$ or $z_{\rm s}$. I model the probability distributions $P(z'_{\rm l}|z_{\rm l})$ and $P(z'_{\rm s}|z_{\rm s})$ as Gaussians, centred respectively upon $z_{\rm l}$ and $z_{\rm s}$ with some standard deviation $\Delta z$, and assume the same $\Lambda$CDM cosmology as described in Section 2.1.5.

Assuming an underlying 'correct' $z_{\rm l}$ and $z_{\rm s}$ and evaluating these integrals numerically, the fractional errors

on a single measurement of shear and flexion due to redshift uncertainties can be estimated as

$$\frac{(\Delta\gamma)_z}{\gamma} \simeq \sqrt{\left\langle \left(\frac{D_{\rm l}D_{\rm ls}}{D_{\rm s}}\right)^2 \right\rangle - \left\langle \frac{D_{\rm l}D_{\rm ls}}{D_{\rm s}} \right\rangle^2} \Big/ \left\langle \frac{D_{\rm l}D_{\rm ls}}{D_{\rm s}} \right\rangle \tag{2.44}$$

$$\frac{(\Delta\mathcal{F})_z}{\mathcal{F}} = \frac{(\Delta\mathcal{G})_z}{\mathcal{G}} \simeq \sqrt{\left\langle \left(\frac{D_{\rm l}^2D_{\rm ls}}{D_{\rm s}}\right)^2 \right\rangle - \left\langle \frac{D_{\rm l}^2D_{\rm ls}}{D_{\rm s}} \right\rangle^2} \Big/ \left\langle \frac{D_{\rm l}^2D_{\rm ls}}{D_{\rm s}} \right\rangle \tag{2.45}$$

Although the size of these fractional errors is a function of the specific underlying lens and source redshift, which thus varies on a galaxy pair-by-pair basis, for the purpose of this first investigation I set $z_{\rm l}$ and $z_{\rm s}$ always equal to the median lens and source redshift respectively for the mock survey sample we consider. Compared to a model in which source and lens redshifts vary, this single-redshift approximation causes a systematic underestimate of redshift errors for higher redshift pairs, and an overestimate of redshift errors for lower redshift pairs. As a first model we assume that these biases cancel on average; this is not strictly true. However, it can be argued that the single-redshift approximation will not significantly damage the results of a comparative analysis, as the redshift errors are a small source of uncertainty when compared to the lensing measurement noise due to intrinsic galaxy shapes.

One further assumption, the availability of reliable photometric redshift estimates for *both* sources and lenses, is also a simplification of the modelling that requires discussion. For many real surveys only the lens sample will have well characterized redshift information; often there is none (see, e.g., HYG04) but this is becoming increasingly rare. In the absence of redshift information there is extra scatter in the signal caused by ignorance of the lensing geometry, which this model fails to take into account. However, Kleinheinrich et al. (2005) show that this scatter is significantly reduced with accurate photometric redshifts even if only available for the lens galaxies, and lensing surveys of the future have high quality multi-band imaging as a high priority. Therefore, and given the largely qualitative aims of this analysis, we assume redshift information for both source and lens samples.

### 2.2.4 Choice of model parameters

For the fiducial virial halo mass I choose $M_{200} = 1 \times 10^{12} h^{-1} M_{\odot}$ (corresponding to a rest-frame B-band luminosity of $L^*_{\rm B} \approx 1.2 \times 10^{10} h^{-2} L_{\rm B,\odot}$ according to the results of HYG04). I choose to model confidence limits for two ground-based surveys; one similar in size to that used by HYG04, and one covering a substantially larger area of 1700 square degrees. I also consider a deeper space-based imaging survey with far smaller area of 0.5 square degrees.

The sample of galaxies used by HYG04 was taken from $R_{\rm c}$ band imaging of the the Red-Sequence Cluster Survey (Yee & Gladders 2002) and contained $N_{\rm l} \sim 1.2 \times 10^5$ lens galaxies and $N_{\rm s} \sim 1.5 \times 10^6$ source galaxies over a sky area of 42 sq deg. This corresponds to sky number densities of $n_{\rm l} \approx 0.8$ arcmin$^{-2}$ for the lenses and $n_{\rm s} \approx 10$ arcmin$^{-2}$ for the source galaxies. For the larger ground-based survey I assume the same depth, but increase the survey area to 1700 sq deg. I assume a redshift uncertainty of $\Delta z = 0.1(1+z)$ for each galaxy in either sample, and use the median lens and source redshifts found by HYG04 of $z_{\rm l} =$

$0.35$ and $z_{\rm s} = 0.53$ for both ground-based mock datasets. I set the underlying NFW lens halo concentration to $c = 7.20$ as in Section 2.1.5.

For the mock space-based dataset I set the survey area to $0.5$ sq deg, with number densities of $n_{\rm l} = 10$ arcmin$^{-2}$ and $n_{\rm s} = 30$ arcmin$^{-2}$ due to the increased depth and quality of imaging expected for space-based results. For the redshift uncertainties I use a value of $\Delta z = 0.05(1 + z)$ (c.f. the COMBO-17 photometric redshift survey, Wolf et al. 2004, which provides redshift information for the GEMS and STAGES surveys, Rix et al. 2004; Gray & STAGES Collaboration 2006), and set $z_{\rm l} = 0.5$ and $z_{\rm s} = 1.0$. Following the predictions of Navarro et al. (1997) I model each lens halo as having a slightly smaller concentration of $c = 7.02$ at this deeper redshift.

### 2.2.5 Simulated galaxy-mass cross correlations

I then generate a set of mock results for the tangential shear and radial flexion, averaged over annuli around the lensing galaxies (at increasing angular separations between lens and source) for the whole ensemble of galaxies in any given survey. These mock results are made by taking the theoretical (NFW) prediction for the average shear or flexion over each annulus of angular separation and offsetting it by a Gaussian random deviate scaled to the estimated overall error for that bin. This overall error is estimated by combining, in quadrature, the error due to redshift uncertainty and the intrinsic scatter for a single measurement. Multiplying this combined error by a factor of $1/\sqrt{N_{\rm bin}}$, where $N_{\rm bin}$ is the number of lens-source pairs within the annulus over which we are averaging our lensing measurements, gives the error on the tangential or radial shear and flexion in a given bin.

All that remains is to choose at what angular separations to impose the divides between annuli for averaging shear and flexion measurements. Since flexion is most useful on small scales, while shear signals remain strong at scales large enough for the flexion to become noise dominated, I divide up the angular scales for measurement according to a geometric binning scheme. I choose 10 annuli such that the centre of the $i$th annulus lies at an angular radius

$$r_i = a f^{(i-1)} \tag{2.46}$$

where $a = 2$ arcsec and the geometric factor $f = 1.5$. In this way I describe annuli which usefully cover both small (down to 2 arcsec) and larger (up to 77 arcsec) scales of angular separation.

### 2.2.6 Confidence estimates on lens model parameters

One final assumption is made, namely that measurements of shear, first flexion and second flexion are mutually statistically independent, which then allows the log-likelihood surfaces derived from each to be summed to give final, combined constraints. We currently have no reliable data concerning the degree of correlation to expect in real data, and so present our results given a degree of warning. In Figure 2.3 we present likelihood contours for fiducial $M_{200}$ and $c$ parameters resulting from a maximum likelihood analysis of the three mock datasets generated using this simple model. The three levels plotted show where $\Delta\chi^2 = 2.3, 4.61$ and $6.17$, corresponding to 1-, 2- and 3-$\sigma$ confidence intervals for normally distributed error distributions (see Press et al. 1992). Again we note that, although we are here modelling the measurement errors as normally distributed, this is not necessarily a good approximation (this will be discussed in

much greater detail in Chapter 4). In addition, the independence of $\gamma$, $\mathcal{F}$ and $\mathcal{G}$ in practical measurement will need to be investigated further to test these results.

The most important and interesting feature of the likelihood contours seen in Figure 2.3 is the qualitative fact that the constraints derived from measurements of shear and the two flexion fields are oriented at different angles in the plane. This allows the three measurables to complement one another, and may offer improved constraints upon the concentration parameter in particular. This should perhaps not come as a surprise; as found by Goldberg & Bacon (2005), the signal-to-noise of flexion is best close to the lensing mass on the sky plane. In fact, flexion is most sensitive on the angular scales at which the logarithmic slope of the NFW halo changes from -1 to -3, typically $\simeq 5$ arcsec for an $M_{200} = 1 \times 10^{12} M_{\odot}$. This is not so for shear, which is a better probe of the outer regions and overall mass.

Further theoretical insight into this result can be found in the fact that, whilst shear is a measure related to the projected mass density $\kappa$, the first and second flexion probe the local gradient of $\kappa$. This gradient is determined by the slope of the halo profile, and the concentration of an NFW profile directly parameterizes what slope we should expect at a given distance from the halo centre. We should therefore expect that flexion has the potential to improve existing constraints on the concentrations of galaxy-sized dark matter haloes, which is what Figure 2.3 concludes.

It is also noted from Figure 2.3 that the size of the 68 per cent confidence interval derived on the fiducial $M_{200}$ for the HYG04-like survey is in good agreement with the mass constraints found by those authors for galaxies scaled to a (slightly smaller) fiducial $L_{\rm B} = 10^{10} h^{-2} L_{\rm B,\odot}$, namely $M_{200} = (8.4 \pm 0.7 \pm 0.4) \times 10^{11} h^{-1} M_{\odot}$. The second error estimate in this value corresponds to a systematic uncertainty due to the fact that HYG04 had no access to multi-colour redshift information for the Red-Sequence Cluster Survey (see HYG04 for details), but assigned distances using the magnitude of objects.

We note that even despite this lack of redshift information, the HYG04 errors due to intrinsic galaxy ellipticity dominate over redshift uncertainties in their investigation of galaxy-galaxy shear. This justifies the simple single-redshift model for the treatment of redshift errors, described in Section 2.2.3. Furthermore, the good agreement between the shear-derived confidence intervals achieved by HYG04 and our own simple model provides some vindication of the single-luminosity approximation described in Section 2.2.1. In the final Section we enter into a thorough discussion of further possible limitations in the modelling, before deciding what firm conclusions, if any, may be drawn.

### 2.2.7 Caveats and conclusions

We have presented an investigation into the halo parameter constraints available from a simple analysis of synthetic galaxy-mass correlation functions, and found results that suggest flexion measurements may improve such analyses when combined with measurements of shear.

However, five important simplifying assumptions went into the model:

1. The modelling of each lens galaxy as having the same luminosity, mass and concentration (see Section 2.2.1), referred to as the single-luminosity approximation.

2. The assumption of Gaussian-distributed measured shear and flexion values.

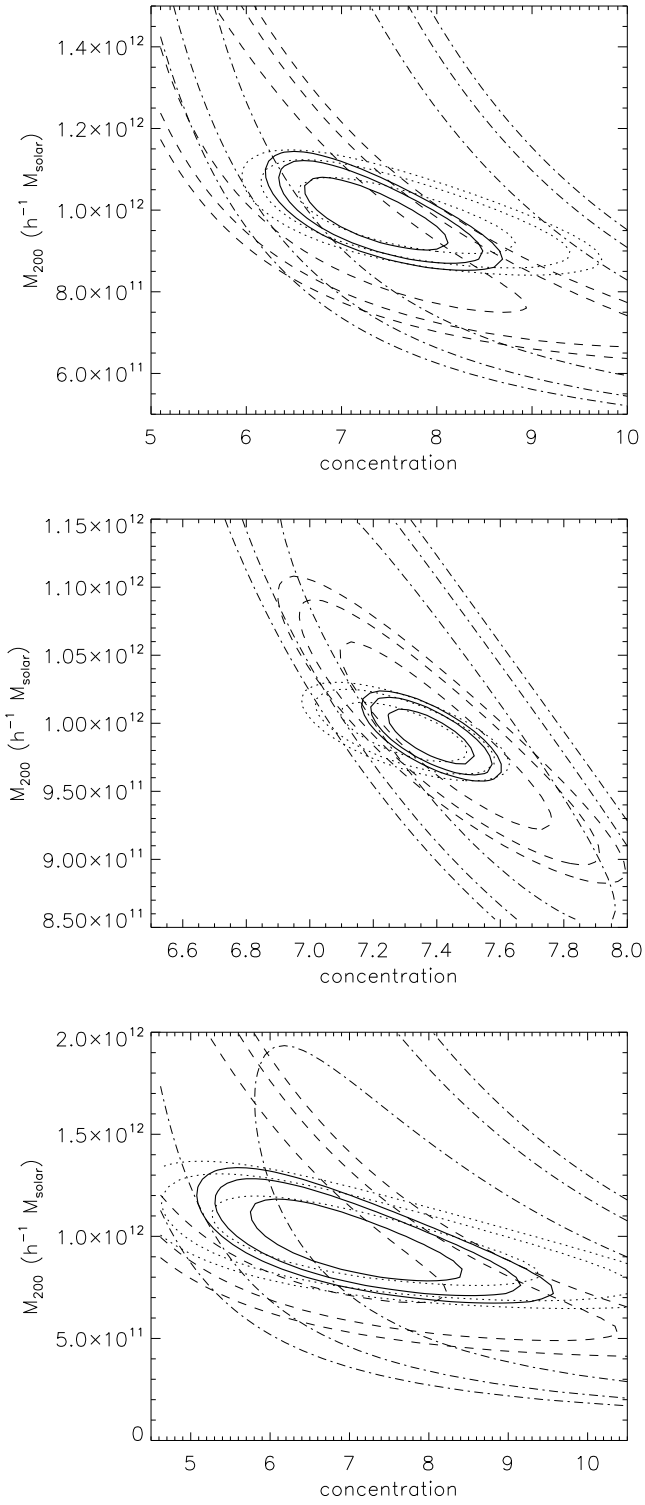


Figure 2.3: Estimated confidence limits on NFW halo parameters available using measurements of (dotted) shear alone, (dashed) first flexion alone, (dot-dashed) second flexion alone and (solid line) combined measurements of shear and both flexions. Top: for a 42 sq deg ground-based survey such as that used by Hoekstra et al. (2004). Middle: for a 1700 sq deg ground-based survey. Bottom: for a 0.5 sq deg space based survey.

3. The placing of the entire lens population at a single, survey-median lens redshift $z_{\rm l}$, and the entire source population at a single, survey-median source redshift $z_{\rm s}$ (see Section 2.2.3). This we have previously referred to as the single-redshift approximation.

4. The assumption that photometric redshift information will be available for both source and lens galaxy samples.

5. The statistical independence of measurements of $\gamma$, $\mathcal{F}$ and $\mathcal{G}$, allowing log-likelihood surfaces to be summed to provide combined constraints on fiducial halo parameters.

The success of our model in matching the shear-derived constraints presented in HYG04, along with the secondary importance of redshift errors in their analysis (despite having no photometric redshifts), provides justification of assumptions 1, 3 and 4 above. Even if these assumptions were not able to reproduce the results of HYG04, these errors would not preferentially strengthen either the shear or flexion signal, and would therefore not prejudice the validity of our comparison between the merits of shear and flexion for galaxy-galaxy lensing.

Unfortunately, data does not exist to quantify the mutual biasing and covariance between simultaneous measurements of $\gamma$, $\mathcal{F}$ and $\mathcal{G}$ (assumption 5 above), although Schneider & Er (2007) have shown evidence that measurements of shear from simple galaxy light profiles become biased in the presence of a gravitational flexion signal. This issue will be of importance in coming years, and will require large quantities of simulation data exploring the lensing of galaxies with accurate morphological characteristics.

The assumption of Gaussian measurement errors (assumption 2) may be most difficult approximation to justify in my analysis. It is known that the distribution of measured shear may be reasonably approximated by a Gaussian distribution (e.g., Schneider & Rix 1997), but this is not known for flexion. In fact, preliminary work suggests that flexion measurements produce highly non-Gaussian distributions, which if sufficiently severe may invalidate the results presented, notwithstanding efforts to use more sophisticated statistical tools to attempt to circumvent the problem.

Being content to trust and interpret these results in a qualitative fashion, the simple models presented in this Chapter suggest that flexion may offer a valuable new way of improving constraints upon the shape of haloes surrounding galaxies. However, the accurate modelling of a galaxy-galaxy lensing analysis designed to cope with the non-Gaussian distribution of measured flexion will be necessary to draw more firm conclusions. Whether such modelling would prove the best way to determine the real extent to which flexion provides useful extra information is doubtful; the final test will lie in the undertaking of a full galaxy-galaxy shear-flexion analysis using real data.

My efforts to do just this, using imaging data from the *HST* GEMS survey (Rix et al. 2004), is the subject of Chapters 4 onwards. In the following Chapter we address an important and related question, namely the practical estimation of flexion from noisy galaxy images, typically heavily distorted by the effects of an anisotropic point spread function.

# CHAPTER 3

# ESTIMATING SHEAR AND FLEXION

The accurate measurement of galaxy shapes, especially in the presence of large systematic distortions due to imperfect telescope optics, is vital if reliable conclusions are to be drawn from weak lensing analyses. In this Chapter I describe a recent development in this field known as the *shapelet* technique, which models galaxies as a sum of basis functions that behave well under deconvolution. This method lends itself naturally to the measurement of flexion, and it was within the shapelet framework that a first practical method for flexion analysis was proposed. I describe how shapelets may be used to deconvolve galaxy images with a model of the anisotropic point spread function, and in the final Section describe how estimators of shear and flexion (presented in Massey et al. 2007d) can be drawn from these deconvolved image models.

# 3.1 Cartesian shapelets

The underlying concept of the shapelet approach, as introduced by Refregier (2003) and Bernstein & Jarvis (2002), is the expression of an object surface brightness as a sum of orthonormal, two-dimensional basis functions:

$$I(\boldsymbol{\theta}) = \sum_{n_1=0}^{\infty} \sum_{n_2=0}^{\infty} f_{n_1,n_2} B_{n_1,n_2}(\boldsymbol{\theta};\beta). \tag{3.1}$$

In the shapelet formalism of Refregier (2003), the basis functions $B_{\boldsymbol{n}} = B_{n_1,n_2}$ have dimensions of inverse angle, the coefficients $f_{\boldsymbol{n}}$ therefore having dimensions flux $\times$ inverse angle, recovering the required dimensionality of surface brightness for $I(\boldsymbol{\theta})$. The choice of basis functions is free in general, but the Cartesian shapelet basis set is defined by the basis function

$$B_{\boldsymbol{n}}(\boldsymbol{\theta};\beta) = \frac{H_{n_1}(\theta_1/\beta) H_{n_2}(\theta_2/\beta) \mathrm{e}^{-|\theta|^2/2\beta^2}}{2^{(n_1 n_2)} \beta \sqrt{\pi n_1 n_2}}, \tag{3.2}$$

where $H_{n_i(x)}$ is a Hermite polynomial of order $n_i$, and the important free quantity $\beta$ is the angular scale size of the shapelet basis set (typically in arcsec). A dimensional basis set is chosen so as to satisfy the following orthonormality relationship

$$\iint B_{n_1,n_2}(\boldsymbol{\theta};\beta) B_{m_1,m_2}(\boldsymbol{\theta};\beta) \mathrm{d}^2\theta = \delta^{n_1}_{m_1} \delta^{n_2}_{m_2}, \tag{3.3}$$

where $\delta^a_b$ is here the Kronecker delta function.

We refer to the sum of the two parameters $n_1$ and $n_2$ as the order of the shapelet basis function, and will generally truncate shapelet models to some limiting order $n_{\max}$ such that $n_1 + n_2 \leq n_{\max}$. Importantly, being weighted by a Gaussian outer envelope, these functions have robust and well described behaviour under mutual convolution which makes them particularly suited towards correcting images for the effects of an instrumental point spread function (PSF). These basis functions are illustrated in Figure 3.1, which is taken from Massey & Refregier (2005).

## 3.1.1 Image transformations in Cartesian shapelets

The Cartesian shapelet basis functions are also the solutions to the two-dimensional quantum harmonic oscillator (QHO) within a geometrically square potential, and so ladder operators can be defined in analogy to the quantum mechanical system:

$$\hat{a}_1 B_{n_1,n_2} = \sqrt{n_1} B_{n_1-1,n_2} \tag{3.4}$$
$$\hat{a}_1^\dagger B_{n_1,n_2} = \sqrt{n_1+1} B_{n_1+1,n_2} \tag{3.5}$$

$$\hat{a}_2 B_{n_1,n_2} = \sqrt{n_2} B_{n_1,n_2-1} \tag{3.6}$$
$$\hat{a}_2^\dagger B_{n_1,n_2} = \sqrt{n_2+1} B_{n_1,n_2+1}. \tag{3.7}$$

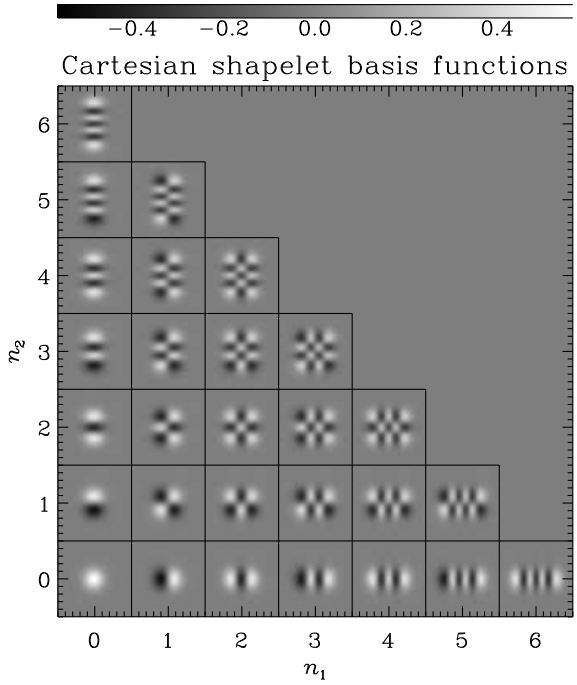


Figure 3.1: Cartesian shapelet basis functions used to decompose galaxy images; shown are only those functions for which $n_{\max} \leq 6$. Figure taken from Massey & Refregier (2005).

Just as ladder operators in quantum mechanics describe transitions between energy and momentum states, and thus changes in the overall wavefunction, these ladder operators may be used to describe transformations upon images represented by a sum of shapelet basis functions.

The analogy between the shapelet basis set and solutions of the QHO is useful as it provides a clear indication as to the relationship between the basis transformations $\hat{a}_i^\dagger$ and $\hat{a}_i$, and the simplest possible linear transformations upon the image plane. Considering the QHO system, the basis functions $B_{\boldsymbol{n}}$ are eigenstates of the Hamiltonian

$$\hat{H} = \frac{1}{2}\left[\left(\hat{x}_1^2 + \hat{x}_2^2\right) + \left(\hat{p}_1^2 + \hat{p}_2^2\right)\right], \tag{3.8}$$

where $\hat{x}_i$ and $\hat{p}_i$ are analagous to dimensionless position and angular momentum operators, and are given on the image plane by

$$\hat{x}_i = \frac{\theta_i}{\beta}, \qquad \hat{p}_i = \frac{\beta}{\mathrm{i}}\frac{\partial}{\partial\theta_i}, \tag{3.9}$$

where it is instructive to reassert that the quantity $\beta$ is the angular scale of the chosen basis set (3.2).

The raising and lowering operators defined in Equations (3.4)-(3.7) may also be defined in terms of these position and momentum operators:

$$\hat{a}_i^\dagger = \frac{1}{\sqrt{2}}\left(\hat{x}_i - \mathrm{i}\hat{p}_i\right), \qquad \hat{a}_i = \frac{1}{\sqrt{2}}\left(\hat{x}_i + \mathrm{i}\hat{p}_i\right), \tag{3.10}$$

where this important result follows directly from the analogy with the QHO (Refregier 2003). The final

step is to use Equations (3.1) and (3.9) to rewrite these results as follows:

$$\theta_i I(\boldsymbol{\theta}) = \beta \hat{x}_i I(\boldsymbol{\theta}) = \frac{\beta}{\sqrt{2}} \sum_{n_1=0}^{\infty} \sum_{n_2=0}^{\infty} f_{n_1,n_2} \left( \hat{a}_i + \hat{a}_i^\dagger \right) B_{\boldsymbol{n}}(\boldsymbol{\theta}; \beta) \tag{3.11}$$

$$\frac{\partial}{\partial \theta_i} I(\boldsymbol{\theta}) = \frac{\mathrm{i}\hat{p}_i}{\beta} I(\boldsymbol{\theta}) = \frac{1}{\beta\sqrt{2}} \sum_{n_1=0}^{\infty} \sum_{n_2=0}^{\infty} f_{n_1,n_2} \left( \hat{a}_i - \hat{a}_i^\dagger \right) B_{\boldsymbol{n}}(\boldsymbol{\theta}; \beta). \tag{3.12}$$

As an example of the practical use of these results, consider that we wish to find an shapelet expression for the partial derivative with respect to $\theta_1$ of a general image $I(\boldsymbol{\theta})$. Again using Equation (3.1) and the results above, we have

$$\begin{aligned} \frac{\partial}{\partial \theta_1} I(\boldsymbol{\theta}) &= \frac{1}{\beta\sqrt{2}} \sum_{n_1=0}^{\infty} \sum_{n_2=0}^{\infty} f_{n_1,n_2} \left( \hat{a}_1 - \hat{a}_1^\dagger \right) B_{n_1,n_2}(\boldsymbol{\theta}; \beta) \\ &= \frac{1}{\beta\sqrt{2}} \sum_{n_1=0}^{\infty} \sum_{n_2=0}^{\infty} f_{n_1,n_2} \left[ \sqrt{n_1}\, B_{n_1-1,n_2}(\boldsymbol{\theta}; \beta) - \sqrt{n_1+1}\, B_{n_1+1,n_2}(\boldsymbol{\theta}; \beta) \right] \\ &= \frac{1}{\beta\sqrt{2}} \sum_{n_1=0}^{\infty} \sum_{n_2=0}^{\infty} \left( \sqrt{n_1+1}\, f_{n_1+1,n_2} - \sqrt{n_1}\, f_{n_1-1,n_2} \right) B_{n_1,n_2}(\boldsymbol{\theta}; \beta), \end{aligned} \tag{3.13}$$

where in the final line we have made two changes of summation variable so as to absorb the transformation of basis functions into the shapelet coefficients $f_{\boldsymbol{n}}$.

The transformations of Equations (3.11), (3.12) and the example Equation (3.13) are linear and may be repeated to describe any general distortion or coordinate transformation upon images represented by a shapelet series, in terms of the ladder operators $\hat{a}_i^\dagger$ and $\hat{a}_i$. Once thus described, short steps similar to those in the example of Equation (3.13) allow any image distortion or transformation to be written entirely in terms of repeated linear transformations upon the shapelet coefficients $f_{\boldsymbol{n}}$.

### 3.1.2 Lensing transformations in Cartesian shapelets

It is now instructive to expand these results to provide a description of coordinate transformations upon the image plane, in particular the coordinate transformations we expect due to weak lensing. For clarity I reproduce Equation (1.92), which describes the effect of weak shear and flexion upon the surface brightness of a source galaxy:

$$I(\boldsymbol{\theta}) \simeq \left\{ 1 + \left[ (A - \mathcal{I})_{ij} \theta_j + \frac{1}{2} D_{ijk} \theta_j \theta_k \right] \frac{\partial}{\partial \theta_i} \right\} I^{\mathrm{s}}(\boldsymbol{\theta}). \tag{3.14}$$

Immediately we see that using the results of Equations (3.11)-(3.13) the effects of weak shear and flexion may be written in terms of shapelet transformations. We recall that the $A_{ij}$ and $D_{ijk}$ matrices may be

written in terms of $\gamma$, $\kappa$, $\mathcal{F}$ and $\mathcal{G}$:

$$A_{ij}(\boldsymbol{\theta}) = \begin{pmatrix} 1-\kappa-\gamma_1 & -\gamma_2 \\ -\gamma_2 & 1-\kappa+\gamma_1 \end{pmatrix}, \tag{3.15}$$

$$D_{ij1}(\boldsymbol{\theta}) = -\frac{1}{2}\begin{pmatrix} 3\mathcal{F}_1+\mathcal{G}_1 & \mathcal{F}_2+\mathcal{G}_2 \\ \mathcal{F}_2+\mathcal{G}_2 & \mathcal{F}_1-\mathcal{G}_1 \end{pmatrix}$$

$$D_{ij2}(\boldsymbol{\theta}) = -\frac{1}{2}\begin{pmatrix} \mathcal{F}_2+\mathcal{G}_2 & \mathcal{F}_1-\mathcal{G}_1 \\ \mathcal{F}_1-\mathcal{G}_1 & 3\mathcal{F}_2-\mathcal{G}_2 \end{pmatrix}. \tag{3.16}$$

Using these expressions for $A_{ij}$ and $D_{ijk}$, we may rewrite Equation (3.14) as

$$I(\boldsymbol{\theta}) \simeq \left(1 + \kappa\hat{K} + \gamma_i\hat{S}_i + \mathcal{F}_i\hat{F}_i + \mathcal{G}_i\hat{G}_i\right) I^{\rm s}(\boldsymbol{\theta}), \tag{3.17}$$

where we have now defined the shapelet lensing operators $\hat{K}$, $\hat{S}_i$, $\hat{F}_i$ and $\hat{G}_i$, each of which is a particular combination of $\hat{a}_i^\dagger$ and $\hat{a}_i$ that can be found by repeatedly substituting the results from Equations (3.11) and (3.12) into the expression for $I(\boldsymbol{\theta})$ given in Equation (3.14).

It should be stressed at this point that the result given in Equation (3.17) is a first order approximation to the effects of weak lensing image transformations, as is Equation (3.14) from which it derives. These results both stem from a Taylor series expansion of the source surface brightness, which I will now briefly discuss. We consider the second order approximation to the lens equation, previously discussed in Section 1.2.8 and given by

$$\beta_i \simeq \theta_i + (A-\mathcal{I})_{ij}\theta_j + \frac{1}{2}D_{ijk}\theta_j\theta_k, \tag{3.18}$$

and rewrite this expression in the simpler form $\beta_i \simeq \theta_i + \Delta\theta_i$, remembering that the vector quantity $\beta_i$ refers to coordinates on the source plane, *not* to the unfortunate yet universally adopted notation for the shapelet basis scale size $\beta$.

Since surface brightness is conserved by lensing, we have $I(\boldsymbol{\theta}) = I^{\rm s}(\boldsymbol{\beta})$, which we may express as a Taylor series expansion in terms of $\theta_i$ and $\Delta\theta_i$:

$$I(\boldsymbol{\theta}) \simeq I^{\rm s}(\boldsymbol{\theta}) + \Delta\theta_i\frac{\partial I^{\rm s}(\boldsymbol{\theta})}{\partial\theta_i} + \frac{\Delta\theta_i\Delta\theta_j}{2!}\frac{\partial^2 I^{\rm s}(\boldsymbol{\theta})}{\partial\theta_i\partial\theta_j} + \frac{\Delta\theta_i\Delta\theta_j\Delta\theta_k}{3!}\frac{\partial^3 I^{\rm s}(\boldsymbol{\theta})}{\partial\theta_i\partial\theta_j\partial\theta_k} + \ldots \tag{3.19}$$

Equations (3.14) and (3.17) amount to a simple truncation of this series at first order. In the shapelet operator notation of Equation (3.17), this series expansion may be written very succinctly as

$$I(\boldsymbol{\theta}) \simeq \left(1 + {\rm e}^{\kappa\hat{K}} + {\rm e}^{\gamma_i\hat{S}_i} + {\rm e}^{\mathcal{F}_i\hat{F}_i} + {\rm e}^{\mathcal{G}_i\hat{G}_i}\right) I^{\rm s}(\boldsymbol{\theta}). \tag{3.20}$$

Note that we refrain from writing these expressions as strict equalities due to the fact that they retain the use of the approximate relation $\beta_i \simeq \theta_i + \Delta\theta_i$.

Whether the truncation represented by Equations (3.14) and (3.17) is a valid approximation depends on whether the error introduced by this truncation is at the same order as the correction we make by expressing $\Delta\theta_i$ to second order. For stronger shear and flexion signals in particular this is a question of some importance. It is also a practical consideration, as it not only depends on the strength of the expected shear and flexion signal but also on the light profiles (and derivatives thereof) of typical galaxy profiles. However,

as will be seen, use of the expression (3.20) to construct shapelet estimators will quickly yield expressions of unpalatable complexity, particularly in the case of flexion. Goldberg & Bacon (2005) discuss this issue briefly and conclude that one may proceed using Equation (3.14), but there is clearly scope for further investigation into this question. In particular, it will be important to more clearly define the regimes in which the strength of the shear or flexion signal renders it an invalid approximation.

In this work I too proceed using only Equation (3.14), which I justify both by confining myself to the weak shear and flexion regime and in the light of the limited statistical confidence expected for flexion measurements using current survey data. As sample sizes increase, it may be necessary to explore possible biases engendered by the truncation of Equation (3.19), a truncation which is currently inherent in all shapelet lensing measurement methods (Bernstein & Jarvis 2002; Refregier & Bacon 2003; Massey & Refregier 2005; Kuijken 2006).

Assuming that Equation (3.14) is a valid approximation to the effects of weak lensing, we may repeatedly substitute the results from Equations (3.11) and (3.12) to express the shapelet transformation operators of Equation (3.17) in terms of $\hat{a}_i^\dagger$ and $\hat{a}_i$. Performing these calculations, Refregier (2003) derives the shapelet expressions for the convergence and shear transformations as

$$\kappa\hat{K} = \kappa + \frac{\kappa}{2}\left(\hat{a}_1^{\dagger 2} + \hat{a}_2^{\dagger 2} - \hat{a}_1^2 - \hat{a}_2^2\right) \tag{3.21}$$

$$\gamma_1\hat{S}_1 = \frac{\gamma_1}{2}\left(\hat{a}_1^{\dagger 2} - \hat{a}_2^{\dagger 2} - \hat{a}_1^2 + \hat{a}_2^2\right) \tag{3.22}$$

$$\gamma_2\hat{S}_2 = \gamma_2\left(\hat{a}_1^\dagger\hat{a}_2^\dagger - \hat{a}_1\hat{a}_2\right). \tag{3.23}$$

Similar expressions for the first and second flexion are considerably more involved but may be derived in exactly the same fashion using Equations (3.11)-(3.17) as described above. In this way, the expressions for $\hat{F}_i$ found to be

$$\begin{aligned}\mathcal{F}_1\hat{F}_1 = {} & \frac{\mathcal{F}_1\beta}{8\sqrt{2}}\left\{3\left(\hat{a}_1^{\dagger 3} - \hat{a}_1^3\right) + 3\left(\hat{a}_1\hat{a}_1^{\dagger 2} - \hat{a}_1^\dagger\hat{a}_1^2\right) + 3\left(\hat{a}_1^\dagger + \hat{a}_1^\dagger\right)\left(\hat{a}_1\hat{a}_1^\dagger - \hat{a}_1^\dagger\hat{a}_1\right)\right. \\ & \left. + \left(3\hat{a}_1^\dagger + \hat{a}_1\right)\left(\hat{a}_2^{\dagger 2} + \hat{a}_2\hat{a}_2^\dagger\right) - \left(\hat{a}_1^\dagger + 3\hat{a}_1\right)\left(\hat{a}_2^\dagger\hat{a}_2 + \hat{a}_2^2\right)\right\},\end{aligned} \tag{3.24}$$

$$\begin{aligned}\mathcal{F}_2\hat{F}_2 = {} & \frac{\mathcal{F}_2\beta}{8\sqrt{2}}\left\{3\left(\hat{a}_2^{\dagger 3} - \hat{a}_2^3\right) + 3\left(\hat{a}_2\hat{a}_2^{\dagger 2} - \hat{a}_2^\dagger\hat{a}_2^2\right) + 3\left(\hat{a}_2^\dagger + \hat{a}_2^\dagger\right)\left(\hat{a}_2\hat{a}_2^\dagger - \hat{a}_2^\dagger\hat{a}_2\right)\right. \\ & \left. + \left(3\hat{a}_2^\dagger + \hat{a}_2\right)\left(\hat{a}_1^{\dagger 2} + \hat{a}_1\hat{a}_1^\dagger\right) - \left(\hat{a}_2^\dagger + 3\hat{a}_2\right)\left(\hat{a}_1^\dagger\hat{a}_1 + \hat{a}_1^2\right)\right\}.\end{aligned} \tag{3.25}$$

In the same way, the expressions for the second flexion $\hat{G}_i$ transformations in terms of the shapelet ladder

operators are

$$\begin{aligned}
\mathcal{G}_1\hat{G}_1 &= \frac{\mathcal{G}_1\beta}{8\sqrt{2}}\Big\{\hat{a}_1^{\dagger 3} + \hat{a}_1^{\dagger 2}\hat{a}_1 - \hat{a}_1^{\dagger}\hat{a}_1^2 - \hat{a}_1^3 \\
&\quad + \left(3\hat{a}_2^{\dagger 2} + 2\hat{a}_2^{\dagger}\hat{a}_2 - \hat{a}_2^2\right)\hat{a}_1^{\dagger} - \left(3\hat{a}_2^2 + 2\hat{a}_2^{\dagger}\hat{a}_2 - \hat{a}_2^{\dagger 2}\right)\hat{a}_1\Big\}, \qquad (3.26)\\
\mathcal{G}_2\hat{G}_2 &= \frac{\mathcal{G}_2\beta}{8\sqrt{2}}\Big\{\hat{a}_2^3 + \hat{a}_2^{\dagger}\hat{a}_2^2 - \hat{a}_2^{\dagger 2}\hat{a}_2 - \hat{a}_2^{\dagger 3} \\
&\quad - \left(3\hat{a}_1^{\dagger 2} + 2\hat{a}_1^{\dagger}\hat{a}_1 - \hat{a}_1^2\right)\hat{a}_2^{\dagger} + \left(3\hat{a}_1^2 + 2\hat{a}_1^{\dagger}\hat{a}_1 - \hat{a}_1^{\dagger 2}\right)\hat{a}_2\Big\}. \qquad (3.27)
\end{aligned}$$

Instantly the complexity of these transformations is clear, especially in the case of the first flexion transformations. This has ramifications for the use of the shapelet method in regimes where it is necessary to use a higher order expansion of the Taylor series for the image surface brightness in Equation (3.19). Calculating explicit second order expressions, using Equation (3.20), for the convergence and shear operators above is a laborious task. For the flexion transfomations, given the non-commutative nature of the $\hat{a}_i^{\dagger}$ and $\hat{a}$ operators, these calculations will be become extremely tedious and difficult to verify. Should it be necessary to use such higher order expressions, i.e. when measuring shear and flexion of sufficient signal strength, care will be necessary in the calculation and presentation of these results.

The effect of these operators can be written equivalently in terms of transformations upon the shapelets coefficients $f_{\boldsymbol{n}}$, by writing the operation upon the full image, as in the example of Equation (3.13), and making a suitable change to the summation variable. Taking Equations (3.21), (3.22) and (3.23), we can rexpress the action of $\hat{K}$, $\hat{S}_1$ and $\hat{S}_2$ as follows:

$$\begin{aligned}
(1+\kappa\hat{K}) : f^{\rm s}_{n_1,n_2} \rightarrow f_{n_1,n_2} &= (1+\kappa) f^{\rm s}_{n_1,n_2} \\
&+ \frac{\kappa}{2}\Big\{\sqrt{(n_1-1)n_1}\, f^{\rm s}_{n_1-2,n_2} \\
&+ \sqrt{(n_2-1)n_2}\, f^{\rm s}_{n_1,n_2-2} \\
&- \sqrt{(n_1+1)(n_1+2)}\, f^{\rm s}_{n_1+2,n_2} \\
&- \sqrt{(n_2+1)(n_2+2)}\, f^{\rm s}_{n_1,n_2+2}\Big\}, \qquad (3.28)\\
(1+\gamma_1\hat{S}_1) : f^{\rm s}_{n_1,n_2} \rightarrow f_{n_1,n_2} &= f^{\rm s}_{n_1,n_2} \\
&+ \frac{\gamma_1}{2}\Big\{\sqrt{(n_1-1)n_1}\, f^{\rm s}_{n_1-2,n_2} \\
&- \sqrt{(n_2-1)n_2}\, f^{\rm s}_{n_1,n_2-2} \\
&- \sqrt{(n_1+1)(n_1+2)}\, f^{\rm s}_{n_1+2,n_2} \\
&+ \sqrt{(n_2+1)(n_2+2)}\, f^{\rm s}_{n_1,n_2+2}\Big\}, \qquad (3.29)\\
(1+\gamma_2\hat{S}_2) : f^{\rm s}_{n_1,n_2} \rightarrow f_{n_1,n_2} &= f^{\rm s}_{n_1,n_2} \\
&+ \frac{\gamma_2}{2}\Big\{\sqrt{n_1 n_2}\, f^{\rm s}_{n_1-1,n_2-1} \\
&- \sqrt{(n_1+1)(n_2+2)}\, f^{\rm s}_{n_1+1,n_2+1}\Big\}, \qquad (3.30)
\end{aligned}$$

where $f^{\rm s}_{\boldsymbol{n}}$ denotes the shapelet coefficients of the unlensed source image. Expressions for the $\hat{F}_i$ and

$\hat{G}_i$ transformations in terms changes to the shapelet coefficients $f_{\boldsymbol{n}}^{\mathrm{s}}$ can also be derived using Equations (3.24)-(3.27) and the steps outlined in Equation (3.13).

Something that will be of use in the later Sections is to notice, as pointed out by Goldberg & Bacon (2005), that the effect of shear and convergence in shapelet space is to transfer between $f_{\boldsymbol{n}}$ coefficients for which $\Delta n_1 + \Delta n_2 = \pm 2$. In contrast, the flexion operators of Equations (3.24) and (3.25) couple pairs of coefficients for which $\Delta n_1 + \Delta n_2 = \pm 1, \pm 3$. This useful property will have ramifications for the construction of Cartesian shapelet estimators in Section 3.4.2, as it allows the action of weak shear and flexion to be treated separately.

It is the knowledge described above, of how lensing image transformations in real space may be related to those in shapelet space, that allows Cartesian shapelet models to be used to create estimators of shear and flexion. Again, this will be described in the later Section 3.4.2, but before proceeding I will first describe an alternative shapelet basis set that has many useful properties, known as polar shapelets.

## 3.2 Polar shapelets

The formalism of polar shapelets, introduced initially by Refregier (2003) and subsequently in greater detail by Massey & Refregier (2005), is closely related to that of Cartesian shapelets. Instead of the basis set defined by Equations (3.1) and (3.2), polar shapelets express the object surface brightness $I(\boldsymbol{\theta})$ as

$$I(\boldsymbol{\theta}) = I(\theta, \phi) = \sum_{n=0}^{\infty} \sum_{m=-n}^{n} f_{n,m} P_{n,m}(\theta, \phi; \beta), \tag{3.31}$$

where $\theta$ and $\phi$ are circular polar coordinates on the image plane, defined as in Section 2.1, and the free parameter $\beta$ is once again the angular scale size of the basis set. The polar shapelet basis functions, which we label $P_{n,m}$, are defined by Massey & Refregier (2005) as

$$P_{n,m}(\theta, \phi; \beta) = \frac{(-1)^{(n-|m|)/2}}{\beta^{|m|+1}} \left\{ \frac{[(n-|m|)/2]!}{\pi[(n-|m|)/2]!} \right\}^{1/2} \theta^{|m|} L^{|m|}_{(n-|m|)/2} \left( \frac{\theta^2}{\beta^2} \right) \mathrm{e}^{-\theta^2/2\beta^2} \mathrm{e}^{-\mathrm{i}m\phi}, \tag{3.32}$$

using the following definition of the associated Laguerre polynomials (see, e.g., Arfken & Weber 2005):

$$L^q_p(x) \equiv \frac{x^{-q}\mathrm{e}^x}{p!} \frac{\mathrm{d}^p}{\mathrm{d}x^p} \left( x^{p+q} \mathrm{e}^{-x} \right). \tag{3.33}$$

An important difference between the Cartesian and polar basis sets is that the functions $P_{n,m}$ are no longer purely real, having complex phase $\mathrm{e}^{-\mathrm{i}m\phi}$. In order to ensure that $I(\boldsymbol{\theta})$ remains real, we require that $f_{n,m}$ is complex in general and that

$$f_{n,m} P_{n,m} + f_{n,-m} P_{n,-m} = f_{n,m} P_{n,m} + f_{n,-m} P^*_{n,m} \tag{3.34}$$

is purely real for all $n$, $m$. This can be done by enforcing the condition $f_{n,m} = f^*_{n,-m}$.

As in the case of the Cartesian basis set, the polar basis set $P_{n,m}$ is defined as having dimensions of inverse angle, and the polar shapelet coefficents $f_{n,m}$ have dimensions flux $\times$ inverse angle. This ensures that we recover the necessary dimensions of surface brightness for $I(\boldsymbol{\theta})$, and that $P_{n,m}$ satisfy the following orthonormality relationship on the image plane:

$$\iint P_{n,m}(\boldsymbol{\theta}; \beta) P_{k,l}(\boldsymbol{\theta}; \beta) \mathrm{d}^2\theta = \delta^n_k \delta^m_l, \tag{3.35}$$

where, as in Equation (3.3), $\delta^a_b$ is the Kronecker delta function. The polar shapelet basis functions are depicted in Figure 3.2, which is taken from Massey & Refregier (2005). As can also be seen from Equation (3.32), each separate member of the basis set is uniquely described using the two integers $n$ and $m$, with $n > 0$ and $|m| \leq n$. These integers form the $x$ and $y$ axis labels of Figure 3.2, which depicts each $P_{n,m}$ basis function up to a maximum order $n \leq 6$.

Once more, it is possible to draw analogies between polar shapelets and the solution to the QHO. The $P_{n,m}$ basis functions correspond to eigenstates of the Hamiltonian for a particle confined in circularly symmetric, two dimensional, harmonic potential centred on the origin of the image plane. The quantities $n$ and $m$ then correspond to the quantum numbers for energy and angular momentum, respectively, for the $P_{n,m}$ eigenstate.

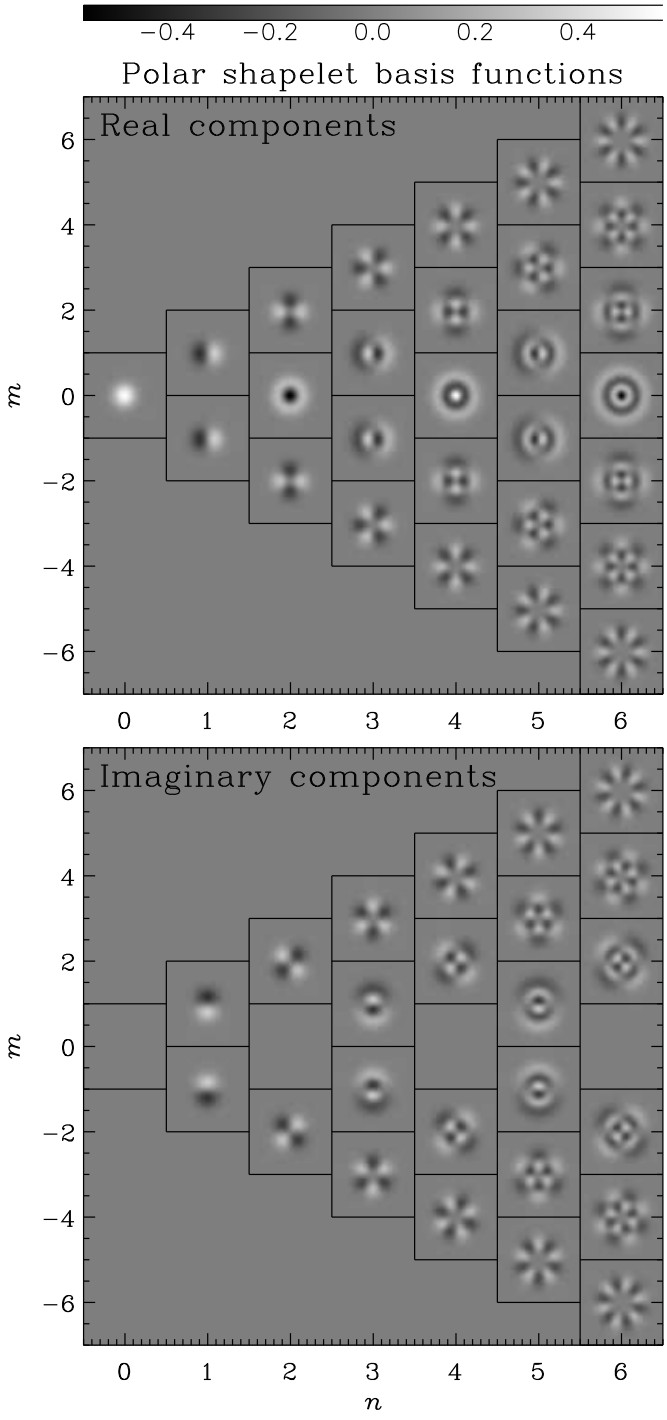


Figure 3.2: Polar shapelet basis functions up to $n_{\max} = 6$, with the real components shown in the top panel and the imaginary components below (note that there are no imaginary components to the $m = 0$ members of the basis set). Figure taken from Massey & Refregier (2005).

### 3.2.1 Image transformations in polar shapelets

Whilst the integers $n$ and $m$ provide the most convenient means of labelling and visualizing the polar basis set $P_{n,m}$, it is most convenient to derive image transformation results using the left-handed and right-handed shapelet numbers $n_r$ and $n_l$, with $n_r = (n+m)/2$ and $n_l = (n-m)/2$. These numbers provide an equivalent, full characterization of the polar basis set, and in the QHO analogy can be thought of as quantum numbers describing the positive and negative spin.

The utility of this description of the polar shapelet basis set, in which basis functions $P_{n,m}$ correspond to an equivalent $P_{n_r,n_l}$, is that simple ladder operators can be defined for raising and lowering left- and right-handed shapelet order, such that

$$\hat{a}_r P_{n_r,n_l} = \sqrt{n_r}\, P_{n_r-1,n_l} = \sqrt{\frac{n+m}{2}}\, P_{n-1,m-1} \tag{3.36}$$

$$\hat{a}_r^\dagger P_{n_r,n_l} = \sqrt{n_r+1}\, P_{n_r+1,n_l} = \sqrt{\frac{n+m+2}{2}}\, P_{n+1,m+1} \tag{3.37}$$

$$\hat{a}_l P_{n_r,n_l} = \sqrt{n_l}\, P_{n_r,n_l-1} = \sqrt{\frac{n-m}{2}}\, P_{n-1,m+1} \tag{3.38}$$

$$\hat{a}_l^\dagger P_{n_r,n_l} = \sqrt{n_l+1}\, P_{n_r,n_l+1} = \sqrt{\frac{n-m+2}{2}}\, P_{n+1,m-1} \tag{3.39}$$

Moreover, the effect of these polar ladder operators can be simply expressed in terms of the Cartesian ladder operators, given in Equations (3.4)-(3.7), as follows:

$$\hat{a}_r^\dagger I(\boldsymbol{\theta}) = \hat{a}_r^\dagger \sum_{n=0}^{\infty}\sum_{m=-n}^{n} f_{n,m}P_{n,m} = \frac{1}{\sqrt{2}}\left(\hat{a}_1^\dagger - \mathrm{i}\hat{a}_2^\dagger\right)\sum_{n_1=0}^{\infty}\sum_{n_2=0}^{\infty} f_{n_1,n_2}B_{n_1,n_2} \tag{3.40}$$

$$\hat{a}_l^\dagger I(\boldsymbol{\theta}) = \hat{a}_l^\dagger \sum_{n=0}^{\infty}\sum_{m=-n}^{n} f_{n,m}P_{n,m} = \frac{1}{\sqrt{2}}\left(\hat{a}_1^\dagger + \mathrm{i}\hat{a}_2^\dagger\right)\sum_{n_1=0}^{\infty}\sum_{n_2=0}^{\infty} f_{n_1,n_2}B_{n_1,n_2} \tag{3.41}$$

$$\hat{a}_r I(\boldsymbol{\theta}) = \hat{a}_r \sum_{n=0}^{\infty}\sum_{m=-n}^{n} f_{n,m}P_{n,m} = \frac{1}{\sqrt{2}}\left(\hat{a}_1 + \mathrm{i}\hat{a}_2\right)\sum_{n_1=0}^{\infty}\sum_{n_2=0}^{\infty} f_{n_1,n_2}B_{n_1,n_2} \tag{3.42}$$

$$\hat{a}_l I(\boldsymbol{\theta}) = \hat{a}_l \sum_{n=0}^{\infty}\sum_{m=-n}^{n} f_{n,m}P_{n,m} = \frac{1}{\sqrt{2}}\left(\hat{a}_1 - \mathrm{i}\hat{a}_2\right), \sum_{n_1=0}^{\infty}\sum_{n_2=0}^{\infty} f_{n_1,n_2}B_{n_1,n_2} \tag{3.43}$$

see Refregier (2003); Massey & Refregier (2005). It is important to be clear here that in the relationships above $f_{n,m}$ are the complex polar shapelet coefficients corresponding to the image as expressed by Equation (3.31), and quite different from the Cartesian shapelet coefficients $f_{n_1,n_2}$ used to express the same image in Equation (3.1).

Close examination of the definition of the polar shapelet basis functions given by Refregier (2003) and Massey & Refregier (2005) reveals a discrepancy between the two in the definition of $n_r$ and $n_l$: in the definitions given above, and below, I follow Massey & Refregier (2005). The simple schematic diagram presented in Figure 3.3 illustrates the directions in which these right- and left-handed operators act within the polar shapelet basis space depicted in Figure 3.2.

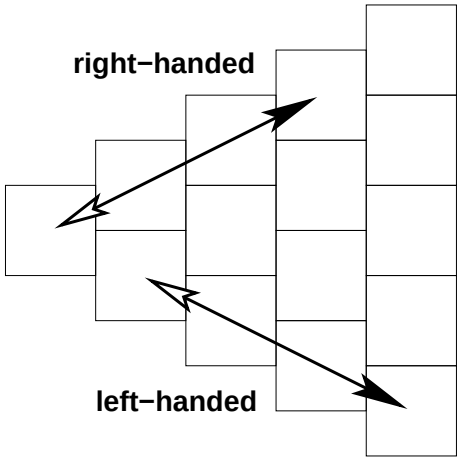


Figure 3.3: Schematic diagram showing the direction of action of the right- and left-handed operators in polar shapelet space. The solid arrows indicate the directions of order raising, and the clear arrows those of order lowering, operations.

We now follow a similar procedure to that of Section 3.1 in order to derive results for the simple, linear image transformation operations $\theta_i I(\boldsymbol{\theta})$ and $\partial_i I(\boldsymbol{\theta})$. Using Equations (3.11) and (3.12) with Equations (3.40)-(3.43), we find

$$\theta_1 I(\boldsymbol{\theta}) = \frac{\beta}{\sqrt{2}} \sum_{n=0}^{\infty} \sum_{m=-n}^{n} f_{n,m} \left( \hat{a}_r^\dagger + \hat{a}_l^\dagger + \hat{a}_r + \hat{a}_l \right) P_{n,m}(\boldsymbol{\theta}; \beta) \tag{3.44}$$

$$\theta_2 I(\boldsymbol{\theta}) = \frac{\beta}{\sqrt{2}} \sum_{n=0}^{\infty} \sum_{m=-n}^{n} f_{n,m} \left( \hat{a}_r^\dagger - \hat{a}_l^\dagger - \hat{a}_r + \hat{a}_l \right) P_{n,m}(\boldsymbol{\theta}; \beta) \tag{3.45}$$

$$\frac{\partial}{\partial \theta_1} I(\boldsymbol{\theta}) = \frac{1}{\beta\sqrt{2}} \sum_{n=0}^{\infty} \sum_{m=-n}^{n} f_{n,m} \left( -\hat{a}_r^\dagger - \hat{a}_l^\dagger + \hat{a}_r + \hat{a}_l \right) P_{n,m}(\boldsymbol{\theta}; \beta) \tag{3.46}$$

$$\frac{\partial}{\partial \theta_2} I(\boldsymbol{\theta}) = \frac{1}{\beta\sqrt{2}} \sum_{n=0}^{\infty} \sum_{m=-n}^{n} f_{n,m} \left( -\hat{a}_r^\dagger + \hat{a}_l^\dagger - \hat{a}_r + \hat{a}_l \right) P_{n,m}(\boldsymbol{\theta}; \beta). \tag{3.47}$$

Repeated use of these linear expressions will allow us to express any general image transformation in terms of simple operations upon the polar basis set $P_{n,m}$, just as the expressions given in Equations (3.11) and (3.12) allowed for the Cartesian basis set.

### 3.2.2 Lensing transformations in polar shapelets

We now derive polar shapelet results for the image transformations we expect in a the specific context of weak gravitational lensing. As in the case of Cartesian shapelets, we make use of the approximate expression for the lensed surface brightness given in Equation (3.14) but emphasise that its validity is likely to be limited to regimes of weaker shear or flexion signals. The complex formulation of the polar shapelet basis set means that it is now convenient to write expressions in terms of complex shear and flexion. As in Section 1.2.9 we define the complex shear $\gamma = \gamma_1 + \mathrm{i}\gamma_2$, first flexion $\mathcal{F} = \mathcal{F}_1 + \mathrm{i}\mathcal{F}_2$, and second flexion

$\mathcal{G} = \mathcal{G}_1 + \mathrm{i}\mathcal{G}_2$. It turns out to be computationally convenient to reformulate the $\hat{S}_i$, $\hat{F}_i$ and $\hat{G}_i$ operators so as to match this complex notation. We define the $\hat{S}_r$ operator as the counterpart to $\gamma$, and the $\hat{S}_l$ operator as the counterpart to $\gamma^*$, such that

$$\left(\gamma\hat{S}_r + \gamma^*\hat{S}_l\right) I(\boldsymbol{\theta}) = \left(\gamma_1\hat{S}_1 + \gamma_2\hat{S}_2\right) I(\boldsymbol{\theta}). \tag{3.48}$$

We also define similar polar shapelet operators for $\mathcal{F}$ and $\mathcal{G}$, and therefore rewrite Equation (3.17) in the following polar shapelet form:

$$I(\boldsymbol{\theta}) \simeq \left(1 + \kappa\hat{K} + \gamma\hat{S}_r + \gamma^*\hat{S}_l + \mathcal{F}\hat{F}_r + \mathcal{F}^*\hat{F}_l + \mathcal{G}\hat{G}_r + \mathcal{G}^*\hat{G}_l\right) I^{\mathrm{s}}(\boldsymbol{\theta}) \tag{3.49}$$

Using Equations (3.14) and (3.49), combined with the polar shapelet transformation expressions of Equations (3.44)-(3.47), we find the following expressions for the weak lensing convergence and shear operators:

$$\kappa\hat{K} = \kappa\left(1 + \hat{a}_l^\dagger\hat{a}_r^\dagger - \hat{a}_l\hat{a}_r\right) \tag{3.50}$$

$$\gamma\hat{S}_r = \frac{\gamma}{4}\left(\hat{a}_r^{\dagger 2} - \hat{a}_l^2\right) \tag{3.51}$$

$$\gamma^*\hat{S}_l = \frac{\gamma^*}{4}\left(\hat{a}_l^{\dagger 2} - \hat{a}_r^2\right). \tag{3.52}$$

Before moving to the calculations for flexion, it will be worthwhile to examine these results a little further. Following steps similar to those described by Equation (3.13), these these operators can be rexpressed in terms of their effects upon the polar shapelet coefficients $f_{n,m}$. We may express the convergence transformation in equivalent form as

$$\begin{aligned}(1 + \kappa\hat{K}) : f^{\mathrm{s}}_{n,m} \rightarrow f_{n,m} &= (1+\kappa) f^{\mathrm{s}}_{n,m} \\ &+ \frac{\kappa}{2}\left\{\sqrt{(n-m)(n+m)}\, f^{\mathrm{s}}_{n-2,m}\right. \\ &- \left.\sqrt{(n-m-2)(n+m+2)}\, f^{\mathrm{s}}_{n+2,m}\right\}.\end{aligned} \tag{3.53}$$

Calculated in the same fashion, the complex shear transformations in polar shapelets are given by

$$\begin{aligned}(1 + \gamma\hat{S}_r) : f^{\mathrm{s}}_{n,m} \rightarrow f_{n,m} &= f^{\mathrm{s}}_{n,m} \\ &+ \frac{\gamma}{4}\left\{\sqrt{(n+m)(n+m-2)}\, f^{\mathrm{s}}_{n-2,m-2}\right. \\ &- \left.\sqrt{(n-m+2)(n-m+4)}\, f^{\mathrm{s}}_{n+2,m-2}\right\}\end{aligned} \tag{3.54}$$

$$\begin{aligned}(1 + \gamma^*\hat{S}_l) : f^{\mathrm{s}}_{n,m} \rightarrow f_{n,m} &= f^{\mathrm{s}}_{n,m} \\ &+ \frac{\gamma^*}{4}\left\{\sqrt{(n-m)(n-m-2)}\, f^{\mathrm{s}}_{n-2,m+2}\right. \\ &- \left.\sqrt{(n+m+2)(n+m+4)}\, f^{\mathrm{s}}_{n+2,m+2}\right\}.\end{aligned} \tag{3.55}$$

These results are also given in Massey & Refregier (2005). It is worth pausing to consider the effect of the transformations described by Equations (3.50)-(3.55) in terms of the diagram of shapelet space presented

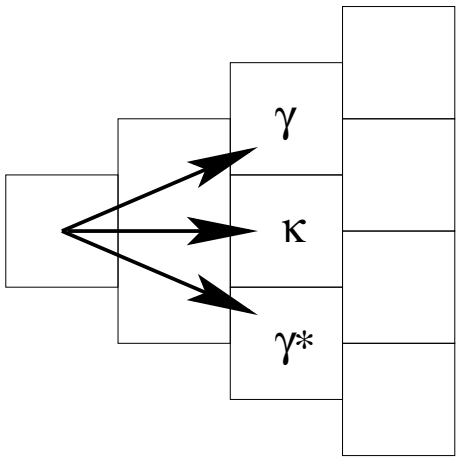


Figure 3.4: Schematic diagram showing the direction of action of the shear and convergence operators in polar shapelet space upon a simple galaxy image with $I(\boldsymbol{\theta}) = f_{0,0}P_{0,0}(\boldsymbol{\theta};\beta)$.

in Figure (3.2). Firstly, for clarity, we reproduce Equation (3.31) once more:

$$I(\boldsymbol{\theta}) = \sum_{n=0}^{\infty}\sum_{m=-n}^{n} f_{n,m}P_{n,m}(\boldsymbol{\theta};\beta). \tag{3.56}$$

In what follows it will be convenient to refer to "shapelet power", which we refer as being the contribution to the image sum above for terms corresponding to a given basis function $P_{n,m}$.

Consider the simplest possible shapelet galaxy image, a Gaussion with $I(\boldsymbol{\theta}) = f_{0,0}P_{0,0}(\boldsymbol{\theta};\beta)$ (i.e. $f_{n,m} = 0$ for all $n$, $m \neq 0$). Looking at Equations (3.50) and (3.53) it can be seen that action of the convergence transformation $\kappa\hat{K}$ in shapelet space is to add shapelet power, proportional to $f_{0,0}$ and $\kappa$, to the $f_{2,0}$ term in the series of Equation (3.31). This will result in an isotropic dilation of the image $I(\boldsymbol{\theta})$, precisely what should be expected for the convergence, as shown in Figure 3.4. Galaxy images for which $f_{n,m}$ is non-zero for a general of $n$ and $m$ will display a more complex response to the convergence operator, but the intuitive picture presented above is applicable nonetheless: the effect of a positive convergence is to shift shapelet power to $\Delta m = +2$ modes in each case.

Turning to the shear transformations, the action of the operators described by Equations (3.51), (3.52), (3.54) and (3.55) upon our simple $f_{0,0}$ image will be to cause shapelet power to exist in the $f_{2,\pm2}$ terms. The power in $f_{2,2}$ will increase proportionally to $f_{0,0}$ and $\gamma$, whilst that in $f_{2,-2}$ will increase proportionally to $f_{0,0}$ and $\gamma^*$. This behaviour is also schematically represented in Figure 3.4. If we consider a non-Gaussian general image sum the action of the shear transformations are of course more complex, but the effect is to shift power from $f_{n.m}$ modes into $f_{n\pm2,m\pm2}$ modes by an amount proportional to $\gamma$ and $\gamma^*$.

Now is a good time to point out that, due to the parity properties of the basis set $P_{n,m}$, it is only $m = 0$ terms that contribute net flux to any image $I(\boldsymbol{\theta})$. These terms are also usually the strongest in typical galaxy shapelet models and so the overall effect is often very similar to the simple case discussed. Moreover, if we consider an ensemble of source galaxies with a distribution of orientations which we assume to be isotropic, the ensemble mean values of $f_{n,m}$ for all $m \neq 0$ will tend towards zero as the ensemble size increases. However, if we introduce the effect of gravitational shear we will increase power in the $m = \pm2$

modes that does *not* cancel out on average, power which may be measured and simply related to the shear $\gamma$ itself and the original power in $f_{n,0}$ modes. This, of course, may be done using Equations (3.51) and (3.52). This is the heart of the polar shapelet method, and illustrates the how the rotational symmetries of the polar shapelet basis set may be elegantly utilized for weak lensing measurements.

We find similar symmetry properties for the flexion transformations. Using Equations (3.14) and (3.49), combined with general linear transformation results of Equations (3.44)-(3.47), I found the following expressions for the $\mathcal{F}\hat{F}_r$ and $\mathcal{F}^*\hat{F}_l$ first flexion transformation operators:

$$\begin{aligned}\mathcal{F}\hat{F}_r &= \frac{\mathcal{F}\beta}{16}\Big\{6\hat{a}_l^\dagger\hat{a}_r^{\dagger 2} + \Big(\hat{a}_r\hat{a}_r^\dagger + 3\hat{a}_r^\dagger\hat{a}_r + 7\hat{a}_l\hat{a}_l^\dagger - 3\hat{a}_l^\dagger\hat{a}_l\Big)\hat{a}_r^\dagger - 2\hat{a}_r^{\dagger 2}\hat{a}_r \\ &\quad - 6\hat{a}_r\hat{a}_l^2 - \Big(\hat{a}_l^\dagger\hat{a}_l + 3\hat{a}_l\hat{a}_l^\dagger + 7\hat{a}_r^\dagger\hat{a}_r - 3\hat{a}_r\hat{a}_r^\dagger\Big)\hat{a}_l + 2\hat{a}_l^2\hat{a}_l^\dagger\Big\} \qquad (3.57)\\ \mathcal{F}^*\hat{F}_l &= \frac{\mathcal{F}^*\beta}{16}\Big\{6\hat{a}_r^\dagger\hat{a}_l^{\dagger 2} + \Big(\hat{a}_l\hat{a}_l^\dagger + 3\hat{a}_l^\dagger\hat{a}_l + 7\hat{a}_r\hat{a}_r^\dagger - 3\hat{a}_r^\dagger\hat{a}_r\Big)\hat{a}_l^\dagger - 2\hat{a}_l^{\dagger 2}\hat{a}_l \\ &\quad - 6\hat{a}_l\hat{a}_r^2 - \Big(\hat{a}_r^\dagger\hat{a}_r + 3\hat{a}_r\hat{a}_r^\dagger + 7\hat{a}_l^\dagger\hat{a}_l - 3\hat{a}_l\hat{a}_l^\dagger\Big)\hat{a}_r + 2\hat{a}_r^2\hat{a}_r^\dagger\Big\}. \qquad (3.58)\end{aligned}$$

Using the same Equations and method as for the first flexion transformations, I found the results for the $\mathcal{G}\hat{G}_r$ and $\mathcal{G}\hat{G}_l$ transformations to be

$$\begin{aligned}\mathcal{G}\hat{G}_r &= \frac{\mathcal{G}\beta}{8}\left(\hat{a}_r^{\dagger 2} - \hat{a}_l^2\right)\left(\hat{a}_r^\dagger + \hat{a}_l\right) \qquad (3.59)\\ \mathcal{G}^*\hat{G}_l &= \frac{\mathcal{G}^*\beta}{8}\left(\hat{a}_l^{\dagger 2} - \hat{a}_r^2\right)\left(\hat{a}_l^\dagger + \hat{a}_r\right). \qquad (3.60)\end{aligned}$$

The relative simplicity of the $\mathcal{G}$ transformations when compared to those for $\mathcal{F}$ is striking, and this will have ramifications in the construction of practical estimators for these quantities (as will be discussed in Section 3.4). As for the case of shear and convergence, these tranformations can be equivalently written in terms of transformations upon the $f_{n,m}$ shapelet coefficients using repeated steps similar to those described by Equation (3.13). The resulting expressions are somewhat long, however, and are reproduced instead in the Appendix, Equations (A-1)-(A-4). This is the form in which the flexion transformations were given in Massey et al. (2007d). Richard Massey and I independently calculated these expressions, and compared our results for verification and the correction of small errors. However, these results in this precise form are not strictly necessary here in the body text in order to visualize the effects of the flexion transformations in polar shapelet space, which we now discuss.

Consider again the simplest possible shapelet galaxy image, a pure Gaussian with $I(\boldsymbol{\theta}) = f_{0,0}P_{0,0}(\boldsymbol{\theta};\beta)$. Using Equations (3.57) and (3.58) we can see that the effect of first flexion upon our image is to cause an increase in shapelet power in the $f_{1,\pm1}$ and $f_{3,\pm1}$ modes, as depicted in Figure 3.5. This is exactly as we would expect given the rotational symmetries of $\mathcal{F}$. We note also that $\mathcal{F}$ does not cause power to move solely to the $f_{1,\pm1}$ modes; this, which would be the shapelet space approximation to a gross shift in the object centroid, would not be sufficient to cause the skewed, dipole-like $\mathcal{F}$ image transformation depicted in Figure 1.5. A more complicated combination of $m = \pm1$ modes is necessary to describe this higher order distortion. The case of $\mathcal{G}$ is somewhat simpler, and we see from Equations (3.59) and (3.60) that the effects of second flexion are to move power from the $f_{0,0}$ mode into $f_{3,\pm3}$ modes, shown in Figure 3.5.

Of course, for a more complicated image the effects of flexion are not so simply described; the first flexion

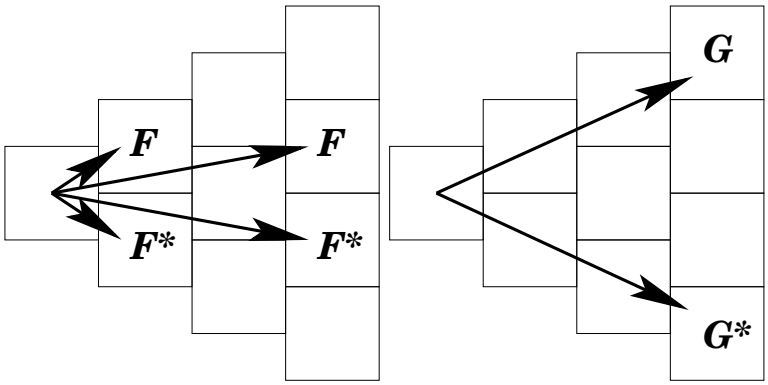


Figure 3.5: Schematic diagrams showing the direction of action of the flexion operators in polar shapelet space upon a simple galaxy image with $I(\boldsymbol{\theta}) = f_{0,0}P_{0,0}(\boldsymbol{\theta};\beta)$.

transformation moves power from $f_{n,m}$ modes into $f_{n\pm1,m\pm1}$ and $f_{n\pm3,m\pm1}$ modes, and the second flexion moves power into $f_{n\pm3,m\pm3}$ and $f_{n\pm1,m\pm3}$ modes. However, we still expect that an ensemble of unlensed images will have an average $f_{n,m}$ that tends towards zero for $m \neq 0$ modes. The effect of lensing flexion will be therefore to introduce power into the $m = \pm1$ and $m = \pm3$ modes that will not average towards zero across an ensemble of images, and so a measured, statistically significant net power in these modes can be used to estimate $\mathcal{F}$ and $\mathcal{G}$. The use of polar shapelets to construct such estimators will be discussed in Section 3.4.

This discussion concludes my outline of basic results in Cartesian and polar shapelets with relevance to lensing image transformations. However, knowing how to make shapelet models and how they might change under weak lensing is not enough: a further issue of importance in weak lensing is the correction for imperfect telescope optics, which I now go on to discuss in the following Section.

## 3.3 Image deconvolution using shapelets

### Overview

The treatment of systematic errors caused by non-gravitational image distortions is vital for a successful weak lensing analysis, as such effects may be an order of magnitude larger than the signal of interest. The effect most difficult to correct is the smearing of galaxy images due to convolution with the PSF (see, e.g., Kaiser 2000) of the observing telescope, and it is the shapelet approach to this issue that I aim to describe in this Section. Instrumental PSFs are generally anisotropic, and so two important effects can be identified. Firstly, the finite size of the PSF will cause blurring and circularization of the galaxy image, causing a biasing reduction in the magnitude of lensing measurements. Secondly, the anisotropy of the PSF will induce a slight residual signal in galaxy images, making them falsely appear gravitationally sheared or flexed.

Aside from shapelets, many of the current methods used to correct for the effects of the PSF are based on the schema proposed by Kaiser et al. (1995), Luppino & Kaiser (1997) and Hoekstra et al. (1998),

commonly referred to as KSB or KSB+. The use of these techniques has proved to be both successful and widespread. They have been implemented many times, with various minor modifications, for the placing of competitive cosmological parameter constraints using both ground-based observations of "cosmic" shear (e.g., Bacon et al. 2000; Kaiser et al. 2000; Van Waerbeke et al. 2000; Wittman et al. 2000; Hoekstra et al. 2006; Hetterscheidt et al. 2006; Semboloni et al. 2006) and similar observations from space (e.g., Hoekstra et al. 1998; Heymans et al. 2005, H05 hereafter; Schrabback et al. 2007; Massey et al. 2007c,a).

Despite its practical success, there are certain elements of the KSB+ treatment that are conceptually unsatisfactory and which potentially limit the accuracy of method (see, e.g., Kaiser 2000). This would then require the development of non-KSB+ alternatives for use on the large, high-quality lensing datasets of the future. Kaiser (2000) provides a thorough discussion of these potential limitations, and this has indeed prompted efforts to develop alternative weak lensing methods (Kaiser 2000; Rhodes et al. 2000; Bernstein & Jarvis 2002; Refregier 2003; Refregier & Bacon 2003; Massey & Refregier 2005; Kuijken 2006; Melchior et al. 2007). The shapelet approach described in this Chapter is just one of many such methods proposed to take galaxy shape measurement to the new levels of accuracy that will be required for the analysis of future lensing surveys. The Shear TEsting Program (STEP: see Heymans et al. 2006b; Massey et al. 2007b, Rhodes et al., in prep.) is coordinating research into the comparison of current weak shear estimation methods, using blind-tests on simulated lensing data.

### 3.3.1 Two shapelet approaches

Within the shapelet framework, there are two possible methods with which to correct galaxy images for the effects of the PSF. Both approaches begin with the construction of a shapelet model of the point source response $g(\boldsymbol{\theta})$; ideally this model will be as accurate as possible (i.e., high $n_{\max}$) and will include the variation of the PSF across the image plane of the instrument. The model may also need to include some treatment of time dependent effects (see, e.g., H05; Schrabback et al. 2007; Rhodes et al. 2007). A detailed description of how this may be done for data from the *Hubble Space Telescope* is given in Chapter 4.

We define the convolution of the two image functions $I(\boldsymbol{\theta})$ and $g(\boldsymbol{\theta})$ to form a convolved image $h(\boldsymbol{\theta})$ as follows:

$$h(\boldsymbol{\theta}) = I(\boldsymbol{\theta}) * g(\boldsymbol{\theta}) = \int_{-\infty}^{\infty} \mathrm{d}^2\theta^{\mathrm{s}} f(\boldsymbol{\theta} - \boldsymbol{\theta}')g(\boldsymbol{\theta}'). \tag{3.61}$$

As described by Refregier (2003), this can be written as a matrix transformation in terms of the shapelet coefficients $f_{\boldsymbol{n}}$, $g_{\boldsymbol{n}}$ etc. In Cartesian shapelets, Equation (3.61) is re-expressed as

$$h_{\boldsymbol{n}} = C_{\boldsymbol{nlk}} f_{\boldsymbol{l}} g_{\boldsymbol{k}}, \tag{3.62}$$

where repeated vector indices are implicitly summed over each component $l_i$, $k_i$ etc. An equivalent expression for polar shapelets is trivially expressed. It should be noted that the convolution tensor $C$ is a function of the respective shapelet scale lengths for the models of $h(\boldsymbol{\theta})$, $I(\boldsymbol{\theta})$ and $g(\boldsymbol{\theta})$ (see Refregier 2003).

The deconvolution scheme proposed by Refregier & Bacon (2003) consists of the solution of Equation (3.62) for $f_{\boldsymbol{n}}$, given measured $h_{\boldsymbol{n}}$ and $g_{\boldsymbol{n}}$, via a matrix inversion. The object requiring inversion, which Refregier & Bacon (2003) define as the "PSF matrix" $P_{\boldsymbol{nl}} = C_{\boldsymbol{nlk}} g_{\boldsymbol{k}}$ must, however, be truncated to entries of sufficiently low order. As argued by Refregier & Bacon (2003) this is because high order modes are smeared during convolution, which then destroys detailed small scale image information. The PSF

matrix may then contain vanishingly small values in the locations corresponding to high order modes, making its inversion unstable. This effect can minimized using a suitably truncated PSF matrix, such that it can be successfully inverted to obtain

$$f_{\boldsymbol{n}} = P^{-1}_{\boldsymbol{nl}} h_{\boldsymbol{l}}. \tag{3.63}$$

The information lost in the truncation is minimal, and reflects the loss of information that is inevitable in the convolution process. Again, a similar expression to that above may be quickly arrived at for polar shapelet models. This estimate for the lower order coefficients of the deconvolved galaxy image can then be used to make reliable estimates of shear and flexion, as described in Sections 3.4.2 and 3.4.3.

The alternative deconvolution method is that proposed by Massey & Refregier (2005), which is that implemented within the shapelet software package made available by these authors upon the world-wide web[1]. The deconvolution proceeds without the need to invert matrices which may often be sparse in practice, despite best efforts at efficient truncation. The deconvolved shapelet coefficients $f_{n_1,n_2}$ are estimated by convolving the shapelet basis functions with the PSF model in advance, creating a new basis set which we label

$$D_{n_1,n_2}(\boldsymbol{\theta};\beta) = g(\boldsymbol{\theta}) * B_{n_1,n_2}(\boldsymbol{\theta};\beta), \tag{3.64}$$

with an equivalent expression for the case of the polar shapelet basis functions $P_{n,m}(\boldsymbol{\theta};\beta)$.

Fitting the data $h(\boldsymbol{\theta})$ with this new basis set $D_{n_1,n_2}$, one returns a deconvolved shapelet model as follows:

$$\begin{aligned} h(\boldsymbol{\theta}) = g(\boldsymbol{\theta}) * I(\boldsymbol{\theta}) &= g(\boldsymbol{\theta}) * \left[ \sum_{n_1=0}^{\infty} \sum_{n_2=0}^{\infty} f_{n_1,n_2} B_{n_1,n_2}(\boldsymbol{\theta};\beta) \right] \\ &= \sum_{n_1=0}^{\infty} \sum_{n_2=0}^{\infty} f_{n_1,n_2} \left[ g(\boldsymbol{\theta}) * B_{n_1,n_2}(\boldsymbol{\theta};\beta) \right] \\ &= \sum_{n_1=0}^{\infty} \sum_{n_2=0}^{\infty} f_{n_1,n_2} D_{n_1,n_2}(\boldsymbol{\theta};\beta). \end{aligned} \tag{3.65}$$

As can be seen by comparison with Equation (3.1), the returned shapelet coefficients $f_{n_1,n_2}$ will reconstruct the deconvolved image when they are used with the original basis set $B_{n_1,n_2}(\boldsymbol{\theta};\beta)$.

There are obvious caveats to the seeming simplicity of this approach, particularly that the basis set $D_{n_1,n_2}(\boldsymbol{\theta};\beta)$ will in general not be orthonormal. However, errors due to this fact are small so long as the scale size of the galaxy image is larger than that of the PSF (Massey & Refregier 2005). It is the robust nature of this method, relying not upon matrix inversions that are slow and may be susceptible to instability, that is the reason for its selection by Massey & Refregier (2005) as the deconvolution approach adopted by the shapelet software suite. As my own analyses use this software extensively (see Chapter 4), this is also the deconvolution scheme I use to make accurate estimates of shear and flexion.

Whilst arriving at a reliable, distortion-corrected model of each galaxy is an important step in making shear and flexion measurements using shapelets, there is considerable freedom in how lensing estimators may be drawn from such models. In the next Section I will go on to describe how estimators for lensing observables may be practically taken from shapelet models of galaxies.

[1] http://www.astro.caltech.edu/∼rjm/shapelets/

# 3.4 Shapelet lensing estimators

## 3.4.1 The flexion centroid shift

Before we discuss the means by which shapelet models (in both Cartesian and polar shapelets) of galaxies may be used to make estimates of the gravitational shear and flexion signal, it is important to consider an important subtlety that comes into play when we are considering the effects of flexion upon galaxy images.

One crucial difference between the flexion and shear transformations regards the issue of the observed galaxy centroid, which is defined as

$$\boldsymbol{\theta}_c = \frac{\iint \mathrm{d}^2\theta \boldsymbol{\theta} I(\boldsymbol{\theta})}{\iint \mathrm{d}^2\theta I(\boldsymbol{\theta})}. \tag{3.66}$$

Goldberg & Bacon (2005) pointed out that, while shear causes no net centroid shift, flexion causes a vector centroid change $\Delta\boldsymbol{\theta}$ given by

$$\Delta\theta_i = (\theta_c)_i - (\theta_c^{\mathrm{s}})_i = \frac{1}{2} D_{jkl} \int \theta_i\theta_j\theta_k \frac{\partial I^{\mathrm{s}}(\boldsymbol{\theta})}{\partial\theta_l} \mathrm{d}^2\theta, \tag{3.67}$$

where we note the correction of a slight typographical error from Equation (22) of Goldberg & Bacon (2005). Expanding and integrating by parts, these authors use this result to give an expression for this centroid shift in terms of elements of $D_{ijk}$.

Performing the same calculation, but re-expressing $D_{ijk}$ in terms of the quantities $\mathcal{F}$ and $\mathcal{G}$, I found this centroid shift to be given by the equivalent expression

$$\Delta\theta = \frac{(R^2)^{\mathrm{s}}}{4} \left(6\mathcal{F} + 5\mathcal{F}^*\varepsilon^{\mathrm{s}} + \mathcal{G}(\varepsilon^{\mathrm{s}})^*\right) . \tag{3.68}$$

Here we once more use the complex notation in which the real part of $\Delta\theta_c$ corresponds to the shift in the $x$ direction and the imaginary part to the $y$ direction on the sky plane. In this expression the $(R^2)^{\mathrm{s}}$ term in the source plane is defined as

$$(R^2)^{\mathrm{s}} = \frac{\iint \mathrm{d}^2\theta^{\mathrm{s}} |\theta^{\mathrm{s}}|^2 I^{\mathrm{s}}(\boldsymbol{\theta}^{\mathrm{s}})}{\iint \mathrm{d}^2\theta^{\mathrm{s}} I^{\mathrm{s}}(\boldsymbol{\theta}^{\mathrm{s}})}, \tag{3.69}$$

where I have labelled the source coordinates $\boldsymbol{\theta}^{\mathrm{s}}$ rather than the commonly written $\boldsymbol{\beta}$ so as to avoid confusion with the shapelet basis angular scale size $\beta$. The quantity $\varepsilon^{\mathrm{s}}$ is the complex ellipticity of the source galaxy, defined as

$$\varepsilon^{\mathrm{s}} = \frac{1}{(R^2)^{\mathrm{s}}} \frac{\iint \mathrm{d}^2\theta^{\mathrm{s}} \left(\theta_1^{\mathrm{s}} + \mathrm{i}\theta_2^{\mathrm{s}}\right)^2 I^{\mathrm{s}}(\boldsymbol{\theta}^{\mathrm{s}})}{\iint \mathrm{d}^2\theta^{\mathrm{s}} I^{\mathrm{s}}(\boldsymbol{\theta}^{\mathrm{s}})} = \frac{1}{(R^2)^{\mathrm{s}}} \frac{\iint \mathrm{d}^2\theta^{\mathrm{s}} \left[(\theta_1^{\mathrm{s}})^2 - (\theta_2^{\mathrm{s}})^2 + \mathrm{i}2\theta_1^{\mathrm{s}}\theta_2^{\mathrm{s}}\right] I^{\mathrm{s}}(\boldsymbol{\theta}^{\mathrm{s}})}{\iint \mathrm{d}^2\theta^{\mathrm{s}} I^{\mathrm{s}}(\boldsymbol{\theta}^{\mathrm{s}})}. \tag{3.70}$$

Both $\varepsilon^{\mathrm{s}}$ and $(R^2)^{\mathrm{s}}$ may be simply estimated from shapelet images, described in Massey & Refregier (2005), and this estimation will be discussed in a little more detail below. Finally, for clarity in what comes below, it will be convenient to write Equation (3.68) out in full component form as follows:

$$\Delta\theta_1 = \frac{(R^2)^{\mathrm{s}}}{4} \left[6\mathcal{F}_1 + 5(\mathcal{F}_1\varepsilon_1 + \mathcal{F}_2\varepsilon_2) + \mathcal{G}_1\varepsilon_1 + \mathcal{G}_2\varepsilon_2\right] \tag{3.71}$$

$$\Delta\theta_2 = \frac{(R^2)^{\mathrm{s}}}{4} \left[6\mathcal{F}_2 + 5(\mathcal{F}_1\varepsilon_2 - \mathcal{F}_2\varepsilon_1) + \mathcal{G}_2\varepsilon_1 - \mathcal{G}_1\varepsilon_2\right] . \tag{3.72}$$

Equations (3.68), (3.71) and (3.72) tell us how much a gravitational flexion will shift the observed centroid of a galaxy image; the shapelet flexion transformations found in Sections 3.1 and 3.2 include this centroid shift effect. They are therefore useful for such applications as applying an artificial flexion to an unlensed galaxy (for example, during the manufacture of simulated images), although this may also be done easily in real space using Equation (1.92). However, for practical flexion measurements the location of the centre of a shapelet decomposition will be the post-lensing (i.e., observed) centre of light $\boldsymbol{\theta}_c$. This consideration is crucial in a flexion analysis, as use of the flexion estimators based on the transformations described in Sections 3.1 and 3.2 will give wrong results if the are used on a shapelet model not constructed upon the *original*, pre-lensing centroid, which we cannot know for certain.

What may be done, however, is to estimate the shift in the centroid described by Equation (3.68) and take it into account using shapelets. Making the valid assumption that the centroid shift due to weak flexion is small compared to the angular scale of the galaxy image, we may write

$$I(\boldsymbol{\theta} - \Delta\boldsymbol{\theta}) \simeq I(\boldsymbol{\theta}) - \Delta\theta_i \frac{\partial I(\boldsymbol{\theta})}{\partial \theta_i}. \tag{3.73}$$

We can express the right hand term of this expression in terms of shapelet transformations. Using Equation (3.12), we have the following Cartesian shapelet results:

$$\Delta\theta_1 \frac{\partial I(\boldsymbol{\theta})}{\partial \theta_1} = \frac{\Delta\theta_1}{\beta\sqrt{2}} \sum_{n_1=0}^{\infty} \sum_{n_2=0}^{\infty} f_{n_1,n_2} \left(\hat{a}_1 - \hat{a}_1^\dagger\right) B_{\boldsymbol{n}}(\boldsymbol{\theta};\beta), \tag{3.74}$$

$$\Delta\theta_2 \frac{\partial I(\boldsymbol{\theta})}{\partial \theta_2} = \frac{\Delta\theta_2}{\beta\sqrt{2}} \sum_{n_1=0}^{\infty} \sum_{n_2=0}^{\infty} f_{n_1,n_2} \left(\hat{a}_2 - \hat{a}_2^\dagger\right) B_{\boldsymbol{n}}(\boldsymbol{\theta};\beta). \tag{3.75}$$

These results can be more succinctly expressed by defining the Cartesian shapelet transformation operators $\hat{T}_i$ as

$$\hat{T}_i = \frac{1}{\beta\sqrt{2}} \left(\hat{a}_i - \hat{a}_i^\dagger\right). \tag{3.76}$$

This then allows us, using Equation (3.73), to write

$$\left(\mathcal{F}_i \hat{F}_i + \mathcal{G}_i \hat{G}_i\right) I(\boldsymbol{\theta} - \Delta\boldsymbol{\theta}_c) \simeq \left(\mathcal{F}_i \hat{F}_i + \mathcal{G} \hat{G}_i - \Delta\theta_i \hat{T}_i\right) I(\boldsymbol{\theta}), \tag{3.77}$$

where we have ignored terms greater than first order in $\mathcal{F}$, $\mathcal{G}$ or $\Delta\theta$. Notice that the right hand side of this expression is precisely what we wish to estimate, the effects of flexion upon the shapelet model centred upon the pre-lensing centre of light.

Another, more useful, way of expressing these results is to define "observable" flexion operators, i.e., those with this centroid shift removed. These then describe the effects of flexion that can be seen in terms of pure distortions to the light profile of galaxy images and cause no net centroid shift. We can then write these effective, translation-corrected flexion operators as

$$\mathcal{F}_i \hat{F}_i^T = \mathcal{F}_i \hat{F}_i - \Delta\theta_i^{\mathcal{F}} \hat{T}_i \tag{3.78}$$

$$\mathcal{G}_i \hat{G}_i^T = \mathcal{G}_i \hat{G}_i - \Delta\theta_i^{\mathcal{G}} \hat{T}_i, \tag{3.79}$$

where we have defined $\Delta\theta^{\mathcal{F}} = [(R^2)^{\rm s}/4](6\mathcal{F} + 5\mathcal{F}^*\varepsilon^{\rm s})$ and $\Delta\theta^{\mathcal{G}} = [(R^2)^{\rm s}/4]\mathcal{G}(\varepsilon^{\rm s})^*$ by splitting Equation (3.68) into first and second flexion terms. The $\hat{F}_i$ and $\hat{G}_i$ operators are simply those described in Section 3.1.2. However, as is often the case in shapelets, the Cartesian representation means that we have a slightly complicated mixing of $\mathcal{F}_1$ and $\mathcal{F}_2$ terms in each component of $\Delta\theta^{\mathcal{F}}$, and likewise for the $\mathcal{G}$ components in $\Delta\theta^{\mathcal{G}}$ (see Equations 3.71 and 3.72). Due to the symmetries of the polar shapelet basis set, these mixing components can be separated out, as I now describe.

We can define polar shapelet versions of the translation operators given in Equation (3.76), splitting the transformation into left and right handed operators such that

$$\left(\Delta\theta_1\hat{T}_1 + \Delta\theta_2\hat{T}_2\right) I(\boldsymbol{\theta}) = \left(\Delta\theta\hat{T}_r + (\Delta\theta)^*\hat{T}_l\right) I(\boldsymbol{\theta}). \tag{3.80}$$

Using Equations (3.46) and (3.47), we can write these translation operators out as

$$\Delta\theta\hat{T}_r = \frac{\Delta\theta}{2\beta}\left(\hat{a}_l - \hat{a}_r^\dagger\right) \tag{3.81}$$

$$(\Delta\theta)^*\hat{T}_l = \frac{(\Delta\theta)^*}{2\beta}\left(\hat{a}_r - \hat{a}_l^\dagger\right). \tag{3.82}$$

Finally, this allows to define a left and right handed pair of polar shapelet transformation operators do describe the observable effect of each of $\mathcal{F}$ and $\mathcal{G}$.

For the first flexion, using Equations (3.81) and (3.82), and the definition of $\Delta\theta^{\mathcal{F}}$ described above, we have the following expression for the observable flexion transformations:

$$\mathcal{F}\hat{F}_r^T = \mathcal{F}\left(\hat{F}_r - \frac{6}{4}\hat{T}_r - \frac{5}{4}(\varepsilon^{\rm s})^*\hat{T}_l\right) \tag{3.83}$$

$$\mathcal{F}^*\hat{F}_l^T = \mathcal{F}^*\left(\hat{F}_l - \frac{6}{4}\hat{T}_l - \frac{5}{4}\varepsilon^{\rm s}\hat{T}_r\right). \tag{3.84}$$

We notice that it is now possible to more cleanly decouple the flexion transformations using the complex conjugates of $\mathcal{F}$ and $\mathcal{G}$; this is due to the rotational symmetry properties of the polar shapelet basis set. For the observable part of the second flexion transformations in polar shapelets, we have

$$\mathcal{G}\hat{G}_r^T = \mathcal{G}\left(\hat{G}_r - \frac{1}{4}(\varepsilon^{\rm s})^*\hat{T}_r\right) \tag{3.85}$$

$$\mathcal{G}^*\hat{G}_l^T = \mathcal{G}^*\left(\hat{G}_l - \frac{1}{4}\varepsilon^{\rm s}\hat{T}_l\right). \tag{3.86}$$

These flexion operators, and those of Equations (3.78) and (3.79), approximately describe the observable, shape-changing part of the flexion transformation by isolating it from the the translatory part of the distortion. In essence, this is done via a simple subtraction of the centroid shift.

The only question remaining is regarding the estimation of $(R^2)^{\rm s}$ and $\varepsilon^{\rm s}$, which are both quantities as measured in the unlensed source plane of the image. It is argued by Goldberg & Bacon (2005) that, for the purposes of constructing workable flexion estimators $\varepsilon^{\rm s}$ and $(R^2)^{\rm s}$, may be estimated from the lensed

galaxy image using the expressions given in Massey & Refregier (2005). This is despite the fact that both quantities will have changed during lensing. However, the change in the centroid shift this represents is small, which can be seen from Equation (3.68), and such changes will cancel on average due to the differing rotational symmetries of $\gamma$, $\mathcal{F}$ and $\mathcal{G}$. If deemed necessary, an estimate of the ellipticity corrected for locally measured shear could even be used, as there is nothing to prevent the galaxy shear analysis from being independently performed prior to any flexion analysis. It is the translation corrected operators of Equations (3.78), (3.79), and Equations (3.83) - (3.86), combined with $\varepsilon^{\rm s}$ and $(R^2)^{\rm s}$ estimated from the observed galaxy image, that will be used to form flexion estimators in the following Sections.

### 3.4.2 Estimating shear and flexion from Cartesian shapelets

In this Section I review and describe the methods presented in Refregier (2003) and Goldberg & Bacon (2005) for estimating shear and flexion, given an accurate Cartesian shapelet model of the lensed galaxy. In most cases this model will have had to undergo some correction for the effects of an anisotropic PSF, using one of the methods described in Section 3.3.

We follow Refregier & Bacon (2003) and label the covariance of the observed shapelet coefficients as $V_{\boldsymbol{n},\boldsymbol{l}} = \mathrm{cov}(f_{\boldsymbol{n}} f_{\boldsymbol{l}})$. As shown by Refregier (2003), for homogeneous, uncorrelated background noise (such as that produced by the sky or thermal instrument noise) this covariance is given simply by

$$V_{\boldsymbol{nl}} = \sigma_{\rm N}^2 \delta_{n_1,l_1} \delta_{n_2,l_2}, \tag{3.87}$$

where $\sigma_{\rm N}$ is the root mean squared noise in the image. This covariance matrix will be necessary in the discussions that follow.

The problem of shear and flexion estimation in Cartesian shapelets can be reduced to the inversion of Equation (3.17), given some important assumptions about the properties of the underlying population of source galaxy images $I^{\rm s}(\boldsymbol{\theta})$. This is simplified significantly if the effects of the convergence term are ignored, which may be justified in the weak, first order limit. It should be noted that under any circumstances the value of the convergence itself cannot be uniquely determined from estimates of shear or flexion alone, and can only be uniquely defined with strong lensing data or other lensing data in which the redshift of more than one source object are well known (see, e.g., Schneider & Er 2007; Massey et al. 2007d; BGRT06; Kaiser & Squires 1993).

Expanding on the description given in Goldberg & Bacon (2005), we consider an ensemble of $N$ unlensed source galaxies. If we label the surface brightness of each source galaxy as $I_i^{\rm s}(\boldsymbol{\theta})$ (where $i = 1, \ldots, N$) and the corresponding Cartesian shapelet coefficients as $(f_{\boldsymbol{n}}^{\rm s})_i$, then we may define the ensemble average of the source coefficients as

$$\mu_{\boldsymbol{n}} = \sum_{i=1}^{N} (f_{\boldsymbol{n}}^{\rm s})_i. \tag{3.88}$$

For an ensemble of galaxies of sufficient size, and sampled across sufficiently large scales, this $\mu_{\boldsymbol{n}}$ may be estimated as the average of the measured shapelet coefficients $f_{\boldsymbol{n}}$; this is assuming that the Universe shows no preferred direction on extremely large scales (see Goldberg & Bacon 2005). Moreover, due to the parity properties of the Cartesian basis set we know and can explicitly set $\mu_{\boldsymbol{n}} = 0$ wherever $n_1 + n_2 =$ odd (see Equation 3.2).

To explore how this definition may be used to construct a Cartesian shapelet estimator for shear and flexion, we consider another ensemble of $M$ galaxies, this time in the lensed image plane, and with surface brightnesses labelled $I_j(\boldsymbol{\theta})$ where $j = 1, \ldots, M$. In addition, we now restrict the ensemble of galaxies to a size $M \ll N$ and reduced scale upon the sky, within which shear and flexion do not vary significantly and cancel. For this ensemble, average $\mu_{\boldsymbol{n}}$ defined in Equation (3.88) will not be well estimated by a simple average of the observed $f_{\boldsymbol{n}}$. Instead, such an average will yield

$$\sum_{j=1}^{M}(f_{\boldsymbol{n}})_j = \mu_{\boldsymbol{n}} + \left(\gamma_i \hat{S}_i + \mathcal{F}_i \hat{F}_i^T + \mathcal{G}_i \hat{G}_i^T\right) \sum_{j=1}^{M}(f^{\rm s}_{\boldsymbol{n}'})_j, \tag{3.89}$$

where the primes on the final $f^{\rm s}_{\boldsymbol{n}'}$ coefficients are there to highlight that these coefficients denote those that will be transformed to $f^{\rm s}_{\boldsymbol{n}}$ by the action of the shear and flexion transformations. Note that we are dealing in observable quantities, and use the centroid shift-corrected flexion transformations of Section 3.4.1. If we follow the method of Goldberg & Bacon (2005) and define another quantity, $\tilde{f}^{\rm s}_{\boldsymbol{n}}$, as the best estimate of the unlensed shapelet coefficients for a single galaxy within our smaller ensemble, we may then approximate the above expression for a single galaxy as

$$f_{\boldsymbol{n}} \simeq \mu_{\boldsymbol{n}} + \left(\gamma_i \hat{S}_i + \mathcal{F}_i \hat{F}_i^T + \mathcal{G}_i \hat{G}_i^T\right) \tilde{f}^{\rm s}_{\boldsymbol{n}'}. \tag{3.90}$$

How this quantity $\tilde{f}^{\rm s}_{\boldsymbol{n}}$ may be estimated in practice depends on whether we are measuring shear or flexion, and so we will return to this point below. At any rate, Equation (3.90) will only be an *extremely* approximate expression for a single galaxy, but it may nonetheless be used to create an estimator of shear and flexion on a galaxy-by-galaxy basis. If $\tilde{f}^{\rm s}$ is estimated appropriately the resulting estimates of shear and flexion will, if averaged across the ensemble of $M$ galaxies, be unbiased to a good approximation.

In order to use Equation (3.90) to create an estimator of shear and flexion we may fit values of $\gamma$, $\mathcal{F}$ and $\mathcal{G}$ for each galaxy that minimize the following $\chi^2$ goodness-of-fit statistic:

$$\begin{aligned} \chi^2 \quad &\equiv \quad \left[\mu_{\boldsymbol{n}} + \left(\gamma_i \hat{S}_i + \mathcal{F}_i \hat{F}_i^T + \mathcal{G}_i \hat{G}_i^T\right) \tilde{f}^{\rm s}_{\boldsymbol{n}'} - f_{\boldsymbol{n}}\right] \\ &\times \quad V^{-1}_{\boldsymbol{n}\boldsymbol{p}} \left[\mu_{\boldsymbol{p}} + \left(\gamma_i \hat{S}_i + \mathcal{F}_i \hat{F}_i^T + \mathcal{G}_i \hat{G}_i^T\right) \tilde{f}^{\rm s}_{\boldsymbol{p}'} - f_{\boldsymbol{p}}\right] \end{aligned} \tag{3.91}$$

It is now important to consider in more detail how we may estimate $\tilde{f}^{\rm s}_{\boldsymbol{n}}$, having access only to the observed coefficients $f_{\boldsymbol{n}}$. In this respect we follow the argument of Goldberg & Bacon (2005), which again treats the $n_1 + n_2 =$ odd, and $n_1 + n_2 =$ even, terms differently. These authors argue that, in the weak lensing regime, the difference between the observed and source even terms will be small in general, and so the best estimate of $\tilde{f}^{\rm s}_{\boldsymbol{n}'}$ is $f_{\boldsymbol{n}'}$ for $n_1 + n_2 =$ even. Obviously, this argument will hold limited validity in stronger lensing regimes. For the $\tilde{f}^{\rm s}_{\boldsymbol{n}}$ where $n_1 + n_2 =$ odd, we set $\tilde{f}^{\rm s}_{\boldsymbol{n}} = 0$; although this will provide inaccurate estimates on a galaxy-by-galaxy basis, it will be true for an ensemble of galaxies of sufficient number $M$, and will thus lead to unbiased lensing estimates.

Assuming these arguments regarding $\tilde{f}^{\rm s}_{\boldsymbol{n}}$, we can split Equation (3.91) into two shear and flexion-only parts. As discussed in Section 3.1.2, the shear transformations only transfers power between pairs of coefficients for which $\Delta n_1 + \Delta n_2 =$ even, and so for a shear estimator only $n_1 + n_2 =$ even coefficients in Equation (3.91) need be considered. For the flexion transformations, which transfer power between $\Delta n_1 + \Delta n_2 = \pm 1, \pm 3$ pairs of coefficients, we need only consider the terms in Equation (3.91) for which

$n_1 + n_2 =$ odd. We then have two independent expressions, as follows:

$$\chi^{2(even)} = \left[\mu_{\boldsymbol{n}} + \gamma_i \hat{S}_i \tilde{f}^{\rm s}_{\boldsymbol{n}'} - f_{\boldsymbol{n}}\right] V^{-1}_{\boldsymbol{np}} \left[\mu_{\boldsymbol{p}} + \gamma_i \hat{S}_i \tilde{f}^{\rm s}_{\boldsymbol{p}'} - f_{\boldsymbol{p}}\right] \tag{3.92}$$

$$\chi^{2(odd)} = \left[\left(\mathcal{F}_i \hat{F}_i^T + \mathcal{G}_i \hat{G}_i^T\right) \tilde{f}^{\rm s}_{\boldsymbol{n}'} - f_{\boldsymbol{n}}\right] V^{-1}_{\boldsymbol{np}} \left[\left(\mathcal{F}_i \hat{F}_i^T + \mathcal{G}_i \hat{G}_i^T\right) \tilde{f}^{\rm s}_{\boldsymbol{p}'} - f_{\boldsymbol{p}}\right], \tag{3.93}$$

where we also note the correction of a sign error from Goldberg & Bacon (2005). An estimator of each of the shear and flexion upon each galaxy can then be calculated by the minimization of $\chi^{2(even)}$ and $\chi^{2(odd)}$ respectively. David Goldberg has made IDL code that performs this minimization available to the public via the world-wide web, at the flexion web page[1]. It should be noted again that the flexion operators $\hat{F}_i$ and $\hat{G}_i$ involve three-step movements in shapelet shape, and as such *any* flexion estimator will require shapelet coefficient information of up to a minimum order of $n_{\rm max} = 3$. Galaxies for which the shapelet series is truncated to $n_{\rm max} \leq 2$ cannot be used to make reliable estimators of flexion.

### 3.4.3 Estimating shear and flexion from polar shapelets

The polar shapelet basis set provides a natural framework for creating weak lensing estimators. This is due to the encapsulation of the differing rotational symmetries of shear and flexion by the rotational symmetries of the basis set itself. As discussed in Section 3.2, weak shear upon a wholly circular object shifts shapelet power in to polar shapelet modes with $m = \pm 2$ exclusively; weak first and second flexion upon the same object create power in the $m = \pm 1$ and $m = \pm 3$ modes respectively. The strength of shapelet coefficient values in these modes, relative to those in the $m = 0$ modes, can then used to generate estimators of shear and flexion very simply, and without the need for minimization of $\chi^2$ statistics described above for the Cartesian estimators.

In this way polar shapelets offers a means of generating "passive" rather than "active" estimators of flexion (for a complete definition of these terms in the weak lensing context see Massey et al. 2007b,d). Simply put, passive estimators are those that use the measured moments of galaxy images, usually with some scheme of image weighting to reduce noise, such as the schemes proposed by Kaiser et al. (1995) for shear and Okura et al. (2007b) for flexion. That polar shapelet estimators based on ratios of shapelet coefficients are analogous to such moment-based approaches can be seen by examination of the overlap integral given in Massey & Refregier (2005):

$$f_{n,m} = \iint {\rm d}^2\theta I(\boldsymbol{\theta}) P_{n,m}(\boldsymbol{\theta};\beta). \tag{3.94}$$

This is a simple consequence of the orthonormality relationship (Equation 3.35) for the polar shapelet basis functions $P_{n,m}(\boldsymbol{\theta};\beta) = P_{n,m}(\theta,\phi;\beta)$. To illustrate this fact, we consider the expression for $f_{2,2}$. Using Equation (3.32), the explicit expression for $P_{2,2}(\theta,\phi;\beta)$ is

$$P_{2,2}(\theta,\phi;\beta) = \frac{\theta^2}{\beta^3} {\rm e}^{-\frac{\theta^2}{\beta^2}} {\rm e}^{2{\rm i}\phi} = \frac{1}{\beta^3}\left(\theta_1^2 - \theta_2^2 + 2{\rm i}\theta_1\theta_2\right) {\rm e}^{-\frac{\theta^2}{\beta^2}}. \tag{3.95}$$

Substituting this expression into Equation (3.94), we see that the quantity

$$\beta^3 f_{2,2} = \iint {\rm d}^2\theta \left(\theta_1^2 - \theta_2^2 + 2{\rm i}\theta_1\theta_2\right) {\rm e}^{-\frac{\theta^2}{\beta^2}} I(\boldsymbol{\theta}) \tag{3.96}$$

[1] http://www.physics.drexel.edu/∼goldberg/flexion/

is simply the quadrupole moment of Kaiser et al. (1995) and Bartelmann & Schneider (2001), weighted by a Gaussian of angular scale $\beta$. For $n = m = 1, 3$ it can be similarly shown that $\beta^{n+1} f_{n,m}$ correspond to Gaussian weighted first and third moments respectively (often equivalently described as dipole and octopole moments).

There are benefits in using shapelets to perform moment calculations, rather than performing the calculation in real space. Shapelets offers a sophisticated treatment of PSF corrections (see Section 3.3), a great deal of freedom in the selection of estimators, and even offers additional tests for systematics. As described in Massey et al. (2007d), if the PSF correction scheme is accurate then there should be no significant difference between different estimators; any discrepancy points to imperfect deconvolution and highlights image scales upon which problems may exist. Massey et al. (2007d) present a variety of shear and flexion estimators, with properties that may be of particular interest in different applications. For the case of shear, there are two estimators which I will now describe.

### Gaussian weighted shear estimator

The first, and simplest, shear estimator uses the $f_{2,2}$ coefficients that I have shown in Equation (3.96) to be simply related to the Gaussian-weighted quadropole moment. Using Equations (3.54) and (3.55) we see that the effect of shear is to transform the $f^{\rm s}_{2,2}$ shapelet coefficient as follows:

$$(1 + \gamma \hat{S}_r + \gamma^* \hat{S}_l) : f^{\rm s}_{2,2} \rightarrow f_{2,2} = f^{\rm s}_{2,2} + \frac{\gamma}{\sqrt{2}} \left( f^{\rm s}_{0,0} - f^{\rm s}_{4,0} \right) - \gamma^* \sqrt{3} f^{\rm s}_{4,4}. \tag{3.97}$$

As in Section 3.4.2, we consider an ensemble of $M$ galaxies across which the shear is approximately constant $\gamma$. Assuming random orientations of these galaxies in the source plane the ensemble average of $f^{\rm s}_{n,m}$ will tend to zero for all coefficients with $m \neq 0$. A simple estimator of shear for each galaxy in this ensemble can therefore be constructed as

$$\tilde{\gamma}^{\rm Gaussian} = \sqrt{2} \frac{f_{2,2}}{\langle f_{0,0} - f_{4,0} \rangle}. \tag{3.98}$$

The angle brackets in the denominator denote an ensemble average across the galaxies in a lensing survey, but it should be stressed that this is *not* the sample of $M$ galaxies across which the shear and other lensing values are approximately constant. As in Section 3.4.2 we need also to consider a larger scale ensemble of $N \gg M$ galaxies, within which the shear, convergence and flexion will vary and tend to cancel due to the overall isotropy of large scale structure. It is over this larger ensemble (i.e., perhaps, the entire galaxy image catalogue in a lensing survey) that the denominator average must be taken. This will ensure that this estimator is approximately unbiased; were the denominator average to be made over the smaller ensemble the action of an overall weak lensing convergence would be to shift power out of the $f_{0,0}$ and $f_{4,0}$ (see Equation 3.53).

This estimator is the Gaussian weighted shear estimator of Massey et al. (2007d), and will obey the necessary unbiased property

$$\frac{1}{M} \sum_{i=1}^{M} \tilde{\gamma}_i^{\rm Gaussian} \simeq \gamma \tag{3.99}$$

for our smaller ensemble of $M$ galaxies across which the shear signal remains constant. It is so named because, as shown by Equation (3.96), the numerator is simply related to a weighted quadrupole moment.

## Unweighted ellipticity shear estimator

The second shear estimator from that I will describe is that based on the shapelets unweighted ellipticity $\varepsilon$, defined in terms of source image moments by Equation (3.70) in Section 3.4.1. Instead, we here use the ellipticity of the lensed images, and so drop the superscript $s$. Massey et al. (2007d) show that the $\varepsilon$ can be used to constructed the following unbiased estimator for shear

$$\tilde{\gamma}^{\rm unweighted} = \frac{\varepsilon}{2\mathcal{R}} = \frac{\varepsilon}{(2-\langle\varepsilon^2\rangle)} = \frac{\sum_{n=0}^{\infty}\sqrt{n(n+2)}\,f_{n,2}}{(2-\langle\varepsilon^2\rangle)\sum_{n=0}^{\infty}\sqrt{(n+1)}\,f_{n,0}}. \tag{3.100}$$

Here we have defined the shear responsivity factor $\mathcal{R} = 1 - \left\langle\varepsilon^2\right\rangle/2$, where the average denoted by the angle brackets should be across as large an ensemble of galaxies as possible to ensure that this estimator satisfies the criterion of being unbiased (c.f. Equation 3.99). It is well known that such a responsivity calibration is necessary for shear estimators based upon the unweighted ellipticity; it is caused by the fact that the more elliptical a galaxy is *before* being sheared, the weaker its response to a lensing shear will be (see, e.g., Bartelmann & Schneider 2001). This estimator performed very well during the blind simulation tests of shear estimators conducted by the second STEP programme (Massey et al. 2007b) and on other lensing image simulations designed to mimic ground-based observations (Massey et al. 2007d). One of the investigations of this Thesis is to explore its efficacy using survey images taken from space-based instruments such as the *Hubble Space Telescope*.

## Gaussian weighted flexion estimators

I will now describe my construction of some passive flexion estimators, as also presented in Massey et al. (2007d). The construction of these estimators drew on our experience with the shear estimators developed in that paper, and are formed in analogy with the same. The simplest flexion estimator can be constructed using a similar approach to that taken with the $\tilde{\gamma}^{\rm Gaussian}$ estimator of Equation (3.98). For that estimator, the coefficients $f_{2,2}$, correpsonding to Gaussian-weighted quadrupole moments, were used; this is a simple first choise since, as was described in Section 3.2.2, these are the lowest modes to be excited by the action of shear upon the shapelet ground state $f_{0,0}$.

For the case of flexion it was shown in Section 3.2.2 that the $f_{1,1}$, $f_{3,1}$ and $f_{3,3}$ shapelet modes are the first to be excited by the action of $\mathcal{F}$ and $\mathcal{G}$ upon a simple $f_{0,0}$ shapelet model. The simplest possible first flexion estimator is therefore one based upon the measured value of the $f_{1,1}$ coefficient for any given galaxy. Using Equations (3.57), (3.58), (3.83) and (3.84), it is easy to show that this coefficient transforms as follows under a first flexion:

$$\begin{aligned}(1+\mathcal{F}\hat{F}_r^T+\mathcal{F}^*\hat{F}_l^T): f^{\rm s}_{1,1}\rightarrow f_{1,1} \;\; &= \;\; f^{\rm s}_{1,1} + \frac{\mathcal{F}\beta}{8}\left\{6\left(1-\frac{(R^2)^{\rm s}}{\beta^2}\right)f^{\rm s}_{0,0} + 6\frac{(R^2)^{\rm s}}{\beta^2}f^{\rm s}_{2,0}\right.\\ &\qquad\left. -\; 6f^{\rm s}_{4,0} - 5\sqrt{2}(\varepsilon^{\rm s})^*\frac{(R^2)^{\rm s}}{\beta^2}f^{\rm s}_{2,2}\right\}\\ &+ \;\; \frac{\mathcal{F}^*\beta}{8}\left\{\; -5\varepsilon^{\rm s}\frac{(R^2)^{\rm s}}{\beta^2}(f^{\rm s}_{0,0}-f^{\rm s}_{2,0})\right.\\ &\qquad\left. +\sqrt{2}\left(1+6\frac{(R^2)^{\rm s}}{\beta^2}\right)f^{\rm s}_{2,2,} - 3\sqrt{6}\,f^{\rm s}_{4,2}\right\}.\end{aligned} \tag{3.101}$$

The correction for the centroid shift adds to the complexity of these transformation expressions but it must be stressed that this correction is extremely important, particularly in the case of the dipole-like first flexion.

In an analagous fashion, the simplest possible second flexion estimator that can be constructed using polar shapelets will be based upon the measured value of the $f_{3,3}$ coefficient. Using Equations (3.59), (3.60), (3.85) and (3.86), the action of second flexion upon $f^{\rm s}_{3,3}$ was calculated as follows:

$$\begin{aligned}(1+\mathcal{G}\hat{G}_r^T+\mathcal{G}^*\hat{G}_l^T):f^{\rm s}_{3,3}\rightarrow f_{3,3} \quad &= \quad f^{\rm s}_{3,3}+\frac{\mathcal{G}\beta}{8}\Bigg\{(\varepsilon^{\rm s})^*\frac{(R^2)_{\rm s}}{\beta^2}(f^{\rm s}_{4,2}-\sqrt{3}\,f^{\rm s}_{2,2})\;+\\ &\qquad\qquad \sqrt{6}\,(f^{\rm s}_{0,0}+f^{\rm s}_{2,0}-f^{\rm s}_{4,0}-f^{\rm s}_{6,0})\Bigg\}\\ &+\quad \frac{\mathcal{G}^*\beta}{8}\left\{2\varepsilon^{\rm s}\frac{(R^2)^{\rm s}}{\beta^2}f^{\rm s}_{4,4}-2\sqrt{30}\,f^{\rm s}_{6,6}\right\}. \end{aligned} \tag{3.102}$$

In order to use these expressions to calculate estimators for flexion, we once again consider an ensemble of $M$ galaxies in a region of sky across which we have roughly constant flexion, and a much larger ensemble of $N$ galaxies (i.e. the entire survey sample) across which there is a vanishing net flexion. We must once more assume that the galaxies in the source plane are randomly oriented. The $\varepsilon^{\rm s}$ terms in Equations (3.101) and (3.102) refer to the unlensed ellipticities of these sources, and will thus cancel when averaging over any sufficiently large population of galaxies, even in the presence of a shear field. Once more, we may go further and expect the average values of $f^{\rm s}_{n,m}$, where $m\neq 0$, to tend to zero in our ensembles; net shapelet power will ony remain in the averaged $m=0$ terms.

Therefore, the simplest possible polar shapelet flexion estimators can be constructed from the combinations

$$\tilde{\mathcal{F}}^{\rm Gaussian}=\frac{4}{3\beta}\frac{f_{1,1}}{\langle(1-(R^2/\beta^2))\,f_{0,0}+(R^2/\beta^2)f_{2,0}-f_{4,0}\rangle} \tag{3.103}$$

and

$$\tilde{\mathcal{G}}^{\rm Gaussian}=\frac{4\sqrt{6}}{3\beta}\frac{f_{3,3}}{\langle f_{0,0}+f_{2,0}-f_{4,0}-f_{6,0}\rangle}, \tag{3.104}$$

where the angle brackets used in the denominator denote an ensemble average across the large ensemble of $N$ galaxies. However, in the first flexion estimator we are forced to use the lensed $R^2/\beta^2$ rather than $(R^2)^{\rm s}/(\beta^2)^{\rm s}$; fortunately, as shown in Massey et al. (2007d), changes in $R^2/\beta^2$ due to a symmetrically varying flexion do not bias $\langle R^2/\beta^2\rangle$ to first order, and so the denominator remains unbiased overall when this average is taken over the sufficiently large ensemble of $N$ galaxies. It should be noted that, despite these estimators being the simplest possible within the polar shapelet framework, $\tilde{\mathcal{F}}^{\rm Gaussian}$ and $\tilde{\mathcal{G}}^{\rm Gaussian}$ require shapelet galaxies to be modelled to orders of $n=4$ and $n=6$ respectively before they may be used to create unbiased estimators. Equations (3.103) and (3.104) are the Gaussian weighted flexion estimators presented in Massey et al. (2007d).

As a final comment, the reason that these estimators are referred to as Gaussian weighted is similar to that for $\tilde{\gamma}^{\rm Gaussian}$. Considering Equation (3.94) and the form of the $P_{1,1}$ and $P_{3,3}$ basis functions, the $f_{1,1}$ and $f_{3,3}$ coefficients can be shown to simply correspond to Gaussian weighted first and third order image moments, just as $f_{2,2}$ was shown to be a Gaussian weighted second moment in Equation (3.96). The Higher Order Lensing Image Characteristics (HOLICs) method proposed by Okura et al. (2007b)

creates estimates of flexion using direct measurements of such weighted moments, and thus the estimators of Equations (3.103) and (3.104) are the shapelets analogue to HOLICs moments in which the scale radius for the Gaussian weighting is simply the angular scale $\beta$. The shapelet estimators above simply represent what $\beta$-weighted HOLICS estimators would return if they acted upon a smoothed, PSF-corrected shapelet model of a galaxy image.

These results do not represent the end point of possible flexion estimators, as any of the $f_{n.m}$ coefficients with $m = 1$ and $m = 3$ may be used as estimators of $\mathcal{F}$ and $\mathcal{G}$, respectively. Indeed, as pointed out in Massey et al. (2007d), significant systematic differences between such estimators effectively point to deficiencies in model used for PSF correction. Comparison of the many possible shapelet estimators therefore represents a new test for the level of residual systematic errors, the successful removal of which is so important for weak lensing. Additionally, the other way in which of higher order estimators may be of use is in their *combination* with estimators built from lower modes; in this way it is possible to generate estimators with any property that may be of interest. Methods and results towards such estimators are discussed in the following Sections.

## Order-by-order shapelet flexion estimators

For the small, faint galaxy images that will inevitably make up the majority of weak lensing survey data, it will be difficult to measure polar shapelet coefficients beyond the $n = 6$ terms needed to make an unbiased estimate $\tilde{\mathcal{G}}_{\rm Gaussian}$ as described above. Yet, for those galaxies for which higher order shapes can be accurately measured, it is possible to generalise these flexion estimators to higher shapelet modes. We may use the measured value of any available $f_{n,1}$ coefficients as an estimator for $\mathcal{F}$, and likewise any available $f_{n,3}$ as an estimator for $\mathcal{G}$.

In order to do this it is necessary to understand how these higher order estimators respond to flexion. In order to describe this information we define the following flexion susceptibility matrices:

$$(P_n^{\mathcal{F}})_{ij} = \frac{\partial (f_{n,1})_i}{\partial \mathcal{F}_j}, \quad (P_n^{\mathcal{G}})_{ij} = \frac{\partial (f_{n,3})_i}{\partial \mathcal{G}_j}. \tag{3.105}$$

For convenience, in the expressions above we have vectorized the complex shapelet coefficients $f_{n,m}$ and defined $(f_{n,m})_i = (\ \mathrm{Re}\{f_{n,m}\},\ \mathrm{Im}\{f_{n,m}\}\ )$. Knowledge of these susceptibility factors for each of the higher order estimators that can be constructed from $f_{n,1}$ and $f_{n,3}$, allows the construction of the flexion estimators

$$\tilde{\mathcal{F}}_i^n \equiv \left\langle (P_n^{\mathcal{F}})_{ij} \right\rangle^{-1} (f_{n,1})_j \tag{3.106}$$

and

$$\tilde{\mathcal{G}}_i^n \equiv \left\langle (P_n^{\mathcal{G}})_{ij} \right\rangle^{-1} (f_{n,3})_j. \tag{3.107}$$

Once again we have vectorized the complex quantities, and the angle brackets denote the average across a large ensemble of galaxies such as the entire survey. The susceptibilities of Equation (3.105) are real, $2 \times 2$ matrices, with terms that may be calculated using the results for the polar shapelet flexion transformations given in Equations (A-1)-(A-4) in the Appendix, and the centroid shift correction terms described by Equations (3.83)-(3.86). I give the results of my calculations for these generalized $(P_n^{\mathcal{F}})_{ij}$ and $(P_n^{\mathcal{G}})_{ij}$ susceptibilities in the Appendix, Equations (A-6)-(A-9).

Differences between the ensemble values of each of these $n$ estimators can be compared as possible evidence for systematics in the lensing analysis or PSF correction (Massey et al. 2007d), but may also be used to construct further new estimators using combinations of $f_{n,1}$ and $f_{n,3}$. Given complete freedom in selection, such estimators can be designed so as to have particular properties of interest. One such combination, leading to the "diagonal" flexion estimators, is discussed in Massey et al. (2007d) and in the following Section I describe my work towards the description of this estimator.

## Flexion estimators with purely diagonal susceptibilities

It was shown in Massey et al. (2007d) that successive off-diagonal terms in the shear susceptibility matrix $(P^{\gamma}_n)_{ij}$, defined for $f_{n,2}$ coefficients in an exactly analogous fashion to Equation (3.105), could be made to cancel out via the suitable addition of $f_{n,2}$ estimators. This led to the shapelets expression for $\tilde{\gamma}^{\rm unweighted}$, which in fact corresponds exactly to the unweighted complex ellipticity $\varepsilon$ defined by Equation (3.70).

In the same way it might be hoped that the same terms of diagonal terms in the flexion susceptibility matrices of Equation (3.105) could be made to cancel, via a suitable weighting scheme $w_n$, where we would then define the resulting purely diagonal estimator $\tilde{p}^{\mathcal{F}}_{\rm diag}$ as

$$(\tilde{p}^{\mathcal{F}}_{\rm diag})_i = \left\langle (P^{\mathcal{F}}_p)_{i,j} \right\rangle^{-1} \sum_{n=1}^{\infty} w_n (f_{n,1})_j, \tag{3.108}$$

where we have once again vectorized the complex notation, and where by definition $(P^{\mathcal{F}}_p)_{i,j} = 0$ for $i \neq j$. We could also define similar expressions for the second flexion estimator $\tilde{p}^{\mathcal{G}}_{\rm diag}$ in terms of weighted $f_{n,3}$ coefficients. Unfortunately, due to the presence of the centroid shift correction which is necessary for reliable flexion estimators, my calculations showed that this is more difficult than in the case of shear, especially for the first flexion.

For the second flexion it is possible to do reasonably well. It is impossible to construct a purely diagonal $\tilde{p}^{\mathcal{G}}_{\rm diag}$ using the centroid shift corrected transformations of Equations (3.85) and (3.86). However, it is possible to find a weighting $w_n$ in which successive diagonal terms in $(P^{\mathcal{G}}_p)_{i,i}$ cancel if we consider only the uncorrected transformations $\mathcal{G}\hat{G}_r$ and $\mathcal{G}^*\hat{G}_l$ of Equations (3.59) and (3.60). Using these Equations, I found this weighting to be $w_n = \sqrt{(n-1)(n+1)(n+3)}$, which can then be used to form the following purely diagonal second flexion estimator

$$\tilde{\mathcal{G}}^{\rm diag} \equiv \tilde{p}^{\mathcal{G}}_{\rm diag} = \frac{2\sqrt{2}}{3\beta\mathcal{R}} \frac{\sum_{n=3}^{\infty} \sqrt{(n-1)(n+1)(n+3)}\, f_{n,3}}{\sum_{n=0}^{\infty} (n^2+2n+2)\, f_{n,0}}. \tag{3.109}$$

Here we have defined the "flexion responsivity" factor as the ensemble average $\mathcal{R} = 1 - \left\langle \delta\rho/\beta^3 \right\rangle/2$, where

$$\rho = \beta^6 \sqrt{32\pi} \sum_{n=3}^{\infty} (n+1) \sqrt{(n-1)(n+1)(n+3)\, f_{n,3}} \tag{3.110}$$

and

$$\delta = \frac{\sqrt{2}}{2\beta} \frac{\sum_{n=3}^{\infty} \sqrt{(n-1)(n+1)(n+3)}\, f_{n,3}}{\sum_{n=0}^{\infty} (n^2+2n+2)\, f_{n,0}}. \tag{3.111}$$

This definition of the quantity $\delta$ exactly mirrors that of the unweighted HOLICs measurable of the same

name, which Okura et al. (2007b) define as

$$\delta = \frac{\iint \mathrm{d}^2\theta I(\boldsymbol{\theta})\theta^3 \mathrm{e}^{3\mathrm{i}\phi}}{\iint \mathrm{d}^2\theta I(\boldsymbol{\theta})|\theta|^4} \tag{3.112}$$

and which they use to create an estimator of the second flexion $\tilde{\mathcal{G}}^{\mathrm{HOLICS}} = 4\delta/3$. The estimator in Equation (3.109) is the shapelet space equivalent of this quantity $4\delta/3$ except for the additional responsivity factor $\mathcal{R}$. This correction is in fact necessary because the denominator of $\delta$ changes during flexion in a way which biases the overall estimator by an amount $(1 - \langle\rho\delta/\beta^3\rangle/2)$, and is analagous to the similar factor of $(2 - \langle\varepsilon^2\rangle)$ introduced to the unweighted ellipticity estimator for shear.

Despite the fact that the estimator of Equation (3.109) does not account for changes to the susceptibility resulting from the flexion induced centroid shift, it will remain unbiased when averaged across an ensemble of galaxies. This is because we may assume that the unlensed ellipticities $\varepsilon^{\mathrm{s}}$ of source galaxies will cancel on average, and because it is known that there is no centroid shift due to $\mathcal{G}$ for galaxies with $\varepsilon^{\mathrm{s}} = 0$ (see Equations 3.85 and 3.86).

In contrast, the first flexion presents greater difficulties. Firstly, there is a flexion-induced centroid shift for even purely circular objects, proportional to $(R^2)^{\mathrm{s}}/\beta^2$. However, even if it were feasible to ignore the translatory part of the practical flexion operator (which it is not), it appears to be impossible to find a weighting scheme $w_n$ capable of cancelling the off-diagonal terms in successive orders of $P^{\mathcal{F}}_{ij}$. The complication arises from the mixing of power between $\Delta m, \Delta n = \pm 1$ coefficients, which becomes extremely complicated for the first flexion, and from the very important fact that shapelet ladder operators are non commutative. This can be expressed as follows

$$\left[\hat{a}_r, \hat{a}_r^\dagger\right] P_{n,m} = \left(\hat{a}_r\hat{a}_r^\dagger - \hat{a}_r^\dagger\hat{a}_r\right) P_{n,m} = P_{n,m} \neq 0 \tag{3.113}$$

$$\left[\hat{a}_l, \hat{a}_l^\dagger\right] P_{n,m} = \left(\hat{a}_l\hat{a}_l^\dagger - \hat{a}_l^\dagger\hat{a}_l\right) P_{n,m} = P_{n,m} \neq 0, \tag{3.114}$$

which can be simply derived using Equations (3.36)-(3.39). We know that $\mathcal{F}$ causes power to transfer between adjacent, $\Delta m, \Delta n = \pm 1$ shapelet coefficients (see Figure 3.5), much like a simple translation of the sort introduced in Section 3.4.1. However, whereas a simple centroid shift involves only the single ladder-operator transformations $\hat{a}_r^\dagger$, $\hat{a}_l^\dagger$, $\hat{a}_r$ and $\hat{a}_l$ (as shown in Equations 3.81 and 3.82), flexion always acts via combinations of three ladder operations, taking three steps but doubling back to move only one step overall. Since $\hat{a}_r^\dagger$ does not commute with $\hat{a}_r$, nor $\hat{a}_l^\dagger$ with $\hat{a}_l$, each $\Delta m, \Delta n = \pm 1$ term in Equations (A-1)-(A-4) is in fact a combination of five separate contributions, each of which representing a different, independent path between the coefficients. For example, to make an overall move to a mode with $\Delta n_r = +1$, any of $\hat{a}_r^{\dagger 2}\hat{a}_r$, $\hat{a}_r^\dagger\hat{a}_r\hat{a}_r^\dagger$, $\hat{a}_r\hat{a}_r^{\dagger 2}$, $\hat{a}_r^\dagger\hat{a}_l\hat{a}_l^\dagger$ or $\hat{a}_r^\dagger\hat{a}_l^\dagger\hat{a}_l$ may be employed, all of which contain one of the non-commuting pairs identified in Equations (3.113) and (3.114). Because it is composed of a different, non-commuting combination of ladder operators, each path contributes a different, $n$-dependent proportion of the overall power in the transformation. This added level of complexity for the first flexion transformation appears to preclude any estimator of first flexion with vanishing off-diagonal terms in the susceptibility matrix.

This concludes the discussion of shapelets, and of the flexion results that I contributed to Massey et al. (2007d), although that paper also discusses other possible estimators using polar shapelets. These include the "radial profile" estimator mentioned previously, and active estimators constructed in a similar fashion

to those discussed in Section 3.4.2 and Goldberg & Bacon (2005). As can be seen, this work offers a variety of possible methods with which to measure flexion accurately using real galaxy images. In the next Chapter I will go on to describe my attempts to perform such an analysis using imaging data from the GEMS survey (Rix et al. 2004), this being the work that has dominated my research and which provides the culminating results of this Thesis.

# CHAPTER 4

# SHAPELET LENSING ANALYSIS OF *HST* SURVEY DATA

In this Chapter I describe my correction for PSF distortions in real galaxy survey data, using the shapelet method described in Chapter 3, and the use of the shapelet shear and flexion estimators. Using data from the Galaxy Evolution from Morphologies and SEDs (GEMS) survey I have accurately measured real galaxy shear using shapelets for the first time, and extended this analysis to flexion, providing reliable catalogues of these lensing measures for the galaxy-galaxy lensing analyses of Chapter 6.

New technical challenges were faced during this work and the methods I developed to meet these challenges are discussed in detail, including the extraction of "postage stamp" images and the construction of a full shapelet model of the PSF based on stars in the galaxy. I use the results from simulated lensing data to choose the current-best shapelet estimators for the extraction of lensing information from GEMS shapelet models. The resulting galaxy shear catalogue is compared with the findings of previous authors having performed independent analyses of the same field, and is found to be in good agreement. Finally, tests for systematics show that the shapelet deconvolution has removed any significant residual shear anisotropy due to the PSF, although there are traces of residual second flexion contamination.

# 4.1 GEMS lensing data

## 4.1.1 Galaxy images

The GEMS survey imaging data used in this analysis, described extensively by Rix et al. (2004), Caldwell et al. (2005), H05, and Schrabback et al. (2007), covers a sky area of $\simeq 796$ arcmin$^2$ centred on the *Chandra* Deep Field South (CDFS). The bulk of the data consists of 125 orbits of *HST*/ACS imaging, combined with a further 15 ACS tiles from the GOODS project (Giavalisco et al. 2004). An image of the mosaic of these tiles, taken from Rix et al. (2004), is shown in Figure 4.1. Images were observed for the GEMS survey in two pass bands: F606W (78 tiles) and F850LP (77 tiles), with $5\sigma$ point source detection limits of $m_{606} = 28.3$ and $m_{850} = 27.1$. In this work, we follow H05 and use only the F606W images in our lensing analysis, as they contain more discernible galaxies (by a factor greater than two) and extend deeper in redshift.

Although it is not necessary to reproduce in full the detailed discussions of this dataset given by Caldwell et al. (2005) and H05, it is important to address those properties of the data that are possible sources of systematic bias, and outline the steps taken to diagnose and limit these effects. Systematic errors important to lensing in particular are well discussed by H05, and much of what we discuss in this Section is presented in greater detail there. However, the method used in this work to correct for the anisotropic ACS PSF differs significantly from the analysis of H05, and this is discussed in greater detail in Sections 4.2.3.

As discussed in H05, each GEMS-observed science tile is a combination of three ACS exposures, dithered by $\simeq 3$ arcsec. The resulting images have a pixel scale chosen as 0.03 arcsec, and the dithering procedure allows the bridging of the gap between the twin charge-coupled device (CCD) chips of the ACS. The images taken from GOODS are a combination of only two dithered exposures, despite the availability of further exposures taken at later dates; this is necessitated by the time instability of the ACS PSF (see H05, Rhodes et al. 2007). The GOODS survey was optimized for supernova searches (Riess et al. 2004), and the ACS data from GOODS was observed in five time-separated epochs. In this work, as in H05, we only use imaging from the first of these GOODS epochs.

Due to the location of the ACS camera away from the *HST* optical axis, images suffer geometrical distortion which is significant but also accurately modelled (Meurer et al. 2003). Caldwell et al. (2005) describe the method used to correct for this distortion, and the fixing of the GEMS astrometry to that of the R-band image of the publicly available COMBO-17 survey (Wolf et al. 2004). Geometrical distortions in the GEMS data due to velocity aberration were not found to be significant for measurements of shear (H05), and similarly I find there to be no significant variation of average galaxy flexion across the ACS chips.

One other source of image distortion to space-based observations is a degraded charge transfer efficiency (CTE) of the on-board CCD instrumentation. Ongoing bombardment by cosmic rays defectively alters the semiconductor structure, causing an image bleed in the direction of read-out which worsens with time (e.g. Rhodes et al. 2004, 2007). Due perhaps to the GEMS observations taking place soon after the ACS installation, H05 and Schrabback et al. (2007) (in their recent analysis of the same data) find no evidence for degraded CTE at a level significant to measurements of weak lensing shear, and so I do not attempt a correction for this effect (Rhodes et al. 2007; Massey et al. 2007c).

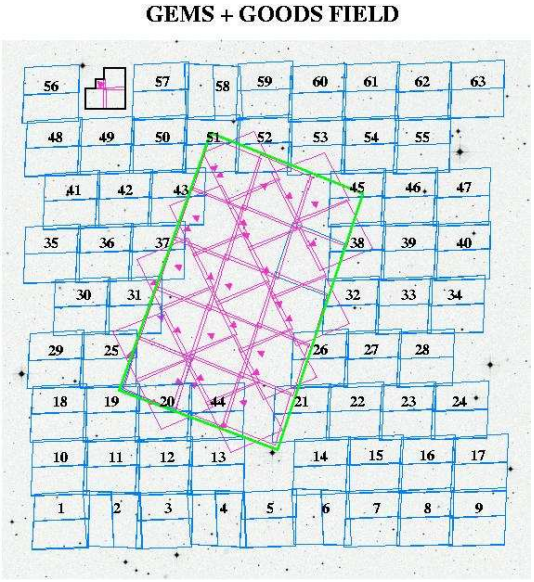


Figure 4.1: Image of the GEMS survey mosaic, showing the position of each tile on the extended *Chandra* Deep Field South. The tiles at the centre of the image, not aligned with the overall field, are from the first epoch observations of GOODS; these have been incorporated into the overall GEMS analysis. The area indicated in the top-left of the image is that of the *Hubble* Deep Field South. Figure taken from Rix et al. (2004).

### 4.1.2 Object catalogues

In this work we take as a starting point the same catalogue of $121\,475$ GEMS objects as used by H05, made with the SExtractor software of Bertin & Arnouts (1996). This catalogue was assembled using the two-pass object detection strategy described in Rix et al. (2004) and Caldwell et al. (2005), which successfully detects faint objects without multiply labelling single large objects. The SExtractor package was also used to determine and subtract each tile's spatially varying sky background (Caldwell et al. 2005). We define the signal-to-noise ratio (SNR) of each object as the ratio of its SExtractor measured flux to the error on this measurement (FLUX and FLUX_ERROR respectively, see Bertin & Arnouts 1996).

The entire GEMS field was masked by hand (H05) to prevent false object detections from diffraction spikes, satellite trails, reflection ghosts and artefacts from chip boundaries. In my analysis, I ensure the single selection of objects from overlapping regions in GEMS as follows: pairs closer than 0.3 arcsec but lying in different tiles were isolated and the object with the lower SNR was then removed from the main catalogue.

All objects with SNR $< 15$ are removed from the catalogue, reducing systematic selection biases which become significant for fainter objects. As pointed out by Kaiser (2000), one source of bias for faint galaxies is the preferential selection of objects which happen to be aligned with an anisotropic PSF. Another effect (Hirata & Seljak 2003) which causes bias is the preferential selection of circular objects over elongated ones (of the same flux) by almost any conceivable detection algorithm. Galaxies which are anti-aligned with the gravitational shear will become circularized upon lensing, and are thus detected in greater numbers than their elongated, shear-aligned counterparts; this has the effect of weakening the measured shear amplitude.

Both these sources of error were found by H05 to be negligible for the GEMS sample once subjected to a significance cut of SNR $> 15$. Issues of possible SExtractor centroid bias, discussed by H05, are now completely resolved by my use here of the shapelet method of Massey & Refregier (2005): an accurate object centroid is an output parameter of the shapelets amoeba fit. The GEMS SExtractor catalogues, having been cleaned as described above, contain a total of $121\,475$ objects.

## GEMS galaxy catalogue

In the selection of galaxy objects for weak lensing measurements, we follow H05 and remove objects with FLUX_RADIUS $< 2.4$ pixels so as to exclude stars and small false detections from the galaxy sample (see Section 4.1.2 below). Again only objects with SExtractor measured magnitude $21.0 < m_{606} < 27.0$ are included, so as to exclude extremely faint galaxies for which lensing measurements become less reliable. All pairs of objects separated by less than 0.6 arcsec are removed, preventing shapelet modelling errors due to extremely close neighbours. This leaves a final total of $52\,669$ selected galaxies for all tiles, and this is the sample from which measurements of galaxy-galaxy shear and flexion will be made.

Seen in Figure 4.3, the construction of these shapelet-ready catalogues was carried out using my IDL code `makegemscats.pro`. These catalogues are required by the shapelet software to contain only certain items of information for each object; the ASCII catalogue columns for these input variables are required to fall in a certain prescribed order (see Bergé 2006). It should be noted that, whilst we only wish to measure shear and flexion from galaxies, the catalogues that we input to the shapelet software must include *all* the $121\,475$ SExtractor detected objects within the GEMS fields, not just those selected as of interest as described above. Shapelets must know about *all* objects in the field so that even objects which will not be modelled can be masked. A subset of the total set of objects, containing the galaxies of interest, is then also supplied to the shapelet software so that only these objects are modelled; it is not necessary to make a shapelet model of every object detected. This is an important consideration in the shapelet technique; without careful masking, nearby objects can be be confused and erroneously modelled as being part of the central galaxy of interest. Henceforth we refer to the catalogues containing every object for each tile, plus the known location of each selected galaxy, as the shapelet-ready catalogues.

For each tile the list of galaxy objects of interest, and their location indices within the shapelet-ready catalogues, is stored by `makegemscats.pro` in separate galaxy reference catalogues (Figure 4.3). These location indices are then supplied to the shapelet routine `shex.pro` (presented in Massey & Refregier 2005 but modified as described in Section 4.2.2) as an array, ensuring that only objects of interest are modelled but all nearby objects are masked. The date upon which each galaxy was observed is also stored by these reference files, and this information is used immediately prior to the running of the shapelet software to build an accurate time-dependent shapelet model of the PSF at the CCD chip location of each galaxy (see Sections 4.1.2 and 4.2.3). This is vital for the successful deconvolution of the GEMS galaxies.

The reference catalogues also include useful information not required by shapelets for modelling, such as the right ascension and declination of each galaxy, and the index location, where applicable, of the same galaxy within Catherine Heymans' (CFH) shear catalogue of H05 (important for later comparison of lensing shear estimates). As shown in Figure 4.3 this information is then passed to the output shear and flexion catalogues. However, before the GEMS deconvolution can proceed, a sample of non-saturated stellar objects must be assembled so that the PSF can be modelled using shapelets; this is described in the following Section.

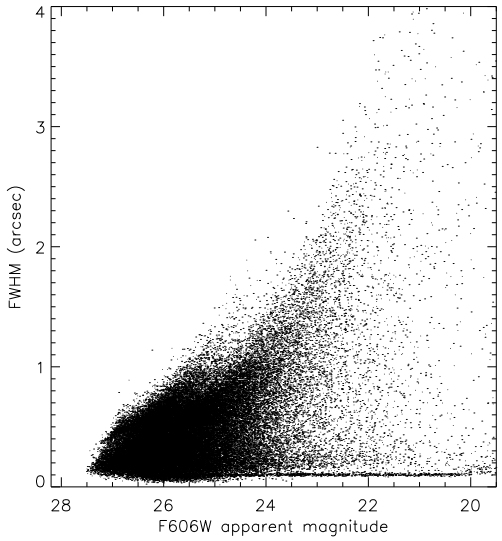


Figure 4.2: SExtractor measured FWHM-magnitude diagram for all GEMS objects with SNR $> 15$ and lying in unmasked regions. The locus of true point sources can be clearly seen along the bottom of the plot. The stellar sample is taken from objects which lie in the non-confused regions of both this locus and its counterpart in the GEMS FLUX_RADIUS-magnitude diagram.

## GEMS point source catalogue

An accurate shapelet model of the GEMS PSF, varying as a function of position on the ACS field of view, is vital for the successful deconvolution of galaxy images. Stars for this modelling were selected from the object catalogue as described by H05, utilizing the constancy of the stellar full width half maximum (FWHM) with apparent magnitude. Candidate objects were identified from the stellar locus of both the FWHM-$m_{606}$ plane and the FLUX_RADIUS-$m_{606}$ plane, as measured by SExtractor, giving a total of $\simeq 950$ stellar objects (see Figure 4.2).

This number corresponds to an average of only $\simeq 12$ stars per ACS tile, insufficient to accurately characterize the PSF as a function of chip position on a tile-by-tile basis. We cannot assume global PSF stability for all the GEMS and GOODS observations as the ACS PSF is known to vary significantly with time (e.g. Rhodes et al. 2007), possibly due to thermal changes on the *HST* during orbit. We therefore break the stellar sample into three sub-samples based on the date of observation for each science tile, assuming PSF stability within each of these sub-samples. This approach is aided by the short duration over which the GEMS and GOODS images were observed: the first epoch GOODS data was observed in five days, and all but three of of the GEMS-observed F606W tiles were imaged within a twenty day period. These three out-of-sequence GEMS tiles are therefore discarded, and the remaining GEMS sample split into two 10 day epochs.

This approach is also that taken by H05, who found that the GEMS PSF remained sufficiently stable within a 10 day epoch to allow a cosmic shear analysis to be performed using the GEMS data (see H05, Figure 4). The measurement of a cosmological lensing signal is a far more ambitious undertaking than the galaxy-galaxy lensing analysis which is the aim of this Thesis. Moreover, it is only the anisotropy of the

ACS PSF that varies significantly with time and not the characteristic angular size (Rhodes et al. 2007). Therefore such changes will not result in a systematic bias to measurements of galaxy-galaxy lensing, for which errors due to residual PSF anisotropy cancel due to the circular averaging over each source-lens pair (Schneider & Rix 1997). Given that anisotropy removal is not a critical requirement of this analysis, and so as to aid direct comparison between my shapelet results and those of H05 (upon the same images), we do not mount a fully independent investigation into the PSF variation and use the exact same time-dependent PSF modelling strategy as those authors. This leaves a catalogue of 919 point source objects in F606W from which we characterize the ACS PSF. In similar fashion to that for galaxies described in the previous Section 4.1.2, the list of the 919 PSF objects destined for shapelet modelling is stored in a series of PSF reference files, one for each tile. The shapelet-ready catalogues, which contain all objects, are then passed to the modified `shex.pro` for the modelling of both stars and galaxies.

# 4.2 GEMS lensing measurements

## 4.2.1 Overview

The lensing analysis of the GEMS (Rix et al. 2004) optical imaging data using the shapelet software of Massey & Refregier (2005) proceeds in five stages, the first being the selection of object catalogues described above. Then, "postage stamp" images and noise maps for each star and galaxy object are created, which I describe in Section 4.2.2 below, including modifications and enhancements to the publicly-available shapelet software. In Section 4.2.3 I describe the next stage, the modelling of the GEMS PSF from stellar postage stamp images.

The fourth stage uses the shapelet software to find best-fitting deconvolved models of the GEMS galaxies, using the shapelet amoeba routines described in Massey & Refregier (2005) and the deconvolution scheme outlined in Section 3.3. This stage uses both the galaxy postage stamp images and models of the GEMS PSF at each galaxy location. The final stage of the lensing analysis draws estimators for shear and flexion from the deconvolved galaxy shapelets catalogues or "shapecats"; the choice of estimator is discussed in Section 4.2.5, and is motivated by the simulation results of Chapter 5. The schematic diagram shown in Figure 4.3 gives a simple picture of how these five stages of reduction and analysis were combined for the GEMS survey data.

In the last Section (4.3.3) of the Chapter, I present the successful results of initial tests for residual lensing systematics, investigate some of the magnitude-dependent properties of the measured shear and flexion, and compare the results of the shapelet shear estimation to the KSB+ results of H05 and Schrabback et al. (2007).

## 4.2.2 Postage stamp extraction

In order to model galaxies and stars in GEMS, postage stamp images of each object must be extracted from the survey image data. This may be done with Richard Massey's IDL script entitled `shapelets_sexcat2pstamp.pro`,

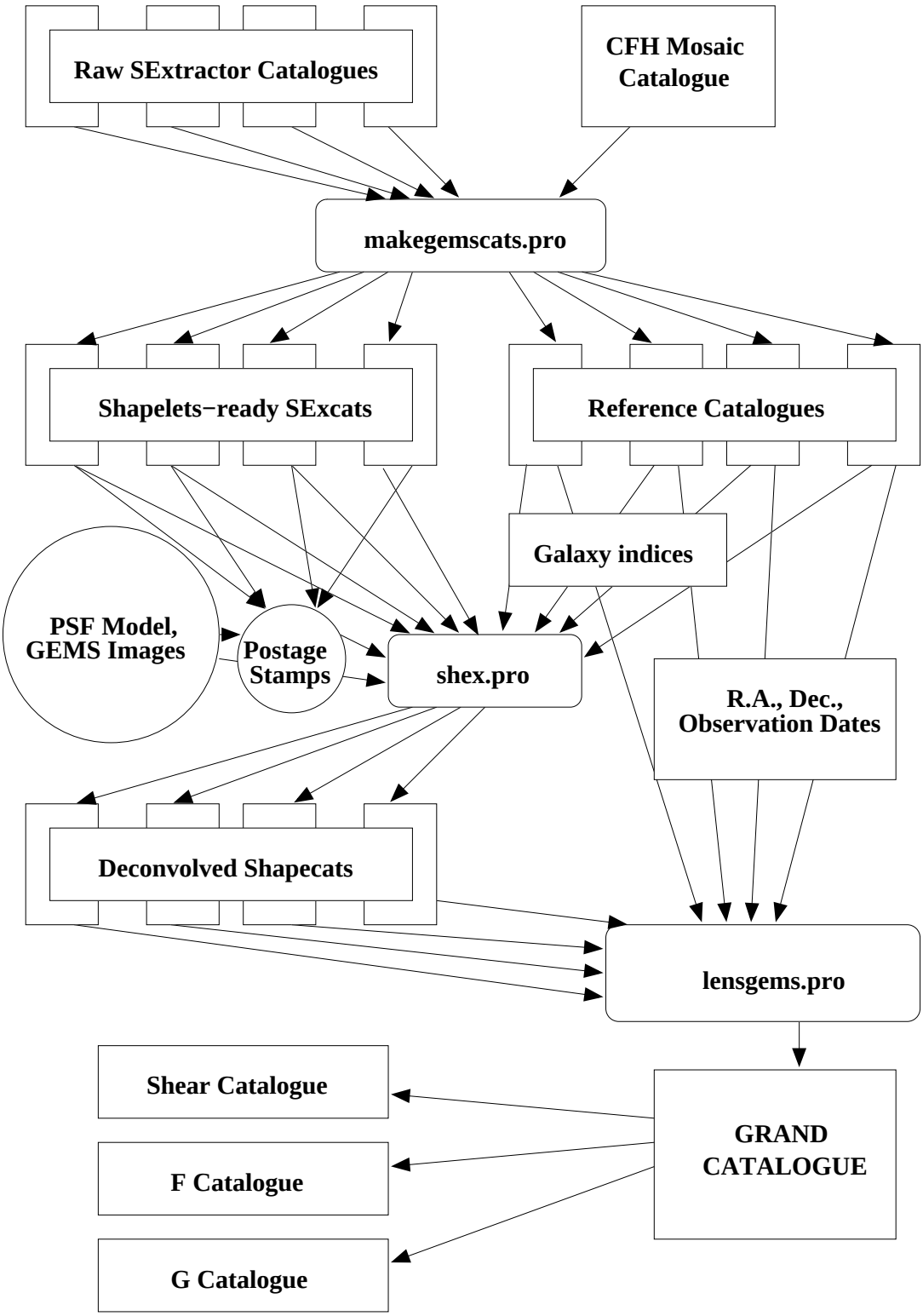


Figure 4.3: Schematic overview of the GEMS shapelet pipeline, see Sections 4.1-4.2 for details.

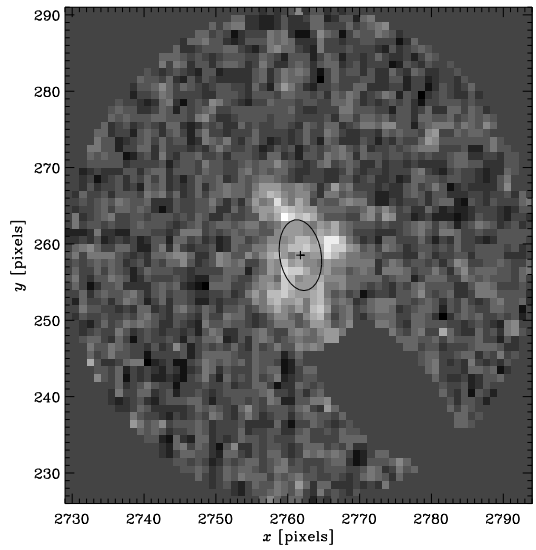


Figure 4.4: Example of a GEMS galaxy postage stamp image, showing a (severely-overlapping) masked neighbour. The small plotted ellipse is that defined by the $a$ and $b$ semi-major and semi-minor axes output by SExtractor

called from within `shex.pro` (see Figure 4.3), using either automatically created noise and segmentation maps or those supplied by the user (from, e.g., SExtractor). In this analysis, I chose to build noise and segmentation maps on a postage stamp-by-postage stamp basis using a modified version of the `shapelets_sexcat2pstamp.pro` routine.

For each star or galaxy a circular postage stamp centred on the SExtractor centroid is created. Using a segmentation map (see, e.g., Bertin & Arnouts 1996) these postage stamps are masked for nearby objects, ensuring that only the object of interest will be modelled by shapelets. In constructing a mask for each object I modified the segmentation map-generating algorithm of the shapelet software, which appeared to produce a large number of masking failures for the GEMS data. In my modified routine an elliptical mask is drawn over each nearby galaxy, of semi-major axis $2.75a$ and semi-minor axis $2.75b$ (where $a$ and $b$ are respectively the SExtractor-output semi-major and semi-minor axes of the object). Visual inspection of masked images showed this to be good compromise between the need to exclude unwanted light from object postage stamps, whilst not over-masking and obscuring the object of interest.

Following on from this, by additionally masking the central galaxy object, a noise map and estimate of the sky background can be made via analysis of the remaining blank sky pixels. The root mean squared pixel value is used to assign a constant background noise level to each postage stamp image, and the sky level itself may be subtracted using a choice of models (Bergé 2006). For the GEMS images, which are already sky-subtracted (see H05), only a very small amount of residual sky background was found and the removal of a simple constant sky level from each postage stamp was sufficient. The noise map is then supplied to the shapelets amoeba focusing routines as the "noise postage stamp", at the deconvolution stage (Section 4.2.4), alongside the masked and sky-subtracted image postage stamp.

It was necessary to make additional changes to the publicly-available shapelet software, of relevance to the construction of postage stamp images. In particular, it was found that whilst the drawing of large postage

stamps around objects was computationally prohibitive at the shapelet modelling stage, smaller postage stamps led to an unacceptable number of model failures. An simple modification that iteratively redraws the postage stamp in the event of model failure provided an efficient solution to this problem, and is now part of the shapelet software, documented and available for download online. This process begins within an initial postage stamp image of radius $n_{\rm FWHM}$ times the full width at half maximum (FWHM) of each galaxy image, as output by SExtractor. If the modelling fails due to the model extending beyond the limits of the postage stamp, the modelling is begun again with a postage stamp that is increased in size increased by a factor $f_{\rm REDRAW}$. This process is repeated up to a maximum of $n_{\rm REDRAWS}$ times, after which a catastrophic failure was flagged. In this analysis, I used an initial postage stamp size of $n_{\rm FWHM} = 6$, a redraw factor $f_{\rm REDRAW} = 1.2$ and a maximum number of redraws $n_{\rm REDRAWS} = 6$.

A further improvement was the estimation the Poisson shot noise on each image pixel, which is then added in quadrature to the sky noise map of each galaxy postage stamp. However, the total integration times of the GEMS and GOODS observations, being 2160 seconds and 1040 seconds respectively, ensured that this shot noise contribution was small in comparison to the sky background.

The postage stamp data for each galaxy is then ready for shapelet modelling, but in order to accurately deconvolve these images the point source postage stamps must first be used to model the GEMS PSF, a process we now describe in detail.

### 4.2.3 Modelling the GEMS PSF

The shapelet characterization of the GEMS PSF proceeds in two stages. Firstly, a shapelet decomposition of each selected stellar object is made, using the postage stamps drawn for each stellar object as described in Section 4.2.2. The output shapelet model then gives a value and error estimate for each shapelet coefficient $f_{n_1,n_2}$. The variation of each of these coefficients across the ACS chip is then approximated by the least-squares fit of a simple two-dimensional function; recombining the coefficients from these best-fit models then allows the full GEMS PSF to be estimated at any point across the field of view. However, this simple picture disguises some significant freedoms at each stage of the modelling process.

#### Individual stellar models

Each star in the point source catalogue was modelled up to a shapelet order $n_{max} = 20$, with a fixed scale size of $\beta = 1.8$ pixels. The optimal choice of these modelling parameters depends sensitively upon the properties of the PSF in question. In particular, the Gaussian envelopes of the shapelet basis functions $B_{n_1,n_2}$, while well suited to fitting typical galaxy profiles, are here an inconvenience: the ACS point source response is extremely non-Gaussian in profile and so requires modelling to a high order $n_{max}$. Using a PSF model of $n_{max} = 20$ slows down the deconvolution and modelling of galaxy images considerably, but this is a necessary concession if both the peak region and wings of the ACS PSF are to be accurately characterized. In the cases of some of the brightest stars even an $n_{\rm max} = 20$ model is insufficient to provide a good fit to every pixel of the stellar observations, due to their extremely high significance.

The choice of a fixed value for the basis function scale radius, $\beta$, can help to minimize the effects of this unavoidable concession. For this reason, considerable care must be taken in this choice. As discussed in

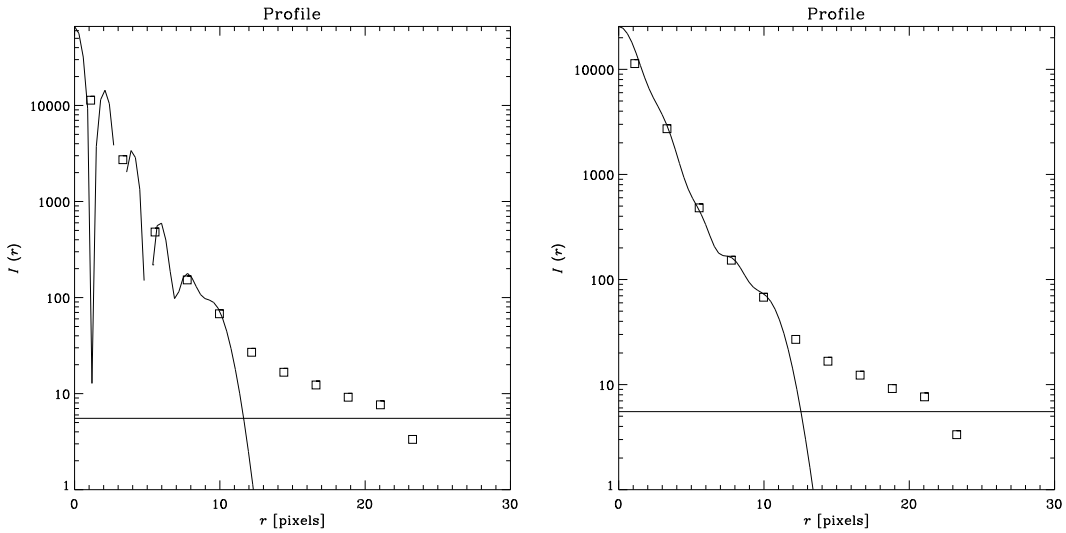


Figure 4.5: Comparison of the radial profiles (line) of a GEMS star model, one using a scale radius $\beta$ assigned by the $\chi^2$ amoeba of Massey & Refregier (2005) (left panel) and one using a fixed $\beta$ of 1.8 (right panel). The square points represent the radial surface brightness measured in angular bins from the image pixels, and the horizontal line shows the level of the root mean squared background noise.

Massey & Refregier (2005) the shapelet software employs an amoeba algorithm to jointly optimise the selection of $\beta$, $n_{max}$ and the centroid on an image-by-image basis. However, in order to fully characterize the PSF across the chip this freedom is not permitted: linear interpolation between shapelet coefficients from models of adjacent stars is only possible if these models share the same $\beta$ (see Refregier 2003; Massey & Refregier 2005).

The choice of a fixed $\beta$ for all stellar models is therefore a considerable freedom in the modelling process, and robust optimization of this choice will require further work to formulate. In this analysis, the choice of $\beta$ was initially taken from the mean value of $\beta \simeq 1.2$ found by allowing the shapelet algorithm to fit it as a free parameter, for fixed $n_{\max}$, using the shapelet amoeba to explore the $\chi^2$ surface of the model fit (Massey & Refregier 2005; Bergé 2006). Importantly, however, it was found that many of the models constructed with a fixed $\beta$ found in this manner were not necessarily providing a smoothly varying model of the PSF; matching the sharply varying observed profiles frequently required rapid 'ringing' of the model on sub-pixel scales. This was a particular problem in cases where even an $n_{\max} = 20$ model was insufficient to represent the brighter stellar images, due to the high significance of bright pixel values and the steeply-varying profile of the ACS PSF.

It was decided instead that the global value of $\beta = 1.8$ be chosen, after inspection of image residual maps, and graphs comparing the radial light profiles of PSF models and corresponding real stars. In this way an acceptable, but subjective, balance was struck between minimizing $\chi^2$ and capturing well the inner regions of the PSF, whilst ensuring it varied smoothly and without becoming negative in flux. A comparison of the radial profiles of a GEMS star modelled with a fixed $\beta$ of 1.8 and a freely varying $\beta$ can be seen in Figure 4.5.

Needless to say, this does not represent a fully rigorous and repeatable procedure for the optimal selection of the PSF $\beta$, a selection made particularly difficult in this case by the extreme non-gaussianity of the ACS

PSF. One solution may lie in a change in choice of basis set for PSF modelling to something more suitable, despite the relative efficiency of shapelets for modelling galaxies. It is not necessary for the PSF model and galaxy models to share the same basis set; however, the convolution operation will become more complex and will likely cease to be analytic.

Despite these reservations, the shapelet modelling of stars to $n_{\max} = 20$ in this analysis represents a significantly more detailed description of the PSF when compared to KSB-style methods. The 909 stellar models (10 catastrophic failures were suffered) were then normalised to unit flux, and ready for use in characterizing the behaviour of the GEMS PSF as a whole.

### Variation of the PSF model across the ACS field of view

Having arrived at a model of the point source response at the position of each chosen star in the GEMS images, it remains to use these models to estimate the PSF at *any* given point.

The variation of the PSF across the field of view was estimated separately for each of the two ACS CCD chips in each of the three GEMS epochs (described in Section 4.1.2). A two-dimensional, second-order polynomial was then fit to each of the 231 shapelet coefficients $f_{n_1,n_2}$. The fit to each $f_{n_1,n_2}$ was simple linear least-squares, implemented using Singular Value Decomposition (SVD: see, e.g., Press et al. 1992), incorporating the modelling uncertainties on each shapelet coefficient as output by the Massey & Refregier (2005) software. The shapelet software can be made to output a full covariance matrix $C_{n_1,n_2}$ and so it is possible to use this information to fit all 231 coefficients simultaneously; in this analysis, however, we make the simplifying assumption that these covariances are small and may be neglected. The fit was therefore made to each coefficient independently, i.e. not taking into account the small covariances present between shapelet coefficients due to pixelization (Massey & Refregier 2005); examaination of the covariance matrices showed these non-diagonal matrix elements to be negligibly small for the bright stellar objects being considered.

A second-order polynomial was chosen rather than a third- or higher order polynomial (which have been more successful in other studies, e.g. Van Waerbeke et al. 2005b) due to concerns over over-fitting of the stellar shape information; even using a second-order polynomial it is necessary to fit $6 \times 231$ parameter values to each star. SVD was used, in combination with the shapelet coefficient error estimates, so as to as suppress this risk of over-fitting for those shapelet coefficients where insufficent information was available to merit such a fit. Third-order polynomials were tried (requiring only a minor modification to the method) but examination of shear and flexion maps for the stellar model did not provide any evidence that they significantly altered the description of the PSF. In light of the expressed concerns regarding over-fitting it was decided to instead minimize this risk and to use a second-order polynomial to model the variation of shapelet coefficient values acros the chip.

Estimates of $\gamma_*$, $\mathcal{F}_*$ and $\mathcal{G}_*$ for the stellar models were then made (as described for galaxies in Section 4.2.5), and stars for which these lay further than 3-$\sigma$ from the model were iteratively removed and the remaining data refit a further two times. Having then made an estimate of the variation of each $f_{n_1,n_2}$ across the field of view, it is possible to construct a model of the estimated PSF at the exact location of each galaxy in the GEMS field. These modelled PSFs are then input at the shapelet decomposition stage, in the form of a shapelets catalogue with a PSF model at the position of each galaxy, and the recovered

shapelet galaxy model is then a good approximation to the galaxy as it would appear in the absence of PSF smearing (Massey & Refregier 2005).

### 4.2.4 Shapelets deconvolution

As shown in Figure 4.3, the shapelet software package uses the IDL wrapper routine `shex.pro` to create output shapelet catalogues of deconvolved galaxy images, referred to as "shapecats". The routine takes as its inputs the shapelets-ready catalogues constructed as described in Section 4.1.2, the GEMS images themselves, and shapelets catalogues containing the estimated PSF at each galaxy location, modelled as described in Section 4.2.3. There is additional freedom in the selection of values for optional input parameters to the shapelets routines, and I now outline our choices of these parameters where they differ from the default values, and describe the reasons for these choices.

The shapelet deconvolution was carried out using the Cartesian shapelet basis set; this is done because the Cartesian basis functions are separable in $x$ and $y$, and, crucially, may be analytically integrated within rectangular pixels. This ensures that the integration of flux into each CCD pixel is accurately described during the direct modelling stage, and is the method used by the publicly available shapelet software. If necessary for the construction of lensing estimators, it is easy to transform between Cartesian shapelet coefficients $f_{n_1,n_2}$ and their polar counterparts $f_{n,m}$ using the following relationship (given in Massey & Refregier 2005):

$$\begin{aligned} f_{n,m} &= \mathrm{i}^m 2^{-\frac{n}{2}} \left\{ \frac{n_1! n_2!}{[(n+m)/2]!\,[(n-m)/2]!} \right\}^{\frac{1}{2}} \delta_n^{n_1+n_2} \\ &\times \sum_{n'_r=0}^{n_r} \sum_{n'_l=0}^{n_l} \mathrm{i}^{m'} \left( \begin{array}{c} \left(\frac{n+m}{2}\right) \\ n'_r \end{array} \right) \left( \begin{array}{c} \left(\frac{n-m}{2}\right) \\ n'_l \end{array} \right) \delta_{n_1}^{n'_r+n'_l} f_{n_1,n_2}, \end{aligned} \tag{4.1}$$

where the reader is referred to the definitions of $n_r$ and $n_l$ in terms of $n$ and $m$ given in Section 3.2.1. Equation (4.1) describes a one-to-one mapping for polar and Cartesian shapelet models that holds when these models are truncated to the same $n_{\max}$, i.e. $n_1+n_2 \leq n_{\max}$ and $n \leq n_{\max}$. This calculation may be quickly performed by a routine available as part of the shapelet software, `shapelets_polar_convert.pro`, which performs the transformation of Equation (4.1) extremely quickly upon both single galaxy models and entire shapelet catalogues.

The GEMS galaxies were modelled only up to a maximum shapelet order $n_{\max} = 16$. This value was chosen due to the disproportionately long time taken to model a small subset of large/bright galaxies in the GEMS dataset; the time taken to model a galaxy increases roughly as $n_{\max}^4$ (Massey & Refregier 2005; Massey et al. 2007d). Given that the largest and brightest galaxies are also most likely to be the closest, it was decided that the importance of perfect modelling of such objects was of secondary importance in a weak lensing analysis. For the galaxy-galaxy lensing analysis described in Chapter 6 it was found that the vast majority of the $\simeq 3000$ galaxy models for which $n_{\max} \leq 16$ represented a significant truncation lay within the foreground lens sample. Similarly, the GEMS galaxies were all modelled to a minimum $n_{\min}$ of 2. This was found to cause overfitting, defined as having a model reduced $\chi^2 < 1$, in only a small minority of cases ($< 200$).

The other input parameter differing significantly from the default value was the choice of $\theta_{\mathrm{min,Geom}}$, defined by (Refregier 2003) as

$$\theta_{\mathrm{min,Geom}} = \beta\sqrt{n_{\mathrm{max}}+1}. \tag{4.2}$$

In this analysis, we enforce the condition $\theta_{\mathrm{min,Geom}} \geq 1$ pixel at the shapelet modelling stage: models for which this condition is not met are remodelled using another choice of $\beta$ and $n_{\mathrm{max}}$. This value was chosen over the smaller, default value of 0.2 pixels in an attempt to reduce the overfitting of correlated noise in the GEMS images, which comes about as a result of the drizzling of the GEMS images using the MULTIDRIZZLE software of Koekemoer et al. (2002) (see also Caldwell et al. 2005). This effect is also discussed in Section 5.4.3, and is of relevance as the shapelet software assumes that noise in adjacent pixels is uncorrelated. In order to accurately treat images in which noise is correlated between adjacent pixels (such as the dithered GEMS images), the shapelet code is required to invert an extremely large pixel noise covariance matrix. The instability and processing time requirements of this process led to it being excluded from the shapelet software of Massey & Refregier (2005), allowing the far simpler inversion of a purely diagonal noise matrix. This currently represents a potential weakness in the shapelet method, as overfitting correlated noise will result in the circularization of output galaxy models, possibly biasing lensing results, and so we take precautions to limit this effect.

Given these input parameters, and with the modifications to the postage stamp extraction described in Section 4.2.2, the routine `shex.pro` was used to create a deconvolved output shapecat of all the galaxy objects in each GEMS image tile. As was discussed in Chapter 3, a number of possible estimators may be used to extract reliable lensing measurements from this significant reservoir of galaxy shape information; the choice of these estimators for the GEMS dataset will now be discussed.

### 4.2.5 Shear and flexion estimation

Given a shapelet derived approximation of each galaxy image prior to PSF distortion, all that remains is to extract accurate and unbiased lensing estimators using the values of the model coefficients $f_{n_1,n_2}$. As described in Chapter 3 (see also Goldberg & Bacon 2005; Goldberg & Leonard 2007; Massey et al. 2007d) there a number of such estimators that might be used. We are free to use any of these methods, aided by the extreme simplicity of transforming between Cartesian and polar shapelet spaces; as described in the previous Section this may simply and quickly done using the function `shapelets_polar_convert.pro` that comes as part of the shapelet software, and which implements the matrix transformation described by Equation (4.1).

For the analysis of the GEMS galaxy images, we employ the $\tilde{\gamma}^{\mathrm{unweighted}}$ shear estimator of Equation (3.100), and the shapelet flexion estimators that work by minimizing the goodness-of-fit statistic $\chi^2$ in Equation (3.91), proposed by Goldberg & Bacon (2005). Use of these estimators requires that galaxies are modelled to $n_{\mathrm{max}} \geq 2$ for shear and $n_{\mathrm{max}} \geq 3$ for flexion, as described in Chapter 3. These choices are motivated by the results of Chapter 5, which tests a variety of shapelet lensing estimators using a realistic simulation of ACS survey imaging data. Although we use the results of this later analysis here, and are thus somewhat guilty of breaking the natural flow of the Thesis, lensing shape measurement is a complex procedure and it has been instructive in the first instance to give a thorough description of the full data reduction methodology that is used in both the real and simulation data analyses.

The results of Chapter 5 also give correcting bias factors necessary for the accurate recovery of shear and

flexion data (see Tables 5.1 and 5.2). Using these bias factors, and the estimator labelling defined in Section 5.1, I define the measured shear and flexion in GEMS as

$$\gamma^{\rm obs} = \frac{\tilde{\gamma}^{\rm unweighted}}{0.82}, \quad \mathcal{F}^{\rm obs} = \frac{\tilde{\mathcal{F}}^{\rm DG}}{1.04}, \quad \mathcal{G}^{\rm obs} = \frac{\tilde{\mathcal{G}}^{\rm DG}}{2.15}. \tag{4.3}$$

In order to calibrate the $\tilde{\gamma}^{\rm unweighted}$ estimator, we measure a shear responsivity factor of

$$\mathcal{R} = 1 - \frac{\langle \varepsilon^2 \rangle}{2} = 0.783, \tag{4.4}$$

which then gives

$$\tilde{\gamma}^{\rm unweighted} = \frac{\varepsilon}{2\mathcal{R}} \tag{4.5}$$

see Equation (3.100). It is noted that this is a different result to that found for the simulated galaxy images of Chapter 5, for which $\mathcal{R} = 0.886$. This is due to a broader distribution of measured ellipticities in the GEMS galaxies as compared to those of the simulated galaxy population. As described in Massey et al. (2007d), galaxies of greater intrinsic ellipticity respond more weakly to applied shear, and the factor $\mathcal{R}$ calibrates for this effect. While differing values between the two analyses point to the simulated galaxy population displaying less ellipticity variance when compared to the GEMS sample, it is right to include the correct calibration based on the properties of the GEMS galaxies being measured. Shear results will be robust despite this difference.

Finally, I remove catastrophic shapelet modelling failures ($\simeq 4\%$) and outlying measurements with $|\gamma^{\rm obs}| < 1$, $|\mathcal{F}^{\rm obs}| < 1$ arcsec$^{-1}$ and $|\mathcal{G}^{\rm obs}| < 2$ arcsec$^{-1}$. I also remove modelled galaxies with $\beta < 2$, so as to ensure accurate deconvolution for all catalogue objects (see Section 5.4; Massey & Refregier 2005). This fully describes the GEMS shear and flexion catalogues, which contain $46\,145$, $26\,999$ and $22\,490$ galaxies for $\gamma^{\rm obs}$, $\mathcal{F}^{\rm obs}$ and $\mathcal{G}^{\rm obs}$ respectively. The fact that the flexion catalogues are significantly smaller than the shear catalogue is largely a consequence of the requirement for galaxies to be modelled to $n_{\rm max} \geq 3$ in order for flexion estimation using the scheme presented by Goldberg & Bacon (2005). I now go on to examine some of the properties of these shear and flexion catalogues, checking for consistency with previous results and quantifying evidence for the successful removal of systematics.

## 4.3 Results

### 4.3.1 Comparison with previous shear studies of the GEMS field

A first indication of the success of the GEMS shapelet pipeline is the comparison of shear results obtained with those of two previous studies of the same field: H05 and Schrabback et al. (2007). Both these analyses used a KSB-style analysis (see, e.g., Kaiser et al. 1995; Hoekstra et al. 1998) to measure the shear and correct for PSF effects, and so it is interesting to see whether results match those of the fundamentally different shapelet analysis presented in Section 4.2.

I compare my $\gamma^{\rm obs}$ with the H05 shear catalogue, provided by Catherine Heymans. I first match the H05 catalogue to my "grand" catalogue of all objects in GEMS, finding a 100% match; this is because

both analyse use exactly the same SExtractor catalogue as starting point. Shear measurements are compared in Figure 4.6.

So as to produce a reliable fit between these coefficients, I make an approximate estimate of the measurement errors on each galaxy shear as follows. Following the results presented in Figure 4.7, I split both shear catalogues into two subsamples. One subsample is bright galaxies having $m_{606} < 23.5$ ($\simeq 3000$ galaxies in each case) and the other faint subsample contains the remaining galaxies with $m_{606} > 23.5$ ($\simeq 42000$). I then assume that measurement errors are negligible for the bright subsample, and estimate the measurement variance for the shear on a typical galaxy as the ensemble value of

$$\sigma^2_{\rm meas} = \sigma^2(m_{606} > 23.5) - \sigma^2(m_{606} < 23.5) \tag{4.6}$$

for each catalogue. This expression assumes that a typical galaxy is measured as poorly as a galaxy in the fainter subsample, which should be a reasonable estimate given to the far greater number of faint galaxies.

Using these simple assumptions I find $\sigma^{\rm obs}_{\rm meas} = 0.19$ and $\sigma^{\rm H05}_{\rm meas} = 0.17$. This is an interesting result in itself, suggesting that shapelet measurements are noisier than the H05 KSB-style analyses. Taking these measurement errors, a line of $\gamma_i^{\rm obs} = a_i \gamma_i^{\rm H05} + b_i$ was fit to the relationship between shear estimates (calculated by David Bacon). Best-fitting slope parameters were

$$a_1 = 0.963 \pm 0.006, \qquad a_2 = 0.977 \pm 0.012, \tag{4.7}$$

suggesting an overall calibrative bias of $(96.7 \pm 0.08)\%$. Best-fitting $y$-offset parameters were found to be

$$b_1 = 0.0012 \pm 0.0046, \qquad b_2 = 0.0012 \pm 0.0045, \tag{4.8}$$

suggesting no significant difference in the residual shear between this analysis and H05. Evidence for such an offset could indicate a poor treatment of PSF effects in one (or possibly both) set of measurements (see Section 4.3.3).

The level of agreement between H05 and the results of my shapelet pipeline is encouraging, and lies within the sample variance achievable for cosmological measurements from a survey the size of GEMS. Schrabback et al. (2007) also found a slight deficit of $\simeq 3.3\%$ in comparison of their shear measurements to H05, and so agreement with these authors is even stronger. Properly calibrated (as is also required by most KSB methods), a first shapelet shear analysis of real data has been made to agree with two independent sets of measurements for the same field.

In Section 4.3.3, I describe a further test for residual systematics that can be made from my own data and results. However, before making statistical estimates of these systematics it is necessary to investigate the nature of the signal that is being measured, particularly for $\mathcal{F}^{\rm obs}$ and $\mathcal{G}^{\rm obs}$, the distributions of which pose extra problems to weak lensing analyses.

### 4.3.2 Distributions of lensing measurements

Figures 4.7, 4.8 and 4.9 (left panels) show the distributions of measured shear and flexion for all the shapelet deconvolved galaxies in the GEMS survey. The most striking feature of these results is the extreme non-Gaussianity of the distributions of measured $\mathcal{F}^{\rm obs}$ and $\mathcal{G}^{\rm obs}$; the large wings of each distribution pose a

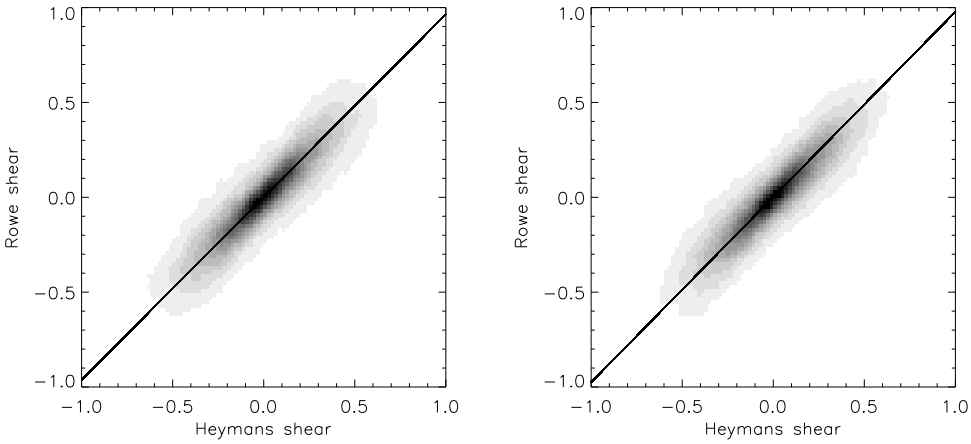


Figure 4.6: Comparison of $\gamma^{\rm obs}$ to shear measurements of the same field from Heymans et al. (2005). The plots show the density of $\gamma_1^{\rm obs}$ versus $\gamma_1^{\rm H05}$ points (left panel) and $\gamma_2^{\rm obs}$ versus $\gamma_2^{\rm H05}$ points (right panel). The solid line represents the best fit to the data once measurement errors are estimated, showing a calibration bias of $(96.7 \pm 0.8)\%$ overall. Figure provided by David Bacon.

significant problem in the extraction of statistical information. This is due to the instability of the arithmetic mean for distributions with a poorly-defined variance. In the Chapters that follow, a number of techniques for coping with this property of shapelet-measured $\mathcal{F}^{\rm obs}$ and $\mathcal{G}^{\rm obs}$ will be discussed.

In the following Section, 4.3.3, I outline one approach for dealing with the large number of outliers in flexion statistics: the use of the statistical sample median rather than the sample mean as a measure of central tendency. Another approach is to apply strict clipping to the measurements, imposing cuts of $|\mathcal{F}^{\rm obs}| < \mathcal{F}_{\rm max}$ and $|\mathcal{G}^{\rm obs}| < \mathcal{G}_{\rm max}$ to remove outlying objects from the lensing catalogues, and then simply using the sample mean. This is an attractive proposal, but will cause biasing of the measured sample mean towards zero. An initial investigation has shown that the error on the measured sample mean can be improved significantly by cuts as severe as $\mathcal{F}_{\rm max} = 0.1$ and $\mathcal{G}_{\rm max} = 0.2$. However, the biasing effect of such clipping needs to be carefully simulated, as it will depend closely upon the underlying signals $\mathcal{F}$ and $\mathcal{G}$. The improvement of flexion measurement using optimised outlier clipping, and the simulation of look-up tables for an accurate estimate of the clipping biasing factor, presents an interesting alternative to median statistics and an important avenue of further work.

Another interesting aspect of the problem of flexion measurement scatter is the degree to which it depends upon the quantity of image information available for each galaxy. The right-hand panels of Figures 4.7, 4.8 and 4.9 show the distributions of $\gamma^{\rm obs}$, $\mathcal{F}^{\rm obs}$ and $\mathcal{G}^{\rm obs}$ for a subset of the GEMS galaxies with magnitudes $m_{606} < 23.5$, as measured using SExtractor (this represents a sample size of $\simeq 6000$ from the total sample of $\simeq 50000$ GEMS galaxies). For shear, this restriction leads to a mild narrowing of the distribution of $\gamma^{\rm obs}$ estimates. However, the $\mathcal{F}^{\rm obs}$ and $\mathcal{G}^{\rm obs}$ distributions of Figures 4.8 and 4.9 are seen to narrow significantly with the restriction to a lower magnitude sub-sample.

In each case, the reduction in the FWHM of the $\mathcal{F}^{\rm obs}$ and $\mathcal{G}^{\rm obs}$ histograms is by a factor of approximately 3, with a significant further reduction in the number of extreme outliers. Interestingly, and perhaps frustratingly, for the purpose of statistical analyses the three-fold reduction in the width of scatter is roughly balanced by the nine-fold decrease in the sample size. It will be important in the future to examine, in greater

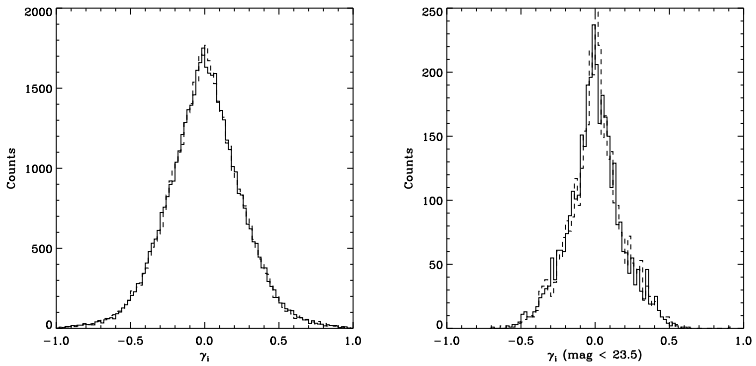


Figure 4.7: Histograms of measured $\gamma^{\rm obs}$ from the PSF deconvolved GEMS galaxy images; the real and imaginary components are represented by dashed and solid lines respectively. The left panel shows the histogram for the entire survey, the right for a subset with SExtractor-measured magnitude $m_{606} < 23.5$.

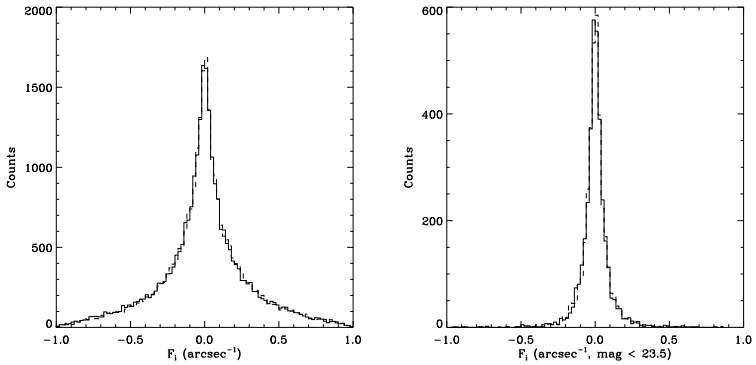


Figure 4.8: Histograms of measured $\mathcal{F}^{\rm obs}$ from the PSF deconvolved GEMS galaxy images, plotted as described for shear in for Figure 4.7.

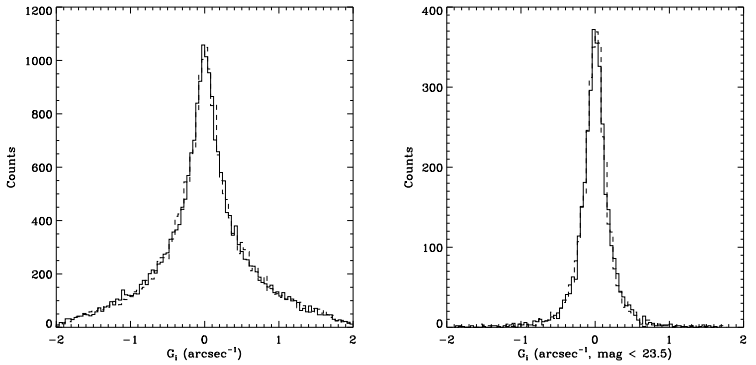


Figure 4.9: Histograms of measured $\mathcal{G}^{\rm obs}$ from the PSF deconvolved GEMS galaxy images, plotted as described for shear in Figure 4.7.

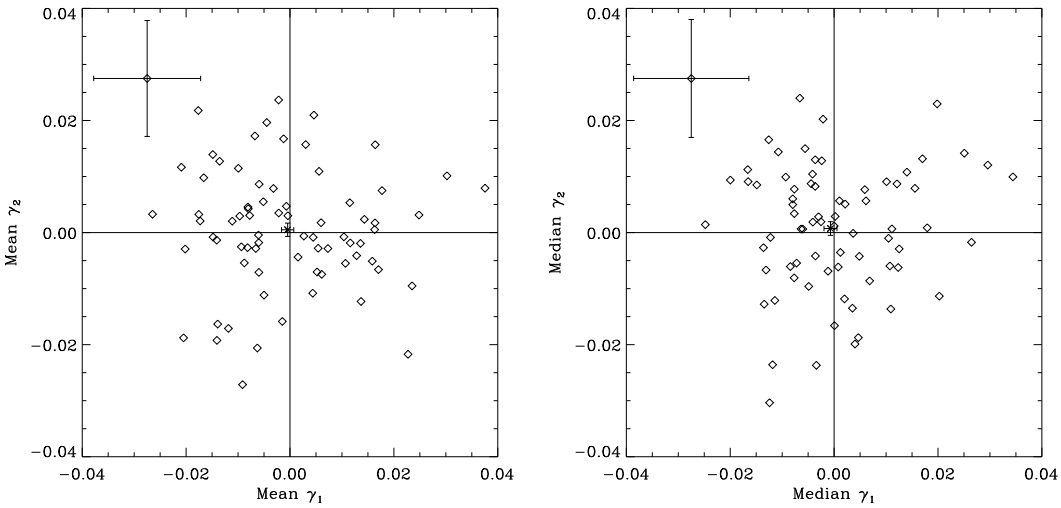


Figure 4.10: Mean (left) and median (right) deconvolved galaxy $\gamma^{\rm obs}$ in the GEMS survey images. The open diamonds represent the signal for each tile, with the large error bars plotted in the top left-hand corner representing the average error on each of these measurements. The cross with the smaller error bars represents the global residual signal, consistent with zero in both cases.

detail, the relationship between the scatter in flexion measurements and galaxy image SNR. Through such an analysis we should hope to discover an optimal depth or SNR criteria for the selection of galaxies for shapelet flexion analysis.

Despite the non-Gaussianity of the flexion distribution, it is still possible to construct estimates of the lensing signal using the sample median, which can then be used to check for systematic errors in the flexion catalogues. An important test of the reliability of the shapelet correction for PSF-induced lensing systematics is to consider the residual signal in $\gamma^{\rm obs}$, $\mathcal{F}^{\rm obs}$ and $\mathcal{G}^{\rm obs}$ for the GEMS image tiles and survey as a whole. Such evidence for the success of the shapelet lensing analysis is considered below, in Section 4.3.3.

### 4.3.3 Tests for residual PSF anisotropy systematics

We expect that, given a complete and successful treatment of lensing systematics due to the anisotropy of the PSF, the total average (whether mean or median) of the $\gamma$, $\mathcal{F}$ and $\mathcal{G}$ signals in the GEMS images will be consistent with zero. It should be noted that in this analysis we need to consider the *unrotated* values of the observed lensing measures, leaving them in the coordinate system defined by the $x$ and $y$ axes of the ACS chip. For the final lensing analysis all measurements are rotated into right ascension and declination coordinates, but the residual signal in these results would inaccurately reflect the success of the PSF correction scheme. In particular, the images in the GEMS dataset which come from the GOODS observations (see Rix et al. 2004; Figure 4.1) are aligned at a significant angle to the GEMS-observed images.

Figure 4.10 shows the mean (left panel) and median (right panel) unrotated $\gamma^{\rm obs}$ in the deconvolved GEMS

survey images, both on a tile-by-tile basis and for the survey overall. The global mean shear is given by

$$\langle \gamma_1 \rangle = -0.0004 \pm 0.0012 \quad (4.9)$$
$$\langle \gamma_2 \rangle = 0.0005 \pm 0.0012, \quad (4.10)$$

and the global median shear by

$$(\gamma_1)_{\rm m} = -0.0007 \pm 0.0012 \quad (4.11)$$
$$(\gamma_2)_{\rm m} = 0.0007 \pm 0.0012. \quad (4.12)$$

Both these measures give zero-consistent results, giving a significant indication of success in the shapelet treatment of PSF anisotropy systematics for $\gamma^{\rm obs}$ in GEMS.

It will be instructive to consider these results somewhat further. Firstly, for weak shears and flexions we may assume that both the mean and median will tend towards the underlying gravitational signal, and so each method provides us with a valid estimator in the weak regime. The errors on the sample median $\gamma_{\rm m}$ are estimated using the result that for large $N$ samples

$$\sigma_{\gamma_{\rm m}} = \frac{1}{\sqrt{4Np^2(\gamma_{\rm m})}}, \quad (4.13)$$

(see, e.g., Lupton 1993), where $N$ is the sample size and $p(\gamma_{\rm m})$ is the estimated value of the probability density distribution at the sample median. For a normally distributed population, the statistical efficiency of the median (defined as the variance ratio of the sample mean to sample median) tends to $2/\pi \simeq 0.7$ for large $N$, but as can be seen from Equations (4.9)-(4.12) the efficiency of the median for shear is in approximately equal to unity. This highlights the weak non-Gaussianity of the distribution of measured $\gamma^{\rm obs}$. As a measure of central tendency, the sample mean relies implicitly on the Central Limit Theorem and so its efficiency suffers increasingly as errors become more non-Gaussian.

For the cases of $\mathcal{F}^{\rm obs}$ and $\mathcal{G}^{\rm obs}$ the efficiency of the median lies in the range $\simeq$ 5-6, due to the extremely non-Gaussian wings of the flexion distribution. For the analysis of the residual flexion signal, shown in Figure 4.11, we therefore plot only median statistics. The global median of the unrotated $\mathcal{F}^{\rm obs}$ signal is found to be

$$(\mathcal{F}_1)_{\rm m} = -0.0009 \pm 0.0009 \quad (4.14)$$
$$(\mathcal{F}_2)_{\rm m} = 0.0015 \pm 0.0010, \quad (4.15)$$

which is marginally inconsistent with a complete removal of $\mathcal{F}^{\rm obs}$ residuals. The global median of the unrotated $\mathcal{G}^{\rm obs}$ is found to be

$$(\mathcal{G}_1)_{\rm m} = 0.0024 \pm 0.0026 \quad (4.16)$$
$$(\mathcal{G}_2)_{\rm m} = 0.0074 \pm 0.0027. \quad (4.17)$$

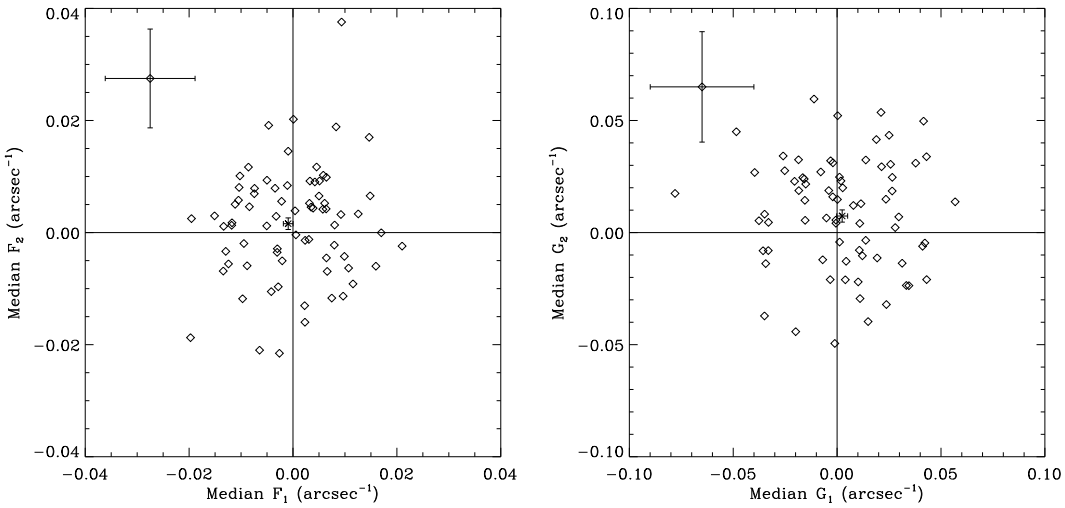


Figure 4.11: Median deconvolved galaxy $\mathcal{F}^{\rm obs}$ (left) and $\mathcal{G}^{\rm obs}$ (right) in the GEMS survey images. The open diamonds represent the signal for each tile, with the large error bars plotted in the top left-hand corner representing the average error on each of these measurements. The cross with the smaller error bars represents the global residual signal; this is mildly inconsistent with zero for $\mathcal{F}^{\rm obs}$, but more significantly so for $\mathcal{G}^{\rm obs}$.

This is significant evidence that the PSF deconvolution method described in Sections 4.2.3 and 4.2.4 has been unsuccessful for the case of $\mathcal{G}^{\rm obs}$.

These results are less conclusively successful than those for the shear estimators, particularly for $\mathcal{G}_2^{\rm obs}$ where we are detecting a clear residual signal. Understanding the reasons for this difference is problematic, particularly given the noise on the flexion measurements. Issues that would also affect shear estimates, such as problems with charge transfer efficiency can be largely ruled out given the success of the shear results and other studies of the GEMS field (H05; Schrabback et al. 2007).

An alternative explanation is simply that the higher order modes of the GEMS PSF were insufficiently well modelled to be able to completely correct for the effects of PSF flexion anisotropy, despite shapelet modelling to $n_{\rm max} = 20$. It is known in particular that the ACS PSF contains a a significant degree of flexion-like anisotropy, particularly in the outer regions of the light distribution. In work completed for the Active Galactic Nuclei hosts analysis of Jahnke et al. (2004), a composite, high SNR image of the GEMS PSF in the F606 band was created (Figure 4.12), and made publicly available[1]. This image is scaled so as to reveal the outer structure of the light profile, and reveals evidence of a $\mathcal{G}_2$-like anisotropy that may be responsible for the detected residual.

As was discussed in Section 4.2.3, and as can be seen in Figure 4.5, the shapelet basis set struggles to describe the ACS PSF profile well over a broad range of scales. In order to completely describe the anisotropic outer wings of Figure 4.12 the shapelet model truncation order needs to be increased substantially beyond $n_{\rm max} = 20$. The shapelet deconvolution then becomes slower, and will require large memory resources to avoid segmentation faults: both the storage requirements and processing time increase roughly as $n^4$. In this analysis, using ten desktop machines (2GHz, 1-2GB RAM) the shapelet deconvolution took approxi-

[1] `http://www.aip.de/%7Ejahnke/research/gems/psf_M15.html`

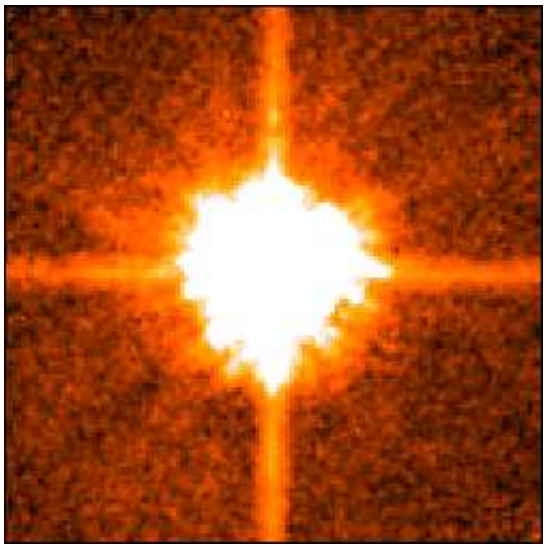

Figure 4.12: Composite image of the average F606W PSF in the GEMS data, scaled so as to reveal the outer wings of the light profile. Figure generated for the AGN analysis of Jahnke et al. (2004) and made available on the world-wide web.

mately 9 days to complete (PSF modelled to $n_{\rm max} = 20$), so there is some room to explore whether more detailed modelling of the PSF can alleviate the presence of residuals.

Nevertheless, in the case of shear and (marginally) the first flexion, we appear to have reasonable control of the systematics due to the anisotropic GEMS PSF. Moreover, the primary cosmological measurement attempted in this Thesis is the galaxy-galaxy shear and flexion signal in GEMS, which will not be adversely affected by any small systematic anisotropy in $\gamma^{\rm obs}$, $\mathcal{F}^{\rm obs}$ or $\mathcal{G}^{\rm obs}$ due to the rotational averaging of such residuals (Brainerd et al. 1996; Schneider & Rix 1997). Induced anisotropy is not the only effect of the PSF, however, which also blurs and circularizes galaxy images causing a weakening bias in the magnitude of extracted lensing measurements. The success of schemes for correcting this effect can only be accurately quantified via the analysis of simulated lensing data, to which we now turn in the following Chapter.

# CHAPTER 5

# SHAPELET LENSING ANALYSIS OF SIMULATED DATA

Optical distortions due to the anisotropic point source response of imaging telescopes can be broadly described as having two effects upon lensing measurements. The first is to induce a residual anisotropy in galaxy images, which may mimic a lensing signal and must be corrected; the level of residual contamination in the GEMS galaxy images is discussed in Chapter 4. The second effect is the circularization of galaxies due to image blurring, causing a reduction in the measured shear or flexion that must be accounted for.

This Chapter quantifies the success of this second correction for the GEMS shapelet pipeline as described in Chapter 4, and the success of the treatment for other issues in lensing measurement such as the effects of image noise. Using simulated, GEMS-like galaxy survey images of known input shear and flexion, pre-convolved with a realistic ACS point spread function and given pixel noise, I test the success of signal retrieval for a variety of shapelet estimators.

## 5.1 The FLexion Implementation Program (FLIP)

In order to more accurately test the success of lensing information recovery in the GEMS shapelet pipeline, I undertook the analysis of a set of simulated images provided by Richard Massey, using the same procedures used for the Shear TEsting Program (STEP) analyses (STEP1: Heymans et al. 2006b; STEP2: Massey et al. 2007b; STEP3: Rhodes et al., in prep.). These images (which will be described more fully in Section 5.2) were designed to closely resemble the GEMS data, including sky background noise and the distorting effect of a point spread function based on that of the *Hubble Space Telescope* ACS.

### 5.1.1 Input lensing signals

Most importantly, the galaxies in each image were subjected to a known input shear, first flexion and second flexion before the degradation of the images. By comparing the recovered lensing measurements with the known inputs, we can calibrate and test a selection of shapelet lensing estimators. The basic strategy is to take 100 GEMS-like simulated galaxy tiles and apply the same gravitational $\gamma$, $\mathcal{F}$ and $\mathcal{G}$ to all the galaxies in each tile, but to vary the chosen signals between tiles. We name this analysis the FLexion Implementation Program (FLIP).

There is significant freedom in the choice of the input gravitational distortions, leading to a large parameter space. Issues such as the covariance and covariant biases between measurements of flexion and shear (Schneider & Er 2007), which are likely to be a function of the relative strengths and relative orientations of the gravitational signals, will require very large simulated datasets in order to be accurately explored. In this work, I confine myself to measurements of gravitational shear and flexion in the configuration of relative orientations depicted in Figure 5.1. This mimics the combined effect due to a single circularly-symmetric mass distribution, and so approximates what we might expect for measurements of galaxy-galaxy lensing. This is particularly true for the GEMS field, which is known not to contain any large mass distribution such as a cluster (H05; Schrabback et al. 2007).

Despite fixing the orientations of shear, first flexion and second flexion relative to one another, the relative *magnitudes* of the input signals are allowed to vary between tiles, reflecting the realistic halo models described in Chapter 2. The overall orientation of the shear-flexion signal is also allowed to vary, so as not to bias results by aligning the signal along potentially preferential directions to the pixel axes.

Input shear signal strengths were chosen to lie in the range defined by $|\gamma| < 0.08$, and flexion signal strengths to lie in the range defined by $|\mathcal{F}| < 0.012$ arcsec$^{-1}$ and $|\mathcal{G}| < 0.036$ arcsec$^{-1}$, again motivated by the results of Chapter 2. Richard Massey then applied these signals to shapelet models of galaxy images made using the galaxy image simulation software of Massey et al. (2004) (see Section 5.2), using the shapelet shear and flexion transformations described in Chapter 3 and in Massey et al. (2007d). After adding noise and the effects of an anisotropic ACS-like PSF, the images were ready to be analysed using the GEMS shapelet pipeline.

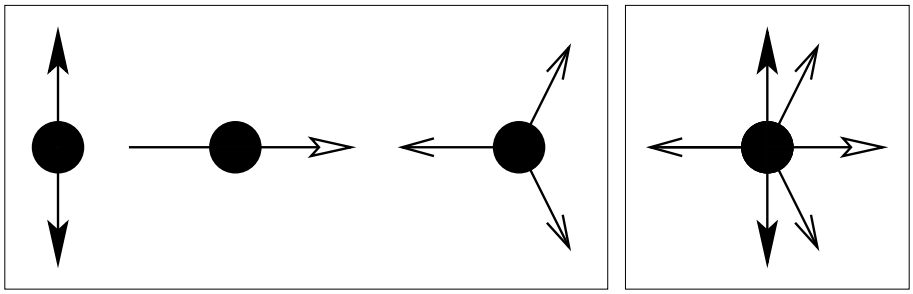

Figure 5.1: Schematic showing the relative orientations of induced gravitational $\gamma$ (solid arrows), $\mathcal{F}$ (clear arrows) and $\mathcal{G}$ (open arrows) in the FLIP images. These relative orientations were chosen as they mimic the combined effect due to a single circularly-symmetric mass distribution, which in this case would lie off the page towards the right; the panel on the right shows this combined effect on a single galaxy. It should be noted that in the FLIP images the relative strengths of each signal vary between tiles, as does the *overall* orientation of the combined configuration.

### 5.1.2 Lensing estimators

As was discussed in Chapter 3, the range of lensing estimators that may be constructed using shapelets is only limited by the number of shapelet modes available ($n_{\max}$). However, in practical cases this information will be limited so as to extract lensing information from as many galaxy images as possible. Estimators which make extensive use of higher order information will prove problematic for many galaxy images, particular those which rely upon the convergence (in the sense of converging to a limit) of sums over shapelet coefficients (see Massey et al. (2007d)).

In order to test shapelet *shear* estimation we apply the following three schemes to the FLIP images:

- Shears measured using the Cartesian shapelet model of each galaxy and David Goldberg's routine `flexion.pro`, available to the public via the flexion web page[1]. This applies a $\chi^2$ minimization of the following expression:

$$\chi^{2(even)} = \left[\mu_{\boldsymbol{n}} + \gamma_i \hat{S}_i \tilde{f}^{\rm s}_{\boldsymbol{n}'} - f_{\boldsymbol{n}}\right] V^{-1}_{\boldsymbol{np}} \left[\mu_{\boldsymbol{p}} + \gamma_i \hat{S}_i \tilde{f}^{\rm s}_{\boldsymbol{p}'} - f_{\boldsymbol{p}}\right] \tag{5.1}$$

  where $\tilde{f}^{\rm s}_{\boldsymbol{n}'}$, $V_{\boldsymbol{np}}$ and $\mu_{\boldsymbol{n}}$, and the method overall, are fully described in Section 3.4.2, Equations (3.87)-(3.91) (see also Goldberg & Bacon 2005). We label these shear measurements $\tilde{\gamma}^{\rm DG}$.

- Shears measured using the polar shapelet model of each galaxy, and the shapelets unweighted ellipticity estimator, described in Section 3.4.3, Equation (3.100), which we reproduce here again for clarity:

$$\tilde{\gamma}^{\rm unweighted} = \frac{\varepsilon}{(2 - \langle\varepsilon^2\rangle)} = \frac{\sum_{n=0}^{\infty} \sqrt{n(n+2)}\, f_{n,2}}{(2 - \langle\varepsilon^2\rangle) \sum_{n=0}^{\infty} \sqrt{(n+1)}\, f_{n,0}}. \tag{5.2}$$

  This is the estimator that was introduced by Massey et al. (2007d).

- Shears measured using the Gaussian weighted estimator described in Section 3.4.3:

$$\tilde{\gamma}^{\rm Gaussian} = \sqrt{2} \frac{f_{2,2}}{\langle f_{0,0} - f_{4,0}\rangle}, \tag{5.3}$$

which was introduced in Massey et al. (2007d) and where, as discussed in Section 3.4.3, the angle brackets in the denominator denote an ensemble average across the entire sample of galaxy images.

These were identified as being the estimators most likely to give reliable and rapidly converging results for typical galaxy images where only limited information is available.

The following three *flexion* estimation schemes were chosen for testing using the FLIP simulations:

- Flexion measured using a Carteisan shapelet model of each galaxy and David Goldberg's routine `flexion.pro`, available at the flexion web page (see above). In a similar fashion to the case of shear, this measures flexion by minimizing the following $\chi^2$ statistic:

$$\chi^{2(odd)} = \left[\left(\mathcal{F}_i\hat{F}_i^T + \mathcal{G}_i\hat{G}_i^T\right)\tilde{f}^{\rm s}_{\boldsymbol{n}'} - f_{\boldsymbol{n}}\right] V^{-1}_{\boldsymbol{np}} \left[\left(\mathcal{F}_i\hat{F}_i^T + \mathcal{G}_i\hat{G}_i^T\right)\tilde{f}^{\rm s}_{\boldsymbol{p}'} - f_{\boldsymbol{p}}\right]. \tag{5.4}$$

  As for the shear estimator given in Equation (5.1), this estimator is fully described in Section 3.4.2, Equations (3.87)-(3.93) (see also Goldberg & Bacon 2005). We label these measurements $\tilde{\mathcal{F}}^{\rm DG}$ and $\tilde{\mathcal{G}}^{\rm DG}$.

- Flexion measured using Cartesian shapelets and `flexion.pro` again, minimizing Equation (5.4) above, but using an input Cartesian shapelet series further truncated to $n_{\rm max} \leq 7$ for all galaxies. This is done to test the assertion of Goldberg & Leonard (2007) that the shapelet series need be truncated for accurate flexion measurement. These measurements are labelled $\tilde{\mathcal{F}}^{\rm DGT}$ and $\tilde{\mathcal{G}}^{\rm DGT}$.

- Flexion measured using a polar shapelet model of each galaxy and the lowest order Gaussian estimators described in Section 3.4.3, Equations (3.103) and (3.104), which we reproduce here once more for continuity:

$$\tilde{\mathcal{F}}^{\rm Gaussian} = \frac{4}{3\beta}\frac{f_{1,1}}{\langle(1-(R^2/\beta^2))\,f_{0,0} + (R^2/\beta^2)f_{2,0} - f_{4,0}\rangle} \tag{5.5}$$

  for the first flexion and

$$\tilde{\mathcal{G}}^{\rm Gaussian} = \frac{4\sqrt{6}}{3\beta}\frac{f_{3,3}}{\langle f_{0,0} + f_{2,0} - f_{4,0} - f_{6,0}\rangle}, \tag{5.6}$$

  for the second flexion. As discussed in Section 3.4.3, the $R^2$ is measured from the lensed galaxy images and the angle brackets denote an average across all the images in the simulated survey sample. These estimators were first introduced in (Massey et al. 2007d).

We describe the results achieved with these shear and flexion estimators in Section 5.3, but first I discuss the galaxy images created for the FLIP analysis.

## 5.2 FLIP images

The FLIP images were created by Richard Massey via the same galaxy image simulation package as was used for STEP2 (Massey et al. 2007b), as described in Massey et al. (2004) and below. The images were

[1] http://www.physics.drexel.edu/ goldberg/flexion/

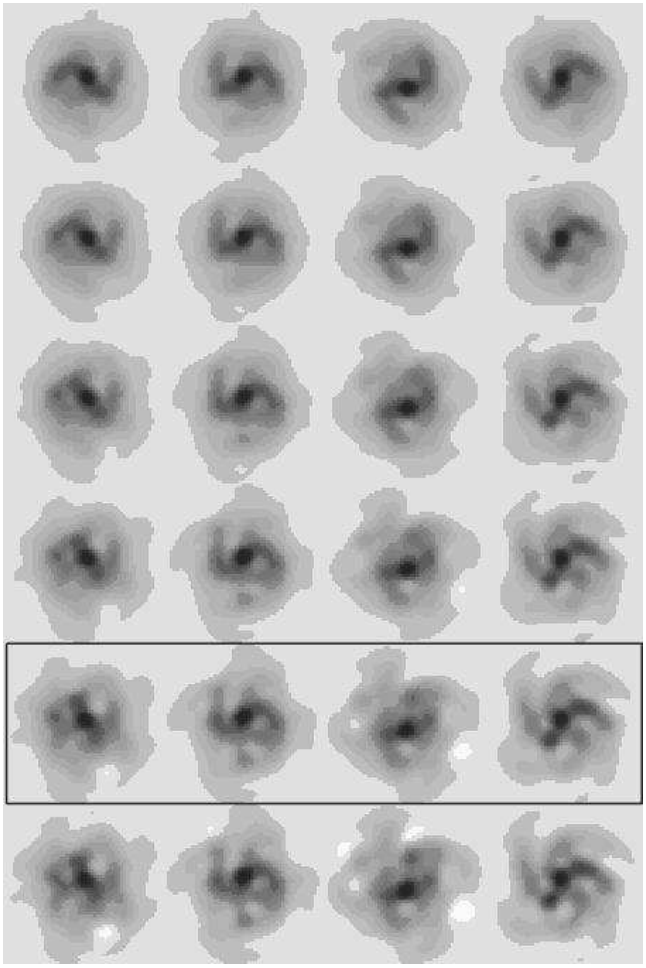

Figure 5.2: Illustration of the effect of perturbing galaxy morphologies in shapelet space, using the method of Massey et al. (2004) and taken from that article. The images in the top row show a shapelet model of a *Hubble* Deep Field galaxy, rotated by various angles. The successive rows below show the same galaxy but with its shapelet coefficients increasingly perturbed; the degree of perturbation $\lambda_{n_1,n_2}$ (see Equation 5.7) chosen by Massey et al. (2004) for realistic simulations of galaxy images is shown in the box. These represent typical shapelet simulated galaxies as used in the FLIP analysis.

created so as to realistically simulate the morphologies of space-based observations of galaxies, and use a realistic model of the ACS PSF to test the accuracy of shear measurement methods for space-based observations. A set of 100 $4096 \times 4096$ pixel images were created, with a pixel scale of 0.03 arcsec (so as to match the GEMS dithered science tiles), resulting in a total area of 419 arcmin$^2$.

### 5.2.1 Simulated galaxies

The galaxy images are based on the shapelet parameterization of galaxy images in the *Hubble* Deep Fields (HDF: Williams et al. 1996, 1998); a shapelet model of each galaxy in the HDF is first made. The simulated

galaxy fields are then populated with model galaxies based upon these modelled real galaxies, but having been given randomized rotations and inversion. Crucially, the shapelet model of each galaxy is then also randomized by a small amount: the coefficients $f_{n_1,n_2}$ of each HDF galaxy are given a small random offset by an amount $\delta_{n_1,n_2}$, so that $f^{\rm sim}_{n_1,n_2} = f_{n_1,n_2} + \delta_{n_1,n_2}$. This offset is chosen to be a random variable following the Epanechnikov probability distribution

$$p(\delta_{n_1,n_2}) = K(\delta_{n_1,n_2}) \equiv \begin{cases} \frac{3}{4\lambda_{n_1,n_2}}\left[1-\left(\frac{\delta_{n_1,n_2}}{\lambda_{n_1,n_2}}\right)^2\right] & \text{for} -\lambda_{n_1,n_2} < \delta_{n_1,n_2} < \lambda_{n_1,n_2}, \\ 0 & \text{elsewhere,} \end{cases} \quad (5.7)$$

where the characteristic width of the offset $\lambda_{n_1,n_2}$ is a free parameter that must be decided. Too large a value of $\lambda_{n_1,n_2}$ creates simulated galaxies that are unrealistically "messy" and can even display large holes of negative flux; setting $\lambda_{n_1,n_2} = 0$ simply reproduces the original HDF galaxy.

Massey et al. (2004) describe their preferred choice of $\lambda_{n_1,n_2}$; they considered each pair of neighrbouing galaxies in the HDF finding that $\lambda_{n_1,n_2} = 4\times[$ mean separation between nearest neighbours for that $f_{n_1,n_2}]$ proved to be a suitable choice. An example of these simulated galaxies, along with its HDF progenitor, can be seen in Figure 5.2 (image taken from Massey et al. 2004). The realism of these simulated galaxies was further tested by through the comparison of a range of galaxy morphology measures with the equivalent measurements for real data. It was found that the ellipticity distributions of simulated galaxies closely mirrored those of real galaxies, as did measures of clumpiness, asymmetry and substructure (see Massey et al. 2004; Conselice 2003; Bershady et al. 2000; Conselice et al. 2000). The randomly inverted, rotated and resampled galaxies then represent realistic but wholly new simulated galaxy images.

Using the lensing transformations described in Sections 3.1.2 and 3.2.2 these shapelet simulated galaxies were then subjected to a range of input shears and flexions as described in Section 5.1. The first simulated image was not lensed, each of the 99 subsequent tiles were subjected to a shear and flexion of a magnitude randomly chosen from the ranges described in Section 5.1 using a uniform probability distribution. The input shear and flexion signals for each tile are orientated at random angles to the pixel grid, but in fixed orientation to one another (again as described in Section 5.1).

In order to test the accurate retrieval of lensing information in the presence of unavoidable observational degradation, such as that due to sky noise and PSF distortions, it is necessary to mimic these effects in the FLIP images. I describe how this was done in the next Section.

## 5.2.2 Simulated observational distortions

### ACS-like point spread function

The point spread function used for the convolution of galaxies in this analysis was PSF "D" in the set of PSFs used for the forthcoming STEP3 analysis ("space STEP", Rhodes et al., in prep.) which is shown in Figure 5.3. This is modelled on the ACS PSF and was chosen as the most likely to resemble the telescope optics in the GEMS images, and to allow these results to be directly compared with the forthcoming STEP3 results. This PSF has been modelled using the shapelet software, up to an order $n_{\rm max} = 20$, and are based on detailed "Tiny Tim" ray-tracing models of the ACS PSF (Krist 1995; Rhodes et al. 2007). As discussed in Section 4.3.3, modelling up to order $n_{\rm max} = 20$ may not be sufficient to completely characterize the

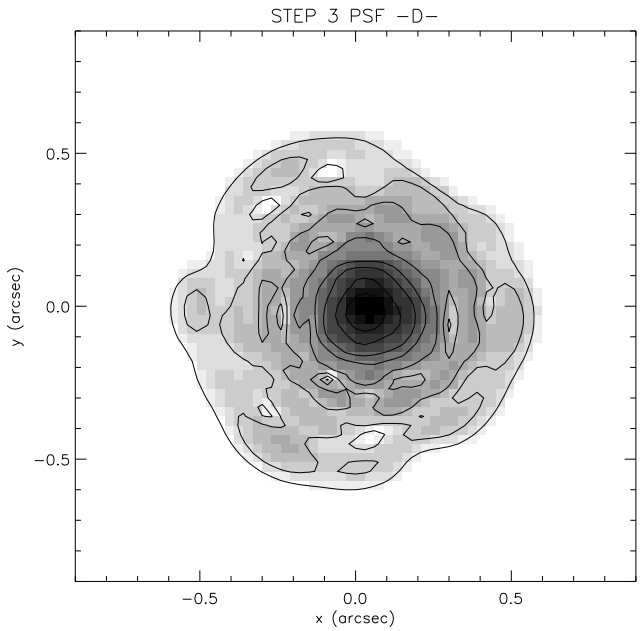


Figure 5.3: The point spread function (STEP3 PSF "D") used to convolve the FLIP simulated galaxy images. The colour scale and contours plotted are logarithmic.

ACS PSF on all scales, due to its extremely non-Gaussian profile. However, it will provide a good first test of the success of shear and flexion measurement using the GEMS pipeline. In subsequent analyses it will be desirable to model the FLIP PSF to higher accuracy, much as it appears to be desirable to do the same for the GEMS images.

Each lensed, shapelet modelled galaxy in the FLIP catalogue was then convolved using this PSF model. An important simplification of the FLIP analysis is that this PSF model is kept constant across the image, and no attempt is made to fit a time or spatially varying PSF model to the FLIP images. This simplification is also observed in the STEP analyses of Heymans et al. (2006b) and Massey et al. (2007b), who argue that the problem of shear measurement precision should be decoupled from the separate question of PSF interpolation. Hoekstra (2004) and Jarvis & Jain (2004) have looked into this problem, but it is certainly likely to add additional uncertainty to the calibration of lensing measurements.

The convolution itself was performed in shapelet space using the convolution matrix transformations described in Refregier (2003) and Refregier & Bacon (2003), as implemented by the IDL routine `shapelets_convolve.pro` in the shapelet software. The resulting shapelet models then represent galaxies smeared by the PSF of the ACS, modelled to the same level as presented for blind tests of shear calibration in the STEP3 analysis of Rhodes et al. (in prep.), allowing for later direct comparison between these results and those of the STEP collaboration when analysing space-based images.

Finally, the convolved shapelet models are pixelized onto a grid of scale 0.03 arcsec, matching the GEMS science tiles. This is done using the routine `shapelets_recomp.pro` in the shapelet software, which performs an integration of the shapelet model across each pixel. The Cartesian shapelet set is analytically integrable across rectangular regions on the two-dimensional plane (Refregier 2003; Massey & Refregier 2005), and so this operation may done quickly and accurately.

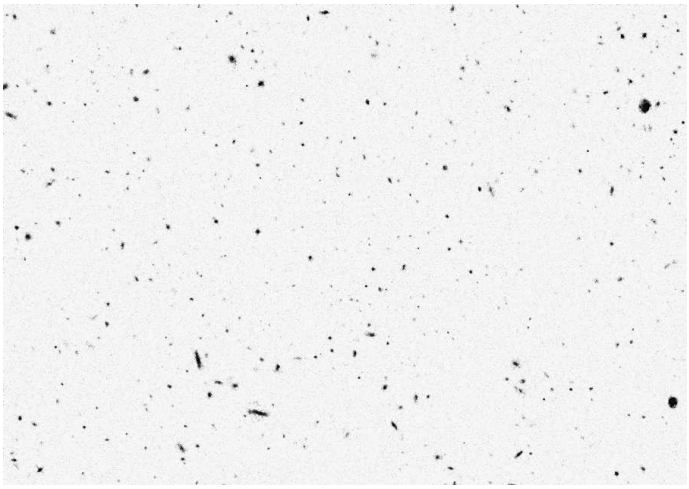

Figure 5.4: Section of one of the FLIP image tiles, created by Richard Massey using the image simulation method of Massey et al. (2004).

### Pixel noise

These pixelized FLIP images then undergo the final stage of processing, the addition of realistic noise. Following STEP2 and STEP3 (Massey et al. 2007b; Rhodes et al., in prep.), a two-component noise model is added to each FLIP image, resulting in the simulated data seen in Figure 5.4.

The first component added is a Poisson shot noise, due to the inevitable uncertainties associated with counting discreet events (in this case the number of photons arriving at each CCD pixel). The noise added is drawn from a Gaussian random variable of variance equal to the photon count. Having added this shot noise, the images are renormalized to counts per second, matching the GEMS images.

The second component added corresponds to a Gaussian background with a root mean square level of 5.0 counts $s^{-1}$, matching that of the GEMS images. The large scale variation in the field background is assumed to be perfectly subtracted (a reasonable assumption for the final reduced versions of the GEMS images, see Section 4.2.2). Correlated pixel noise of the sort described by Massey et al. (2007b) is not added, following the prescription of the STEP3 analysis (Rhodes et al., in prep.); GEMS itself does contain correlated pixel noise due to the dithering of images, and I will discuss the implications of this in Section 5.4.3. Finally, in the galaxy image simulation stage, faint objects are created well below the level of the GEMS sensitivity. These objects are subsequently lost in the noise, causing a slight but realistic addition to the noise level overall. The FLIP images, a section of the second of which can be seen in Figure 5.4, now encapture many of the most important properties of the GEMS lensing data and are ready for shapelet analysis using the GEMS pipeline of Chapter 4. I now describe this analysis, the extraction of lensing measurements, and the success of the different estimators for shear and flexion.

## 5.3 FLIP data analysis and results

The FLIP image tiles were analysed using exactly the same pipeline as described in Chapter 4, with one important difference. No stars are simulated in the FLIP images, and knowledge of the convolving PSF comes instead in the direct form of the $n_{\max} = 20$ shapelet model describing STEP3 PSF "D" shown in Figure 5.3. There is therefore no need to model the FLIP PSF using the methods described in Section 4.2.3; the GEMS images required detailed modelling firstly from the stars themselves and then modelling of that variation of stellar shapes as a function of chip position.

In this way we are simulating shapelet shear and flexion measurement given *perfect* knowledge of the distorting PSF, a luxury which is not attainable for real data. Future analyses will be necessary to ascertain the extra uncertainty in shear and flexion measurements due to imperfect modelling of the PSF (such as may well be evident even for the $n_{\max} = 20$ GEMS PSF model, see Section 4.3), but it is nevertheless interesting to explore the undeniable limits of shape measurement accuracy even given a well-modelled PSF.

Using the SExtractor software (Bertin & Arnouts 1996) I extracted a catalogue of 33 601 galaxies having SNR $> 15$, as was done for the GEMS galaxies (see Section 4.1.2). This represents a slightly higher number density of galaxies than that found using the similar criterion in the GEMS images ($\simeq 80$ arcmin$^{-2}$ as opposed to $\simeq 65$ arcmin$^{-2}$), but this can be explained by the paucity of objects in the GEMS field (e.g., Schrabback et al. 2007), the masking of the GEMS images, and the necessary imposition of further selection criteria upon the GEMS galaxies to avoid confusion with stars or imaging anomalies.

These SExtractor catalogues were then used as the input to `shex.pro`, using the same postage stamp extraction scheme and input parameters as described in Chapter 4. The PSF model input to `shex.pro`, the same for each galaxy, was the STEP3 PSF "D" as described above. I then used the 100 deconvolved output shapelet catalogues to make an estimate of shear and flexion for each FLIP galaxy, using each of the estimators listed in Section 5.1.

In a similar fashion to the published STEP analyses (Heymans et al. 2006b; Massey et al. 2007b), the chosen figure of merit was based upon the mean (or median) $\gamma^{\rm obs}$, $\mathcal{F}^{\rm obs}$ or $\mathcal{G}^{\rm obs}$ from each tile, and its relationship to the corresponding input signal. For the flexion analyses, the median was again found to significantly outperform the mean as a measure of central tendency, and so is used exclusively. As was the case for the GEMS data, the mean and median are equally efficient statistics for the FLIP shear measurements; we thus make comparisons using the mean shear, a measure more likely to be used in shear-only shapelet analyses of the future. In my FLIP analysis the mean and median shear performed equivalently, with no significant sign of any relative bias between the two for any of the shear estimators.

Specifically, the success of each lensing estimator is quantified by two measurements: the multiplicative calibration bias $m$ and the residual shear or flexion offset bias $c$. These are the same comparison criteria used in the STEP studies (Heymans et al. 2006b; Massey et al. 2007b). Using the 200 data points provided by the two components of mean shear measured for each tile, we fit the following relationship for each estimator:

$$\left\langle \gamma^{\rm obs} \right\rangle - \gamma^{\rm input} = m_\gamma \gamma^{\rm input} + c_\gamma. \tag{5.8}$$

Table 5.1: Tabulated shear calibration bias for each estimator tested on the FLIP images.

| Estimator | $m_\gamma$ | $c_\gamma$ |
|---|---|---|
| $\tilde{\gamma}^{\rm DG}$ | -0.235±0.013 | 0.0016±0.0005 |
| $\tilde{\gamma}^{\rm unweighted}$ | -0.178±0.014 | 0.0016±0.0006 |
| $\tilde{\gamma}^{\rm Gaussian}$ | -0.137±0.020 | 0.0012±0.0008 |

In the same way, we fit the median flexion measured from each tile as

$$(\mathcal{F}^{\rm obs})_{\rm m} - \mathcal{F}^{\rm input} = m_{\mathcal{F}}\mathcal{F}^{\rm input} + c_{\mathcal{F}}, \quad (5.9)$$

$$(\mathcal{G}^{\rm obs})_{\rm m} - \mathcal{G}^{\rm input} = m_{\mathcal{G}}\mathcal{G}^{\rm input} + c_{\mathcal{G}}. \quad (5.10)$$

It should be noted that we do not consider the two components of shear or flexion separately as a function of the orientation of the input signal, as was done by Massey et al. (2007b) for STEP2. In considering the overall response to components we maximise the signal-to-noise of our lensing measurement calibration, and postpone an investigation of angular dependence to a later analysis. For the galaxy-galaxy lensing measurements of Chapter 6 this will be a sufficient test of signal recovery, as any angular bias will cancel on average and add only a small extra component to the measurement noise. I now discuss the results for each of the estimators proposed in Section 5.1, and begin with the shear.

### 5.3.1 Shear measurement results

The analysis of the shear results begins with an outlier cut, all galaxies with $|\gamma^{\rm obs}| > 1$ being removed from consideration. This degree of trimming will not significantly bias output shear statistics, and is commonly used for shear measurements (e.g., HO5). For the estimators constructed in a "passive" fashion (Massey et al. 2007b,d) from combinations of polar shapelet coefficients $f_{n,m}$ we normalise each coefficient by the flux of the object in question. This is a simple first approach to addressing the problem of reducing the otherwise extremely wide scatter in shapelet coefficient values ($f_{n,m}$ being linearly related to the image surface brightness). This and related problems are discussed in greater detail in Section 5.4. In order to calculate the $\tilde{\gamma}^{\rm unweighted}$ estimator, a shear responsivity factor $\mathcal{R}$ (see Equation 3.100) for the galaxy sample is needed, and is calculated to be

$$\mathcal{R} = 1 - \frac{\langle \varepsilon^2 \rangle}{2} = 0.886 \quad (5.11)$$

for the FLIP images. We note that this is different to the result obtained for GEMS, pointing to a possible difference in the properties of the GEMS galaxies when compared to those in the FLIP images (see Sections 4.2.4 and 5.1).

In Table 5.1 we present the results for the three shear estimators tested using the FLIP simulations, and in Figure 5.5 plot the tile-by-tile results for each estimator that were used to fit the $m_\gamma$ and $c_\gamma$ figures of merit for each estimator. These results show a clear underestimating bias in each shear estimator considered,

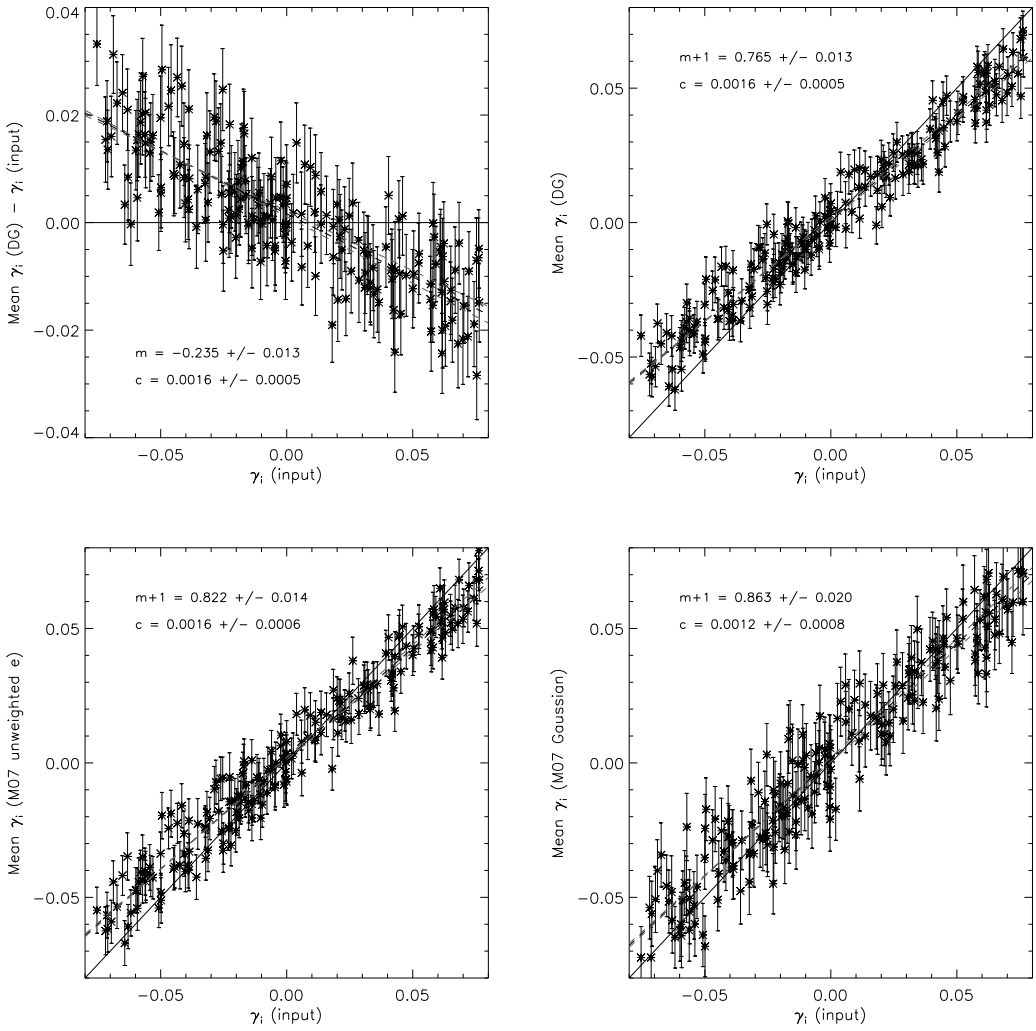


Figure 5.5: FLIP results for the $\tilde{\gamma}^{\rm DG}$, $\tilde{\gamma}^{\rm unweighted}$ and $\tilde{\gamma}^{\rm Gaussian}$ estimators. Plotted are $(\tilde{\gamma}^{\rm DG} - \gamma^{\rm input})$ versus $\gamma^{\rm input}$ for each tile (top left panel), from which the calibration fit is calculated, and the output $\tilde{\gamma}^{\rm DG}$ versus $\gamma^{\rm input}$ for each tile (top right panel). In the bottom left panel is plotted $\tilde{\gamma}^{\rm unweighted}$ versus $\gamma^{\rm input}$ for each tile, and the bottom right panel shows $\tilde{\gamma}^{\rm Gaussian}$ versus $\gamma^{\rm input}$. The dashed lines represent the fit and the solid line depicts perfect performance.

recovering only $(76.5 \pm 1.3)\%$, $(82.2 \pm 1.4)\%$ and $(86.3 \pm 2.0)\%$ of the input shear signal for $\tilde{\gamma}^{\rm DG}$, $\tilde{\gamma}^{\rm unweighted}$ and $\tilde{\gamma}^{\rm Gaussian}$ respectively. The evidence for the imperfect removal of PSF anisotropy, given by the value of the offset parameter $c_\gamma$, is also significant; although this sensitivity to a residual systematic is less secure for $\tilde{\gamma}^{\rm Gaussian}$ there is some sign that this estimator is also affected by imperfect PSF removal. These results are discussed in Section 5.4.

### 5.3.2 Flexion estimator results

As for the case of shear we exclude measurements for which $|\mathcal{F}^{\rm obs}|, |\mathcal{G}^{\rm obs}| > 1$, and for the passive (Gaussian) estimators normalize each shapelet coefficient by the observed flux for that galaxy. In Table 5.2 we present the results for the flexion estimators described in Section 5.1.2 when tested using the FLIP simulated images. Figure 5.6 shows the results of these estimators on a tile-by-tile basis, and the best-fitting lines that give the $m$ and $c$ figures of merit for each estimator.

These results are interesting in comparison to those for shear. The multiplicative bias $m_{\mathcal{F}}^{\rm DG}$ for the $\tilde{\mathcal{F}}^{\rm DG}$ measurements appears to be well controlled, showing an overall bias ratio of $1.04 \pm 0.12$. It is clear, however, that the uncertainty on this figure is significantly greater than that for its shear counterparts. Also of interest is the fact that the $\tilde{\mathcal{G}}^{\rm DG}$ appears to significantly *overestimate* the input gravitational signal, with a bias of $(215 \pm 12)\%$. This unexpected result will be discussed later on in the Chapter (see Section 5.4). As in the case of the shear measurements, the $\tilde{\mathcal{F}}^{\rm DG}$ estimator seems to show some residual offset bias. The offset is somewhat more marginal than for shear, possibly due to the more severe noise in the flexion measurements, and no significant residual is evident for $\tilde{\mathcal{G}}^{\rm DG}$.

The results for the truncated DGT estimators $\tilde{\mathcal{F}}^{\rm DGT}$ and $\tilde{\mathcal{G}}^{\rm DGT}$ are similar to those for the DG estimators, but somewhat noisier and less accurate. Contrary to the findings of Goldberg & Leonard (2007) and Leonard et al. (2007), who found that truncation improved shapelet estimates of $\mathcal{F}$ and $\mathcal{G}$, for the GEMS pipeline it to be appears advantageous not to truncate shapelet models before measuring flexion using the $\chi^2$ minimization of Equation (3.91). In particular, the multiplicative bias $m_{\mathcal{F}}^{\rm DGT}$ for the $\tilde{\mathcal{F}}^{\rm DGT}$ measurements appears to be less well controlled than for $\tilde{\mathcal{F}}^{\rm DG}$, showing an overall positive bias of $(34 \pm 15)\%$. Again, $\tilde{\mathcal{G}}^{\rm DGT}$ appears to overestimate the input gravitational signal, with an even greater positive bias of $(290 \pm 16)\%$. The control of residual offsets is again better than for the shear estimators, with a non-detection for $\tilde{\mathcal{F}}^{\rm DGT}$ and a marginal negative detection in $\tilde{\mathcal{G}}^{\rm DGT}$.

The $\tilde{\mathcal{F}}^{\rm Gaussian}$ and $\tilde{\mathcal{G}}^{\rm Gaussian}$ flexion estimators perform, perhaps, the worst of the three tested. The $\tilde{\mathcal{F}}^{\rm Gaussian}$ estimator now shows severe overestimating bias of the input signal, at $(270 \pm 16)\%$. As opposed to the DG estimators, the bias in $\tilde{\mathcal{G}}^{\rm Gaussian}$ is a less severe (but still significant) $(176 \pm 17)\%$. Control of residual offsets appears reasonable for $\tilde{\mathcal{G}}^{\rm Gaussian}$ and poor for $\tilde{\mathcal{F}}^{\rm Gaussian}$. In the following Section I will now attempt to discuss these results which, especially for the case of the flexion estimators tested, appear in some cases to be disappointing and alarming in equal measure. It may be that further work, using a larger suite of simulated images, will be necessary to really explore these biases and uncertainties. However, I will attempt to investigate and discuss some the more obvious shortcomings and problems inherent in the shapelet estimators, shortcomings that have only become apparent in the practical application of the method.

## 5.4 Discussion

I now attempt to draw some conclusions, based on the results presented above and on other observations which I will discuss, regarding the reliability of the tested shapelet lensing measurement schemes. Many of the estimators above appear perform poorly, and more work will be necessary to understand the issues

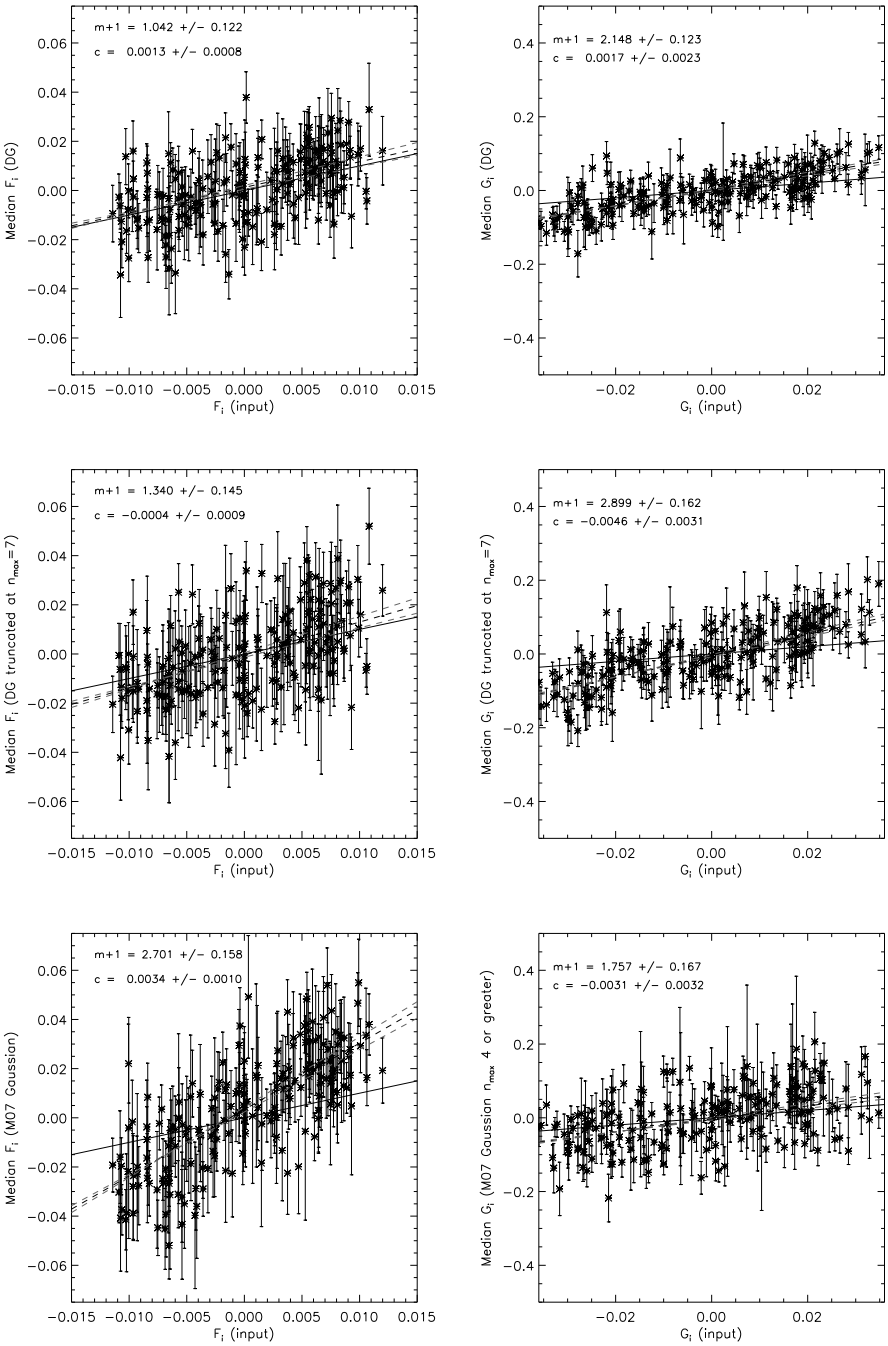


Figure 5.6: FLIP results for the flexion estimators tested. In the top left panel is plotted the median $\tilde{\mathcal{F}}^{\rm DG}$ versus $\mathcal{F}^{\rm input}$ for each tile, and the top right panel shows the median $\tilde{\mathcal{G}}^{\rm DG}$ versus $\mathcal{G}^{\rm input}$. Also shown are $\tilde{\mathcal{F}}^{\rm DGT}$ (mid left) and $\tilde{\mathcal{G}}^{\rm DGT}$ (mid right), and $\tilde{\mathcal{F}}^{\rm Gaussian}$ (bottom left) and $\tilde{\mathcal{G}}^{\rm Gaussian}$ (bottom right), versus the respective input flexion signals. The differing scales of the various plots should be noted. The dashed lines represent the fit and the solid line depicts perfect performance.

Table 5.2: Tabulated flexion calibration bias for each estimator tested on the FLIP images.

| Estimator | $m$ | $c$ |
|---|---|---|
| $\tilde{\mathcal{F}}^{\mathrm{DG}}$ | 0.04±0.12 | 0.0013±0.0008 |
| $\tilde{\mathcal{F}}^{\mathrm{DGT}}$ | 0.34±0.15 | -0.0004±0.0009 |
| $\tilde{\mathcal{F}}^{\mathrm{Gaussian}}$ | 1.70±0.16 | 0.0034±0.0010 |
| $\tilde{\mathcal{G}}^{\mathrm{DG}}$ | 1.15±0.12 | 0.0017±0.0023 |
| $\tilde{\mathcal{G}}^{\mathrm{DGT}}$ | 1.90±0.16 | 0.0046±0.0031 |
| $\tilde{\mathcal{G}}^{\mathrm{Gaussian}}$ | 0.76±0.17 | -0.0031±0.0032 |

affecting the accuracy of shapelet estimation. Still more work may be necessary before all of the schemes presented above can be made as reliable as the best alternative methods.

### 5.4.1 Multiplicative bias

To begin, I will consider the results for the bias factor $m$, which is perhaps the most pernicious systematic bias affecting lensing measurements as it *requires* lensing simulations such as STEP and FLIP in order to be accurately quantified. In contrast, the offset bias can be constrained using tests on the lensing data in question, such as those described in Section 4.3.3 (see also Bacon et al. 2003 for a further test of shear residual systematics in cosmic shear analyses).

On the strength of the results presented in Section 5.3.1 it is tempting to assume that the shear is best measured by $\tilde{\gamma}^{\mathrm{Gaussian}}$. This estimator displays an underestimating multiplicative bias of $\simeq 86\%$ in comparison to the $\simeq 82\%$ of $\tilde{\gamma}^{\mathrm{Gaussian}}$ or the even more severe underestimating bias for the David Goldberg shear estimator. It also appears to have the least sensitivity to what, for an unknown reason that will be speculated upon later, must be an imperfect treatment of the PSF anisotropy. There are, however, important problems with this estimator and others similar to it for both shear and flexion. These are likely to be due to the simple way it has been implemented for this analysis, and will need significant further investigation.

Firstly, $\tilde{\gamma}^{\mathrm{Gaussian}}$ is noisier than the unweighted ellipticity and DG estimators. This in may in fact be a consequence of another important property of this estimator, which relates to the calculation of its shear susceptibility. As described in Section 3.4.3, the $\tilde{\gamma}^{\mathrm{Gaussian}}$ estimator may be constructed simply as

$$\tilde{\gamma}^{\mathrm{Gaussian}} = \frac{\sqrt{2} f_{2,2}}{\langle f_{0,0} - f_{4,0} \rangle}, \tag{5.12}$$

where the angle brackets $\langle\ \rangle$ denote an ensemble average. As mentioned above, for this analysis we took the additional step of normalizing each $f_{n,m}$ in the above expression by the flux of the galaxy in question (remembering from Section 3.2 that the units of $f_{n,m}$ are flux $\times$ inverse angle). This does something to reduce the extremely large scatter in these quantities due to the large range of galaxy fluxes, but a large scatter (and extremely skewed distribution) for these coefficients still remains. The correct calculation of this ensemble average is vital to the accuracy of the entire estimator.

In the FLIP analysis I have presented, this ensemble average was naïvely calculated as the arithmetic mean of the entire shear catalogue, finding $\langle f_{0,0}/F - f_{4,0}/F \rangle = 2.49$, where $F$ is the galaxy flux. As an illustration of the instability of this measurement, the median of this quantity is found to be 1.89, pointing towards a skewed distribution within the galaxy population. If this median is then used in the calculation of $\tilde{\gamma}^{\rm Gaussian}$ it is found that $m_\gamma^{\rm Gaussian}$ is closely consistent with zero. It seems unjustifiable to draw strong conclusions regarding the reliability of the Gaussian shear estimator without a better understanding of the correct way to estimate this susceptibility factor. This instability is also likely to be a partial cause of the extra noise seen in the Gaussian shear measurements.

An obvious conclusion is that the quantity $\langle f_{0,0} - f_{4,0} \rangle$ should be fitted as a function of galaxy flux, apparent size, and possibly morphological type whilst ensuring that estimators constructed in this fashion take proper account of biases due to "Kaiser flow" of galaxies between flux and size bins (see, e.g., Kaiser 2000; Massey et al. 2007d). These considerations will also be vital in the calculation of $\mu_{n_1,n_2}$ for David Goldberg's shear estimator, and for the calculation of correct susceptibilities in the Gaussian and radial profile flexion estimators.

The calculation of accurate susceptibilities for the more complicated polar shapelet flexion estimators, such as the radial profile estimator, is made more difficult still by a further problem: the slow convergence of shapelet coefficient sums such as

$$P^{\mathcal{G}}_{\rm radial} = \frac{\beta}{16\sqrt{2}} \sum \sqrt{(n-3)(n-1)(n+1)}\,(f_{n-3,0} + f_{n-1,0} - f_{n+1,0} - f_{n-3,0})\,, \tag{5.13}$$

which expresses the susceptibility of the radial profile $\mathcal{G}$ estimator (Massey et al. 2007d). The radial profile estimators for $\mathcal{F}$ and $\mathcal{G}$ were also constructed and tested on the FLIP images, but could not be made to yield meaningful results for this reason. A further issue of importance to $\mathcal{F}$ estimators is the convergence of the quantity $R^2/\beta^2$ (see Section 3.4.3). For a small but significant population of FLIP galaxy image models the convergence of this measure was so poor that negative values were returned (these models were rejected from subsequent analysis), which adds a significant source of extra noise and possibly bias to the Gaussian and radial profile estimators for $\mathcal{F}$. This could be one explanation for the overestimation of the $\mathcal{F}$ signal by $\tilde{\mathcal{F}}^{\rm Gaussian}$, seen in Figure 5.6.

In contrast, the calculation of the unweighted ellipticity and the Goldberg flexion estimators proceeds on a galaxy-by-galaxy basis, without needing the ensemble average of quantities that will vary wildly with galaxy population and due to inevitable shapelet series truncation. The shear responsivity factor $\mathcal{R}$, which is used as a susceptibility factor in the unweighted ellipticity, is a fairly robust statistic that does not change significantly between galaxy populations (although it does appear to change somewhat, c.f. Section 4.2.5).

To conclude, therefore, $\tilde{\mathcal{F}}^{\rm Gaussian}$, $\tilde{\mathcal{G}}^{\rm Gaussian}$ and $\tilde{\gamma}^{\rm DG}$ fare poorly in this first FLIP comparison. More importantly, the calibrative bias factors for these measures *and* for the more successful $\tilde{\gamma}^{\rm Gaussian}$ cannot be trusted without significant improvements to the calculation of shear and flexion susceptibilities they require. The investigation of whether more sophisticated treatments of the required susceptibilities (e.g., as a function of galaxy size and flux) improve the reliability of these measures to a level greater than that offered by $\tilde{\gamma}^{\rm unweighted}$ (or by $\tilde{\mathcal{F}}^{\rm DG}$ and $\tilde{\mathcal{G}}^{\rm DG}$ will be useful further work, but beyond the scope of this Thesis.

Instead, we adopt the unweighted ellipticity as the favoured means of shapelet shear estimation in GEMS, and include a multiplicative correction by a factor of $(1/0.82)$ to all shear estimates in the galaxy-galaxy lensing analysis of Chapter 6. I will discuss the implications of the need to introduce such a factor, and

how it compares to the results for the shapelet pipeline tested in STEP3, in Section 5.4.3. For the flexion estimated using Equation (3.93), I found there to be no advantage in truncating the shapelet series as suggested by Goldberg & Leonard (2007). This is likely due to important differences at the shapelet modelling stage; Goldberg & Leonard (2007) and Leonard et al. (2007) do not use the shapelet amoeba routine to optimise their shape measurements, and are thus often left with very high order shapelet models containing relatively little information. We thus adopt the $\tilde{\mathcal{F}}^{\rm DG}$ and $\tilde{\mathcal{G}}^{\rm DG}$ estimators for flexion, and correct measurements by bias factors of $(1/1.04)$ and $(1/2.15)$ respectively.

### Overestimation in the $\mathcal{G}$ estimators

Finally, and on a related note, the large, systematic overestimation of the $\mathcal{G}$ signal by all of the estimators tested presents an unsolved question. The estimation of $\mathcal{G}$ is likely to be the most problematic of all the weak lensing signals as it involves the accurate determination of image variation on the smallest scales. However, explanations for overestimation of the signal that would affect all the estimators tested are difficult to conceive, although image overfitting at the shapelet modelling stage is one possibility.

In order to investigate the problem further, I undertook to split the the FLIP survey images into subsamples and examine the dependency of $m_{\mathcal{G}}$ upon various properties of the simulated images. The obvious place to begin an investigation is the signal-to-noise ratio (SNR) of the galaxy, defined as the ratio of the FLUX to the FLUX_ERROR as measured by SExtractor for each simulated galaxy. It should be expected that the brighter a galaxy image, and the more securely it is detected, the more secure the shape measurement should be. The total sample of FLIP galaxies was split into three bins of SNR, having a range so as each to contain the same number of galaxies. The figures of merit described by Equations (5.8)-(5.10) were then calculated using the tile-by-tile relationship of $\mathcal{G}^{\rm obs}$ to $\mathcal{G}^{\rm input}$ as before, but in each tile using using only the relevant subsample for that bin. Due to the concerns voiced in the previous Section regarding the accurate determination of denominator of the Gaussian estimators, we do not consider $\tilde{\mathcal{G}}^{\rm Gaussian}$ but restrict ourselves to investigating $\tilde{\mathcal{G}}^{\rm DG}$ and $\tilde{\mathcal{G}}^{\rm DGT}$. In Figure 5.7 we see plotted the variation of $m_{\mathcal{G}}^{\rm DG}$ and $m_{\mathcal{G}}^{\rm DGT}$ with three different SNR subsamples (upper two panels) and compared this to the variation of $m_{\gamma}^{\rm unweighted}$ across the same SNR bins (lower panel).

The results shown in Figure 5.7 are interesting, and for the $\tilde{\mathcal{G}}^{\rm DG}$ and $\tilde{\mathcal{G}}^{\rm DGT}$ are somewhat unexpected. The $\tilde{\mathcal{G}}^{\rm DG}$ and $\tilde{\mathcal{G}}^{\rm DGT}$ estimators appear to show an approximately consistent overestimation of the input signal for all three SNR bins. There is no clear dependence of the success of $\mathcal{G}$ measurement upon SNR for the FLIP images, whereas for the shear estimator $\tilde{\gamma}^{\rm unweighted}$ we see that the shear recovery improves as the galaxies increase in SNR. In other respects Figure 5.7 seems reasonable; for both the $\tilde{\gamma}^{\rm unweighted}$ and for the $\mathcal{G}$ estimators it can be seen that the uncertainties upon $m$ are greater for the lower SNR galaxies. This is a simple consequence of the increase of measurement uncertainties for fainter galaxies (see Figures 4.7-4.9 in Section 4.3.2). In addition, uncertainties upon $m_{\mathcal{G}}^{\rm DGT}$ are typically greater than those upon $m_{\mathcal{G}}^{\rm DG}$, as found before for the full sample of FLIP galaxies. However, the approximate constancy of $m_{\mathcal{G}}^{\rm DG}$ and $m_{\mathcal{G}}^{\rm DGT}$ with SNR presents no real insight into what might be causing the overestimation of $\mathcal{G}$.

We therefore investigated the variation of $m_{\mathcal{G}}$ with other galaxy properties, in the hope that they may correlate more strongly with other variables. In the same fashion as for the SNR subsamples described above and seen in Figure 5.7, we chose to split the FLIP galaxies by two more image properties: the shapelet scale size $\beta$ (as chosen by the shapelet software of Massey & Refregier 2005) and the value of the

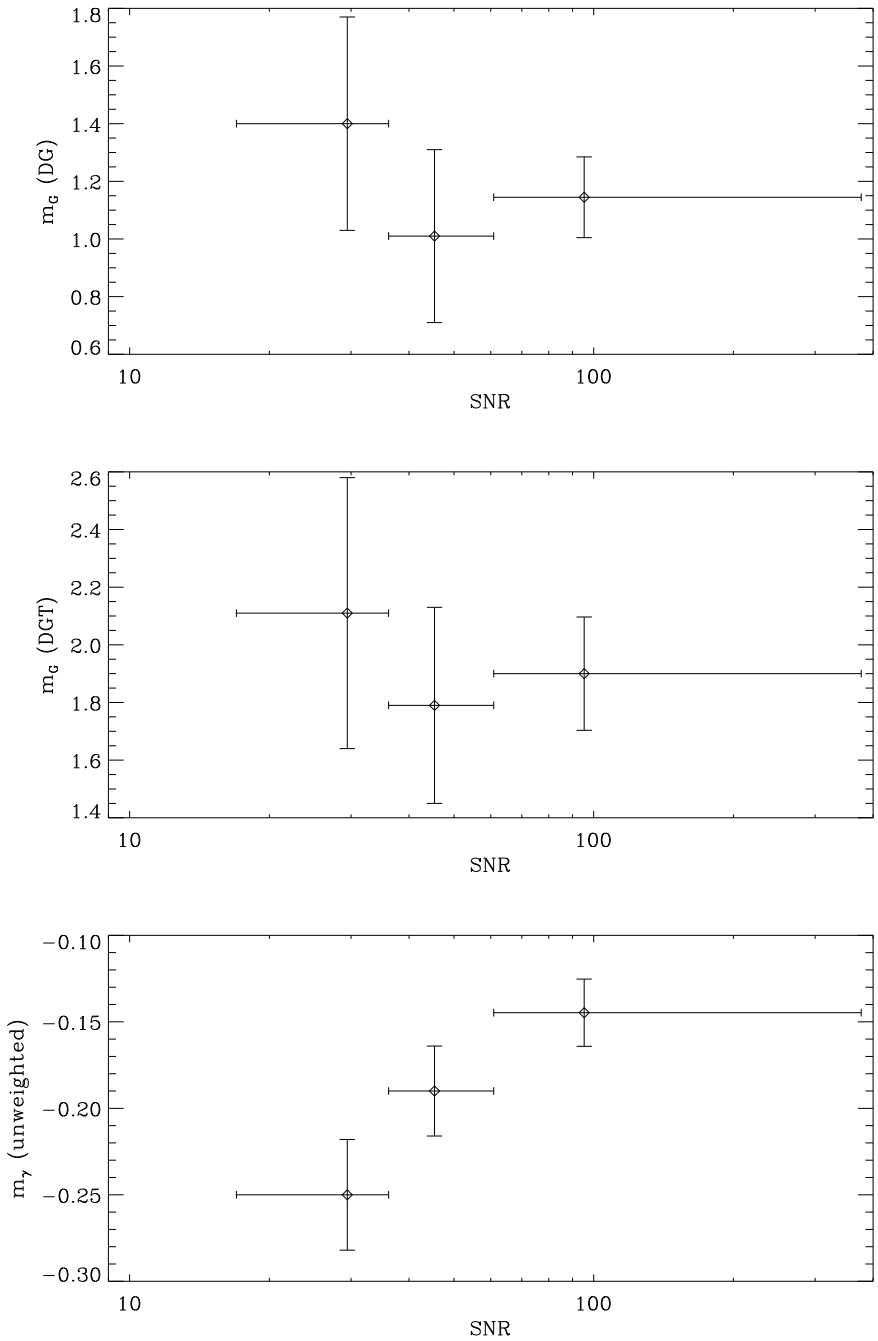


Figure 5.7: Multiplicative bias factors for $\tilde{\mathcal{G}}^{\rm DG}$ (upper panel), $\tilde{\mathcal{G}}^{\rm DGT}$ (middle panel) and $\tilde{\gamma}^{\rm unweighted}$ (lower panel) for SNR subsamples of the FLIP galaxies. The scale for the abscissa is logarithmic, and the error bars in this SNR direction give the extent of the SNR bin for that subsample. Points are plotted at the median SNR for each of the three bins.

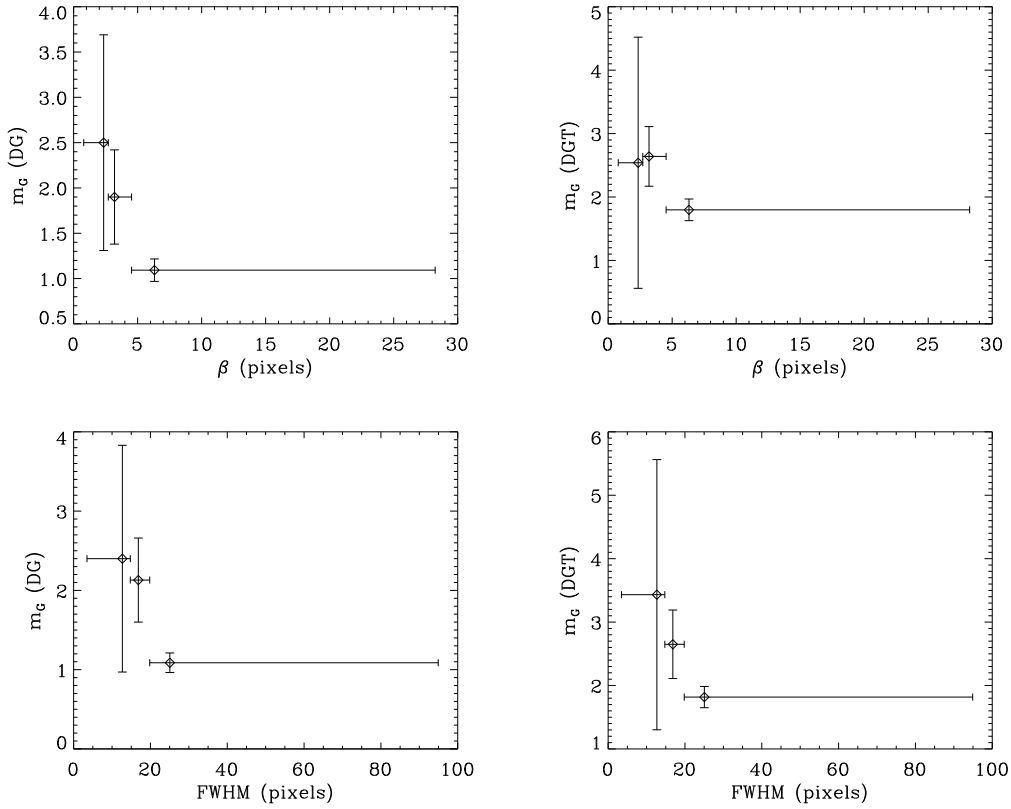


Figure 5.8: Multiplicative bias factors for $\tilde{\mathcal{G}}^{\mathrm{DG}}$ (left panels) and $\tilde{\mathcal{G}}^{\mathrm{DGT}}$ (right panels) for $\beta$ (upper panels) and FWHM (lower panels) subsamples of the FLIP galaxies. The error bars in the abscissa give the extent of the $\beta$ or FWHM bin for that subsample. Points are plotted at the median $\beta$ or FWHM for each of the three bins.

full width at half maximum (FWHM) as measured by SExtractor. As before, the FLIP galaxies are split into three subsample bins of $\beta$ and FWHM, each containing the same number of galaxies. The $m_{\mathcal{G}}^{\mathrm{DG}}$ and $m_{\mathcal{G}}^{\mathrm{DGT}}$ figures of merit were then calculated for each bin, and the results are plotted in Figure 5.8.

The results of Figure 5.8 are interesting, as they hint at what may be one cause of the overestimation of $\mathcal{G}$ by the estimators tested. Whereas the SNR parameter describes the relative brightness of the FLIP images, both $\beta$ and FWHM are directly related to the size of the FLIP galaxies (the relationship is not precise for $\beta$, however, as galaxies displaying significant substructure are modelled using a lower $\beta$ and higher $n_{\mathrm{max}}$). Both $\tilde{\mathcal{G}}^{\mathrm{DG}}$ and $\tilde{\mathcal{G}}^{\mathrm{DGT}}$ appear to show signs of more significant overestimation for low FWHM and low $\beta$ galaxies, although this correlation is less strong in the DGT estimators due to the size of the uncertainties. Interestingly, the values of $m_{\mathcal{G}}$ for each estimator are extremely poorly defined for the smaller galaxies, which can be seen in the size of the particularly large error bars in the first bins of Figure 5.8. We now consider the ramifications of these results.

Firstly, it seems clear that $\mathcal{G}$ is very poorly measured for small galaxies, and poorly measured overall, using the shapelet technique described in Section 3.4.2 as implemented by the `flexion.pro` code of David Goldberg. While the problem is particularly bad for the smaller galaxies, as can be seen from Figure 5.8

there is still an overestimation even for the the larger galaxies. One explanation for these results might lie in the pixellization of galaxy images; it is known that this causes degeneracies and covariances between shapelet coefficients, particularly those containing information on the variation of the image of small scales (Massey & Refregier 2005). As discussed in Section 3.2.2, the second flexion transformations cause distortions in galaxy images that may be detected only by considering higher order shapelet coefficients than for the first flexion or shear.

This may go a long way to account for the extreme noise upon the $\mathcal{G}$ measurements for small galaxies, but it is more difficult to account for the overestimation of the effect. The problem may be related, however; although the shapelet software of Massey & Refregier (2005) can be made to output covariance matrices for the shapelet coefficients of the final galaxy model, it does not take these covariances into account during the actual modelling stage. Importantly, the `flexion.pro` routine of David Goldberg does not take these covariances into account, using instead the expression of Equation (3.87) for the covariance matrix $V_{\boldsymbol{n},\boldsymbol{p}}$ (i.e. purely diagonal). It may be that this neglect of the full covariance between shapelet coefficients leads to overfitting, both in the direct modelling stage and in the minimization of the $\chi^2$ statistic used to construct flexion estimators:

$$\chi^{2(odd)} = \left[\left(\mathcal{F}_i\hat{F}_i^T + \mathcal{G}_i\hat{G}_i^T\right)\tilde{f}^{\rm s}_{\boldsymbol{n}'} - f_{\boldsymbol{n}}\right] V^{-1}_{\boldsymbol{n}\boldsymbol{p}} \left[\left(\mathcal{F}_i\hat{F}_i^T + \mathcal{G}_i\hat{G}_i^T\right)\tilde{f}^{\rm s}_{\boldsymbol{p}'} - f_{\boldsymbol{p}}\right]. \tag{5.14}$$

That the overfitting leads to more severe overestimation for $\mathcal{G}$ than for $\mathcal{F}$ may be a consequence of the fact that the second flexion moves a greater proportion of shapelet power to higher order coefficients than the first flexion (again see Sections 3.1.2 and 3.2.2).

However, the discussion above is speculative. The overestimation may also be a consequence of simple errors in the `flexion.pro` routine of David Goldberg, or perhaps in the strength of the $\mathcal{G}^{\rm input}$ signal given to the simulation images by Richard Massey, or perhaps in my own measurements. It will be extremely important to investigate this effect further, both to understand the cause of these results and hopefully to improve on the performance of future second flexion estimators. To these ends, I intend to construct my own independent simulations of galaxy images, covering a much wider area than these first FLIP images; this will be necessary in order to fully explore the correlations between lensing recovery and parameters such as SNR or FWHM, and also the covariances and biases between simulataneous measurement of shear and flexion. This work is sadly beyond the scope of this Thesis. In the future it will also be extremely interesting to see whether HOLICs based approaches (Okura et al. 2007b,a) manifest the same overestimating behaviour.

The problem may be not be of vital importance, as the noise properties of the measured second flexion currently make its use for accurate cosmological measurement difficult; it is, for example, completely ignored by Leonard et al. (2007) and Okura et al. (2007a) (see also Section 6.2.3). Having completed my discussion of multiplicative bias in the FLIP analysis, I now go on to discuss the success of the chosen measurement schemes at avoiding additive biases.

### 5.4.2 Additive bias - shear and flexion residual offsets

The other figure of merit chosen in the FLIP analysis, as in the STEP analyses, was the offset bias $c$ defined in Equations (5.8), (5.9) and (5.10). There was evidence for a residual offset bias in the measurements from

all of the shear estimators (of varying significance), and some evidence in the flexion estimators, although these measurements were noisier. This raises interesting questions, as one of the unrealistic simplifications of the FLIP analysis was the fact that the convolving PSF was known perfectly, in the precise form of the shapelet model used. There was no need for PSF modelling from noisy stellar images, or for the interpolation of PSF properties in the regions between stars.

An explanation for the offset is most likely to lie in the shapelet treatment of the galaxy deconvolution. The shapelet software is known to treat both image deconvolution only inexactly (Massey & Refregier 2005; Section 3.3). The inexact treatment of correlated pixel noise by the shapelet method (discussed in Section 4.2.4 and below) is not an issue here, as the pixel noise in the FLIP images is uncorrelated as described in Section 5.2.

The shapelet software adopts a practical approach to deconvolution that is described in Section 3.3. Galaxy images are fit to a model using a basis set that has already been convolved with the PSF model, recovering the shapelet coefficients for the deconvolved image as shown in Equation (3.65). However, this convolved basis set is no longer strictly orthonormal, which introduces errors in the modelling when the scale size $\beta$ of the modelled galaxies is not large in comparison to that of the PSF (Massey & Refregier 2005). It is possible that this will be the case for galaxies in the FLIP analysis. The authors of the STEP3 analysis chose to model the ACS PSF using an $n_{\max} = 20$ model with $\beta = 2.86$; this was done so as to accurately model the wings of the light distribution, whereas in GEMS it was my decision that the accurate modelling of the PSF interior was also of significant importance. One consequence of this choice is that the PSF scale size is much closer to that of many of the FLIP galaxies, as can be seen in Figure 5.9. This may be one source of this residual lensing signal as detected in the FLIP measurements of $c$. Re-analysing $\tilde{\gamma}^{\rm unweighted}$ but excluding all galaxies with $\beta < 3$, we find $m_\gamma^{\rm unweighted} = -0.168 \pm 0.018$ (consistent with the previous result) but $c_\gamma^{\rm unweighted} = 0.0001 \pm 0.0007$, suggesting that this is indeed the reason for the shear offsets found in Section 5.3.

Interestingly, the PSF shear residuals apparent in the FLIP results are not detected in the GEMS shears, as described in Section 4.3.3, possibly as a consequence of the smaller $\beta$ of the PSF model. However, significant residuals are detected in the second flexion, in a manner aligned to the signal apparent in the wings of the GEMS PSF; these wings are more poorly modelled as a direct consequence of the smaller choice of $\beta$. The ideal solution is likely to be some compromise, modelling of the PSF with as small a $\beta$ as possible, whilst capturing as much of the light profile as possible on all scales. Increasing the value of $n_{\max}$ for the PSF model allows both these aims to be realised, but at the cost of increases to the computing resources required in shapelet modelling.

### 5.4.3 Wider applicability of the FLIP results

In the final Section of this chapter, I aim to briefly discuss the implications of the FLIP results in the wider context of weak lensing. Perhaps most importantly, I found there to be significant instabilities inherent in the calculation of certain amongst the shapelet shear and flexion estimators proposed by Refregier & Bacon (2003), Goldberg & Bacon (2005) and Massey et al. (2007d). This was due in each case to the need for these estimators to invoke ensemble averages of shapelet coefficients so as to estimate the lensing susceptibility of the measure in question. Unfortunately, these averages will vary strongly with galaxy type (and therefore telescope filter) and overall image quality (due to convergence issues in the larger shapelet sums). Careful

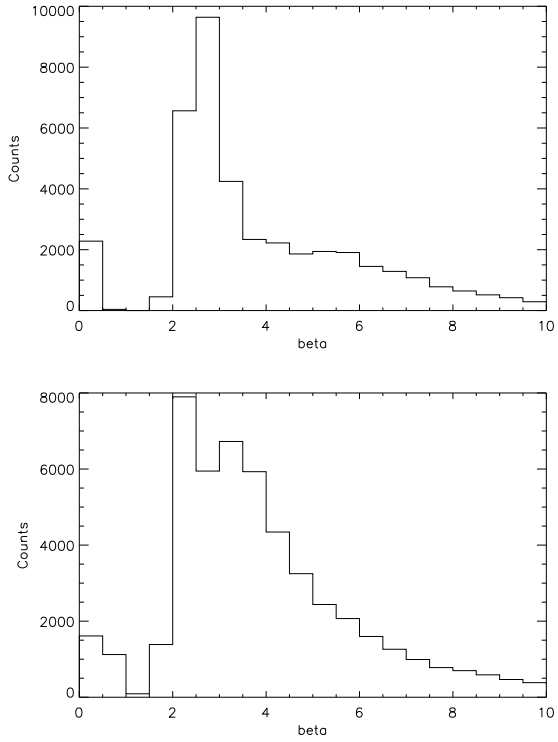


Figure 5.9: Histogram of shapelet scale size $\beta$ for FLIP (left panel) and GEMS (right panel) galaxy models as estimated by the GEMS pipeline. The small peaks at $\beta \simeq 0$ are due to catastrophic failures in the shapelet modelling and imperfect removal of anomalies from the GEMS catalogue. Note that for the GEMS analysis we remove all objects with $\beta < 2$ at the lensing measurement stage.

calculation of these susceptibilities as a function of flux, size and galaxy type will be necessary for them to be used in truly reliable estimators. Subsequent accurate calibration of these measures will require galaxy image simulations which very accurately reflect the flux, size and morphology of the real data sample, presenting a further, and perhaps more serious, technical challenge.

Regarding the methods that succeed by estimating shear and flexion without recourse to unstable ensemble averaging, I found evidence for significant multiplicative bias factors for both shear and the second flexion. For the measure $\tilde{\gamma}^{\rm unweighted}$, a calibration factor of 1/0.82 is required to match the input shears, and this is a calibration factor that I include when making the cosmological measurements presented in Chapter 6. One important question is where this bias might come from, a question that is also being posed by the STEP3 project; this found that Joel Bergé's shapelet pipeline (also based on Massey & Refregier 2005 software) needed a similar factor of $\simeq 1/0.9$, although this was using the $\tilde{\gamma}^{\rm Gaussian}$ estimator (c.f. my result for $\tilde{\gamma}^{\rm Gaussian}$ of 1/0.86). A possible conclusion might lie in the shape of the shapelet basis set itself, which includes a Gaussian outer envelope for both the polar and Cartesian varieties (Refregier 2003). Real galaxies are known to have more gently decaying light curves, often being well fit by curves such as exponentials and Sérsic profiles. It is thought (Richard Massey, priv. comm.; Rhodes et al., in prep.) that systematic truncation of the outer galaxy profile, inherent in optimised shapelet model fitting in schemes such as presented by (Massey & Refregier 2005), may cause the preferential circularization of galaxy images. This would, inevitably, weaken measured lensing signals.

The results from $\tilde{\mathcal{F}}^{\rm DG}$ were rather too affected by noise to be able to truly investigate whether this problem was also biasing the first flexion signal, but the measurements currently appear unbiased to within 10% accuracy. In order to tighten this constraint many more FLIP images of the sort described will need to be analysed; it is also hoped that further analysis may help discover the serious issues affecting the estimation of $\mathcal{G}$. The high level of measurement noise on even the best shapelet estimators of flexion, illustrated by Figures 4.7, 4.8 and 4.9, is also a significant problem. An alternative flexion analysis method, based directly upon the KSB schema of Kaiser et al. (1995), has recently been described (Okura et al. 2007a). It will be very interesting to see if this approach, based on the measurement of Higher Order Lensing Image CharacteristicS (HOLICS: Okura et al. 2007b) yields better results. Recent work which compared HOLICS to shapelet flexion estimators Goldberg & Leonard (2007); Leonard et al. (2007) found that it did indeed perform better and was less noisy in particular. Unfortunately this comparison did not extend to a full PSF treatment with either method, and so a fair comparison of HOLICS and shapelet flexion measurements using FLIP-like images would be very interesting.

Finally, it is right to discuss whether the results of the FLIP analysis (and the bias factors calculated therefrom) are applicable to my analysis of the GEMS survey data. The FLIP data is not a perfect match to GEMS. The GEMS PSF varies with tile and chip position, and is not so well modelled. The FLIP galaxies, constructed as described in Section 5.2, will be different from those in GEMS, leading to differences such as that seen in the shear responsivity factor $\mathcal{R}$ (see Sections 4.2.5 and 5.3). Importantly also, the FLIP images do not contain correlated pixel noise such as that exhibited by GEMS due to the dithering processes in its data reduction (Caldwell et al. 2005). This may lead to additional circularization due to shapelet overfitting of correlated noise peaks, something I have tried to limit by setting $\theta_{\rm min,geom} = 1$ (Section 4.2.4), but also makes it more difficult to calculate the true SNR of any object. Due to this fact, the sample of tested FLIP galaxies and the GEMS sample are not more than roughly equivalent, and so any results must be treated with a certain amount of caution.

However, the results of the FLIP analysis have taught much about the practical considerations of shapelet

lensing measurement, and highlighted some important issues with proposed estimators. They also provide a first estimate of the typical bias expected in measurements of shear and flexion using the GEMS pipeline of Chapter 4. These bias factors will improve the accuracy of cosmological measurements made using $\gamma^{\rm obs}$, $\mathcal{F}^{\rm obs}$ and $\mathcal{G}^{\rm obs}$. It is such measurements that I now describe in the following Chapter, where I present a first combined galaxy-galaxy shear-flexion analysis of the GEMS survey data.

# CHAPTER 6

# GALAXY-GALAXY SHEAR-FLEXION

The ultimate aim of weak lensing measurement is to gain a better understanding of the structure and dynamics of the Universe on large scales. As was discussed in Chapter 1, there are many untested predictions of the ΛCDM model; testing these predictions offers hope for placing constraints on the properties of dark matter and dark energy. In particular, combined analyses of shear and flexion show promise for better understanding the physical interplay of visible and dark matter in the denser regions surrounding galaxies and galaxy clusters.

In this Chapter I present the results of a first, combined shear-flexion galaxy-galaxy lensing analysis using the lensing signal measured in the GEMS survey data. It was suggested in the results of Chapter 2 that study of both the shear and flexion signal around galaxies would lead to improvements in the constraints upon the halo mass distribution, when compared to a study of the shear signal alone. I discuss the constraints we place on the haloes of the GEMS galaxies using both shear and flexion, the implications for shapelet measurement of flexion, and the wider cosmological implications of the work.

## 6.1 Galaxy-galaxy lensing

Galaxy-galaxy lensing is the study of the weak gravitational distortion induced in distant background galaxies (often referred to as "sources") by the matter haloes of galaxies lying in the foreground ("lenses"). Suggested by Tyson et al. (1984), it was amongst the very first weak gravitational lensing signals to be detected (Brainerd et al. 1996), and is an attractive means of placing constraints on the mass distributions around visible galaxies. Since that time, significant constraints have been placed on models of galaxy dark matter haloes, using galaxy-galaxy lensing analyses of large datasets such as the Red Sequence Cluster Survey (RCS, see Hoekstra et al. 2004, hereafter HYG04 in this Chapter) and the Sloan Digital Sky Survey (SDSS, see Guzik & Seljak 2002; Sheldon et al. 2004; Mandelbaum et al. 2005, 2006a, hereafter M06 in this Chapter).

The first, and simplest means to quantify the galaxy-galaxy lensing signal is through the construction of galaxy-mass correlation functions, such as those presented by, for example, Brainerd et al. (1996), HYG04 and Sheldon et al. (2004). I present the analysis of the GEMS galaxy-mass correlation on small scales in Section 6.2, and use the results to place first fits on halo parameters for both the SIS and NFW mass models (see Chapters 1 and 2).

Section 6.3 describes my maximum likelihood treatment of the galaxy-galaxy lensing signal in the GEMS images, using a method based on that of Schneider & Rix (1997) but including modifications necessary for the accurate treatment of flexion measurements. Using multi-band galaxy photometry from the COMBO-17 survey (Classifying Objects by Medium-Band Observations in 17 filters, Wolf et al. 2003), which encompasses the GEMS field in the *Chandra* Deep Field South, I examine the dependence of SIS and NFW model parameters upon host galaxy colours and GEMS-derived morphology characteristics.

In this way I analyse the GEMS galaxy-galaxy signal by fitting measurements of the galaxy-mass cross-correlation, and through a complete maximum likelihood analysis of the total dataset; the results of each analysis are seen to be consistent with one another. Finally, implications for the success of shapelet flexion measurements in improving halo constraints are considered in Section 6.3.5, along with the cosmological implications of the maximum likelihood results.

## 6.2 Galaxy-mass cross-correlation functions

The galaxy-mass cross-correlation function may be obtained by measuring the shear and flexion of sources around foreground lenses, as a function of the angular source-lens separation on the sky plane $\theta_{\rm sep}$, and provides a useful illustration of the GEMS galaxy-galaxy lensing signal. For the shear, the quantity of interest is the "E-mode" tangential shear of the $i$th source-lens pair, defined as

$$\gamma_{\rm E}(\theta^i_{\rm sep}) = -\gamma^i_1 \cos(2\alpha^i) - \gamma^i_2 \sin(2\alpha^i), \tag{6.1}$$

where $\gamma^i_1$ and $\gamma^i_2$ are the measured components of the shear for the source galaxy, and $\alpha^i$ is the coordinate angle at the position of the lens between the $x$ axis (or negative RA axis) and the line joining the lens to the source. Similarly, the source "B-mode" shear is defined as

$$\gamma_{\rm B}(\theta^i_{\rm sep}) = \gamma^i_1 \sin(2\alpha^i) - \gamma^i_2 \cos(2\alpha^i), \tag{6.2}$$

which corresponds to the E-mode that would be measured if all sources were rotated by $45^\circ$. For the flexion, the signal of interest can again be encapsulated into source E-modes that are defined as

$$\mathcal{F}_{\rm E}(\theta^i_{\rm sep}) = -\mathcal{F}^i_1 \cos(\alpha^i) - \mathcal{F}^i_2 \sin(\alpha^i), \qquad \mathcal{G}_{\rm E}(\theta^i_{\rm sep}) = \mathcal{G}^i_1 \cos(3\alpha^i) + \mathcal{G}^i_2 \sin(3\alpha^i). \tag{6.3}$$

These E-modes will be equivalently referred to as radial flexions, due to their orientation relative to the sky position of the lens. The choice of signs is motivated by the results of Chapter 2, in which it was seen that the circularly symmetric density profiles of typical lens models (such as the SIS and NFW haloes) result in flexion that is directed inwardly towards the lens centre for $\mathcal{F}$ and outwardly for $\mathcal{G}$; see, e.g., Equations (2.9) and (2.10). This ensures that, as in the case of the shear E-mode of Equation (6.1), the flexion E-modes will be positive if we assume typical mass profiles around foreground lens galaxies. The B-mode signals are given by

$$\mathcal{F}_{\rm B}(\theta^i_{\rm sep}) = \mathcal{F}^i_1 \sin(\alpha^i) - \mathcal{F}^i_2 \cos(\alpha^i), \qquad \mathcal{G}_{\rm B}(\theta^i_{\rm sep}) = -\mathcal{G}^i_1 \sin(3\alpha^i) + \mathcal{G}^i_2 \cos(3\alpha^i), \tag{6.4}$$

which correspond to the E-mode signal of sources rotated by $90^\circ$ and $30^\circ$ for $\mathcal{F}$ and $\mathcal{G}$ respectively.

Measurements of these quantities can be used to estimate the galaxy-mass cross-correlation functions, defined as the average $\gamma_{\rm E}(\theta_{\rm sep})$, $\mathcal{F}_{\rm E}(\theta_{\rm sep})$ and $\mathcal{G}_{\rm E}(\theta_{\rm sep})$. Each source-lens pair is considered in turn, and the average (whether mean or median) tangential or radial signal is calculated for the total sample, binned in annuli of $\theta_{\rm sep}$. Weak lensing around foreground masses cannot produce a B-mode signal, and so analysis of the B-mode presents an opportunity for a check on the level of errors in the measurements.

Despite the fact that, when wishing to constrain the mass around individual galaxy haloes, galaxy-galaxy lensing data is generally best analysed as described in Section 6.3, simple fits to the galaxy-mass cross-correlation provide a useful check on these more sophisticated maximum likelihood results. I will present these fits to the cross-correlation functions in Section 6.2.2, but first describe the steps that went into the calculation of the galaxy-mass cross-correlation functions themselves.

### 6.2.1 Calculating the radial and tangential lensing signals

We select a sample of foreground lenses from a catalogue of GEMS galaxies matched to those in the COMBO-17 survey (Classifying Objects by Medium-Band Observations in 17 filters, Wolf et al. 2003) that lie within the GEMS field. The use of the 17-band photometric data of COMBO-17, combined with the *HST* image quality provided by GEMS, allows for the classification of the lens sample by both morphology and colour sequence, as will be seen in Section 6.3. Importantly, the COMBO-17 multi-band colour data allows the assignation of high quality photometric redshift estimates for a large proportion of the sample, which have been made publicly available by Wolf et al. (2004). The most reliable redshift estimates exist for galaxies with a COMBO-17 R-band magnitude $R < 24$, these objects reaching a typical redshift accuracy of $\Delta z \simeq 0.02(1+z)$ (Wolf et al. 2004).

The COMBO-GEMS matched catalogue used, which was supplied by Catherine Heymans, is that constructed by Marco Barden for the GEMS galaxy surface brightness and surface mass evolution analysis of Barden et al. (2005). This matches the $R < 24$ COMBO-17 catalogue to the catalogue of GEMS galaxies in the ACS F850LP filter image (see Caldwell et al. 2005), identifying pairs of galaxies between surveys with a centroid tolerance of 0.5 arcsec. The matched catalogue then describes 8407 galaxies in

the GEMS field, containing reliable redshift estimates and multicolour photometry from the COMBO-17 catalogue, GEMS-measured astrometry, and Sérsic profile morphology estimates made from GEMS using the GALFIT fitting code (Peng et al. 2002) as described in Barden et al. (2005). Finally, a redshift cut of $0.2 < z < 0.8$ is imposed upon the catalogue so as to match the sample of galaxies analysed in Section 6.3 (the reasons for this cut are described in Section 6.3.3) and extremely bright objects with $R < 18$ are removed. The remaining 4995 galaxies are then used to define the lens catalogue, which has a median redshift of $z_{\rm m} = 0.58$. The COMBO-17 catalogue also contains estimates of the SDSS $r$-band absolute magnitude for each object, and from this we calculate a median $r$-band luminosity of $(L_r^*)_{\rm m} = 0.33L_r^*$, where $L_r^* = 10^{10}h^{-2}L_\odot$.

The background sources are taken from the shapelet measured $\gamma^{\rm obs}$, $\mathcal{F}^{\rm obs}$ and $\mathcal{G}^{\rm obs}$ catalogues created using the GEMS F606W images as described in Chapter 4. The source sample is defined as galaxies with SExtractor measured magnitudes lying in the range $24.0 < m_{606} < 27.0$. I take a two-stage approach in order to minimise the confusion between foreground and background for objects in the source and lens samples. Firstly, I performed a match of the objects in the Barden et al. (2005) COMBO-GEMS F850LP catalogue to those in the grand catalogue of shapelet modelled galaxies in the GEMS F606W images; using a centroid tolerance of 0.5 arcsec I found a successful, non-confused match for 6674 of the 8407 objects ($\simeq 80\%$). The E-modes and B-modes of source-lens pairs for which the lens redshift is known to be higher than that of the source are then excluded from the calculation of sample averages.

For sources without a match to the COMBO-GEMS catalogue (i.e., the vast majority) we instead make an estimate of the likely source redshift. H05 present the following linear relationship between magnitude $m_{606}$ and median redshift for a population of galaxies at that magnitude:

$$z_{\rm m} = -3.132 + 0.164m_{606} \ \ (21.8 < m_{606} < 24.4). \tag{6.5}$$

This relationship is calculated using photometric redshift data from the COMBO-17 survey (Wolf et al. 2004) and spectroscopic redshifts from the CDFS VIRMOS-VLT Deep Survey (Le Fèvre et al. 2004). To estimate the the median redshift of our source galaxies beyond $m_{606} = 24.4$ we extrapolate the above relationship, as justified in H05 using measurements of the Hubble Deep Field North (HDFN) (see Lanzetta et al. 1996; Fernández-Soto et al. 1999). Source galaxy redshifts are then estimated using Equation (6.5), and if the redshift is found to lie within $\Delta z = 0.1$ of the lens redshift, the source-lens pair is excluded from the calculation of average E- and B-mode signals.

I calculated the mean $\gamma_{\rm E}$ and $\gamma_{\rm B}$ in ten angular bins in the range 2 arcsec $< \theta_{\rm sep} <$ 60 arcsec, using the $\gamma^{\rm obs}$ for each source described in Section 4.2.5. The lower limit on $\theta_{\rm sep}$ was chosen to avoid significant contamination of lensing measurements due to overlapping galaxy isophotes, and is the same level chosen by Heymans et al. (2006a) for their subsample of large, elliptical GEMS galaxies. The upper limit was chosen as the separation beyond which the signal becomes difficult to discern from sample noise. The median E- and B-mode flexion signals were similarly calculated, but using 10 angular bins in the range 2 arcsec $< \theta_{\rm sep} <$ 10 arcsec for $\mathcal{F}^{\rm obs}$ and 2 arcsec $< \theta_{\rm sep} <$ 20 arcsec for $\mathcal{G}^{\rm obs}$. Figure 6.1 shows the E-mode and B-mode shear and flexion signals as measured for our GEMS source and lens galaxy samples.

The dashed lines plotted in Figure 6.1 depict approximate predictions for NFW halos made using the results of Navarro et al. (1997), Guzik & Seljak (2002), HYG04 and Section 2.1.4. Assuming a mass scaling of $M_{200} \propto L^{1.2}$ motivated by the results of Guzik & Seljak (2002), HYG04 found a best-fitting fiducial virial mass of $M_{200}^* = (8.4 \pm 1.1) \times 10^{11}h^{-1}M_\odot$ for galaxies with B-band luminosity $L_B^* = 10^{10}h^{-2}L_\odot$;

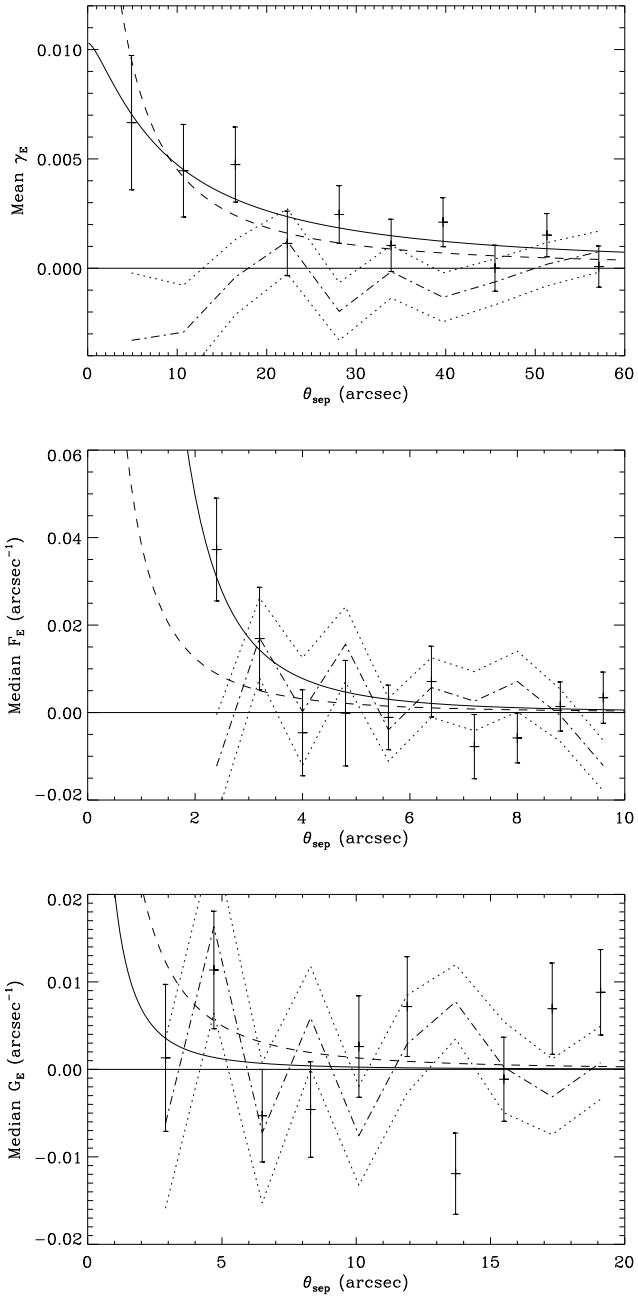


Figure 6.1: (*a*) Mean $\gamma_{\rm E}$ within angular annuli around foreground lenses (points). (*b*) Median $\mathcal{F}_{\rm E}$, and (*c*) median radial $\mathcal{G}_{\rm E}$, within angular annuli around foreground lenses (points). The dot-dashed and dotted lines show the B-mode signals and uncertainty, which we note are largely consistent with zero but noisy for $\mathcal{F}$ and $\mathcal{G}$. Note also the reductions in angular scale between (*a*) and (*b*), and (*c*). The dashed line shows a prediction based on the results of HYG04 and Navarro et al. (1997), while the solid line shows the best fitting NFW model (see Section 6.2.2).

Guzik & Seljak (2002) themselves found $M_{200} = (9.3 \pm 1.6) \times 10^{11} h^{-1} M_{\odot}$ for galaxies with SDSS $g$-band luminosity of $L_g \simeq 1.1. \times 10^{10} h^{-2} M_{\odot}$, in good agreement (see HYG04). Taking these results (which also agree with Kleinheinrich et al. 2006), and including evidence for the growth of the virial mass to stellar mass ratio with redshift (Heymans et al. 2006a), I make an approximate prediction for the fiducial virial mass in our lens sample of $M^*_{200} \simeq 9 \times 10^{11} h^{-1} M_{\odot}$, corresponding to an $r$-band luminosity of $L^*_r = 10^{10} h^{-2} L_{\odot}$.

As described above, the luminosity of our lens sample is $0.33 L^*_r$, which if we adopt the same scaling as HYG04 leads to a value of $(M_{200})_{\rm m} \simeq 2.4 \times 10^{11} h^{-1} M_{\odot}$ as our approximate estimate for the median virial mass of our lens sample. In order to estimate the corresponding concentration $c$ we use Julio Navarro's program `charden.f` to calculate the Navarro et al. (1997) prediction for an NFW halo of this mass at redshift $z = 0.58$. Assuming a flat $\Lambda$CDM cosmology with $\Omega_{m,0} = 0.25$ and $\Omega_{\Lambda,0} = 0.75$ (Spergel et al. 2007), and a mass variance $\sigma_8 = 0.8$ (Benjamin et al. 2007), a concentration prediction of 7.41 is calculated; note that we will assume this cosmological model in all subsequent calculations in this Chapter. The dashed line in Figure 6.1 shows the NFW shear and flexion predicted for a halo of this mass, concentration and redshift, with source redshifts of $z_{\rm s} = 1.08, 1.03$ and 1.02 for $\gamma$, $\mathcal{F}$ and $\mathcal{G}$ respectively (these being the median redshift of the source samples for each measure, calculated using Equation 6.5).

The quality of the match of my measurements from the GEMS data to this prediction will be discussed in Section 6.2.3. Firstly, we describe the $\chi^2$ fitting of SIS and NFW halo models to the galaxy-mass cross-correlation functions, and examine the constraints these simple galaxy-galaxy lensing results place on the lens sample haloes.

### 6.2.2 Fitting lens models to the galaxy-mass cross-correlation functions

It is useful and illustrative to fit simple lens models to E-mode measurements seen in Figure 6.1, which constitute a first simple measurement of the global average lens properties for our sample. This also allows a check for consistency both between shear and flexion, and with the maximum likelihood results of Section 6.3.

To begin with, I performed a fit of the shear and flexion data using a simple SIS lens model. Following Kleinheinrich et al. (2006), I use a Faber-Jackson and Tully-Fisher type parameterization of the relationship between the SIS velocity dispersion and galaxy luminosity:

$$\frac{\sigma_v}{\sigma^*_v} = \left( \frac{L_r}{L^*_r} \right)^{\eta}, \tag{6.6}$$

where $\sigma^*_v$ is then the velocity dispersion for a galaxy of luminosity $L^*_r$. I first performed a $\chi^2$ fit using a simple SIS lens model to the shear galaxy-mass correlation functions, corresponding to a galaxy of $L_r = 0.33 L^*_r$ and $z_{\rm l} = 0.58$ (the median values for this lens sample, as described in Section 6.2.1). Fitting the data directly, I measure a lensing signal equivalent to a lens with $\sigma_v = 88^{+9}_{-10}$ kms$^{-1}$ at the median lens redshift. Assuming a fixed value of $\eta = 0.28$, motivated by Kleinheinrich et al. (2006), this leads to an estimate of $\sigma^*_v = 120^{+12}_{-14}$ kms$^{-1}$. This is marginally lower lower than the $\sigma^*_v = 156^{+18}_{-24}$ kms$^{-1}$ found by Kleinheinrich et al. (2006) in their galaxy-galaxy lensing analysis of all three COMBO-17 fields.

If each annular bin of median $\mathcal{F}_{\rm E}$ and $\mathcal{G}_{\rm E}$ contains a sufficient number of source-lens pairs, then the sample median in that bin will be approximately normally distributed (see Lupton (1993)). The smallest number of source-lens pairs is found in the most interior bin of the median $\mathcal{F}_{\rm E}$ measurements, having only 336. Assuming this is sufficient (see Section 6.2.3), a $\chi^2$ fit to the median $\mathcal{F}_{\rm E}$ measurements gives $\sigma_v^* = 219^{+37}_{-45}$ kms$^{-1}$, which is inconsistent with the shear measurements from GEMS by around $2\sigma$. In contrast to this result, the second flexion signal gives a far lower estimate for the fiducial velocity dispersion, finding $\sigma_v^* = 59^{+43}_{-59}$ kms$^{-1}$. The lower limit in this measurement is imposed only by the prior that $\sigma_v^* > 0$. I discuss some of the implications of these results in Section 6.2.3, but before doing that investigate the parameter constraints for NFW halo models.

In estimating the NFW parameter constraints from a simple fit to the E-mode lensing signals from GEMS, I assume the virial mass scales with luminosity as $M_{200} \propto L_r^{1.2}$ (HYG04, Guzik & Seljak 2002). Combining this result with the theoretical findings of Neto et al. (2007) and Macciò et al. (2007), I assume that the concentration of NFW haloes varies with luminosity as $c \propto L_r^{-0.083}$. I then analyse the data in a similar fashion to the SIS fits, by comparing the E-mode data to predictions for a single lens model corresponding to a galaxy of the lens sample median luminosity and redshift.

Again assuming the errors on annular estimates of the E-mode signal to be normally distributed, I calculated contours of constant $\chi^2$ for the fiducial parameters $M_{200}^*$ and $c^*$ required for the single NFW lens fit to the data, using the scalings described above. This was done by calculating the $\chi^2$ for each point in a $250 \times 250$ grid of evenly spaced mass and concentration values. The resulting confidence contours are plotted in Figure 6.2 and the best-fitting curves are shown as the solid lines in Figure 6.1. The parameter estimates from the $\mathcal{F}_{\rm E}$ appear to support an almost arbitrarily large $c^*$, so I limit this figure by imposing a prior of $c^* < 50$ throughout the analysis (this being significantly larger than that predicted by simulation results, e.g., Neto et al. 2007; Macciò et al. 2007, and by observational studies HYG04).

These results appear qualitatively similar to those for the SIS lens model, finding a $\simeq 2\sigma$ discrepancy between the results from $\gamma_{\rm E}$ and $\mathcal{F}_{\rm E}$, and more severe tension between results from $\mathcal{F}_{\rm E}$ and $\mathcal{G}_{\rm E}$. The addition of flexion measurements could not be said to significantly improve confidence intervals on the fitted parameters here. Using shear alone, I find a single lens model fiducial mass of $M_{200}^* = 1.60^{+1.06}_{-0.74} \times 10^{12} h^{-1} M_\odot$, larger than but consistent with previous estimates (Guzik & Seljak 2002; HYG04; Kleinheinrich et al. 2006). For the fiducial concentration I find $c^* = 2.9^{+4.3}_{-1.9}$, which is lower than the $c > 7$ (at 2-$\sigma$ confidence) found by Kleinheinrich et al. (2006), but in better agreement with the Navarro et al. (1997) prediction of $c^* = 6.6$ for a halo of this best-fitting mass, as calculated using `charden.f`.

Combining measurements of $\gamma_{\rm E}$ and $\mathcal{F}_{\rm E}$ (top panel of Figure 6.2) I find instead a best fitting fiducial mass of $M_{200}^* = 1.49^{+0.99}_{-0.70} \times 10^{10} h^{-1} M_\odot$ and concentration $c^* = 3.8^{+7.2}_{-2.2}$. The high concentration of the fit to the $\mathcal{F}_{\rm E}$ data has in fact caused a widening of concentration parameter constraints, and slight reduction ($\simeq 6\%$) in constraints upon the mass. Combining measurements from all three E-mode signals (whether this is justified will be discussed in Section 6.2.3 below) gives constraints of $M_{200}^* = 1.48^{+1.04}_{-0.69} \times 10^{10} h^{-1} M_\odot$, $c^* = 4.9^{+2.2}_{-3.6}$. These last parameter constraints offer no significant improvement over those for shear alone, due to the apparent tension between measurements of $\mathcal{F}_{\rm E}$ and $\mathcal{G}_{\rm E}$.

As can be seen from Figure 6.2, the first flexion data fit the predicted NFW halo model poorly, and is incompatible with the shear results at an approximately 2-$\sigma$ level. In the following Section I go on to discuss these results, including possible reasons for the disparities between shear and flexion, and implications for the more detailed maximum likelihood analysis that will follow in Section 6.3.

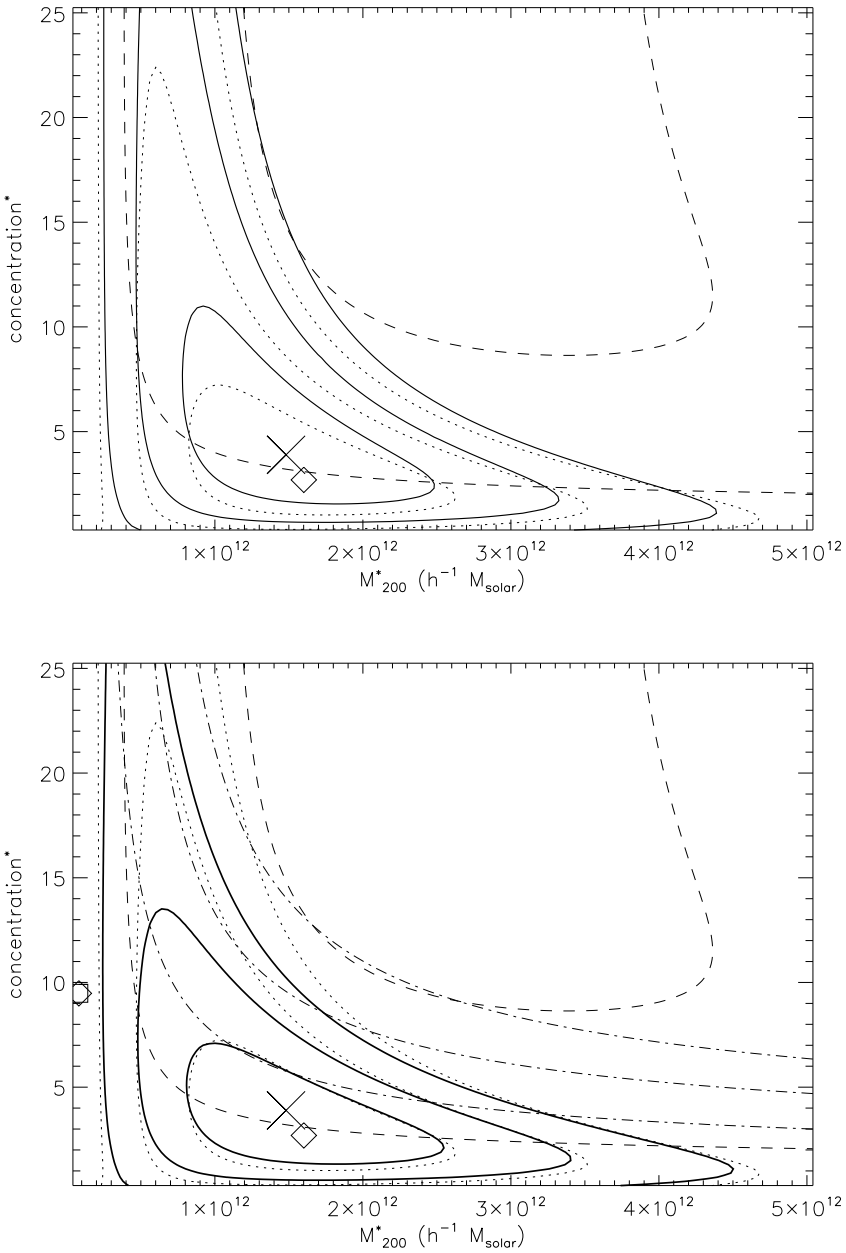


Figure 6.2: Confidence contours for fiducial NFW halo parameters from fits to the galaxy-mass cross-correlation functions. The top panel shows the fiducial NFW parameter constraints from fits to the E-mode $\gamma$ (dotted lines), $\mathcal{F}$ (dashed lines) and combined measurements (solid lines) in GEMS. The shear best fit is marked by a diamond, the flexion best fit lies outside the area shown, falling at $M^*_{200} = 2.36 \times 10^{12} M_\odot$ and the prior limited concentration $c = 50$. The combined best estimate is marked by a cross. The bottom panel shows the same but also includes measurements using $\mathcal{G}$ (dot-dashed line, best fit marked by a star). The contour intervals correspond to regions of 68%, 95% and 99.7% confidence, estimated by assuming normally distributed errors on the binned sample mean and median for shear and flexion.

### 6.2.3 Discussion of fitting results

Measurements of flexion made using the shapelet pipeline of Chapter 4 make little improvement to the fitted parameters for the lens models described in Section 6.2.2. Looking at Figure 6.1, this is perhaps unsurprising given the large noise and scatter on estimates for the median E and B-mode flexion. It seems clear that, in order to realise the potential improvements suggested the results of Chapter 2, flexion needs to be measured more stably than can be achieved using the GEMS shapelet pipeline. Reassuringly, fitting a simple lens model using the shear measurements from GEMS gives results that are entirely consistent with previous lensing studies.

Apart from the large noise in estimates of the sample median, the most striking result from the $\mathcal{F}_{\rm E}$ analysis is that tends to predict more massive and more concentrated halo models than found by the GEMS shears and elsewhere in the literature (e.g., HYG04). The $\mathcal{F}_{\rm E}$ best fit concentration was particularly large, and limited by the prior to $c^* = 50$ (at an $M^*_{200} = 2.36 \times 10^{12} h^{-1} M_\odot$. This concentration agrees better the findings of Kleinheinrich et al. (2006), although whether this agreement is for the same reasons in each study is less clear. Examination of the measured $\mathcal{F}_{\rm E}$ in Figure 6.1 reveals two points of interest. Firstly, the signal is consistent with zero, except for the two interior points; indeed, the outermost of these is closely consistent with the non-zero B-mode and so could be considered non-significant. Secondly, the inner point appears to be a relatively strong ($3.2\sigma$) detection of flexion signal, but at a level that is larger than expected given the existing predictions for NFW haloes described in Section 6.2.1.

This discrepancy could be a fluke of the noise (the discrepancies between $\gamma$ and $\mathcal{F}$ results for the SIS and NFW parameters appear, from 6.2, to be in the range 1-$2\sigma$), a previously unconsidered systematic effect, or evidence for tension between lensing measurements that probe the SIS and NFW haloes on differing scales. Regarding the noise, I may be underestimating the uncertainty in the $\mathcal{F}$-derived constraints by assuming the sample median for the innermost bin to be normally distributed. As mentioned above, this bin contains as few as 336 source-lens pairs, which may be insufficient given the highly non-Gaussian shape of the underlying flexion distribution. This is one more reason to embark on a full, maximum likelihood analysis of the sort described in Section 6.3.

A plausible systematic explanation for the discrepancy is the contamination of source light profiles due to the outer light profiles of the nearby, bright foreground lens galaxies. This could create a light gradient across the source that mimics a higher order gravitational signal, and could be a serious consideration (requiring careful correction) in the measurement of the first flexion. Shapelets could model such contamination, as the current code applies a top-hat mask to nearby galaxies and therefore misses their outer regions (Section 4.2.2). In Chapter 7, I will discuss this problem further and suggest means by which the effect could be calibrated in the future. If such calibration shows that this artificial "flexion bleed" effect is minimal, then the measurement must either be explained by noise or by divergence from either the SIS or NFW halo model at small scales, which will also be discussed further in Chapter 7.

I now consider the results from the second flexion, for which $\mathcal{G}_{\rm E}$ is ubiquitously consistent with zero (see Figure 6.1). The significant noise in these measurements is also indicated by the B-mode signal. This still allows the placing of limiting upper bounds on velocity dispersion, mass and concentration parameters as described in Section 6.2.1 and shown in the lower panel of Figure 6.2. However, even this may be fraught with uncertainty, due to the large calibration factor of (1/2.15) used in the best estimate for $\mathcal{G}^{\rm obs}$ (See Sections 4.2.5, 5.3 and 5.4). The reason why the shapelet software consistently overestimates input second

flexions is unclear, and it seems a substantial risk to place too much faith in upper limits that are based solely on the value of a poorly understood bias factor.

For this reason I exclude the GEMS second flexion results from any further cosmological analysis; this same step was also taken by Leonard et al. (2007) and Okura et al. (2007a) in their flexion analyses of the Abell 1689 galaxy cluster, although this was simply because they found the measure too noisy. The remaining cosmological measurements which I make in this Thesis take the form of a maximum likelihood investigation of the galaxy-galaxy lensing information in GEMS. This technique, based on that proposed by Schneider & Rix (1997), allows the full extraction of galaxy halo information from weak lensing data. I have modified the technique to make it suitable for use with flexion and in doing so have improved its treatment of shear also, as I will now describe.

## 6.3 Modified maximum likelihood analysis

In order to use measurements of shear and flexion to place accurate constraints upon the properties of galaxy dark matter halos I employ a modified form of the Schneider & Rix (1997) maximum likelihood analysis (for recent implementations see Kleinheinrich et al. 2006; Heymans et al. 2006a). In a similar fashion to Section 6.2.2, I assume two different models in turn, a luminosity-scaling SIS lens model and a luminosity-scaling NFW halo model. Using the modified Schneider & Rix (1997) method described below, I place constraints on the values of fiducial model parameters and luminosity scalings using all the galaxy-galaxy lensing information available from the GEMS shear and flexion catalogues described in Chapter 4. It should be stressed that the results obtained should be interpreted as parameter constraints only under the assumption that our adopted lens model is the *correct* model, a common feature of all maximum likelihood analyses. This entails understanding that the choice of model will directly impact any results, and that inconsistencies in the results may be evidence for imperfections in the model.

In carrying out such an analysis, it is also necessary to assume that all the lensing mass in our system is associated with galaxy haloes. It is known (H05; Schrabback et al. 2007) that the GEMS field covers a significantly underdense region of the Universe, and so this assumption here represents a better approximation than in many previous studies. Furthermore, Kleinheinrich et al. (2006) found that corrections made for the presence of the Abell 901/2 supercluster in their COMB0-17 fields made little difference to lens model parameter constraints, suggesting that the approximation is reasonable even in more dense regions of space. Given these considerations, I now go on to outline the basics of the Schneider & Rix (1997) galaxy-galaxy lensing analysis method, before describing the modifications made to suit both the GEMS data and measurements of gravitational flexion.

### 6.3.1 Standard formalism

In the formalism specified by Schneider & Rix (1997), we first define an angle $\theta_{\rm max}$, which is the maximum separation scale on which we will consider the galaxy-galaxy lensing of source-lens pairs. We must then immediately remove all sources less than $\theta_{\rm max}$ away from the field boundary, as these may have been affected by unseen lenses. Each remaining source can then be assigned a predicted shear or flexion by

summing contributions from the lens models of all foreground galaxies within $\theta_{\rm max}$. Although shears and flexions from multiple lens deflections do not add linearly, this is a reasonable approximation for the weak lensing we expect around galaxy haloes (Schneider & Rix 1997; Schneider & Er 2007).

In the GEMS data the redshifts of source galaxies are unknown, and we must therefore assign these galaxies a magnitude dependent redshift probability distribution $p(z|m_{606})$. We choose the same dependence used by Heymans et al. (2006a) and H05,

$$p(z|m_{606}) \propto z^2 \exp\left[-\left(\frac{z}{z_0(m_{606})}\right)^{1.5}\right], \tag{6.7}$$

where $z_0$ is calculated from the median redshift $z_{\rm m}(m_{606})$ with $z_0 = z_m/1.4142$ (Baugh & Efstathiou 1994). This median redshift can be estimated using Equation (6.5). Note that if the estimate for the source galaxy places it within $\Delta z = 0.1$, or in the foreground of the lens galaxy, then a zero $\xi$ is calculated.

Recent work by Schrabback et al. (2007) presents a different model for the redshift distribution in the GEMS, based on a careful analysis of GEMS imaging data compared with redshift results from the GOODS-MUSIC catalogue of Grazian et al. (2006). From a maximum likelihood fit to a catalogue of redshift-matched GEMS source galaxies they derive a redshift distribution that is less narrowly peaked, and with fewer galaxies at high redshift, than the distribution in Equation (6.7). Using this Schrabback et al. (2007) fit model (rather than the directly calculated median as used by H05) these authors also derive a different expression for Equation (6.5), with a significantly steeper gradient of increasing median redshift against magnitude. For the maximum likelihood method I present, this analysis is not repeated for my GEMS shear and flexion catalogue galaxies and I use the H05 estimates of Equations (6.5) and (6.7).

As a check on the level of possible errors caused by neglecting the fuller treatment of Schrabback et al. (2007), I compare my predicted median source redshift (taken from the magnitude-selected catalogue of objects with measured $\gamma^{\rm obs}$, described in Section 6.2.1) with the Schrabback et al. (2007) prediction, finding

$$z_{\rm m}^{\rm H05} = 1.1 \pm 0.1, \quad z_{\rm m}^{\rm S07} = 1.3 \pm 0.1 \tag{6.8}$$

for the median source redshift of our sample as calculated using the H05 and Schrabback et al. (2007) redshift prescription respectively. Using these results with Equations (2.28) and (2.30), and assuming the Schrabback et al. (2007) model to be correct, use of the H05 redshift estimate for a median redshift source would lead to an underprediction of the lensing signal. Assuming a lens at the sample median redshift $z = 0.58$, we can estimate a typical underestimation factor of

$$f_z = \frac{D_{\rm ls}^{\rm H05}}{D_{\rm s}^{\rm H05}} \times \frac{D_{\rm s}^{\rm S07}}{D_{\rm ls}^{\rm S05}} \approx 0.81 \tag{6.9}$$

for the GEMS galaxies. This is certainly within the sample variance of our galaxy-galaxy flexion measurements as seen in Figure 6.1, and roughly within those of shear. It will be interesting in the future to make a more thorough comparison of the error impact upon galaxy-galaxy lensing constraints due of the use of a poor source redshift distribution; such an analysis was conducted for cosmic shear by van Waerbeke et al. (2006).

Given the H05 redshift distribution, but with the caveats expressed above, the expectation value of the galaxy-galaxy lensing signal at each source, due to the summed contributions from nearby lenses, may

then be calculated. This can be done using Monte Carlo integration. A source galaxy redshift estimate $z_s^i$ is drawn from $p(z|m_{606})$, for $i = 1, ..., N_{\rm MC}$ where $N_{\rm MC} = 50$ (Schneider & Rix 1997 found that typically any number above 20 was sufficient). The expectation of the weak lensing signal for each source is then simply

$$\langle \xi \rangle = \frac{1}{N_{\rm MC}} \sum_{i=1}^{N_{\rm MC}} \xi^i, \tag{6.10}$$

where $\xi = \gamma, \mathcal{F}$ or $\mathcal{G}$, calculated using the lens model being tested (see, e.g., Chapter 2 which describes how to make these model calculations). Using this prediction, the *intrinsic* value $\xi^{\rm s}$ for each source, i.e. that which we would expect in the absence of lensing, can be approximated. With a measured value of the signal $\xi^{\rm obs}$ for this source, we may write $\xi^{\rm s} \simeq \xi^{\rm obs} - \langle \xi \rangle$ where we again assume that lensing-induced $\xi$ is small. Given an assumed or approximate form for the probability distribution $p_\xi(\xi^{\rm s}){\rm d}^2\xi^{\rm s}$, the best-fitting dark matter halo parameters are determined by maximising likelihoods

$$L_\xi = \prod_j [p_\xi(\xi^{\rm s})_j], \tag{6.11}$$

where the product is carried over all source galaxies, labelled by $j$. The total likelihood, using all measurements of $\xi = \gamma, \mathcal{F}$ and $\mathcal{G}$, is then $L = L_\gamma \times L_\mathcal{F} \times L_\mathcal{G}$. This last expression makes the assumption that each of the likelihoods is independent; we now briefly discuss this assumption.

The correlation in measurements of shear and flexion due to the gravitational distortions will be negligible for the weak shear and flexion we expect for the galaxy-galaxy lensing signal in the GEMS images. As shown by Schneider & Er (2007) this statistical independence may break down in the regimes between strong and weak lensing, but for typical GEMS galaxies we do not expect $\gamma$, $\mathcal{F}$ or $\mathcal{G}$ of sufficient strength to make this a significant effect.

However, there may be correlations in the measurements of shear and flexion due to imperfections in the measurement method itself. This is discussed briefly in Section 5.4, but will require simulations of a size significantly larger than the FLIP images (which were of a comparable size to the GEMS survey images) in order to be fully explored; this is an opportunity for future work. However, as seen in Figure 6.1, the galaxy-galaxy flexion in the GEMS survey is not detected at very high significance, and is indeed not detected at all for measurements of the $\mathcal{G}_{\rm E}$ signal. In the FLIP analysis, there was no sign of the 20-30% covariance biases between $\gamma$ and $\mathcal{F}$ measurement that would be necessary to make such a systematic significant at a level greater than the statistical uncertainty upon $\mathcal{F}_{\rm E}$ (on the limited scales where it is detected). We therefore neglect any such covariances, and make the first approximation that our measurements of shear and flexion can be considered independent.

### 6.3.2 Flexion modifications

With the extension of the Schneider & Rix (1997) technique to include measurements of gravitational flexion it is necessary to alter certain assumptions and input parameters. Foremost is the need to assume a realistic functional form for the distribution of intrinsic signal $p_\xi(\xi^{\rm s}){\rm d}^2\xi^{\rm s}$. For the case of shear, Schneider

& Rix (1997) and all subsequent analyses have assumed a Gaussian distribution of the form:

$$p_\xi(\xi^{\rm s}) = \frac{1}{2\pi\sigma_\xi^2}\exp\left[-\frac{|\xi^{\rm s}|^2}{2\sigma_\xi^2}\right]. \tag{6.12}$$

This is an acceptable approximation in the case of observed weak shear, but as seen in Figures 4.8 and 4.9 it would constitute a severe misrepresentation in the cases of $\xi = \mathcal{F}^{\rm obs}$ or $\xi = \mathcal{G}^{\rm obs}$. Instead, we must find more realistic representations of $p_{\mathcal{F}}(\mathcal{F}^s)$ and $p_{\mathcal{G}}(\mathcal{G}^s)$.

The distribution of measured flexions (and indeed also shears) in the absence of gravitational lensing may be accurately estimated from the lensing data itself. In the weak regime of GEMS galaxy-galaxy lensing the presence of a gravitational lensing signal will contribute only to a minor broadening of the distributions seen in Figures 4.7, 4.8 and 4.9. In short, we may use measurements of $\xi^{\rm obs}$ to approximate $p_\xi(\xi^{\rm s}) \simeq p_\xi(\xi^{\rm obs})$. The extent to which this approximation causes artificial broadening of the probability density function can be easily estimated for typical galaxy haloes (see, e.g., Chapter 2; BGRT06), and is found to be negligible.

Given the distributions of measured $\gamma$, $\mathcal{F}$ and $\mathcal{G}$ from Section 4.2.5, there are two methods of approximating the relevant probability functions. The first is to simply use suitably binned, count-normalised histograms as discrete representations of $p_\xi$. However, this approach will add noise and potentially bias constraints in cases where variations in the input halo parameters alter $\langle\xi\rangle$ by an amount smaller than the bin scale. GEMS does not provide enough data to make the histograms of $\gamma$, $\mathcal{F}$ and $\mathcal{G}$ smooth on sufficiently small scales to avoid this problem, but this method may perhaps be useful for future survey datasets.

The second approach is to fit smoothly-varying analytic functions to the discretely measured distributions of $\xi^{\rm obs}$ across the $\xi_1$-$\xi_2$ plane. This may be done simply if we make the reasonable assumption of circular symmetry in the bivariate distribution, so that $p_\xi(\xi^{\rm s}) \equiv p_\xi(|\xi^{\rm s}|,\phi) = p_\xi(|\xi^{\rm s}|)$ only. In this case, the probability of finding a galaxy with $\xi^{\rm s}$ of magnitude between $|\xi^s|$ and $|\xi^s| + {\rm d}|\xi^{\rm s}|$ is described by the one-dimensional, marginalized density

$$p_m(|\xi|) = \oint p_\xi(\xi)|\xi|{\rm d}\phi = 2\pi|\xi|p_\xi(\xi). \tag{6.13}$$

The quantity $p_m(|\xi|)/(2\pi|\xi|)$ may be easily estimated from the data, and fit using suitable functions to estimate $p_\xi(\xi)$.

For the shear, it was found that functions of the form

$$p_\gamma(\gamma^{\rm s}) = \frac{b^{\left(\frac{2}{c}\right)}c}{2\pi\Gamma\left(\frac{2}{c}\right)}\exp\left[-b|\gamma^{\rm s}|^c\right], \tag{6.14}$$

which is essentially a generalized form of a Gaussian with a correctly normalizing prefactor. This proved to give a good representation of the data. Using the Levenberg-Marquardt algorithm (see, e.g., Press et al. 1992) to perform a non-linear, least-squares fit, I found values of $b = 6.674 \pm 0.033$ and $c = 1.350 \pm 0.013$, again indicating the small but significant non-Gaussianity in the distribution of measured shears.

In the case of $\mathcal{F}^{\rm obs}$ and $\mathcal{G}^{\rm obs}$, the function expressed in Equation (6.14) was not able to reproduce the shape of $p_\xi(\xi^{\rm s})$. However, generalizing (6.14) to

$$p_\xi(\xi^{\rm s}) = \frac{b^{\left(\frac{2+a}{c}\right)}c}{2\pi\Gamma\left(\frac{2+a}{c}\right)}(\xi^{\rm s})^a\exp\left[-b|\xi^{\rm s}|^c\right] \tag{6.15}$$

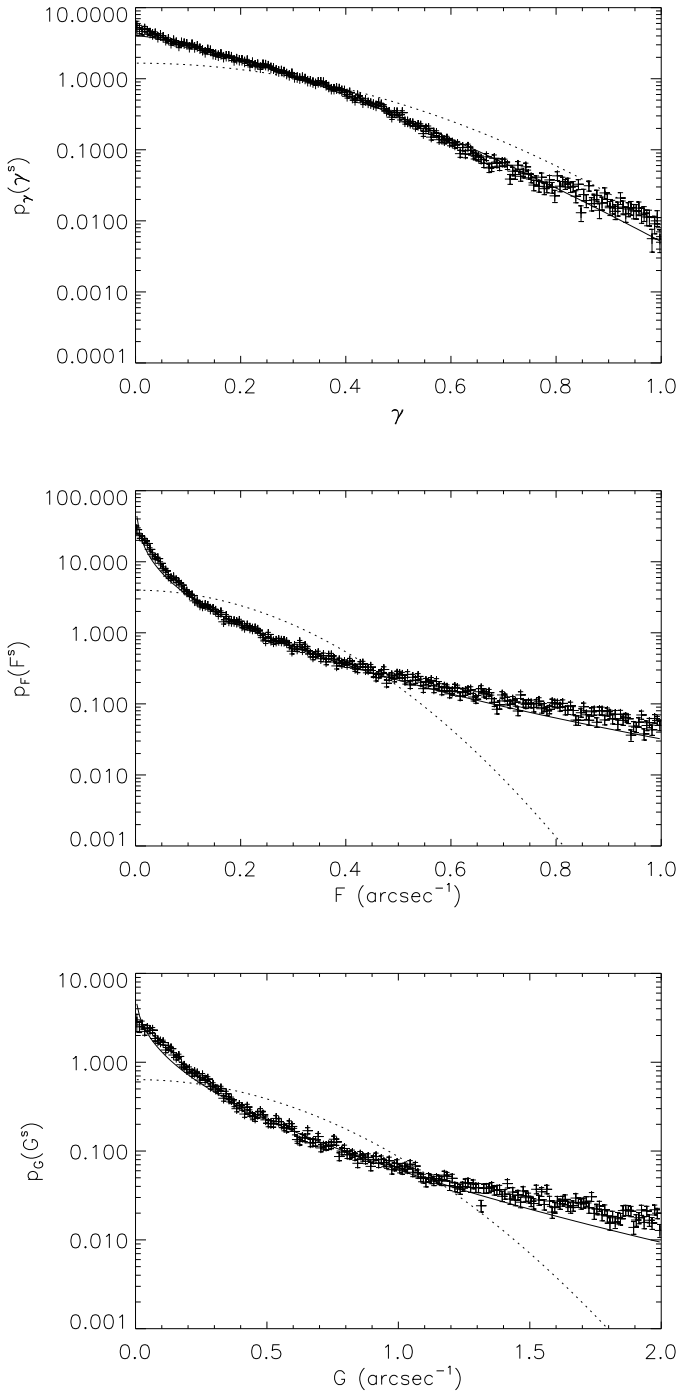


Figure 6.3: Measured $p_m(|\xi|)/(2\pi|\xi|)$ and best fitting curve (solid line) for (*a*) shear, (*b*) first flexion and (*c*) second flexion. Poisson errors alone, from the histograms used to estimate $p_m(|\xi|)$, are plotted on each measured point; no estimate of measurement uncertainty is included. For comparison, we also plot normalized Gaussian curves (dotted line), with $\sigma_\gamma = 0.31$ (the value used in the analysis of Heymans et al. 2006a), and illustrative values of $\sigma_{\mathcal{F}} = 0.2$ and $\sigma_{\mathcal{G}} = 0.5$.

provided a reasonable fit to the data, with values of $a = -0.260 \pm 0.061$, $b = 5.99 \pm 0.37$ and $c = 0.491 \pm 0.026$ for $\mathcal{F}^{\rm obs}$; $a = -0.118 \pm 0.069$, $b = 3.90 \pm 0.34$ and $c = 0.547 \pm 0.031$ for $\mathcal{G}^{\rm obs}$. In Figure 6.3 we plot these best fitting probability density functions for shear and flexion, along with Gaussian curves for comparison; it can be seen that Equations (6.14) and (6.15) provide an improvement, especially in the case of flexion. The fit to $p_\gamma(\gamma^{\rm s})$ performs better than a Gaussian particularly at describing the central peak. Reduced $\chi^2$ for these fits varied from $\simeq 2$ (shear) to $\simeq 4$ (second flexion).

As a final check for consistency, the probability distributions we expect for the individual components $\xi_1$ and $\xi_2$ may be recovered by marginalization:

$$p_i(\xi_i^{\rm s}) = \int_0^\infty p_\xi(\xi^{\rm s}) {\rm d}\xi_j^{\rm s}, \tag{6.16}$$

where $i, j = 1, 2$ and $i \neq j$. For (6.14) and (6.15) this must be done numerically. The resulting one-dimensional distributions are plotted as a solid line in Figure 6.4 (having been scaled to the number of source objects), and can be seen to provide a good fit to the measured histograms of $\gamma_i^{\rm obs}$, $\mathcal{F}_i^{\rm obs}$ and $\mathcal{G}_i^{\rm obs}$. It is noted noted that there is slight evidence for a deficit in $p_\mathcal{F}$ and $p_\mathcal{G}$ in the central regions of the distributions: the fitting function of (6.15) is clearly not a perfect match. The description of the non-Gaussian wings is very good, however, and I reserve the selection of more apposite fitting functions to future work.

A more minor modification that can be made to the standard Schneider & Rix (1997) method is in the choice of $\theta_{\rm max}$. Given the short range nature of flexion it will be advantageous to use smaller values for this parameter than those used for shear. Additionally, following Heymans et al. (2006a), we make use of the COMBO-17 redshift estimates for our lens sample to define $\theta_{{\rm max},\xi}$ on a lens-by-lens basis, only considering the signal from lens masses lying within a projected distance (in the plane of each lens itself) of $r_\xi$. The parameter $\theta_{{\rm max},\xi}$ for each lens is then given by

$$\theta_{{\rm max},\xi} = \frac{r_\xi}{D_{\rm l}}. \tag{6.17}$$

Finally, as in Heymans et al. (2006a), we need to define a single cutoff angle for sources lying close to the edge of the field. This was $\theta_{\rm max}$ itself in the original Schneider & Rix (1997) implementation, and we instead chose $\theta(z_{\rm min}) = r_\xi / D_{\rm A}(z_{\rm min})$, where $z_{\rm min}$ is the lowest redshift in the lens object sample. This concludes my discussion of the modifications to the Schneider & Rix (1997) galaxy-galaxy lensing analysis technique necessary for the extraction of halo constraints from shear and flexion in the GEMS data.

### 6.3.3 Choice of models, lens samples and input parameters

Having described the analysis method being used on the GEMS data, I will now describe the SIS and NFW lens models chosen for the placing of parameter constraints. Following Kleinheinrich et al. (2006), and as described in Section 6.2.2, I place constraints on a galaxy luminosity-dependant SIS halo model parameterized by a fiducial velocity dispersion $\sigma_v^*$ and luminosity scaling $\eta$ (see Equation 6.6). Shear and flexion predictions for each lens are then made using this lens model and the results of Chapter 2.

A single NFW halo is completely defined by the two parameters $M_{200}$ and $c$, and so a simple galaxy

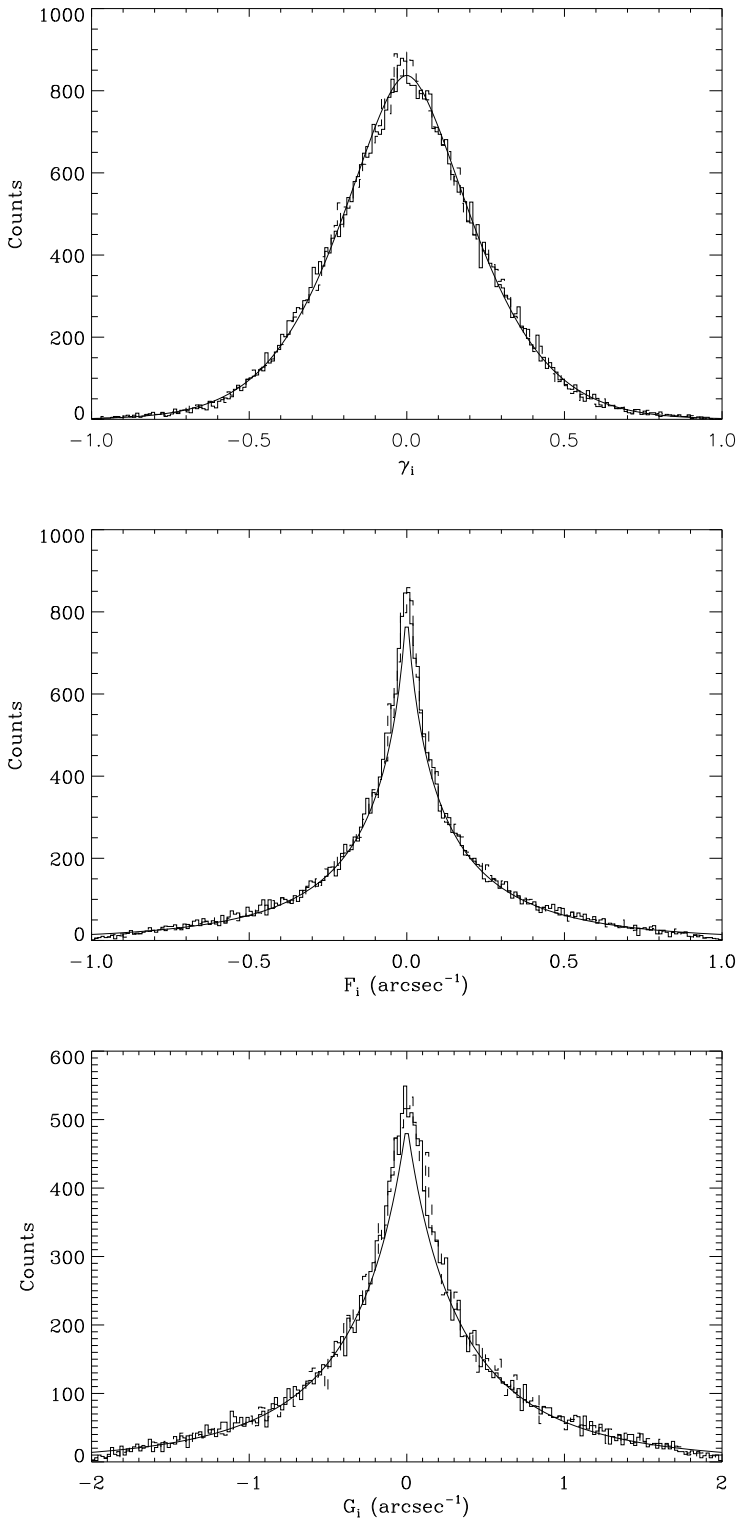


Figure 6.4: Histograms of measured (*a*) shear, (*b*) first flexion and (*c*) second flexion, showing the marginalized best-fitting distribution curve for each case, scaled to the number of sources observed, as described in Section 6.3.2.

luminosity-dependent NFW model can be constructed by assuming

$$\frac{M_{200}}{M_{200}^*} = \left(\frac{L_r}{L_r^*}\right)^{\mu} \tag{6.18}$$

and

$$\frac{c}{c^*} = \left(\frac{L_r}{L_r^*}\right)^{\nu}. \tag{6.19}$$

Using these models we may then calculate predictions for the lensing signal $\xi$ due to each lens, using the results of Chapter 2. There is good observational evidence for an approximate power law scaling of virial mass with luminosity (see, e.g., Guzik & Seljak 2002; HYG04; Hoekstra et al. 2005; Mandelbaum et al. 2006a). This evidence, in combination with theoretical predictions for a single power law scaling of $c$ with $M_{200}$ (Neto et al. 2007; Macciò et al. 2007), suggests that the NFW model defined by Equations (6.18) and (6.19) should provide a good approximation to the physical Universe. We therefore aim to place constraints on the four parameters $M_{200}^*$, $c^*$, $\mu$ and $\nu$ through our maximum likelihood analysis.

Ideally, a four-dimensional maximum likelihood analysis of these NFW parameters should be undertaken. For the placing of meaningful constraints this would require significant computing resources, and so instead I split the testing of the NFW model into three sub-models, defined as follows:

- The first sub-model, which I refer to as NFWm1, assumes a fixed $c^* = 6.85$, based on the `charden.f` calculation for an NFW halo of virial mass $M_{200} = 9 \times 10^{11} h^{-1} M_{\odot}$ (HYG04; Kleinheinrich et al. 2006). I also assume a fixed $\nu = -0.083$ (HYG04; Macciò et al. 2007; Neto et al. 2007) as described in Section 6.2.2. I then place constraints on the fiducial parameter $M_{200}^*$ and mass-luminosity scaling $\mu$.
- The second sub-model, NFWm2, assumes a fixed $\mu = 1.2$ (HYG04; Mandelbaum et al. 2006a), and a fixed $\nu = -0.083$ as for NFWm1. I then place constraints on the two fiducial parameters $M_{200}^*$ and $c^*$.
- The third sub-model, NFWm3, assumes a fixed $M_{200}^*$ as for NFWm1 and a fixed $\mu = 1.2$ as for NFWm2. I then attempt to place constraints on the fiducial parameters $c_{200}^*$ and the concentration-luminosity scaling $\nu$.

In this way I am able to reduce the dimensionality of the parameter space by a factor of two in each case, significantly reducing the computation time of the problem, whilst still probing relationships of interest to theories of galaxy formation and hierarchical halo collapse models.

There will be scatter in the parameters that neither the SIS or the NFW model are able to describe, the natural scatter in halo properties that will occur between galaxies of similar luminosity. A broader difference might be expected between galaxies of different morphological types or stages of evolution, such as spirals and ellipticals. We will attempt to characterize differences in the best fit model parameters by splitting the lens sample described in Section 6.2.1. Due to the multi-band photometry available from the COMBO-17 survey data, and the high quality imaging from the *HST*-ACS GEMS data, it is possible to split the sample both by colour and morphological characteristics.

I therefore define four subsamples of the overall sample of 4995 lenses, based on spiral and elliptical morphology discrimination and membership of the red and blue galaxy sequence as follows:

- The "spiral" sample is defined as those galaxies in the lens sample having a Sérsic index of $n < 2.5$, as found in the GALFIT analysis of GEMS galaxies conducted by Barden et al. (2005). This gives a total of 3770 spiral lenses, after also excluding galaxies with $n < 0.2$ for which we assume some serious failure in the modelling.

- The "elliptical" sample is defined as those galaxies in the lens sample having a Sérsic index of $n > 2.5$ as found in the same GALFIT analysis of GEMS galaxies. This results in a total of 1061 elliptical lenses, where this also takes account of the exclusion of galaxies with $n > 8$ (again this is assumed to be due to catastrophic modelling failure). There are therefore a total of 124 galaxies in the main lens sample that are included in neither of the elliptical or spiral classes, due to possible errors in classification (see also Häussler et al. 2007).

- The "blue" sample is defined as those galaxies in the lens sample which lie in the COMBO-17 red sequence as defined by Bell et al. (2004). This involves a cut for galaxies with $U - V \leq 1.06 - 0.352z - 0.08(V + 0.775 + 20.0)$, leaving 3984 galaxies in the blue lens sample.

- The "red" sample is defined as those galaxies in the lens sample which lie in the COMBO-17 red sequence, defined as being those for which the $U - V$ colour is greater than the redshift-dependent line described above. There are then 971 galaxies in the red lens sample.

These are the classifications I use to split the lens sample, using two different (but related) classifications of galaxy type. I will fit constraints to each of the pairs of the parameters of the SIS model and NFWm1-3 models described above, for each of these galaxy subsamples and for the total lens sample. I present these results in 6.3.4.

Finally, there is the choice of the parameters $r_\xi$ described in Section 6.3.2. I follow Heymans et al. (2006a) and set $r_\gamma = 150h^{-1}$ kpc. For flexion, motivated by the results shown in Figure 6.1 due to the extremely rapid fall in the flexion signal with distance from typical lensing masses (see Chapter 2; BGRT06) , we reduce this physical impact parameter to $r_\mathcal{F} = 50h^{-1}$ kpc.

Interestingly, tests using a synthetic dataset of known-redshift sources showed that the flexion results were somewhat sensitive to the choice of this parameter. Values of $r_\mathcal{F} \gtrsim 100h^{-1}$ kpc, for which the vast majority of source-lens pairs contain no detectable galaxy-galaxy flexion signal, began to show biases towards low-mass, high-concentration fits in the maximum likelihood results. I put this down to a detection of subtle biases inherent in the Monte-Carlo estimation of $\langle\xi\rangle$ (Equation 6.10), which, due to the asymmetric scatter in $z_\mathrm{s}^i$ and related angular diameter distances, causes a systematic bias in the best estimate of $\langle\xi\rangle$. For the high accuracy work of the future, it will be important to investigate this effect in more thorough detail.

Using each of the models, lens samples and input parameters detailed above, I now go on to describe the results obtained from a full maximum likelihood analysis of the GEMS galaxy-galaxy shear-flexion signal.

### 6.3.4 Maximum likelihood results

The modified maximum likelihood analysis method described in Sections 6.3.1, 6.3.2, and 6.3.3 is used to calculate arrays of log-likelihood $\ln\left[L_\gamma(i,j)\right]$, $\ln\left[L_\mathcal{F}(i,j)\right]$ and combined (i.e., total) log-likelihood

$\ln[L(i,j)]$ for a $25 \times 25$ grid of parameters, chosen for each of the SIS and NFWm1-3 models, and for each of the lens samples.

In order to estimate likelihood regions in these arrays, I ran a first maximum likelihood analysis using model parameter ranges of sufficient size to encompass a region of total confidence greater than $99.7\%$. This was in fact not always possible, particularly for the $\mathcal{F}^{\rm obs}$ data, and so as in Section 6.2.2 we must impose a prior on the fiducial concentration. We choose, in estimating these confidence levels, a more conservative prior of $c^* < 400$. This was done to encompass as much of the probability space as possible, so that the choice of prior would not significantly influence either the parameter constraints from $\mathcal{F}$ alone or, more importantly, the combined parameter constraints from measurements of shear and flexion. For a prior of $c^* < 50$ there was still a significant region of probability space being artificially excluded, whereas for the larger prior of $c^* < 400$ this was not the case. While a later prior upon $c^*$ may be imposed if desired (this will almost certainly be the case), the interpretation of likelihood contours in terms of formal confidence intervals should not be influenced by such choices.

The total probability enclosed by each of these parameter ranges, defined by

$$P^{\rm tot} \approx \sum_{i,j} \exp\{\ln[L_\xi(i,j)]\} \tag{6.20}$$

was calculated by David Bacon, and used by him to estimate values of $\Delta\ln[L]$, measured relative to the maximum likelihood, that correspond to confidence intervals of 68%, 95% and 99.7%. This was done separately for shear and flexion (which is vital as $p_\gamma(\gamma^{\rm s}) \neq p_{\mathcal{F}}(\mathcal{F}^{\rm s})$), and for the combined likelihood contours, for each model in turn. Typical values for these calculated levels are illustrated by the flexion result of $-2\Delta\ln[L_{\mathcal{F}}] = (2.5, 7.1, 13.4)$, corresponding to the 1-,2- and 3-$\sigma$ confidence levels described above for the SIS halo model parameters. This is in reasonable agreement with the $-2\Delta\ln[L_{\mathcal{F}}] = (2.3, 6.7, 11.8)$ levels we expect for normally-distributed errors, which we use to estimate confidence on the NFWm1 parameters. Unfortunately, due to the sparseness of the parameter grid available for analysis, calculations of these levels for $\gamma^{\rm obs}$ and $\mathcal{F}^{\rm obs}$ are approximate estimates only, but will be more accurate than assuming the Gaussian results.

In my calculation of the likelihood contours described above, using the theoretical methods of Sections 6.3.1 and 6.3.2, I made use of a piece of code provided by Catherine Heymans (`galgal.f`) that calculated log-likelihood contours for SIS models based on the Schneider & Rix (1997) analysis technique. Parts of this code persist in my analysis routines (as built into my code `gemsggflex.f90`). However, my routine builds substantially upon `galgal.f`, implementing the improvements of Section 6.3.2 and making other significant modifications necessary for the calculation of NFW shear and flexion signals. As an indication of Catherine's contribution to my analysis code, the original `galgal.f` was just under 1000 lines in length, much of which was omitted from my final program of over 4000 lines in length.

In calculating the final constraints upon the SIS and NFW model parameters I again assume a prior of $c^* < 50$, but use the confidence contour levels calculated above for a less severe prior. The parameter constraints placed upon the total lens sample for the assumed SIS, NFWm1, NFWm2 and NFWm3 models can be seen in Figure 6.5. Constraints placed assuming the SIS model for each of the spiral, elliptical, blue and red subsamples can be seen in Figure 6.6. Parameter constraints placed assuming the NFWm1 model for and each of the same subsamples can be seen in Figure 6.7. Constraints placed assuming the NFWm2 model for and each of these subsamples can be seen in Figure 6.8. Finally, the constraints upon NFWm3

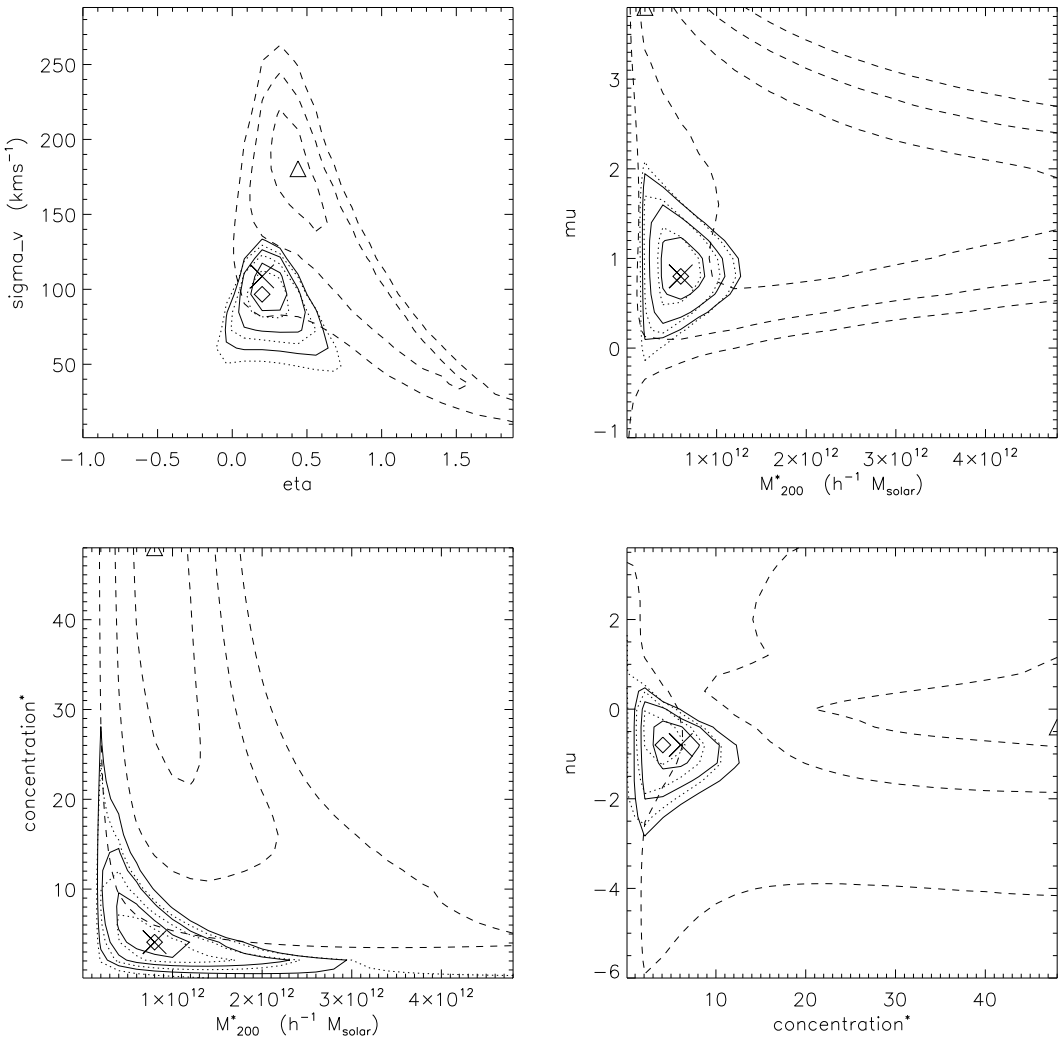


Figure 6.5: Maximum likelihood confidence constraints upon SIS and NFW halo model parameters for the total GEMS lens sample: SIS (top left), NFWm1 (top right), NFWm2 (bottom left) and NFWm3 (bottom right). Intervals of 68%, 95% and 99.7% confidence are plotted from measurements of $\gamma^{\rm obs}$ (dotted line), $\mathcal{F}^{\rm obs}$ (dashed line) and from combining these measurements (solid line). The $\gamma^{\rm obs}$ best fit parameters are marked by diamonds, the $\mathcal{F}^{\rm obs}$ best fit parameters by triangles, and the combined best fit parameters marked by a large cross. As for the results of Figure 6.2, we have assumed $c \leq 50$ as a prior in the final fit analysis.

parameters for each of these subsamples can be seen in Figure 6.9. I discuss these results in the following Section.

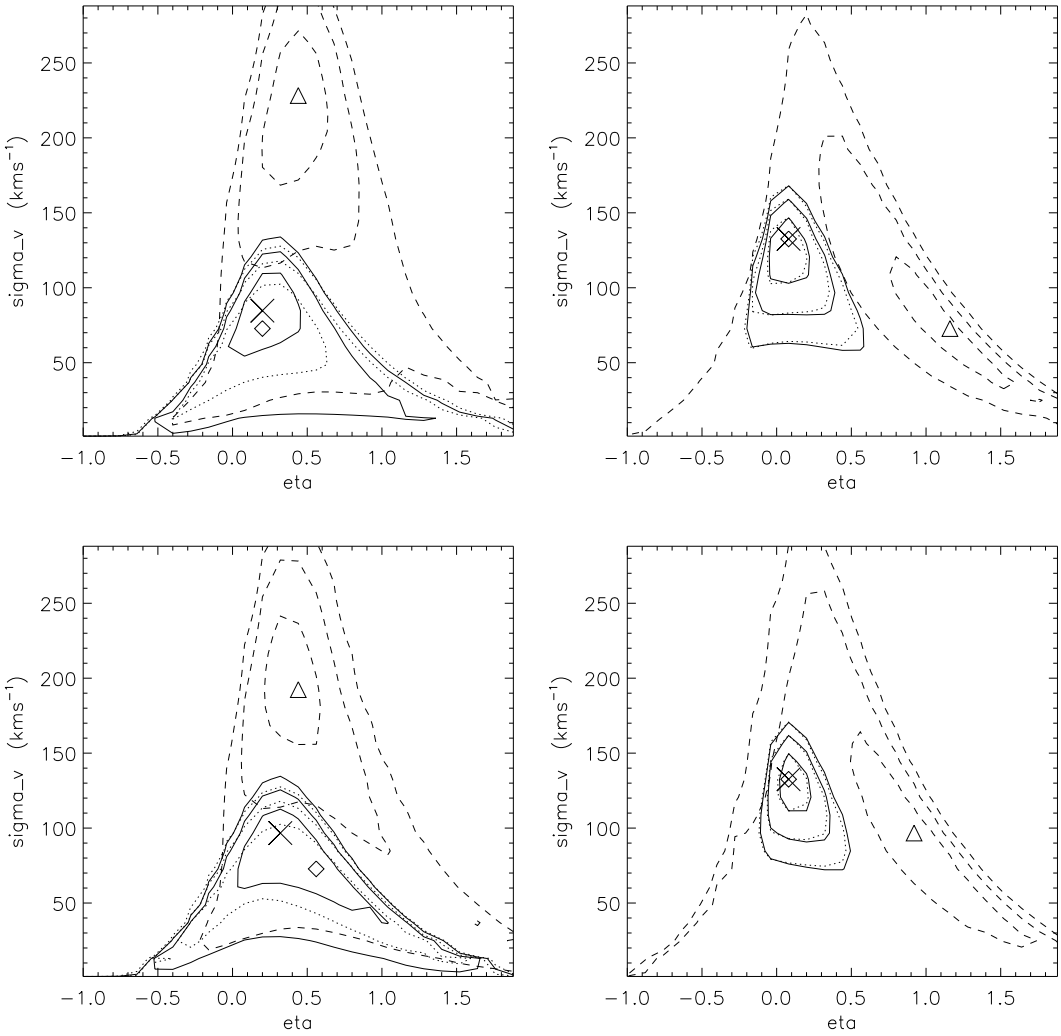


Figure 6.6: Maximum likelihood confidence constraints upon SIS model parameters for the GEMS lens subsamples: spiral (top left), elliptical (top right), blue (bottom left) and red (bottom right). Intervals and best fit values indicated as for Figure 6.5, with an assumed prior $c^* < 50$.

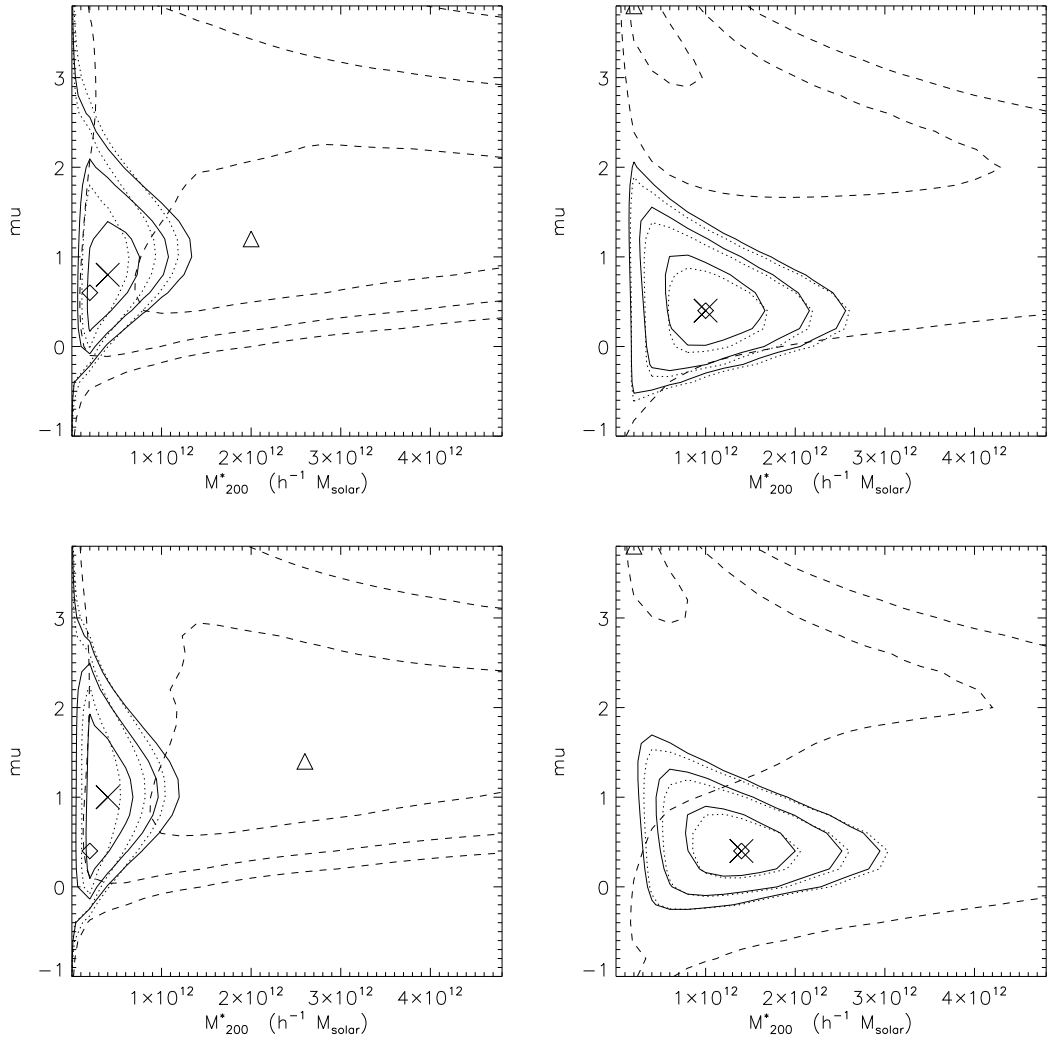


Figure 6.7: Maximum likelihood confidence constraints upon NFWm1 model parameters for the GEMS lens subsamples: spiral (top left), elliptical (top right), blue (bottom left) and red (bottom right). Intervals and best fit values indicated as for Figure 6.5, with an assumed prior $c^* < 50$.

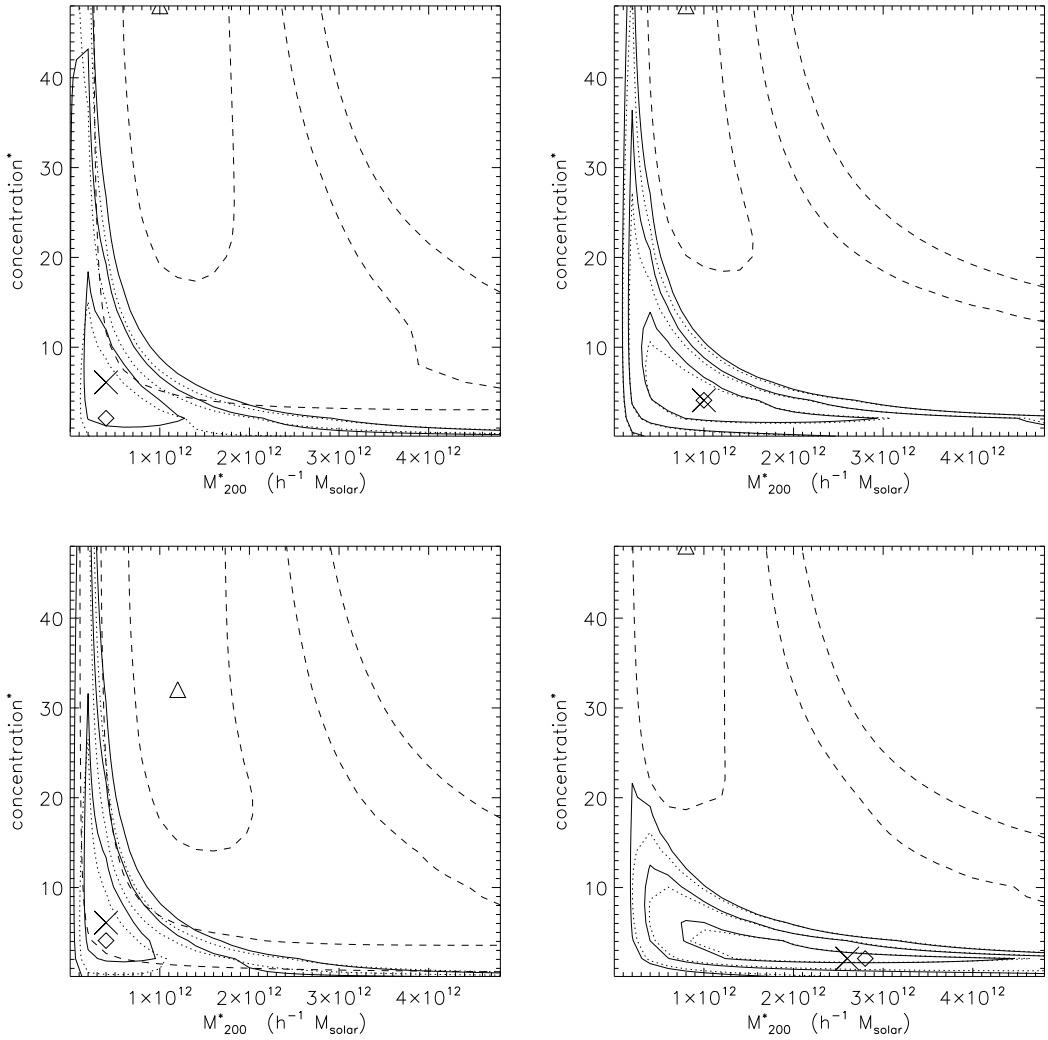


Figure 6.8: Maximum likelihood confidence constraints upon NFWm2 model parameters for the GEMS lens subsamples: spiral (top left), elliptical (top right), blue (bottom left) and red (bottom right). Intervals and best fit values indicated as for Figure 6.5, with an assumed prior $c^* < 50$.

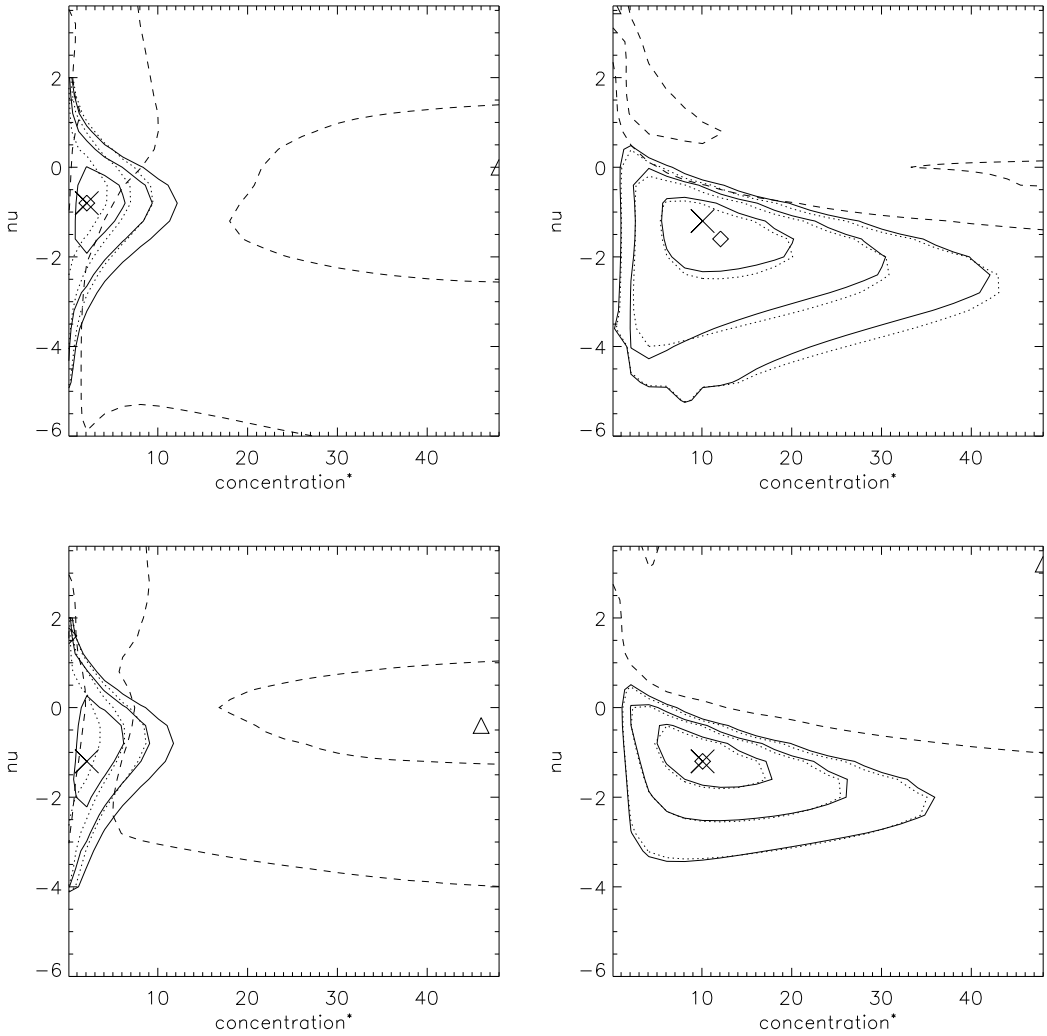


Figure 6.9: Maximum likelihood confidence constraints upon NFWm3 model parameters for the GEMS lens subsamples: spiral (top left), elliptical (top right), blue (bottom left) and red (bottom right). Intervals and best fit values indicated as for Figure 6.5, with an assumed prior $c^* < 50$.

### 6.3.5 Discussion of maximum likelihood results

#### Overview of results and flexion implications

I begin with a discussion of the results shown in Figures 6.5-6.9, which appear largely consistent with the findings of previous galaxy-galaxy lensing studies, but also point towards some interesting issues and conclusions regarding flexion. For the full lens sample, I place SIS model parameter constraints of $\sigma_v^* = 110^{+10}_{-20}$ kms$^{-1}$, and $\eta = 0.24^{+0.24}_{-0.12}$, in marginal disagreement with the results of Kleinheinrich et al. (2006), who favour a larger fiducial velocity dispersion. It should be noted that, due to the sparseness of the parameter grid used in this analysis, all the constraints from this analysis will be subject to small amount of extra uncertainty of the order $(1/2) \times p_{\rm max}/25$, where $p_{\rm max}$ is the maximum parameter value in the range considered (this can be taken from the axis range of each plot). Where combined constraints are limited to a small region of the parameter space, I therefore quote results to 1 significant figure only, aiming to highlight this limitation. Further numerical analysis is planned to improve the resolution of these calculated likelihood surfaces.

For the combined constraints on the NFWm1 model, I fit $\mu = 0.8^{+0.4}_{-0.2}$, $M^*_{200} = 6.0^{+3}_{-2} \times 10^{11} h^{-1} M_\odot$, in agreement with the results of HYG04 and Mandelbaum et al. (2006b), although preferring a lower $\mu$ than found in Hoekstra et al. (2005). The NFWm2 combined fit yields $c^* = 4^{+4.5}_{-1.5}$, $M^*_{200} = 8.0^{+4}_{-4} \times 10^{11} h^{-1} M_\odot$, in good agreement with theoretical predictions and observational constraints. Finally, the NFWm3 parameter constraints found from shear and flexion combined are $\nu = -1.5^{+1}_{-1.25}$, $c^* = 6^{+2}_{-3}$; this may hint towards some tension with theoretical predictions for $\nu$, although this conclusion rests on the correct choice of the observationally constrained fixed parameters $M^*_{200}$ and $\mu$, which is not certain. This issue, that of possible conflicts due to parameter degeneracies and faulty modelling, will be discussed later.

In all cases, as for the E-mode fitting constraints, the fit is largely determined by the contours placed using the shear results and the flexion makes only minor alterations to the best fit contours. This appears to be a combination of two effects. Firstly, examination of the likelihood surfaces produced by flexion measurements shows them to be of rather shallow gradient in outlying regions. This is as opposed to the shear, for which the likelihood surface steepens considerably at distance from the best fit regions. This fact, when combined with the further evidence for tension between shear and flexion results (also found in Section 6.2.2), means that the shear constraints tend to lie in regions where the flexion likelihood is varying only slowly.

The existence of this "3-$\sigma$ plateau" for flexion likelihoods can be understood by considering the broad wings of the modelled flexion distribution, for which significant numbers of outliers are expected. The importance of our accurate characterization of $p_{\mathcal{F}}(\mathcal{F}^{\rm s})$ is now clear: proper accounting for non-Gaussian flexion noise is vital if flexion measurements are going to be correctly combined with those from shears. Interestingly, the 3-$\sigma$ plateau in flexion likelihoods does not extend all the way to the inner confidence regions, which have sharper gradients. In cases where there is better agreement between shear and flexion results we can expect flexion to provide more significant improvements to measured parameter constraints. Also, any alternative flexion estimation scheme (such as that of Okura et al. 2007a) that could reduce the scatter in flexion measurements and decrease the number of outliers would likewise steepen the gradient in the outer regions of the flexion likelihood surface.

The results of this Section make it more certain that tension between shear and flexion exists in the data itself, rather than in errors of methodology, as I have completed two different analyses of the galaxy-galaxy

lensing signal in GEMS and both yield entirely consistent results. If the explanation is some kind of flexion bleed, as discussed in 6.2.3 and in Chapter 7, then accurate calibration for the effect would allow flexion to exert more influence upon combined parameter constraints; this would happen simply by virtue of the best-fitting regions being moved out of the 3-$\sigma$ plateau and into regions where the flexion likelihood surface is varying more rapidly. If the effect is real, however, and due to failures in the NFW mass model close to baryon-dominated regions, then sample sizes will simply need to be increased in order to expose the shear-flexion inconsistency at greater significance. Larger sample size *and* an improved flexion estimation method could yield results at greater significance still. These and related topics will be discussed again in Chapter 7. I now turn to look at some of the results obtained for the lens subsamples, split by galaxy and morphology as describe in Section 6.3.3.

### Results as a function of galaxy type

The SIS and NFWm1-3 parameter results for lens samples split by galaxy colour (blue/red) and morphology (spiral/elliptical) are shown in Figures 6.6-6.9. In the discussion that follows I will not generally quote marginalized error estimates for NFW halo parameters, but instead refer to overall trends in the contours for different subsamples. In many cases quoting best fit values and marginalized error bounds would be misleading, as the reliability of these results relies implicitly on accurate values of the *fixed* parameters (see Section 6.3.3) chosen for each submodel. I did not vary these fixed parameters for different subsamples, and there is evidence (in the form of inconsistent results between NFW submodels) that this is an oversimplification that needs to be addressed. Note that issues do not affect the two parameter SIS model, which I now discuss.

The results shown in Figure 6.6 show broad agreement between the results for blue galaxies and spiral galaxies, with similar agreement for red and elliptical galaxies, suggesting that both cuts identify haloes with similar lens properties. To avoid confusion, where contours agree, I refer to these populations as early-type lenses (elliptical/red) and late-type lenses (spiral/blue). There are signs of a significant difference in the velocity dispersions of these broad classes. For the red sample I find $\sigma_v^* = 130^{+20}_{-20}$ kms$^{-1}$, and for the blue sample $\sigma_v^* = 96^{+20}_{-40}$ kms$^{-1}$. Values for the luminosity scaling parameters are entirely consistent. These results replicate the findings of Kleinheinrich et al. (2006) for the split between red and blue galaxies, although again I find consistently lower velocity dispersions in each case.

Turning now to the NFW halo model parameters (Figures 6.7-6.8), it appears that lens populations are equally well divided by either colour or morphology (except, perhaps, in the case of NFWm2); as for the SIS model, there is good contour agreement between the spiral and blue galaxy samples, and between the red and elliptical galaxy samples. Reliable conclusions regarding *differences* in the underlying early/late-type lens populations are harder to draw. For NFWm1, there appears to be no significant sign of differences in the mass-luminosity scaling $\mu$, but some evidence for early-types favouring higher mass models (in agreement with the SIS results and Kleinheinrich et al. (2006).

The NFWm2 and NFWm3 model results are more difficult to interpret, due to simplifying assumptions built into my submodel parameterizations of the overall NFW model presented in Equations (6.18) and (6.19). The situation is worsened by the strong degeneracy between the mass and concentration parameters for NFW halos; noisy lensing measurements can often be fit equally well by NFW models with high (low) mass and low (high) concentrations. This degeneracy is clearly seen in the results of the NFWm2 submodel (Figure 6.8).

The limitations of my submodel parameterization are suggested by an inconsistency between the results of NFWm2 and NFWm3, seen in Figures 6.8 and Figures 6.9. For the NFWm2 model, there is evidence that the red galaxies inhabit a lower-concentration, higher-mass region of the parameter space than blue galaxies, which favour a higher-concentration, lower-mass region. This is an extremely interesting result, as it lends observational weight to galaxy formation models in which early-type galaxies form in the course of large halo mergers (see, e.g., De Lucia et al. 2006; Springel et al. 2005; Baugh 2006): this would naturally cause their haloes to be less concentrated. If such mergers trigger rapid starburst activity that then largely ceases, we expect such galaxies to be red in colour and less luminous than star-forming galaxies of the same mass.

However, in Figure 6.9, we see evidence that early-type lenses favour a *higher* $c^*$ than the late-type sample. The issue most likely to have caused this inconsistency is the fact that for the NFWm3 model I have assumed the same, fixed $M^*_{200} = 9 \times 10^{11} h^{-1} M_\odot$ for each sample. If this is an overestimate of the fiducial viral mass for the blue lenses (as is suggested by the NFWm1 results) then the degeneracy between $c$ and $M_{200}$ will artificially force blue lens best fits towards lower $c^*$. As stressed at the beginning of Section 6.3, maximum likelihood results are only as good as the models they test, and will *always* give an answer.

The most obvious solution to this problem is to parameterize the full NFW model in four dimensions, and perform the same maximum likelihood analysis. However, this would be prohibitive in terms of computing resources using my current method: analysis of GEMS data for a $25 \times 25$ grid of parameters takes around 6 hours to complete for the spiral/blue samples using a standard desktop PC. Finding likelihoods for a four-dimensional array of the same resolution would then take more than 5 months. Use of Monte-Carlo Markov Chain methods would increase the speed of this process, or an iterative solution could be reached via successive runs of lower dimensionality models, each time adopting the best-fitting values from the previous analysis. Given the suggestions of real, physical differences between early-type and late-type haloes in the GEMS galaxy galaxy lensing signal, these considerations will be the the subject of much useful research. If the treatment of the NFW halo models can be improved, increases in size for future survey datasets will provide a wealth of galaxy-galaxy lensing information.

This concludes my discussion of the maximum likelihood results, and indeed the description of the primary results in my Thesis. I now go on to a Chapter in which I summarize my findings, conclusions, and proposals for future work.

# CHAPTER 7

# CONCLUSIONS

In this Thesis I have presented a number of important developments, results and unsolved issues relevant to the field of weak lensing. The primary achievements of this work began with the development of theoretical predictions for weak gravitational flexion and culminated, via accurate measurement, in a detailed analysis of a cosmological flexion signal. As part of this process I have completed a first, full (i.e., PSF treating), shapelet lensing analysis of real space-based data from the GEMS survey, something that has not otherwise been done for shear or for flexion. I have calibrated my shear and flexion measurements using a sophisticated simulated dataset, and used the results to perform a first combined galaxy-galaxy shear-flexion analysis. In doing this I improved existing techniques by accurately describing the statistical distributions of both measured shear and flexion in GEMS, providing useful tools for future galaxy-galaxy lensing analyses.

My GEMS measurements (and those of the FLIP analysis) raise important issues that will be of much relevance to the accurate analysis of future survey data, particularly if this measurement is to proceed via shapelets or related methods. The shapelet analysis of GEMS demonstrates the viability of the method and thus provides a template for future pipelines, whilst highlighting areas in which such pipelines could improve on my methods. Finally, the galaxy-galaxy lensing constraints I place upon lens galaxies in GEMS provide a realistic picture of the utility of shapelet-measured flexion as a cosmological tool, and the shear results suggest interesting differences in the halo properties of spiral and elliptical galaxies.

## Flexion from theory to measurement

The intention at the outset of this work was to show that measurements of flexion could be used to improve the knowledge of the cosmological matter distribution, particularly on small scales. Having made analytic predictions presented in Chapter 2, I began work on a shapelet pipeline so as to accurately measure the flexion signal for the first time, including necessary PSF corrections. The direct first result of this work can be seen in Figure 6.1, Chapter 6 (see also Figure 7.1, this Chapter), which shows a clear detection of galaxy-galaxy flexion signal in annuli of 2-4 arcsec away from foreground lenses. This result is not for a sample of lens galaxies that have been specifically chosen as of high mass, with the median $r$-band luminosity of our sample being $\simeq 3 \times 10^9 h^{-2} L_\odot$. More importantly, unlike that of Goldberg & Bacon (2005), my analysis includes a thorough treatment of systematic errors and biases using shapelets (see Chapters 4 and 5), and takes account of the realistic distribution of flexion measurements (Goldberg & Bacon 2005 used a Gaussian of width $\sigma_{\mathcal{F}} = 0.04$, possibly due to their bright sample of galaxies). These considerations may explain the fact that, contrary to Goldberg & Bacon (2005), I find no evidence for a flexion signal beyond 5 arcsec from typical foreground lenses.

The maximum likelihood results of Chapter 6 also suggest that we have a strong detection of a first flexion signal, with the flexion contours for the SIS and NFWm1 models in Figure 6.5 ruling out zero-mass models at 3-$\sigma$ significance or greater. These results are more difficult to interpret, however, as a poor choice of model will give inaccurate results in any maximum likelihood analysis.

There were two further important features of the maximum likelihood analysis of particular importance to flexion. Firstly, the measurement of flexion in my GEMS pipeline is still too noisy for it to be able to significantly improve constraints on model parameters for lenses such as the SIS or NFW; the confidence contours seen for the combined signal do not often differ significantly for those from shear alone (section 6.3, Chapter 6). Despite the sometimes significant tension between flexion and shear parameter results (3-$\sigma$

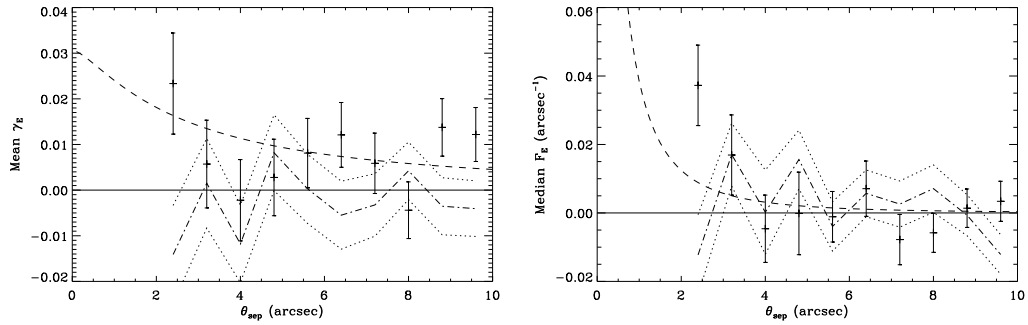


Figure 7.1: Comparison of GEMS E-mode shear (left) and flexion (right) for $\theta_{\rm sep}$ between 2 and 10 arcsec. As for Figure 6.1, the B-mode signal and uncertainties are plotted as dot-dashed and dotted lines respectively. The dashed line is the predicted halo based on HYG04 and Navarro et al. (1997).

for NFWm2 and NFWm3), the flexion likelihood surface is generally shallow-sided when compared to that of shear, causing the combined surface to be dominated by the shear results. This shallow-sided likelihood behaviour is a consequence of the broad wings in the measured distribution of $p_{\mathcal{F}}(\mathcal{F}^{\rm s})$, and highlights the importance of taking this distribution into account when using flexion statistics. Modelling of the flexion distribution as a Gaussian, such as in Goldberg & Bacon (2005), BGRT06, Okura et al. (2007b) and Section 2.2, will inevitably lead to flawed conclusions.

Despite the noise of flexion measurement, the tension that exists between flexion and shear is striking, and could point to the failure of SIS and NFW models in the regions where the interplay between baryons and dark matter would become a significant consideration. It is not known whether lens models based on pure $\Lambda$CDM simulations will apply in the small scale, baryon-influenced regime close to halo centres; it should be expected that they do not (see, e.g., Sections 1.1.9 and 1.1.10). An indication that flexion has the potential to provide useful information on these scales is demonstrated in Figure 7.1, which compares the measured $\gamma_{\rm E}$ and $\gamma_{\rm B}$ from GEMS on the scales of flexion sensitivity. If the flexion measurements could be made more accurate, either by increasing the sample size or by improving estimation techniques, then flexion could offer competitive constraints in this regime, especially if the NFW model underestimates the mass or concentration on these scales (a prediction of adiabatic quenching, see, e.g., Blumenthal et al. 1986; Sellwood & McGaugh 2005; Gustafsson et al. 2006). The persistence of the strong flexion signal at $\theta_{\rm sep} \approx$ 2-3 arcsec would present a real difficulty to NFW halo models, and a step forward in the understanding of the dark matter-visible matter relationship.

The question of how flexion estimation can be made more accurate is important, as the shapelet technique seems to add a significant measurement noise to the underlying intrinsic flexion variance possessed by real galaxies. The HOLICS technique of Okura et al. (2007b), recently extended to include a full KSB-style treatment of PSF anisotropy (Okura et al. 2007a), is in this respect a promising development. Work by Goldberg & Leonard (2007) and Leonard et al. (2007) found it to provide a significantly less noisy flexion estimator than shapelets, and adopted it as their preferred technique. It may also be that severe outlier clipping can provide a solution to the problem of flexion noise, but such schemes would need to be carefully calibrated for the downward biasing effect this has upon statistical estimates.

As well as reducing the noise in flexion, it will be important to uncover and understand possible systematic effects that could bias flexion in real lensing data. Particularly, the “flexion bleed” hypothesis described

in Section 6.2.2, could account for the strong $\mathcal{F}_{\rm E}$ signal seen at small $\theta_{\rm sep}$. I now propose a method for the calibration of this effect using a combination of real data and simulated galaxies of the sort used in the FLIP analysis of Chapter 5. The first step is to take a sample of FLIP-type galaxy models, chosen to be representative of the lensing *source* sample, and pixellize to the scale of the dataset in question. These models should be chosen to be isotropic on average with respect to all lensing measurements. Co-adding large numbers of these isotropic, pixellized, noiseless models to the pixels in the vicinity of representative members of the actual *lens* sample, one can quickly quantify the biasing effect of flexion bleed by calculating the E-mode signal in these synthesized source-lens pairs. This simple analysis is a priority if we are to place greater faith in the $\mathcal{F}_{\rm E}$ results found in GEMS, and wish to make a first calibration of the effect for future flexion measurements.

## Shapelet lensing measurements

The presentation of a shapelet pipeline suitable for the accurate analysis of real, space-based data is another important result of this Thesis. The results of Section 4.3.1, Chapter 4, suggest agreement between my shapelet shears and those of Heymans et al. (2005) at the level $(96.7 \pm 0.8)\%$, with no evidence for a shear offset bias such as might be caused by a poor PSF treatment in either analysis. This result agrees with the GEMS analysis performed by Schrabback et al. (2007), who find a similar discrepancy of $\simeq 3.3\%$ between their shear estimates and those of Heymans et al. (2005). Tests for shear residual offsets also proved consistent with zero, but the results for the flexion measurements were less successful, particularly for $\mathcal{G}^{\rm obs}$ (Section 4.3.3, Chapter 4). Imperfect modelling of the outer wings of the ACS PSF is hypothesised as a potential cause for this systematic, as the induced residual second flexion is aligned with a clear $\mathcal{G}$-like morphology in the outer light profile of stacked stellar images.

However, in order to achieve accurate agreement with previous lensing studies it was necessary to multiply my chosen shear estimator by a bias factor of (1/0.82), motivated by my shapelet analysis of simulated galaxy images (FLIP, Chapter 5). A reducing bias factor was found to be necessary to correct for overestimation of $\mathcal{G}$, and recovery of $\mathcal{F}$ appeared to be unbiased, if similarly noisy. The reason for the overestimation of the $\mathcal{G}$ input signal is unclear, but was a common feature among the estimators tested. It is thought that the systematic underestimation of shears may be a consequence of the shapelet truncation of natural galaxy light profiles, an issue which will be discussed in the forthcoming STEP3 analysis of Rhodes et al. (in prep.).

The results of the FLIP analysis also highlight important shortcomings in certain shapelet lensing estimators, such as those proposed by Refregier & Bacon (2003), Goldberg & Bacon (2005) and some amongst those I proposed in Chapter 3 (see also Massey et al. 2007d). Estimators formed without the need to calculate ensemble averages over shapelet coefficients, which may vary wildly between galaxies, will show greater stability and can be implemented more simply. Many among the proposed shapelet lensing estimators will need accurate calibration of their susceptibilties, as functions of galaxy properties such as size, brightness and morphological type. A final finding of the FLIP analysis was the poor treatment of PSF systematics for galaxies of scale size close to that of the PSF, leading to detectable residual offsets for these objects. This is a natural consequence of the Massey & Refregier (2005) shapelet deconvolution approach.

## Maximum likelihood analysis

I have described my maximum likelihood analysis of galaxy-galaxy lensing in the GEMS data (Chapter 6), which required modifications to the assumed forms of the probability distributions for the intrinsic shear and flexion of unlensed galaxies. Simple analytic functions are shown to provide an improved fit to the GEMS data when compared to the Gaussian curves used by Schneider & Rix (1997) and subsequent analyses based on this scheme.

The maximum likelihood analyses agree well with the results of simpler fits to the $\gamma_{\rm E}$ and $\mathcal{F}_{\rm E}$ signal in GEMS, and using the total lens sample I place constraints upon lens model parameters that are in agreement with the findings of other authors (Guzik & Seljak 2002; Hoekstra et al. 2004; Kleinheinrich et al. 2006; Mandelbaum et al. 2006b). Using galaxy morphology (Barden et al. 2005) and rest-frame colour (Bell et al. 2004) information I show a clear variation in lens properties with both indicators of the late/early-type galaxy dichotomy. There is an interesting suggestion in the NFWm2 model (see Section 6.3.5, Chapter 6) of significant differences in the mass and concentration parameters of red and blue galaxies. The red galaxies appear better fit by higher mass, lower concentration halo models than blue galaxies, which would be a natural prediction of hierarchical galaxy formation models (see, e.g., De Lucia et al. 2006). However, limitations in the simplified parameterizations of NFW halo models currently prevent firmer conclusions being drawn. Placing firmer confidence constraints on this result is a natural extension of the work in this Thesis; I now go on to describe how this might be done, along with other potential research opportunities that arise as a direct consequence of my investigations.

## Further work

The opportunities for further work are clear. If flexion can be estimated more accurately for real galaxy images then there is potential, as suggested by the simplified analysis presented in Chapter 2, for it to be a useful addition to shear for certain cosmological applications. The shapelet formalism of Refregier (2003) provides an elegant framework for constructing shapelet estimators. What is unclear is whether the least-squares shapelet model fitting of Massey & Refregier (2005) is able to characterize higher order shape galaxy information with sufficient reliability to prevent such estimators from being both noisy and, potentially, biased.

The HOLICS image moment scheme presented by Okura et al. (2007b), now adapted to include a full treatment of anisotropic PSF corrections (Okura et al. 2007a), is an exciting alternative to shapelets and early results show signs of superior flexion measurement for real galaxies (Leonard et al. 2007). Alternative options such as heavy outlier clipping of shapelet measurements may also provide a working solution. An important future study will be the comparison of flexion measurement from each of these different estimation schemes using simulated galaxy datasets such as the FLIP images. Following the STEP analyses, this work would compare estimates for both space-based and ground-based datasets.

The possibility of the extension of flexion to ground-based imaging surveys is a related issue, and one of increased importance due to the unavailability of substantial, new, space-based imaging survey datasets in the short-to-medium term. The question of whether flexion can be accurately recovered in the presence of atmospheric image degradation remains open. First instincts would suggest that it would be more difficult than from space, but the shapelet method was found to be very successful in STEP2 (Massey et al. 2007b),

which simulated ground-based imaging data, and less successful in STEP3 (Rhodes et al., in prep.). It may be that objects blurred by a degree of atmospheric seeing are better fit by the shapelet basis set than high quality images of galaxies convolved with the highly non-Gaussian ACS PSF.

If flexion can be successfully measured from the ground, then datasets such as the Canada France Hawaii Telescope Legacy Survey (CFHTLS, see, e.g., Hoekstra et al. 2006) would be able to provide a 10-fold increase in signal to noise on galaxy-galaxy flexion measurements (based on an assumed source number density of $\simeq 10$ arcmin$^{-2}$). This would bring any discrepancy between shear and flexion for the SIS and NFW halo models into sharp relief, assuming that the potentially biasing effects of flexion bleed can be checked and, if necessary, accurately accounted for.

Future surveys also offer the possibility of an improved maximum likelihood analysis of galaxy-galaxy lensing, with the specific aim of testing galaxy formation models by probing the lens properties of galaxy host haloes. A ten-fold increase in signal to noise from CFHTLS would place firm constraints on the differences between the halo hosts of red and blue galaxies, differences which are tantalisingly suggested by the results of my work. This study would need to be accompanied by a more sophisticated parameterization of luminosity-scaled NFW halo models, and if the shear signal can be augmented by accurate flexion measurements then powerful new insight into galaxy formation could be gained.

Finally, galaxy-galaxy lensing is not the only cosmological measurement which flexion has the potential to improve. Cluster mass reconstructions may also see significant benefits (Okura et al. 2007a), but if this is to be the case then the properties of reduced flexion need to be correctly accounted for in order to make mass reconstructions as unbiased as possible (Schneider & Er 2007). Although flexion in the galaxy-galaxy lensing regime primarily considered in this Thesis is not significantly biased as a result of the sheet-mass degeneracy, if the utility of flexion is to be extended then this needs to be taken into account. Schneider & Er (2007) present extremely important first results in this direction, but more work can be done. It seems that the problem of mutual biases between reduced shear and reduced flexion cannot be solved analytically, and so it may require a group effort in order for these effects to be accurately characterized.

# Bibliography

Abadi, M. G., Navarro, J. F., Steinmetz, M., Eke, V. R. 2003, ApJ, 597, 21

Allgood, B., Flores, R. A., Primack, J. R., Kravtsov, A. V., Wechsler, R. H., Faltenbacher, A., Bullock, J. S. 2006, MNRAS, 367, 1781

Angus, G. W., Shan, H. Y., Zhao, H. S., Famaey, B. 2007, ApJ, 654, L13

Arfken, G. B., Weber, H. J. 2005, Materials and Manufacturing Processes

Astier, P., Guy, J., Regnault, N., Pain, R., Aubourg, E., Balam, D., Basa, S., Carlberg, R. G., Fabbro, S., Fouchez, D., Hook, I. M., Howell, D. A., Lafoux, H., Neill, J. D., Palanque-Delabrouille, N., Perrett, K., Pritchet, C. J., Rich, J., Sullivan, M., Taillet, R., Aldering, G., Antilogus, P., Arsenijevic, V., Balland, C., Baumont, S., Bronder, J., Courtois, H., Ellis, R. S., Filiol, M., Gonçalves, A. C., Goobar, A., Guide, D., Hardin, D., Lusset, V., Lidman, C., McMahon, R., Mouchet, M., Mourao, A., Perlmutter, S., Ripoche, P., Tao, C., Walton, N. 2006, A&A, 447, 31

Bacon, D. J., Goldberg, D. M., Rowe, B. T. P., Taylor, A. N. 2006, MNRAS, 365, 414

Bacon, D. J., Massey, R. J., Refregier, A. R., Ellis, R. S. 2003, MNRAS, 344, 673

Bacon, D. J., Refregier, A. R., Ellis, R. S. 2000, MNRAS, 318, 625

Bardeen, J. M., Bond, J. R., Kaiser, N., Szalay, A. S. 1986, ApJ, 304, 15

Barden, M., Rix, H.-W., Somerville, R. S., Bell, E. F., Häußler, B., Peng, C. Y., Borch, A., Beckwith, S. V. W., Caldwell, J. A. R., Heymans, C., Jahnke, K., Jogee, S., McIntosh, D. H., Meisenheimer, K., Sánchez, S. F., Wisotzki, L., Wolf, C. 2005, ApJ, 635, 959

Barnes, J., Hut, P. 1986, Nature, 324, 446

Bartelmann, M. 1996, A&A, 313, 697

Bartelmann, M., Huss, A., Colberg, J. M., Jenkins, A., Pearce, F. R. 1998, A&A, 330, 1

Bartelmann, M., Narayan, R., Seitz, S., Schneider, P. 1996, ApJ, 464, L115+

Bartelmann, M., Schneider, P. 2001, Phys. Rep., 340, 291

Baugh, C. M. 2006, Reports of Progress in Physics, 69, 3101

Baugh, C. M., Efstathiou, G. 1994, MNRAS, 267, 323

Bekenstein, J. D. 2004, Phys. Rev. D, 70(8), 083509

Bell, E. F., Wolf, C., Meisenheimer, K., Rix, H.-W., Borch, A., Dye, S., Kleinheinrich, M., Wisotzki, L., McIntosh, D. H. 2004, ApJ, 608, 752

Benjamin, J., Heymans, C., Semboloni, E., van Waerbeke, L., Hoekstra, H., Erben, T., Gladders, M. D., Hetterscheidt, M., Mellier, Y., Yee, H. K. C. 2007, MNRAS, 381, 702

Bennett, C. L., Halpern, M., Hinshaw, G., Jarosik, N., Kogut, A., Limon, M., Meyer, S. S., Page, L., Spergel, D. N., Tucker, G. S., Wollack, E., Wright, E. L., Barnes, C., Greason, M. R., Hill, R. S., Komatsu, E., Nolta, M. R., Odegard, N., Peiris, H. V., Verde, L., Weiland, J. L. 2003, ApJS, 148, 1

Bergé, J. 2006, Shapelets Manual Volume 1, http://www.astro.caltech.edu/ jberge/shapelets/manual/

Bernstein, G. M., Jarvis, M. 2002, AJ, 123, 583

Bershady, M. A., Jangren, A., Conselice, C. J. 2000, AJ, 119, 2645

Bertin, E., Arnouts, S. 1996, A&AS, 117, 393

Bertschinger, E. 1985, ApJS, 58, 39

Binney, J., Tremaine, S. 1987, Galactic dynamics, Princeton, NJ, Princeton University Press, 1987, 747 p.

Blandford, R., Narayan, R. 1986, ApJ, 310, 568

Blumenthal, G. R., Faber, S. M., Flores, R., Primack, J. R. 1986, ApJ, 301, 27

Bolton, A. S., Burles, S., Koopmans, L. V. E., Treu, T., Moustakas, L. A. 2006, ApJ, 638, 703

Bond, J. R., Efstathiou, G. 1984, ApJ, 285, L45

Bradač, M., Clowe, D., Gonzalez, A. H., Marshall, P., Forman, W., Jones, C., Markevitch, M., Randall, S., Schrabback, T., Zaritsky, D. 2006, ApJ, 652, 937

Bradač, M., Erben, T., Schneider, P., Hildebrandt, H., Lombardi, M., Schirmer, M., Miralles, J.-M., Clowe, D., Schindler, S. 2005a, A&A, 437, 49

Bradač, M., Schneider, P., Lombardi, M., Erben, T. 2005b, A&A, 437, 39

Bradač, M., Schneider, P., Lombardi, M., Steinmetz, M., Koopmans, L. V. E., Navarro, J. F. 2004, A&A, 423, 797

Brainerd, T. G., Blandford, R. D., Smail, I. 1996, ApJ, 466, 623

Bremer, M. N., Jensen, J. B., Lehnert, M. D., Schreiber, N. M. F., Douglas, L. 2004, ApJ, 615, L1

Broadhurst, T., Benítez, N., Coe, D., Sharon, K., Zekser, K., White, R., Ford, H., Bouwens, R., Blakeslee, J., Clampin, M., Cross, N., Franx, M., Frye, B., Hartig, G., Illingworth, G., Infante, L., Menanteau, F., Meurer, G., Postman, M., Ardila, D. R., Bartko, F., Brown, R. A., Burrows, C. J., Cheng, E. S., Feldman, P. D., Golimowski, D. A., Goto, T., Gronwall, C., Herranz, D., Holden, B., Homeier, N., Krist, J. E., Lesser, M. P., Martel, A. R., Miley, G. K., Rosati, P., Sirianni, M., Sparks, W. B., Steindling, S., Tran, H. D., Tsvetanov, Z. I., Zheng, W. 2005, ApJ, 621, 53

Brownstein, J. R., Moffat, J. W. 2007, ArXiv Astrophysics e-prints:astro-ph/0702146

Bullock, J. S., Kolatt, T. S., Sigad, Y., Somerville, R. S., Kravtsov, A. V., Klypin, A. A., Primack, J. R., Dekel, A. 2001, MNRAS, 321, 559

Caldwell, J. A. R., McIntosh, D. H., Rix, H., Barden, M., Beckwith, S. V. W., Bell, E. F., Borch, A., Heymans, C., Haeussler, B., Jahnke, K., Jogee, S., Meisenheimer, K., Peng, C. Y., Sanchez, S. F., Somerville, R. S., Wisotzki, L., Wolf, C. 2005, ArXiv Astrophysics e-prints: astro-ph/0510782

Carlberg, R. G., Yee, H. K. C., Ellingson, E. 1997, ApJ, 478, 462

Carroll, S. M., Press, W. H., Turner, E. L. 1992, ARA&A, 30, 499

Castro, P. G., Heavens, A. F., Kitching, T. D. 2005, Phys. Rev. D, 72(2), 023516

Clowe, D., Bradač, M., Gonzalez, A. H., Markevitch, M., Randall, S. W., Jones, C., Zaritsky, D. 2006, ApJ, 648, L109

Cole, S., Percival, W. J., Peacock, J. A., Norberg, P., Baugh, C. M., Frenk, C. S., Baldry, I., Bland-Hawthorn, J., Bridges, T., Cannon, R., Colless, M., Collins, C., Couch, W., Cross, N. J. G., Dalton, G., Eke, V. R., De Propris, R., Driver, S. P., Efstathiou, G., Ellis, R. S., Glazebrook, K., Jackson, C., Jenkins, A., Lahav, O., Lewis, I., Lumsden, S., Maddox, S., Madgwick, D., Peterson, B. A., Sutherland, W., Taylor, K. 2005, MNRAS, 362, 505

Coles, P., Lucchin, F. 1995, Cosmology. The origin and evolution of cosmic structure, Chichester: Wiley, —c1995

Comerford, J. M., Natarajan, P. 2007, MNRAS, 379, 190

Condon, J. J., Cotton, W. D., Greisen, E. W., Yin, Q. F., Perley, R. A., Taylor, G. B., Broderick, J. J. 1998, AJ, 115, 1693

Conley, A., Goldhaber, G., Wang, L., Aldering, G., Amanullah, R., Commins, E. D., Fadeyev, V., Folatelli, G., Garavini, G., Gibbons, R., Goobar, A., Groom, D. E., Hook, I., Howell, D. A., Kim, A. G., Knop, R. A., Kowalski, M., Kuznetsova, N., Lidman, C., Nobili, S., Nugent, P. E., Pain, R., Perlmutter, S., Smith, E., Spadafora, A. L., Stanishev, V., Strovink, M., Thomas, R. C., Wood-Vasey, W. M. 2006, ApJ, 644, 1

Conselice, C. J. 2003, ApJS, 147, 1

Conselice, C. J., Bershady, M. A., Jangren, A. 2000, ApJ, 529, 886

Dalal, N., Holder, G., Hennawi, J. F. 2004, ApJ, 609, 50

Das, S., Bode, P. 2007, ArXiv e-prints, 711

Davis, M., Efstathiou, G., Frenk, C. S., White, S. D. M. 1985, ApJ, 292, 371

De Lucia, G., Kauffmann, G., Springel, V., White, S. D. M., Lanzoni, B., Stoehr, F., Tormen, G., Yoshida, N. 2004, MNRAS, 348, 333

De Lucia, G., Springel, V., White, S. D. M., Croton, D., Kauffmann, G. 2006, MNRAS, 366, 499

Diemand, J., Moore, B., Stadel, J. 2004, MNRAS, 352, 535

Diemand, J., Zemp, M., Moore, B., Stadel, J., Carollo, C. M. 2005, MNRAS, 364, 665

Dolag, K., Bartelmann, M., Perrotta, F., Baccigalupi, C., Moscardini, L., Meneghetti, M., Tormen, G. 2004, A&A, 416, 853

D'Onghia, E., Lake, G. 2004, ApJ, 612, 628

D'Onghia, E., Maccio', A. V., Lake, G., Stadel, J., Moore, B. 2007, ArXiv e-prints, 704

Efstathiou, G., Davis, M., White, S. D. M., Frenk, C. S. 1985, ApJS, 57, 241

Egami, E., Kneib, J.-P., Rieke, G. H., Ellis, R. S., Richard, J., Rigby, J., Papovich, C., Stark, D., Santos, M. R., Huang, J.-S., Dole, H., Le Floc'h, E., Pérez-González, P. G. 2005, ApJ, 618, L5

Eisenstein, D. J., Hu, W. 1998, ApJ, 496, 605

Eisenstein, D. J., Seo, H.-J., White, M. 2007, ApJ, 664, 660

Eisenstein, D. J., Zehavi, I., Hogg, D. W., Scoccimarro, R., Blanton, M. R., Nichol, R. C., Scranton, R., Seo, H.-J., Tegmark, M., Zheng, Z., Anderson, S. F., Annis, J., Bahcall, N., Brinkmann, J., Burles, S., Castander, F. J., Connolly, A., Csabai, I., Doi, M., Fukugita, M., Frieman, J. A., Glazebrook, K., Gunn, J. E., Hendry, J. S., Hennessy, G., Ivezić, Z., Kent, S., Knapp, G. R., Lin, H., Loh, Y.-S., Lupton, R. H., Margon, B., McKay, T. A., Meiksin, A., Munn, J. A., Pope, A., Richmond, M. W., Schlegel, D., Schneider, D. P., Shimasaku, K., Stoughton, C., Strauss, M. A., SubbaRao, M., Szalay, A. S., Szapudi, I., Tucker, D. L., Yanny, B., York, D. G. 2005, ApJ, 633, 560

Eke, V. R., Cole, S., Frenk, C. S. 1996, MNRAS, 282, 263

Eke, V. R., Cole, S., Frenk, C. S., Patrick Henry, J. 1998, MNRAS, 298, 1145

Eke, V. R., Navarro, J. F., Steinmetz, M. 2001, ApJ, 554, 114

Ellis, R., Santos, M. R., Kneib, J.-P., Kuijken, K. 2001, ApJ, 560, L119

Falco, E. E., Gorenstein, M. V., Shapiro, I. I. 1985, ApJ, 289, L1

Fernández-Soto, A., Lanzetta, K. M., Yahil, A. 1999, ApJ, 513, 34

Filippenko, A. V. 1997, ARA&A, 35, 309

Fillmore, J. A., Goldreich, P. 1984, ApJ, 281, 1

Gao, L., White, S. D. M., Jenkins, A., Stoehr, F., Springel, V. 2004, MNRAS, 355, 819

Gavazzi, R., Soucail, G. 2007, A&A, 462, 459

Gavazzi, R., Treu, T., Rhodes, J. D., Koopmans, L. V., Bolton, A. S., Burles, S., Massey, R., Moustakas, L. A. 2007, ArXiv Astrophysics e-prints: astro-ph/0701589

Ghigna, S., Moore, B., Governato, F., Lake, G., Quinn, T., Stadel, J. 1998, MNRAS, 300, 146

Giavalisco, M. et al. 2004, ApJ, 600, L93

Gilmore, G., Wilkinson, M. I., Wyse, R. F. G., Kleyna, J. T., Koch, A., Evans, N. W., Grebel, E. K. 2007, ApJ, 663, 948

Gladders, M. D., Yee, H. K. C., Majumdar, S., Barrientos, L. F., Hoekstra, H., Hall, P. B., Infante, L. 2007, ApJ, 655, 128

Goldberg, D. M., Bacon, D. J. 2005, ApJ, 619, 741

Goldberg, D. M., Leonard, A. 2007, ApJ, 660, 1003

Goldberg, D. M., Natarajan, P. 2002, ApJ, 564, 65

Gorenstein, M. V., Shapiro, I. I., Falco, E. E. 1988, ApJ, 327, 693

Gray, M. E., STAGES Collaboration 2006, in Bulletin of the American Astronomical Society, Vol. 38 of *Bulletin of the American Astronomical Society*, p. 146

Grazian, A., Fontana, A., de Santis, C., Nonino, M., Salimbeni, S., Giallongo, E., Cristiani, S., Gallozzi, S., Vanzella, E. 2006, A&A, 449, 951

Gunn, J. E. 1977, ApJ, 218, 592

Gunn, J. E., Gott, J. R. I. 1972, ApJ, 176, 1

Gustafsson, M., Fairbairn, M., Sommer-Larsen, J. 2006, Phys. Rev. D, 74(12), 123522

Guy, J., Astier, P., Baumont, S., Hardin, D., Pain, R., Regnault, N., Basa, S., Carlberg, R. G., Conley, A., Fabbro, S., Fouchez, D., Hook, I. M., Howell, D. A., Perrett, K., Pritchet, C. J., Rich, J., Sullivan, M., Antilogus, P., Aubourg, E., Bazin, G., Bronder, J., Filiol, M., Palanque-Delabrouille, N., Ripoche, P., Ruhlmann-Kleider, V. 2007, A&A, 466, 11

Guzik, J., Seljak, U. 2002, MNRAS, 335, 311

Haiman, Z., Allen, S., Bahcall, N., Bautz, M., Boehringer, H., Borgani, S., Bryan, G., Cabrera, B., Canizares, C., Citterio, O., Evrard, A., Finoguenov, A., Griffiths, R., Hasinger, G., Henry, P., Jahoda, K., Jernigan, G., Kahn, S., Lamb, D., Majumdar, S., Mohr, J., Molendi, S., Mushotzky, R., Pareschi, G., Peterson, J., Petre, R., Predehl, P., Rasmussen, A., Ricker, G., Ricker, P., Rosati, P., Sanderson, A., Stanford, A., Voit, M., Wang, S., White, N., White, S. 2005, ArXiv Astrophysics e-prints

Häussler, B., McIntosh, D. H., Barden, M., Bell, E. F., Rix, H.-W., Borch, A., Beckwith, S. V. W., Caldwell, J. A. R., Heymans, C., Jahnke, K., Jogee, S., Koposov, S. E., Meisenheimer, K., Sánchez, S. F., Somerville, R. S., Wisotzki, L., Wolf, C. 2007, ApJS, 172, 615

Hennawi, J. F., Dalal, N., Bode, P., Ostriker, J. P. 2007, ApJ, 654, 714

Henry, J. P. 2004, ApJ, 609, 603

Hernquist, L. 1990, ApJ, 356, 359

Hernquist, L., Bouchet, F. R., Suto, Y. 1991, ApJS, 75, 231

Hetterscheidt, M., Simon, P., Schirmer, M., Hildebrandt, H., Schrabback, T., Erben, T., Schneider, P. 2006, ArXiv Astrophysics e-prints: astro-ph/0606571

Hetterscheidt, M., Simon, P., Schirmer, M., Hildebrandt, H., Schrabback, T., Erben, T., Schneider, P. 2007, A&A, 468, 859

Heymans, C. et al. 2005, MNRAS, 361, 160

Heymans, C. et al. 2006a, MNRAS, 371, L60

Heymans, C. et al. 2006b, MNRAS, 368, 1323

Hirata, C., Seljak, U. 2003, MNRAS, 343, 459

Hockney, R. W., Eastwood, J. W. 1988, Computer simulation using particles, Bristol: Hilger, 1988

Hoekstra, H. 2004, MNRAS, 347, 1337

Hoekstra, H., Franx, M., Kuijken, K., Squires, G. 1998, ApJ, 504, 636

Hoekstra, H., Hsieh, B. C., Yee, H. K. C., Lin, H., Gladders, M. D. 2005, ApJ, 635, 73

Hoekstra, H., Mellier, Y., van Waerbeke, L., Semboloni, E., Fu, L., Hudson, M. J., Parker, L. C., Tereno, I., Benabed, K. 2006, ApJ, 647, 116

Hoekstra, H., Yee, H. K. C., Gladders, M. D. 2004, ApJ, 606, 67

Hopkins, P. F., Bahcall, N. A., Bode, P. 2005, ApJ, 618, 1

Horesh, A., Ofek, E. O., Maoz, D., Bartelmann, M., Meneghetti, M., Rix, H.-W. 2005, ApJ, 633, 768

Hu, W., Sugiyama, N. 1995, ApJ, 444, 489

Hu, W., Sugiyama, N. 1996, ApJ, 471, 542

Ilbert, O., Arnouts, S., McCracken, H. J., Bolzonella, M., Bertin, E., Le Fèvre, O., Mellier, Y., Zamorani, G., Pellò, R., Iovino, A., Tresse, L., Le Brun, V., Bottini, D., Garilli, B., Maccagni, D., Picat, J. P., Scaramella, R., Scodeggio, M., Vettolani, G., Zanichelli, A., Adami, C., Bardelli, S., Cappi, A., Charlot, S., Ciliegi, P., Contini, T., Cucciati, O., Foucaud, S., Franzetti, P., Gavignaud, I., Guzzo, L., Marano, B., Marinoni, C., Mazure, A., Meneux, B., Merighi, R., Paltani, S., Pollo, A., Pozzetti, L., Radovich, M., Zucca, E., Bondi, M., Bongiorno, A., Busarello, G., de La Torre, S., Gregorini, L., Lamareille, F., Mathez, G., Merluzzi, P., Ripepi, V., Rizzo, D., Vergani, D. 2006, A&A, 457, 841

Irwin, J., Shmakova, M. 2003, ArXiv Astrophysics e-prints

Irwin, J., Shmakova, M. 2005, New Astronomy Review, 49, 83

Irwin, J., Shmakova, M., Anderson, J. 2007, ApJ, 671, 1182

Jahnke, K., Sánchez, S. F., Wisotzki, L., Barden, M., Beckwith, S. V. W., Bell, E. F., Borch, A., Caldwell, J. A. R., Häussler, B., Heymans, C., Jogee, S., McIntosh, D. H., Meisenheimer, K., Peng, C. Y., Rix, H.-W., Somerville, R. S., Wolf, C. 2004, ApJ, 614, 568

Jarvis, M., Jain, B. 2004, ArXiv Astrophysics e-prints

Jha, S., Riess, A. G., Kirshner, R. P. 2007, ApJ, 659, 122

Jing, Y. P. 2000, ApJ, 535, 30

Jing, Y. P., Suto, Y. 2002, ApJ, 574, 538

Kaiser, N. 2000, ApJ, 537, 555

Kaiser, N., Squires, G. 1993, ApJ, 404, 441

Kaiser, N., Squires, G., Broadhurst, T. 1995, ApJ, 449, 460

Kaiser, N., Wilson, G., Luppino, G. A. 2000, ArXiv Astrophysics e-prints: astro-ph/0003338

Kassiola, A., Kovner, I. 1993, ApJ, 417, 450

Kasun, S. F., Evrard, A. E. 2005, ApJ, 629, 781

Kleinheinrich, M., Rix, H.-W., Erben, T., Schneider, P., Wolf, C., Schirmer, M., Meisenheimer, K., Borch, A., Dye, S., Kovacs, Z., Wisotzki, L. 2005, A&A, 439, 513

Kleinheinrich, M., Schneider, P., Rix, H.-W., Erben, T., Wolf, C., Schirmer, M., Meisenheimer, K., Borch, A., Dye, S., Kovacs, Z., Wisotzki, L. 2006, A&A, 455, 441

Klypin, A., Gottlöber, S., Kravtsov, A. V., Khokhlov, A. M. 1999a, ApJ, 516, 530

Klypin, A., Kravtsov, A. V., Valenzuela, O., Prada, F. 1999b, ApJ, 522, 82

Kneib, J.-P., Ellis, R. S., Santos, M. R., Richard, J. 2004, ApJ, 607, 697

Kneib, J.-P., Ellis, R. S., Smail, I., Couch, W. J., Sharples, R. M. 1996, ApJ, 471, 643

Kneib, J.-P., Hudelot, P., Ellis, R. S., Treu, T., Smith, G. P., Marshall, P., Czoske, O., Smail, I., Natarajan, P. 2003, ApJ, 598, 804

Koch, A., Kleyna, J. T., Wilkinson, M. I., Grebel, E. K., Gilmore, G. F., Evans, N. W., Wyse, R. F. G., Harbeck, D. R. 2007, AJ, 134, 566

Kochanek, C. S. 2006, in G. Meylan, P. Jetzer, P. North, P. Schneider, C. S. Kochanek, J. Wambsganss (eds.), Saas-Fee Advanced Course 33: Gravitational Lensing: Strong, Weak and Micro, p. 91

Kochanski, G. P., dell'Antonio, I. P., Tyson, J. A. 1996, in Bulletin of the American Astronomical Society, Vol. 28 of *Bulletin of the American Astronomical Society*, p. 1368

Koekemoer, A. M., Fruchter, A. S., Hook, R. N., Hack, W. 2002, in S. Arribas, A. Koekemoer, B. Whitmore (eds.), The 2002 HST Calibration Workshop : Hubble after the Installation of the ACS and the NICMOS Cooling System, Proceedings of a Workshop held at the Space Telescope Science Institute, Baltimore, Maryland, October 17 and 18, 2002. Edited by Santiago Arribas, Anton Koekemoer, and Brad Whitmore. Baltimore, MD: Space Telescope Science Institute, 2002., p.337, p. 337

Kogut, A., Spergel, D. N., Barnes, C., Bennett, C. L., Halpern, M., Hinshaw, G., Jarosik, N., Limon, M., Meyer, S. S., Page, L., Tucker, G. S., Wollack, E., Wright, E. L. 2003, ApJS, 148, 161

Koopmans, L. V. E. 2005, MNRAS, 363, 1136

Koopmans, L. V. E., Treu, T., Bolton, A. S., Burles, S., Moustakas, L. A. 2006, ApJ, 649, 599

Koposov, S., Belokurov, V., Evans, N. W., Hewett, P. C., Irwin, M. J., Gilmore, G., Zucker, D. B., Rix, H. ., Fellhauer, M., Bell, E. F., Glushkova, E. V. 2007, ArXiv e-prints:astro-ph/0706.2687, 706

Kosowsky, A. 2003, New Astronomy Review, 47, 939

Kosowsky, A., Milosavljevic, M., Jimenez, R. 2002, Phys. Rev. D, 66(6), 063007

Kovac, J., BICEP/SPUD Collaboration 2006, in Bulletin of the American Astronomical Society, Vol. 38 of *Bulletin of the American Astronomical Society*, p. 913

Kovac, J. M., Barkats, D. 2007, ArXiv e-prints, 707

Krist, J. 1995, in R. A. Shaw, H. E. Payne, J. J. E. Hayes (eds.), Astronomical Data Analysis Software and Systems IV, Vol. 77 of *Astronomical Society of the Pacific Conference Series*, p. 349

Kroupa, P., Theis, C., Boily, C. M. 2005, A&A, 431, 517

Kuhlen, M., Strigari, L. E., Zentner, A. R., Bullock, J. S., Primack, J. R. 2005, MNRAS, 357, 387

Kuijken, K. 2006, A&A, 456, 827

Lanzetta, K. M., Yahil, A., Fernández-Soto, A. 1996, Nature, 381, 759

Le Fèvre, O. et al. 2004, A&A, 428, 1043

Lehár, J., Falco, E. E., Kochanek, C. S., McLeod, B. A., Muñoz, J. A., Impey, C. D., Rix, H.-W., Keeton, C. R., Peng, C. Y. 2000, ApJ, 536, 584

Lehár, J., Falco, E. E., Kochanek, C. S., McLeod, B. A., Muñoz, J. A., Impey, C. D., Rix, H.-W., Keeton, C. R., Peng, D. C. Y. 2002, ApJ, 571, 1021

Leonard, A., Goldberg, D. M., Haaga, J. L., Massey, R. 2007, ArXiv Astrophysics e-prints: astro-ph/0702242

Lewis, A., Challinor, A. 2006, Phys. Rep., 429, 1

Lewis, A., Challinor, A., Lasenby, A. 2000, ApJ, 538, 473

Li, G. L., Mao, S., Jing, Y. P., Mo, H. J., Gao, L., Lin, W. P. 2006, MNRAS, 372, L73

Libeskind, N. I., Frenk, C. S., Cole, S., Helly, J. C., Jenkins, A., Navarro, J. F., Power, C. 2005, MNRAS, 363, 146

Limousin, M., Richard, J., Jullo, E., Kneib, J.-P., Fort, B., Soucail, G., Elíasdóttir, Á., Natarajan, P., Ellis, R. S., Smail, I., Czoske, O., Smith, G. P., Hudelot, P., Bardeau, S., Ebeling, H., Egami, E., Knudsen, K. K. 2007, ApJ, 668, 643

Łokas, E. L., Mamon, G. A. 2003, MNRAS, 343, 401

Luppino, G. A., Kaiser, N. 1997, ApJ, 475, 20

Lupton, R. 1993, Statistics in theory and practice, Princeton, N.J.: Princeton University Press, —c1993

Lynds, R., Petrosian, V. 1986, in Bulletin of the American Astronomical Society, Vol. 18 of *Bulletin of the American Astronomical Society*, p. 1014

Lynds, R., Petrosian, V. 1989, ApJ, 336, 1

Macciò, A. V., Dutton, A. A., van den Bosch, F. C., Moore, B., Potter, D., Stadel, J. 2007, MNRAS, 378, 55

Mainini, R., Macciò, A. V., Bonometto, S. A., Klypin, A. 2003, ApJ, 599, 24

Mandelbaum, R., Hirata, C. M., Seljak, U., Guzik, J., Padmanabhan, N., Blake, C., Blanton, M. R., Lupton, R., Brinkmann, J. 2005, MNRAS, 361, 1287

Mandelbaum, R., Seljak, U., Cool, R. J., Blanton, M., Hirata, C. M., Brinkmann, J. 2006a, MNRAS, 372, 758

Mandelbaum, R., Seljak, U., Cool, R. J., Blanton, M., Hirata, C. M., Brinkmann, J. 2006b, MNRAS, 372, 758

Massey, R. et al. 2007a, Nature, 445, 286

Massey, R., Heymans, C., Bergé, J., Bernstein, G., Bridle, S., Clowe, D., Dahle, H., Ellis, R., Erben, T., Hetterscheidt, M., High, F. W., Hirata, C., Hoekstra, H., Hudelot, P., Jarvis, M., Johnston, D., Kuijken, K., Margoniner, V., Mandelbaum, R., Mellier, Y., Nakajima, R., Paulin-Henriksson, S., Peeples, M., Roat, C., Refregier, A., Rhodes, J., Schrabback, T., Schirmer, M., Seljak, U., Semboloni, E., van Waerbeke, L. 2007b, MNRAS, 376, 13

Massey, R., Refregier, A. 2005, MNRAS, 363, 197

Massey, R., Refregier, A., Conselice, C. J., Bacon, D. J. 2004, MNRAS, 348, 214

Massey, R., Rhodes, J., Leauthaud, A., Capak, P., Ellis, R., Koekemoer, A., Réfrégier, A., Scoville, N., Taylor, J. E., Albert, J., Bergé, J., Heymans, C., Johnston, D., Kneib, J.-P., Mellier, Y., Mobasher, B., Semboloni, E., Shopbell, P., Tasca, L., Van Waerbeke, L. 2007c, ApJS, 172, 239

Massey, R., Rowe, B., Refregier, A., Bacon, D. J., Bergé, J. 2007d, MNRAS, 380, 229

McGaugh, S. S., de Blok, W. J. G. 1998, ApJ, 499, 66

Meiksin, A., White, M., Peacock, J. A. 1999, MNRAS, 304, 851

Melchior, P., Meneghetti, M., Bartelmann, M. 2007, A&A, 463, 1215

Metcalf, R. B. 2005, ApJ, 622, 72

Meurer, G. R., Lindler, D. J., Blakeslee, J., Cox, C. R., Martel, A., Tran, H. D., Bouwens, R., Ford, H. C., Clampin, M., Hartig, G. F., Sirianni, M., De Marchi, G. 2003, in J. C. Blades, O. H. W. Siegmund (eds.), Proceedings of the SPIE, Volume 4854, pp. 507-514 (2003)., Vol. 4854, p. 507

Milgrom, M. 1983, ApJ, 270, 365

Milgrom, M., Sanders, R. H. 2007, ApJ, 658, L17

Miralda-Escudé, J. 1991, ApJ, 370, 1

Moore, B., Ghigna, S., Governato, F., Lake, G., Quinn, T., Stadel, J., Tozzi, P. 1999a, ApJ, 524, L19

Moore, B., Governato, F., Quinn, T., Stadel, J., Lake, G. 1998, ApJ, 499, L5+

Moore, B., Katz, N., Lake, G. 1996, ApJ, 457, 455

Moore, B., Quinn, T., Governato, F., Stadel, J., Lake, G. 1999b, MNRAS, 310, 1147

Narayan, R., Bartelmann, M. 1999, in A. Dekel, J. P. Ostriker (eds.), Formation of Structure in the Universe, p. 360

Natarajan, P., Springel, V. 2004, ApJ, 617, L13

Navarro, J. F., Frenk, C. S., White, S. D. M. 1995, MNRAS, 275, 720

Navarro, J. F., Frenk, C. S., White, S. D. M. 1996, ApJ, 462, 563

Navarro, J. F., Frenk, C. S., White, S. D. M. 1997, ApJ, 490, 493

Navarro, J. F., Hayashi, E., Power, C., Jenkins, A. R., Frenk, C. S., White, S. D. M., Springel, V., Stadel, J., Quinn, T. R. 2004, MNRAS, 349, 1039

Neto, A. F., Gao, L., Bett, P., Cole, S., Navarro, J. F., Frenk, C. S., White, S. D. M., Springel, V., Jenkins, A. 2007, ArXiv e-prints, 706

Noordermeer, E., van der Hulst, J. M., Sancisi, R., Swaters, R. S., van Albada, T. S. 2007, MNRAS, 376, 1513

Nurmi, P., Heinämäki, P., Saar, E., Einasto, M., Holopainen, J., Mart{\'\i}nez, V. J., Einasto, J. 2006, ArXiv Astrophysics e-prints:astro-ph/0611941

Oguri, M. 2007, ApJ, 660, 1

Oguri, M., Lee, J., Suto, Y. 2003, ApJ, 599, 7

Okura, Y., Umetsu, K., Futamase, T. 2007a, ArXiv e-prints, 710

Okura, Y., Umetsu, K., Futamase, T. 2007b, ApJ, 660, 995

O'Shea, B. W., Nagamine, K., Springel, V., Hernquist, L., Norman, M. L. 2005, ApJS, 160, 1

Page, L., Nolta, M. R., Barnes, C., Bennett, C. L., Halpern, M., Hinshaw, G., Jarosik, N., Kogut, A., Limon, M., Meyer, S. S., Peiris, H. V., Spergel, D. N., Tucker, G. S., Wollack, E., Wright, E. L. 2003, ApJS, 148, 233

Peacock, J. A. 1999, Cosmological Physics, Cosmological Physics, by John A. Peacock, pp. 704. ISBN 052141072X. Cambridge, UK: Cambridge University Press, January 1999.

Pedersen, K., Dahle, H. 2007, ApJ, 667, 26

Peebles, P. J. E., Yu, J. T. 1970, ApJ, 162, 815

Pelló, R., Schaerer, D., Richard, J., Le Borgne, J.-F., Kneib, J.-P. 2004, A&A, 416, L35

Peng, C. Y., Ho, L. C., Impey, C. D., Rix, H.-W. 2002, AJ, 124, 266

Percival, W. J., Cole, S., Eisenstein, D. J., Nichol, R. C., Peacock, J. A., Pope, A. C., Szalay, A. S. 2007a, ArXiv e-prints, 705

Percival, W. J., Nichol, R. C., Eisenstein, D. J., Weinberg, D. H., Fukugita, M., Pope, A. C., Schneider, D. P., Szalay, A. S., Vogeley, M. S., Zehavi, I., Bahcall, N. A., Brinkmann, J., Connolly, A. J., Loveday, J., Meiksin, A. 2007b, ApJ, 657, 51

Perlmutter, S., Aldering, G., Goldhaber, G., Knop, R. A., Nugent, P., Castro, P. G., Deustua, S., Fabbro, S., Goobar, A., Groom, D. E., Hook, I. M., Kim, A. G., Kim, M. Y., Lee, J. C., Nunes, N. J., Pain, R., Pennypacker, C. R., Quimby, R., Lidman, C., Ellis, R. S., Irwin, M., McMahon, R. G., Ruiz-Lapuente, P., Walton, N., Schaefer, B., Boyle, B. J., Filippenko, A. V., Matheson, T., Fruchter, A. S., Panagia, N., Newberg, H. J. M., Couch, W. J., The Supernova Cosmology Project 1999, ApJ, 517, 565

Phillips, M. M. 1993, ApJ, 413, L105

Phillips, M. M., Lira, P., Suntzeff, N. B., Schommer, R. A., Hamuy, M., Maza, J. 1999, AJ, 118, 1766

Press, W. H., Teukolsky, S. A., Vetterling, W. T., Flannery, B. P. 1992, Numerical recipes in FORTRAN. The art of scientific computing, Cambridge: University Press, —c1992, 2nd ed.

QUaD Collaboration: P. Ade, Bock, J., Bowden, M., Brown, M. L., Cahill, G., Carlstrom, J. E., Castro, P. G., Church, S., Culverhouse, T., Friedman, R., Ganga, K., Gear, W. K., Hinderks, J., Kovac, J., Lange, A. E., Leitch, E., Melhuish, S. J., Murphy, J. A., Orlando, A., Schwarz, R., O'Sullivan, C., Piccirillo, L., Pryke, C., Rajguru, N., Rusholme, B., Taylor, A. N., Thompson, K. L., Wu, E. Y. S., Zemcov, M. 2007, ArXiv e-prints, 705

Reed, D., Governato, F., Quinn, T., Gardner, J., Stadel, J., Lake, G. 2005, MNRAS, 359, 1537

Refregier, A. 2003, MNRAS, 338, 35

Refregier, A., Bacon, D. 2003, MNRAS, 338, 48

Rhodes, J., Refregier, A., Collins, N. R., Gardner, J. P., Groth, E. J., Hill, R. S. 2004, ApJ, 605, 29

Rhodes, J., Refregier, A., Groth, E. J. 2000, ApJ, 536, 79

Rhodes, J. D., Massey, R., Albert, J., Collins, N., Ellis, R. S., Heymans, C., Gardner, J. P., Kneib, J.-P., Koekemoer, A., Leauthaud, A., Mellier, Y., Refregier, A., Taylor, J. E., Van Waerbeke, L. 2007, ArXiv Astrophysics e-prints: astro-ph/0702140

Riess, A. G., Filippenko, A. V., Challis, P., Clocchiatti, A., Diercks, A., Garnavich, P. M., Gilliland, R. L., Hogan, C. J., Jha, S., Kirshner, R. P., Leibundgut, B., Phillips, M. M., Reiss, D., Schmidt, B. P., Schommer, R. A., Smith, R. C., Spyromilio, J., Stubbs, C., Suntzeff, N. B., Tonry, J. 1998, AJ, 116, 1009

Riess, A. G., Strolger, L.-G., Casertano, S., Ferguson, H. C., Mobasher, B., Gold, B., Challis, P. J., Filippenko, A. V., Jha, S., Li, W., Tonry, J., Foley, R., Kirshner, R. P., Dickinson, M., MacDonald, E., Eisenstein, D., Livio, M., Younger, J., Xu, C., Dahlén, T., Stern, D. 2007, ApJ, 659, 98

Riess, A. G., Strolger, L.-G., Tonry, J., Casertano, S., Ferguson, H. C., Mobasher, B., Challis, P., Filippenko, A. V., Jha, S., Li, W., Chornock, R., Kirshner, R. P., Leibundgut, B., Dickinson, M., Livio, M., Giavalisco, M., Steidel, C. C., Benítez, T., Tsvetanov, Z. 2004, ApJ, 607, 665

Rindler, W. 2001, Relativity: special, general, and cosmological, Relativity: special, general, and cosmological / Wolfgang Rindler, Oxford, UK: Oxford University Press. ISBN 0-19-850835-2, 2001, XIII + 428 p.

Rix, H.-W., Barden, M., Beckwith, S. V. W., Bell, E. F., Borch, A., Caldwell, J. A. R., Häussler, B., Jahnke, K., Jogee, S., McIntosh, D. H., Meisenheimer, K., Peng, C. Y., Sanchez, S. F., Somerville, R. S., Wisotzki, L., Wolf, C. 2004, ApJS, 152, 163

Rusin, D., Kochanek, C. S., Falco, E. E., Keeton, C. R., McLeod, B. A., Impey, C. D., Lehár, J., Muñoz, J. A., Peng, C. Y., Rix, H.-W. 2003, ApJ, 587, 143

Saha, P., Coles, J., Macciò, A. V., Williams, L. L. R. 2006, ApJ, 650, L17

Sales, L. V., Navarro, J. F., Abadi, M. G., Steinmetz, M. 2007, MNRAS, 379, 1464

Salucci, P. 2007, ArXiv e-prints:astro-ph/0707.4370, 707

Sánchez, A. G., Baugh, C. M., Percival, W. J., Peacock, J. A., Padilla, N. D., Cole, S., Frenk, C. S., Norberg, P. 2006, MNRAS, 366, 189

Sanders, R. H., Noordermeer, E. 2007, MNRAS, 379, 702

Sanders, R. H., Verheijen, M. A. W. 1998, ApJ, 503, 97

Santos, M. R., Ellis, R. S., Kneib, J.-P., Richard, J., Kuijken, K. 2004, ApJ, 606, 683

Saraniti, D. W., Petrosian, V., Lynds, R. 1996, ApJ, 458, 57

Schneider, P. 2006, in G. Meylan, P. Jetzer, P. North, P. Schneider, C. S. Kochanek, J. Wambsganss (eds.), Saas-Fee Advanced Course 33: Gravitational Lensing: Strong, Weak and Micro, p. 269

Schneider, P., Ehlers, J., Falco, E. E. 1992, Gravitational Lenses, Gravitational Lenses, XIV, 560 pp. 112 figs.. Springer-Verlag Berlin Heidelberg New York. Also Astronomy and Astrophysics Library

Schneider, P., Er, X. 2007, ArXiv e-prints, 709

Schneider, P., Kochanek, C. S., Wambsganss, J. (eds.) 2006, Gravitational Lensing: Strong, Weak and Micro

Schneider, P., Rix, H.-W. 1997, ApJ, 474, 25

Schneider, P., Seitz, C. 1995, A&A, 294, 411

Schrabback, T., Erben, T., Simon, P., Miralles, J.-M., Schneider, P., Heymans, C., Eifler, T., Fosbury, R. A. E., Freudling, W., Hetterscheidt, M., Hildebrandt, H., Pirzkal, N. 2007, A&A, 468, 823

Seitz, S., Schneider, P., Bartelmann, M. 1998, A&A, 337, 325

Sellwood, J. A., McGaugh, S. S. 2005, ApJ, 634, 70

Semboloni, E., Mellier, Y., van Waerbeke, L., Hoekstra, H., Tereno, I., Benabed, K., Gwyn, S. D. J., Fu, L., Hudson, M. J., Maoli, R., Parker, L. C. 2006, A&A, 452, 51

Shaw, L. D., Weller, J., Ostriker, J. P., Bode, P. 2007, ApJ, 659, 1082

Sheldon, E. S., Johnston, D. E., Frieman, J. A., Scranton, R., McKay, T. A., Connolly, A. J., Budavári, T., Zehavi, I., Bahcall, N. A., Brinkmann, J., Fukugita, M. 2004, AJ, 127, 2544

Silk, J. 1968, ApJ, 151, 459

Smail, I., Swinbank, A. M., Richard, J., Ebeling, H., Kneib, J.-P., Edge, A. C., Stark, D., Ellis, R. S., Dye, S., Smith, G. P., Mullis, C. 2007, ApJ, 654, L33

Smith, G. P., Kneib, J.-P., Smail, I., Mazzotta, P., Ebeling, H., Czoske, O. 2005, MNRAS, 359, 417

Smith, K. M., Zahn, O., Doré, O. 2007, Phys. Rev. D, 76(4), 043510

Soucail, G., Fort, B., Mellier, Y., Picat, J. P. 1987, A&A, 172, L14

Spergel, D. N., Bean, R., Doré, O., Nolta, M. R., Bennett, C. L., Dunkley, J., Hinshaw, G., Jarosik, N., Komatsu, E., Page, L., Peiris, H. V., Verde, L., Halpern, M., Hill, R. S., Kogut, A., Limon, M., Meyer, S. S., Odegard, N., Tucker, G. S., Weiland, J. L., Wollack, E., Wright, E. L. 2007, ApJS, 170, 377

Spergel, D. N., Verde, L., Peiris, H. V., Komatsu, E., Nolta, M. R., Bennett, C. L., Halpern, M., Hinshaw, G., Jarosik, N., Kogut, A., Limon, M., Meyer, S. S., Page, L., Tucker, G. S., Weiland, J. L., Wollack, E., Wright, E. L. 2003, ApJS, 148, 175

Springel, V., Frenk, C. S., White, S. D. M. 2006, Nature, 440, 1137

Springel, V., White, S. D. M., Jenkins, A., Frenk, C. S., Yoshida, N., Gao, L., Navarro, J., Thacker, R., Croton, D., Helly, J., Peacock, J. A., Cole, S., Thomas, P., Couchman, H., Evrard, A., Colberg, J., Pearce, F. 2005, Nature, 435, 629

Stark, D. P., Ellis, R. S., Richard, J., Kneib, J.-P., Smith, G. P., Santos, M. R. 2007, ApJ, 663, 10

Stoehr, F., White, S. D. M., Tormen, G., Springel, V. 2002, MNRAS, 335, L84

Strigari, L. E., Bullock, J. S., Kaplinghat, M., Diemand, J., Kuhlen, M., Madau, P. 2007, ArXiv e-prints, 704

Summers, F. J., Davis, M., Evrard, A. E. 1995, ApJ, 454, 1

Sunyaev, R. A., Zeldovich, Y. B. 1970, Ap&SS, 7, 3

Taylor, J. E., Babul, A. 2004, MNRAS, 348, 811

Taylor, J. E., Babul, A. 2005a, MNRAS, 364, 515

Taylor, J. E., Babul, A. 2005b, MNRAS, 364, 535

Tegmark, M., Eisenstein, D. J., Strauss, M. A., Weinberg, D. H., Blanton, M. R., Frieman, J. A., Fukugita, M., Gunn, J. E., Hamilton, A. J. S., Knapp, G. R., Nichol, R. C., Ostriker, J. P., Padmanabhan, N., Percival, W. J., Schlegel, D. J., Schneider, D. P., Scoccimarro, R., Seljak, U., Seo, H.-J., Swanson, M., Szalay, A. S., Vogeley, M. S., Yoo, J., Zehavi, I., Abazajian, K., Anderson, S. F., Annis, J., Bahcall, N. A., Bassett, B., Berlind, A., Brinkmann, J., Budavari, T., Castander, F., Connolly, A., Csabai, I., Doi, M., Finkbeiner, D. P., Gillespie, B., Glazebrook, K., Hennessy, G. S., Hogg, D. W., Ivezić, Ž., Jain, B., Johnston, D., Kent, S., Lamb, D. Q., Lee, B. C., Lin, H., Loveday, J., Lupton, R. H., Munn, J. A., Pan, K., Park, C., Peoples, J., Pier, J. R., Pope, A., Richmond, M., Rockosi, C., Scranton, R., Sheth, R. K., Stebbins, A., Stoughton, C., Szapudi, I., Tucker, D. L., Berk, D. E. V., Yanny, B., York, D. G. 2006, Phys. Rev. D, 74(12), 123507

Tegmark, M., Strauss, M. A., Blanton, M. R., Abazajian, K., Dodelson, S., Sandvik, H., Wang, X., Weinberg, D. H., Zehavi, I., Bahcall, N. A., Hoyle, F., Schlegel, D., Scoccimarro, R., Vogeley, M. S., Berlind, A., Budavari, T., Connolly, A., Eisenstein, D. J., Finkbeiner, D., Frieman, J. A., Gunn, J. E., Hui, L., Jain, B., Johnston, D., Kent, S., Lin, H., Nakajima, R., Nichol, R. C., Ostriker, J. P., Pope, A., Scranton,

R., Seljak, U., Sheth, R. K., Stebbins, A., Szalay, A. S., Szapudi, I., Xu, Y., Annis, J., Brinkmann, J., Burles, S., Castander, F. J., Csabai, I., Loveday, J., Doi, M., Fukugita, M., Gillespie, B., Hennessy, G., Hogg, D. W., Ivezić, Ž., Knapp, G. R., Lamb, D. Q., Lee, B. C., Lupton, R. H., McKay, T. A., Kunszt, P., Munn, J. A., O'Connell, L., Peoples, J., Pier, J. R., Richmond, M., Rockosi, C., Schneider, D. P., Stoughton, C., Tucker, D. L., vanden Berk, D. E., Yanny, B., York, D. G. 2004, Phys. Rev. D, 69(10), 103501

The Planck Collaboration 2006, ArXiv Astrophysics e-prints:astro-ph/0604069

Tonini, C., Lapi, A., Salucci, P. 2006, ApJ, 649, 591

Treu, T., Koopmans, L. V. E., Bolton, A. S., Burles, S., Moustakas, L. A. 2006, ApJ, 650, 1219

Tyson, J. A., Kochanski, G. P., dell'Antonio, I. P. 1998, ApJ, 498, L107+

Tyson, J. A., Valdes, F., Jarvis, J. F., Mills, Jr., A. P. 1984, ApJ, 281, L59

van Albada, T. S., Bahcall, J. N., Begeman, K., Sancisi, R. 1985, ApJ, 295, 305

van Albada, T. S., Sancisi, R. 1986, Royal Society of London Philosophical Transactions Series A, 320, 447

Van Waerbeke, L., Mellier, Y., Erben, T., Cuillandre, J. C., Bernardeau, F., Maoli, R., Bertin, E., Mc Cracken, H. J., Le Fèvre, O., Fort, B., Dantel-Fort, M., Jain, B., Schneider, P. 2000, A&A, 358, 30

Van Waerbeke, L., Mellier, Y., Hoekstra, H. 2005a, A&A, 429, 75

Van Waerbeke, L., Mellier, Y., Hoekstra, H. 2005b, A&A, 429, 75

van Waerbeke, L., White, M., Hoekstra, H., Heymans, C. 2006, Astroparticle Physics, 26, 91

Walker, M. G., Mateo, M., Olszewski, E. W., Gnedin, O. Y., Wang, X., Sen, B., Woodroofe, M. 2007, ArXiv e-prints, 708

Walsh, D., Carswell, R. F., Weymann, R. J. 1979, Nature, 279, 381

Wang, L., Goldhaber, G., Aldering, G., Perlmutter, S. 2003, ApJ, 590, 944

Weatherley, S. J., Warren, S. J., Babbedge, T. S. R. 2004, A&A, 428, L29

White, S. D. M. 1976, MNRAS, 177, 717

White, S. D. M., Davis, M., Efstathiou, G., Frenk, C. S. 1987, Nature, 330, 451

White, S. D. M., Rees, M. J. 1978, MNRAS, 183, 341

Williams, R., Baum, S. A., Bergeron, L. E., Blacker, B., Boyle, B. J., Brown, T. M., Bernstein, N., Carollo, C. M., Casertano, S., de Mello, D., Dickinson, M., Espey, B. R., Ferguson, H. C., Fruchter, A. S., Gardner, J. P., Gonnella, A., Gonzalez, R., Hayes, J., Hewett, P., Heyer, I., Hook, R. N., Jones, D., Kaiser, M. E., Lubenow, A., Lucas, R. A., Mack, J., MacKenty, J. W., Madau, P., Makidon, R., Martin, C. L., Mazzuca, L., Mutchler, M., Norris, R. P., Perriello, B., Postman, M., Royle, P., Sahu, K. C., Savaglio, S., Sherwin, A., Smith, E., Stiavelli, M., Teplitz, H. I., van der Marel, R., Weymann, R. J., Wiggs, M. S., Williger, G. M., Wilson, J., Zurek, D. 1998, in Bulletin of the American Astronomical Society, Vol. 30 of *Bulletin of the American Astronomical Society*, p. 1366

Williams, R. E., Blacker, B., Dickinson, M., Dixon, W. V. D., Ferguson, H. C., Fruchter, A. S., Giavalisco, M., Gilliland, R. L., Heyer, I., Katsanis, R., Levay, Z., Lucas, R. A., McElroy, D. B., Petro, L., Postman, M., Adorf, H.-M., Hook, R. 1996, AJ, 112, 1335

Wilson, O. C. 1939, ApJ, 90, 634

Wittman, D. M., Tyson, J. A., Kirkman, D., Dell'Antonio, I., Bernstein, G. 2000, Nature, 405, 143

Wolf, C., Meisenheimer, K., Kleinheinrich, M., Borch, A., Dye, S., Gray, M., Wisotzki, L., Bell, E. F., Rix, H.-W., Cimatti, A., Hasinger, G., Szokoly, G. 2004, A&A, 421, 913

Wolf, C., Meisenheimer, K., Rix, H.-W., Borch, A., Dye, S., Kleinheinrich, M. 2003, A&A, 401, 73

Wood-Vasey, W. M., Miknaitis, G., Stubbs, C. W., Jha, S., Riess, A. G., Garnavich, P. M., Kirshner, R. P., Aguilera, C., Becker, A. C., Blackman, J. W., Blondin, S., Challis, P., Clocchiatti, A., Conley, A., Covarrubias, R., Davis, T. M., Filippenko, A. V., Foley, R. J., Garg, A., Hicken, M., Krisciunas, K., Leibundgut, B., Li, W., Matheson, T., Miceli, A., Narayan, G., Pignata, G., Prieto, J. L., Rest, A., Salvo, M. E., Schmidt, B. P., Smith, R. C., Sollerman, J., Spyromilio, J., Tonry, J. L., Suntzeff, N. B., Zenteno, A. 2007, ApJ, 666, 694

Wright, C. O., Brainerd, T. G. 2000, ApJ, 534, 34

Yoo, J., Kochanek, C. S., Falco, E. E., McLeod, B. A. 2006, ApJ, 642, 22

Yoon, K. W., Ade, P. A., Barkats, D., Battle, J. O., Bierman, E. M., Bock, J. J., Chiang, H. C., Dowell, C. D., Duband, L., Griffin, G. S., Hivon, E. F., Holzapfel, W. L., Hristov, V. V., Keating, B. G., Kovac, J. M., Kuo, C., Lange, A. E., Leitch, E. M., Mason, P. V., Nguyen, H. T., Ponthieu, N., Takahashi, Y. D. 2006, in Bulletin of the American Astronomical Society, Vol. 38 of *Bulletin of the American Astronomical Society*, p. 963

Zhao, D. H., Jing, Y. P., Mo, H. J., Börner, G. 2003, ApJ, 597, L9

Zhao, H. 1996, MNRAS, 278, 488

Zucker, D. B., Belokurov, V., Evans, N. W., Kleyna, J. T., Irwin, M. J., Wilkinson, M. I., Fellhauer, M., Bramich, D. M., Gilmore, G., Newberg, H. J., Yanny, B., Smith, J. A., Hewett, P. C., Bell, E. F., Rix, H.-W., Gnedin, O. Y., Vidrih, S., Wyse, R. F. G., Willman, B., Grebel, E. K., Schneider, D. P., Beers, T. C., Kniazev, A. Y., Barentine, J. C., Brewington, H., Brinkmann, J., Harvanek, M., Kleinman, S. J., Krzesinski, J., Long, D., Nitta, A., Snedden, S. A. 2006, ApJ, 650, L41

Zwicky, F. 1933, Helvetica Physica Acta, 6, 110

Zwicky, F. 1937, ApJ, 86, 217

# Appendix: Polar Shapelet Results

This Appendix provides details of polar shapelet results which proved too long to justify inclusion in the main body of the Thesis text.

## Flexion in terms of transformations upon the $f_{n,m}$ polar coefficients

In Section 3.2.2 we described the transformations for convergence, shear and flexion in terms of the polar shapelet ladder operators $\hat{a}_r$, $\hat{a}_r^\dagger$, $\hat{a}_l$, and $\hat{a}_l^\dagger$ (Equations 3.50-3.52, and 3.57-3.60). In Equations (3.53)-(3.55) we wrote the shear and convergence transformations in equivalent form, in terms of their action upon the shapelet coefficients $f_{n,m}$ that describe the shapelet model of the galaxy image $I(\boldsymbol{\theta}) = \sum f_{n,m} P_{n,m}(\boldsymbol{\theta};\beta)$. Similar expressions to these may be derived for flexion, expressing the transformations given in Equations (3.57)-(3.60) in terms of mappings upon the $f_{n,m}$ shapelet coefficients.

Using Equations (3.57) and (3.58), and following simple steps such as shown in Equation (3.13), I found the following expressions for the action of the first flexion transformation upon the shapelet coefficients $f^{\rm s}_{n,m}$ of an unlensed galaxy

$$
\begin{aligned}
(1+\mathcal{F}\hat{F}_r) \quad &: \\
f^{\rm s}_{n,m} \rightarrow f_{n,m} \quad &= \quad f^{\rm s}_{n,m} \\
&+ \quad \frac{\mathcal{F}\beta}{16\sqrt{2}} \Big\{ 3\sqrt{(n-m)(n+m)(n+m-2)}\, f^{\rm s}_{n-3,m-1} \\
&\qquad + (3n-m+10)\sqrt{(n+m)}\, f^{\rm s}_{n-1,m-1} \\
&\qquad - (3n+m-4)\sqrt{(n-m+2)}\, f^{\rm s}_{n+1,m-1} \\
&\qquad -3\sqrt{(n+m+2)(n-m+2)(n-m+4)}\, f^{\rm s}_{n+3,m-1} \Big\}, \qquad \text{(A-1)}
\end{aligned}
$$

$$
\begin{aligned}
(1+\mathcal{F}^*\hat{F}_l) \quad &: \\
f^{\rm s}_{n,m} \rightarrow f_{n,m} \quad &= \quad f^{\rm s}_{n,m} \\
&+ \quad \frac{\mathcal{F}^*\beta}{16\sqrt{2}}\Big\{\, 3\sqrt{(n+m)(n-m)(n-m-2)}\, f^{\rm s}_{n-3,m+1} \\
&\qquad + (3n+m+10)\sqrt{(n-m)}\, f^{\rm s}_{n-1,m+1} \\
&\qquad - (3n-m-4)\sqrt{(n+m+2)}\, f^{\rm s}_{n+1,m+1} \\
&\qquad -3\sqrt{(n-m+2)(n+m+2)(n+m+4)}\, f^{\rm s}_{n+3,m+1}\Big\}. \qquad \text{(A-2)}
\end{aligned}
$$

In a similar fashion, using Equations (3.59) and (3.60), we can represent the effects of the second flexion upon unlensed $f^{\rm s}_{n,m}$ coefficients as follows:

$$
\begin{aligned}
(1+\mathcal{G}\hat{G}_r) \quad &: \\
f^{\rm s}_{n,m} \rightarrow f_{n,m} \quad &= \quad f^{\rm s}_{n,m} \\
&+ \quad \frac{\mathcal{G}\beta}{16\sqrt{2}}\Big\{\, \sqrt{(n+m)(n+m-2)(n+m-4)}\, f^{\rm s}_{n-3,m-3} \\
&\qquad + \sqrt{(n+m)(n+m-2)(n-m+2)}\, f^{\rm s}_{n-1,m-3} \\
&\qquad - \sqrt{(n+m)(n-m+2)(n-m+4)}\, f^{\rm s}_{n+1,m-3} \\
&\qquad -\sqrt{(n-m+2)(n-m+4)(n-m+6)}\, f^{\rm s}_{n+3,m-3}\Big\}, \qquad \text{(A-3)}
\end{aligned}
$$

$$
\begin{aligned}
(1+\mathcal{G}^*\hat{G}_l) \quad &: \\
f^{\rm s}_{n,m} \rightarrow f_{n,m} \quad &= \quad f^{\rm s}_{n,m} \\
&+ \quad \frac{\mathcal{G}^*\beta}{16\sqrt{2}}\Big\{\, \sqrt{(n-m)(n-m-2)(n-m-4)}\, f^{\rm s}_{n-3,m+3} \\
&\qquad + \sqrt{(n-m)(n-m-2)(n+m+2)}\, f^{\rm s}_{n-1,m+3} \\
&\qquad - \sqrt{(n-m)(n+m+2)(n+m+4)}\, f^{\rm s}_{n+1,m+3} \\
&\qquad -\sqrt{(n+m+2)(n+m+4)(n+m+6)}\, f^{\rm s}_{n+3,m+3}\Big\}\,. \qquad \text{(A-4)}
\end{aligned}
$$

These are the polar shapelet expressions for the flexion transformation given in Massey et al. (2007d).

## The susceptibility of generalized $f_{n,1}$ and $f_{n,3}$ flexion estimators

In Section 3.4.3 it was described how flexion estimators could be constructed from any $f_{n,1}$ and $f_{n,3}$ coefficients (for first and second flexion respectively). In order to do this, however, it is necessary to know exactly how these coefficients respond to the action of flexion, information that can be represented by the $(P^{\mathcal{F}}_n)_{i,j}$ and $(P^{\mathcal{G}}_n)_{i,j}$ susceptibility matrices defined by Equation (3.105), which for clarity I reproduce here:

$$
(P^{\mathcal{F}}_n)_{ij} = \frac{\partial (f_{n,1})_i}{\partial \mathcal{F}_j}, \quad (P^{\mathcal{G}}_n)_{ij} = \frac{\partial (f_{n,3})_i}{\partial \mathcal{G}_j}. \qquad \text{(A-5)}
$$

In the expressions above we have represented the complex shapelet coefficients $f_{n,m}$ in a vectorized form, defining $(f_{n,m})_i = (\ \mathrm{Re}\{f_{n,m}\},\ \mathrm{Im}\{f_{n,m}\}\ )$.

Since we are constructing estimators of gravitational flexion but may only use the observable (i.e. non centroid shifting) effects of this distortion, it is necessary that we correct for the gravitational shift. I therefore used Equations (3.83), (3.84), and Equations (A-1) and (A-2) to find the following expressions (in a somewhat compactified form) for the first flexion susceptiibilty matrix for a generalized $f_{n,1}$ estimator:

$$\begin{aligned}(P_n^{\mathcal{F}})_{11} + \mathrm{i}(P_n^{\mathcal{F}})_{21} \;=\; & \frac{\beta}{16\sqrt{2}}\Bigg\{ 3\sqrt{n+1}\Big[(n-1)(f^{\mathrm{s}}_{n-3,0} - f^{\mathrm{s}}_{n+1,0}) \;+ \\ & \qquad (n+3)(f^{\mathrm{s}}_{n-1,0} - f^{\mathrm{s}}_{n+3,0})\Big] \\ & + \; 3\sqrt{(n-3)(n-1)(n+1)}\; f^{\mathrm{s}}_{n-3,2} \\ & + \; (3n+11)\sqrt{n-1}\; f^{\mathrm{s}}_{n-1,2} \\ & - \; (3n-5)\sqrt{n+3}\; f^{\mathrm{s}}_{n+1,2} \\ & - \; 3\sqrt{(n+1)(n+3)(n+5)}\; f^{\mathrm{s}}_{n+3,2} \\ & + \; 2\frac{(R^2)^{\mathrm{s}}}{\beta^2}(6+5\varepsilon^{\mathrm{s}})\sqrt{n+1}(f^{\mathrm{s}}_{n+1,0} - f^{\mathrm{s}}_{n-1,0}) \\ & + \; 2\frac{(R^2)^{\mathrm{s}}}{\beta^2}(6+5(\varepsilon^{\mathrm{s}})^*)(\sqrt{n+3}f^{\mathrm{s}}_{n+1,2} - \sqrt{n-1}f^{\mathrm{s}}_{n-1,2})\Bigg\}\end{aligned} \tag{A-6}$$

$$\begin{aligned}(P_n^{\mathcal{F}})_{22} + \mathrm{i}(P_n^{\mathcal{F}})_{12} \;=\; & \frac{\beta}{16\sqrt{2}}\Bigg\{ 3\sqrt{n+1}\Big[(n-1)(f^{\mathrm{s}}_{n-3,0} - f^{\mathrm{s}}_{n+1,0}) \;+ \\ & \qquad (n+3)(f^{\mathrm{s}}_{n-1,0} - f^{\mathrm{s}}_{n+3,0})\Big] \\ & - \; 3\sqrt{(n-3)(n-1)(n+1)}\; f^{\mathrm{s}*}_{n-3,2} \\ & - \; (3n+11)\sqrt{n-1}\; f^{\mathrm{s}*}_{n-1,2} \\ & + \; (3n-5)\sqrt{n+3}\; f^{\mathrm{s}*}_{n+1,2} \\ & + \; 3\sqrt{(n+1)(n+3)(n+5)}\; f^{\mathrm{s}*}_{n+3,2} \\ & + \; 2\frac{(R^2)^{\mathrm{s}}}{\beta^2}(6-5(\varepsilon^{\mathrm{s}})^*)\sqrt{n+1}(f^{\mathrm{s}}_{n+1,0} - f^{\mathrm{s}}_{n-1,0}) \\ & - \; 2\frac{(R^2)^{\mathrm{s}}}{\beta^2}(6-5\varepsilon^{\mathrm{s}})\big(\sqrt{n+3}f^{\mathrm{s}*}_{n+1,2} - \sqrt{n-1}f^{\mathrm{s}*}_{n-1,2}\big)\Bigg\}\,.\end{aligned} \tag{A-7}$$

In each expression, the last two lines correspond to the contribution owing to the correction necessary to account for the first flexion centroid shift.

Similarly, the second flexion susceptibility matrices for the $f_{n,3}$ estimators may be calculated using Equations (3.85) and (3.86), and Equations (A-3) and (A-4). These matrices are then found to be given by the

following expressions:

$$
\begin{aligned}
(P_n^{\mathcal{G}})_{11} + \mathrm{i}(P_n^{\mathcal{G}})_{21} \;=\; & \frac{\beta}{16\sqrt{2}} \Bigg\{ \sqrt{(n-1)(n+1)(n+3)} \times \\
& \qquad \left(f^{\mathrm{s}}_{n-3,0} + f^{\mathrm{s}}_{n-1,0} - f^{\mathrm{s}}_{n+1,0} - f^{\mathrm{s}}_{n+3,0}\right) \\
& + \sqrt{(n-7)(n-5)(n-3)}\, f^{\mathrm{s}}_{n-3,6} \\
& + \sqrt{(n-5)(n-3)(n+5)}\, f^{\mathrm{s}}_{n-1,6} \\
& - \sqrt{(n-3)(n+5)(n+7)}\, f^{\mathrm{s}}_{n+1,6} \\
& - \sqrt{(n+5)(n+7)(n+9)}\, f^{\mathrm{s}}_{n+3,6} \\
& + 2\frac{R^{\mathrm{s}2}}{\beta^2}\varepsilon^{\mathrm{s}}\left(\sqrt{n-1} f^{\mathrm{s}*}_{n+1,2} - \sqrt{n+3} f^{\mathrm{s}*}_{n-1,2}\right) \\
& + 2\frac{R^{\mathrm{s}2}}{\beta^2}\varepsilon^{\mathrm{s}*}\left(\sqrt{n+5} f^{\mathrm{s}*}_{n+1,4} - \sqrt{n-3} f^{\mathrm{s}*}_{n-1,4}\right) \Bigg\}
\end{aligned}
\tag{A-8}
$$

$$
\begin{aligned}
(P_n^{\mathcal{G}})_{22} + \mathrm{i}(P_n^{\mathcal{G}})_{12} \;=\; & \frac{\beta}{16\sqrt{2}} \Bigg\{ \sqrt{(n-1)(n+1)(n+3)} \times \\
& \qquad \left(f^{\mathrm{s}}_{n-3,0} + f^{\mathrm{s}}_{n-1,0} - f^{\mathrm{s}}_{n+1,0} - f^{\mathrm{s}}_{n+3,0}\right) \\
& - \sqrt{(n-7)(n-5)(n-3)}\, f^{\mathrm{s}*}_{n-3,6} \\
& - \sqrt{(n-5)(n-3)(n+5)}\, f^{\mathrm{s}*}_{n-1,6} \\
& + \sqrt{(n-3)(n+5)(n+7)}\, f^{\mathrm{s}*}_{n+1,6} \\
& + \sqrt{(n+5)(n+7)(n+9)}\, f^{\mathrm{s}*}_{n+3,6} \\
& + 2\frac{R^{\mathrm{s}2}}{\beta^2}\varepsilon^{\mathrm{s}*}\left(\sqrt{n-1} f_{n+1,2} - \sqrt{n+3} f_{n-1,2}\right) \\
& + 2\frac{R^{\mathrm{s}2}}{\beta^2}\varepsilon^{\mathrm{s}}\left(\sqrt{n+5} f^{\mathrm{s}}_{n+1,4} - \sqrt{n-3} f^{\mathrm{s}}_{n-1,4}\right) \Bigg\}.
\end{aligned}
\tag{A-9}
$$

As in the case of the first flexion, the final two lines emerge due to the need to correct for the shift in an object's apparent centroid during flexion. Equations (A-6)-(A-9) are the expressions given for the flexion susceptibility matrices in Massey et al. (2007d).